



**HAL**  
open science

# Bulk and surface modifications of metals submitted to hydrogen plasmas: the case of aluminum and tungsten Jury

Catalina Quiros Lara

► **To cite this version:**

Catalina Quiros Lara. Bulk and surface modifications of metals submitted to hydrogen plasmas: the case of aluminum and tungsten Jury. Chemical and Process Engineering. Université Sorbonne Paris Cité, 2017. English. NNT : 2017USPCD057 . tel-02288579

**HAL Id: tel-02288579**

**<https://theses.hal.science/tel-02288579>**

Submitted on 14 Sep 2019

**HAL** is a multi-disciplinary open access archive for the deposit and dissemination of scientific research documents, whether they are published or not. The documents may come from teaching and research institutions in France or abroad, or from public or private research centers.

L'archive ouverte pluridisciplinaire **HAL**, est destinée au dépôt et à la diffusion de documents scientifiques de niveau recherche, publiés ou non, émanant des établissements d'enseignement et de recherche français ou étrangers, des laboratoires publics ou privés.



Thèse présentée par  
Catalina QUIROS LARA

Pour obtenir le grade de

*Docteur de l'Université Paris XIII Sorbonne Paris Cité*

*Discipline: Génie des Procédés*

12 décembre 2017

---

# **Bulk and surface modifications of metals submitted to hydrogen plasmas: the case of aluminum and tungsten**

---

Jury:

Thierry BELMONTE, DR-CNRS, IJL, Nancy (Rapporteur)

Xavier BONNIN, Scientist ITER Organization, St-Paul les Durance (Examineur)

Yann CHARLES, MCF-HDR, CNRS-LSPM, Université Paris XIII (Examineur)

Gregory DE TEMERMAN, Scientist ITER Organization St-Paul Les Durance (Invité)

Christian GRISOLIA, DR-CEA, IRFM, Cadarache (Rapporteur)

Khaled HASSOUNI, Professeur, CNRS-LSPM, Université Paris XIII (Directeur)

Guillaume LOMBARDI, MCF-HDR, CNRS-LSPM, Université Paris XIII (Encadrant)

Jonathan MOUGENOT, MCF, CNRS-LSPM, Université Paris XIII (Invité)

Michael REDOLFI, MCF, CNRS-LSPM, Université Paris XIII (Invité)

Philippe SUPIOT, Professeur, IEMN-USTL, Lille (Examineur)



## Abstract

Plasma facing components in fusion reactors are exposed to intense thermal loads, plasma disruptions and high-flux particle bombardment. This leads to a plasma wall interaction that degrades the overall performance of the materials, limits the lifetime of the components and has a strong influence on the plasma performance. One problem derived from plasma wall interactions is bubble and blister formation in materials. This poses a great concern since it changes the material properties and favors hydrogen isotope (HI) retention. Since tritium, a HI, is radioactive, its inventory is quite limited. Experiments have shown that surface modifications are highly influenced by several parameters such as incident ion energy, fluence and crystallographic orientation. This work focuses on analyzing blister and bubble dynamics due to hydrogen plasma exposure in materials with a cubic crystal system and a low hydrogen solubility (*i.e.* Al and W). This provides a suitable background to understand phenomena related to crystallographic structure in hexagonal systems such as beryllium. In order to perform the experiments, the samples were polished and submitted to a heat treatment to obtain a well-defined low-roughness base material. Afterwards, they were exposed to a fully characterized hydrogen plasma in which several parameters were varied, such as incident ion energy, fluence and discharge regime. The latter was performed in order to study the effects stress, relaxation and cooling have on bubble and blister formation given that current plasma reactors work in cycles instead of continuous plasma exposure. In addition, the microstructure and crystallographic orientation of the materials was varied during the experiments. The analysis of crystallographic orientation were performed by using  $\{100\}$ ,  $\{110\}$  and  $\{111\}$  single crystals. This allows studying blister morphology without the effect of grain boundaries and setting the basis to understand hexagonal crystal systems. Finally, in order to understand hydrogen dynamics in materials a 1D macroscopic rate equations model with a code named Hydrogen Isotope Inventory Processes Code (HIIPC) was used. This model allows predicting the amount of retained HI's in materials and the physical processes involved in this interaction such as HI implantation, migration, depth distribution and their release. The results obtained with HIIPC support the results obtained in the experimental section and contribute in the understanding of hydrogen dynamics in material.

**Thesis title:** Bulk and surface modifications of metals submitted to hydrogen plasmas: the case of aluminum and tungsten

**Keywords:** Hydrogen plasma, aluminum, beryllium, tungsten, blisters, bubbles, plasma wall interaction

## Résumé

Les éléments de parois des réacteurs de fusion nucléaire sont soumis à de forts flux de chaleur, des disruptions du plasma et des forts flux des particules. Cette interaction donne lieu à la dégradation de la performance globale des matériaux, diminue la durée de vie des composants et a une forte influence sur la performance du plasma. Un des gros problèmes des interactions plasma-surface est la formation de bulles dans les matériaux, et de cloques en surface. En effet, la formation des bulles et des cloques modifie les propriétés du matériaux et favorise la rétention d'hydrogène. Les expériences ont montré que ce phénomène est influencé par plusieurs paramètres tels que l'énergie des ions impactant la surface, la fluence du plasma, la microstructure et la direction cristallographique des matériaux. Ce travail se concentre sur l'analyse de la dynamique de croissance des bulles et des cloques due à l'exposition à un plasma d'hydrogène dans des matériaux avec un système cristallin cubique et une faible solubilité de l'hydrogène, *i.e.* l'aluminium. Cela fournit un contexte approprié pour comprendre les phénomènes liés à la structure cristallographique dans des systèmes hexagonaux plus complexes tels que le béryllium. Afin d'effectuer les expériences, les échantillons sont polis et soumis à un traitement thermique pour obtenir un matériau de base de basse rugosité sans contraintes. Par la suite, les échantillons ont été exposés à un plasma d'hydrogène entièrement caractérisé dans lequel plusieurs paramètres ont été variés, tels que l'énergie ionique incidente, la fluence du plasma et la nature de l'exposition. Ce dernier point a été réalisé afin d'étudier les effets de la contrainte, de la relaxation et du refroidissement sur la formation de bulles et de cloques, étant donné que les réacteurs plasma de fusion actuels fonctionnent en cycles au lieu de l'exposition continue au plasma. De plus, la microstructure et l'orientation cristallographique des matériaux ont été investiguées au cours des expériences. L'analyse de l'orientation cristallographique a été effectuée en utilisant des monocristaux  $\{100\}$ ,  $\{110\}$  and  $\{111\}$ . Cela permet d'étudier la morphologie des cloques sans l'effet des joints des grains et de poser les bases pour comprendre les systèmes de cristaux hexagonaux. Finalement, afin de comprendre la dynamique de l'hydrogène dans les matériaux, un modèle d'équations macroscopiques 1D avec un code appelé Hydrogen Isotope Inventory Processes Code (HIIPC) a été utilisé. Ce modèle permet de prédire la quantité des isotopes d'hydrogène (HI) retenue dans les matériaux et les processus physiques impliqués dans cette interaction,

telles que l'implantation des HI, leur migration, leur distribution en profondeur, et leur libération. Les résultats obtenus avec HIIPC corroborent les résultats obtenus dans la section expérimentale et contribuent à la compréhension de la dynamique de l'hydrogène dans les matériaux.

**Titre de la thèse:** Modifications en bulk et en surface des matériaux métalliques soumis aux plasmas d'hydrogène: le cas de l'aluminium et du tungstène

**Keywords:** plasma d'hydrogène, aluminum, beryllium, tungsten, bulles, cloques, interaction plasma surface



## **Acknowledgements**

Firstly, I would like to express my sincere gratitude to my thesis director, Khaled Hassouni for his patience, motivation, and immense knowledge. His guidance and scientific discussions were essential for the development of this work. I would also like to thank my thesis supervisor, Guillaume Lombardi, for always being there to discuss my work, help me solve problems and encourage me during the past four years.

I would like to express my gratitude to the members of the examining board, who devoted their time to this thesis and more particularly to Thierry Belmonte, Christian Grisolia and Gregory DE Temmerman for having agreed to read and comment my thesis work.

I am extremely grateful with all the researchers, engineers and technicians at LSPM who contributed to this work. In particular, Ovidiu Brinza for helping me and guiding me during the experiments. Thierry Chauveau for helping me understand the complicated world of crystallography, Jonathan Mougnot for all the patience and time devoted to help me with HIIPC, Michael Redolfi for always helping solve problems with the CASIMIR reactor, Ludovic William for always being there to help me repair the reactor, Bermene and Wisline Beucia for your valuable advice and help with the EBSD measurements and Arlette Vega for the incredible help during these four years.

I would also like to acknowledge Bavani and Walid for helping me perform the experiments. Also, I would like to thank my fellow PhD labmates, Salima, Mine, Kader, Sarah, Vasuki, Lahcene, Pauline, Benoit and Zofia for the encouragement and fun we had these past years. Additionally, thanks to my family, which has always been there for me for his unconditional support and encouragement during this time.



# Table of contents

<b>Nomenclature</b>	<b>xi</b>
<b>Introduction</b>	<b>1</b>
<b>1 Theoretical background of the thesis: Fundamentals of Plasma Physics, Materials Science and Plasma Surface Interactions in the frame of fusion plasmas</b>	<b>5</b>
1.1 Nuclear Fusion and ITER project . . . . .	6
1.1.1 Plasma facing components in ITER . . . . .	8
1.2 Plasma sheath . . . . .	11
1.3 Plasma wall interactions . . . . .	14
1.3.1 Chemical Sputtering . . . . .	15
1.3.2 Sputtering . . . . .	16
1.3.3 Ionization, Multi-wall Interaction and Redeposition . . . . .	20
1.3.4 Ion implantation . . . . .	21
1.4 The structure of crystalline solids . . . . .	23
1.4.1 Poly-crystalline materials . . . . .	27
1.4.2 Single crystals . . . . .	28
1.4.3 Defects or imperfections in solids . . . . .	28
1.5 Hydrogen in metals: solubility and diffusion . . . . .	34
1.5.1 Solubility . . . . .	34
1.5.2 Diffusion . . . . .	35
1.6 Bubble formation and material modifications . . . . .	38
1.6.1 Introduction . . . . .	38
1.6.2 Mechanisms of bubble nucleation and growth . . . . .	40
1.7 Aluminum as a possible proxy for Beryllium . . . . .	45
1.7.1 Physical properties of Al and Be . . . . .	46
1.7.2 Chemical properties of Al and Be . . . . .	52
1.8 Context of this PhD project . . . . .	54

---

1.9	Research proposal . . . . .	55
<b>2</b>	<b>Materials, Methods and Plasma Characterization</b>	<b>57</b>
2.1	Experimental set-up . . . . .	57
2.1.1	Mono-source . . . . .	58
2.1.2	CASIMIR . . . . .	60
2.2	Sample characterization tools . . . . .	62
2.2.1	Scanning Electron Microscopy . . . . .	62
2.2.2	Confocal microscopy . . . . .	65
2.2.3	X-Ray Diffraction . . . . .	67
2.3	Sample preparation and characterization . . . . .	76
2.3.1	Polishing procedure . . . . .	76
2.3.2	Heat treatment . . . . .	78
2.4	Plasma Characterization . . . . .	80
2.4.1	Plasma potential . . . . .	81
2.4.2	Electron temperature and density in a hydrogen plasma . . . . .	82
2.5	Flux and fluence in a hydrogen plasma . . . . .	82
2.6	Optical spectroscopy and dust collection of aluminum dust containing plasmas	84
2.7	Aluminum dust formation . . . . .	86
2.7.1	Aluminum dust formation using argon plasma . . . . .	87
2.7.2	Aluminum dust formation using hydrogen plasma . . . . .	89
<b>3</b>	<b>Plasma surface interaction between hydrogen plasma and an aluminum target</b>	<b>91</b>
3.1	Introduction . . . . .	92
3.1.1	Major observed surface modifications . . . . .	93
3.1.2	Experimental conditions used in the experiments . . . . .	97
3.2	Influence of incident ion energy . . . . .	98
3.2.1	Blister formation . . . . .	99
3.2.2	Cross section . . . . .	102
3.3	Influence of fluence . . . . .	107
3.3.1	Surface morphology after continuous plasma exposure . . . . .	109
3.3.2	Surface morphology after cyclic plasma exposure . . . . .	119
3.3.3	Cross-section of Al samples after continuous plasma treatment . . . . .	126
3.3.4	Comparison between continuous and cyclic plasma exposure . . . . .	130
3.4	Influence of surface finish . . . . .	133
3.5	Influence of grain boundary misorientation . . . . .	135
3.6	Influence of crystallographic orientation . . . . .	136

3.7	Summary and discussion . . . . .	148
<b>4</b>	<b>Plasma surface interaction between hydrogen plasma and tungsten</b>	<b>153</b>
4.1	Tungsten polycrystalline textured samples . . . . .	155
4.1.1	Production of textured polycrystalline samples . . . . .	155
4.1.2	Experimental procedure . . . . .	160
4.1.3	Experimental results . . . . .	162
4.2	Tungsten single crystals . . . . .	166
4.3	Summary and discussion . . . . .	177
<b>5</b>	<b>Macroscopic Rate Equations model of hydrogen retention in metals</b>	<b>179</b>
5.1	Overview of MRE models . . . . .	180
5.2	HIIPC model . . . . .	183
5.2.1	Rate equation for diffusion and trapping . . . . .	184
5.2.2	Traps creation due to ion bombardment . . . . .	192
5.2.3	Bubble kinetics growth model . . . . .	193
5.3	Model Solution . . . . .	197
5.4	General Model Results . . . . .	198
5.4.1	Isothermal hydrogen dynamics . . . . .	199
5.4.2	Non-isothermal hydrogen dynamics . . . . .	200
5.4.3	Non-isothermal cyclic hydrogen dynamics . . . . .	201
5.4.4	MRE simulation of thermal desorption . . . . .	202
5.5	Simulations for specific aluminum loading experiments . . . . .	203
5.5.1	Aluminum single crystals exposed to hydrogen plasma . . . . .	203
5.5.2	Aluminum exposed to hydrogen plasma at different incident ion energies . . . . .	206
5.5.3	Bubble growth in an aluminum sample . . . . .	210
5.5.4	Thermal desorption Spectroscopy . . . . .	212
5.6	Differences in HI retention mechanisms between aluminum and beryllium .	214
5.7	Simulation for specific tungsten experiments . . . . .	217
5.8	Summary and discussion . . . . .	220
<b>6</b>	<b>Conclusions and Perspectives</b>	<b>223</b>
6.1	Conclusions . . . . .	223
6.2	Perspectives . . . . .	226
	<b>References</b>	<b>231</b>



# Introduction

Man-made plasmas are subject, in most cases, to interactions between the plasma and a solid surface. Plasma surface interactions (PSI's) involves key phenomena that determine the capability of the plasma to be used in a wide variety of applications such as etching and chemical vapor deposition in micro-electronics, thermal spray coatings, production of diamond films and amorphous silicon for solar cells, plasma hardening of surgically implanted hip joints, treatment of synthetic fabrics and other polymer materials, and residual cleaning of organics at the molecular level on several materials, among plenty others (Adamovich et al., 2017; Fridman, 2008; Lieberman and Lichtenberg, 2005). However, not all PSI are beneficial. This is the case of plasma wall interactions (PWI's) in thermonuclear fusion reactors. In these reactors, deuterium and tritium are confined as fuel that is then heated up to high temperatures so as the nuclei can fuse. Due to the high temperatures, in the order of  $1 \times 10^8$  K, needed in order to achieve nuclear fusion, plasma must be confined using strong magnetic fields. However, this confinement is not perfect and there are always particles that manage to escape and interact with the surrounding walls. The PWI in fusion reactors degrades the overall performance of the materials, limits the lifetime of the plasma facing components (PFC's) and has a strong influence on the plasma performance. Therefore, it is of paramount importance to understand the processes occurring at this interface with the aim of developing new approaches to overcome this problem.

At the moment there are no available materials that fulfill the requirements to withstand the harsh conditions present in the vacuum chamber. The PWI in fusion reactors gives way to diverse and complex phenomena that change the properties of materials and degrade the lifetime of the PFC's. Additionally, due to sputtering and erosion there might be formation of dust particles that contaminate the plasma and interfere with fuel management in fusion reactors. In other words, plasma wall interaction phenomena affects the plasma characteristics and the confinement quality. Another problem in PFC is that fuel trapping limits its availability and poses a serious security risk. This is due to the fact that tritium is a radioactive material and its inventory in ITER is limited. Therefore there is an ongoing

research in this field to find the most suitable materials to be used as PFC's. In the mean time, the most appropriate available materials are used and wall conditioning techniques are implemented to counteract the degradation caused by plasma wall interactions. The PFC's of ITER are foreseen to be composed of two different materials: beryllium and tungsten. The former was chosen due to its low atomic number, high thermal conductivity, low neutron activation and high oxygen gettering ability whereas the latter was chosen because it has a high melting point, high threshold for sputtering, low vapor pressure, low neutron activation, no chemical erosion and low tritium retention. Each of these characteristics is determined by the conditions experienced by these materials in the fusion reactors. Tungsten is expected to occupy a limited area where it will receive very high fluxes. On the other hand, beryllium is expected to occupy a larger area, is closer to the plasma, but is expected to receive lower fluxes.

Both tungsten and beryllium will be exposed to intense thermal loads (up to 20 MW/m<sup>2</sup>), plasma disruptions and high-flux particle bombardment ( $10^{20} - 10^{24}$  ions/m<sup>2</sup>s) (ITER, 1999; Konings, 2012). Under these conditions, materials undergo different surface and volume modifications such as bubble and blister formation, cracking and surface erosion. As a result, thermal and mechanical properties of the materials are affected. It is required to understand surface and volume modifications in materials in order to minimize or avoid their formation. The main objective of this thesis is to study the surface and volume modification mechanisms involved in PSI relevant for edge fusion plasmas. Emphasis is made on modifications of either ITER relevant materials, or a suggested proxy of these materials, after hydrogen plasma exposure. The investigation of basic phenomena in PWI between PFC and hydrogen plasma can be performed by using electron cyclotron resonance (ECR) microwaves reactors. These reactors allow the partial simulation of some of the phenomena that occurs in edge plasma by providing high atomic, ionic and electronic densities, and hence, high ion fluxes.

When materials are exposed to hydrogen flux, hydrogen atoms can be implanted in the material. These atoms may diffuse in the material and be trapped in defects such as vacancies. It is possible to achieve extremely high concentrations of hydrogen, higher than the solubility limit, in materials exposed to sufficiently high fluxes. At high hydrogen concentrations, it is energetically favorable for hydrogen atoms to precipitate into hydride phases or gas bubbles, depending on the nature of the material (Post and Behrisch, 1986).

This thesis work focuses on bubble and blister formation in materials. This phenomenon is influenced by a large number of parameters such as fluence, incident ion energy, bulk

structure of the material and methods of production or pre-treatment among others (Behrish, 1983). During this work, these parameters are studied in detail for ITER relevant materials, or a suggested proxy of these materials, in order to understand the bubble formation mechanisms. Nevertheless, beryllium is a toxic material that should be manipulated under strictly controlled conditions. Therefore, a proxy material should be used during the experiments. During this work, the use of aluminum as a stand-in for beryllium is analyzed. This work includes 5 chapters and is divided as follows:

**Chapter 1** introduces the fundamental topics of nuclear fusion and thermonuclear reactors. Additionally, the basic aspects on materials science such as structure of crystalline solids, single crystals, poly-crystalline solids and defects on solid materials are presented. These concepts aid in providing a suitable background to understand the physics behind the interactions occurring at the plasma surface interface in fusion reactors. Emphasis is made on describing hydrogen implantation in metals and bubble formation mechanisms, given that these phenomena play an important role in the experiments performed throughout the present work. Additionally, the different characteristics of tungsten and beryllium, the PFC materials of ITER, are presented. Finally, the use of aluminum as a possible proxy for beryllium is discussed.

**Chapter 2** describes the plasma devices used during this work and their characterization in terms of flux, fluence, temperature and ion energy. Then the techniques used to characterize the samples used in the experiments are presented. These devices are: confocal optical microscopy, electron microscopy and X-ray measurements. The initial characterization of the samples and their pre-treatments.

**Chapter 3** focuses on the analysis of plasma wall interactions with aluminum. Different parameters that affect surface morphology and bubble and blister formation in materials were analyzed. These parameters are: incident ion energy, plasma fluence, sample roughness and micro-structure. In some cases, the cross-section of the sample was analyzed with the aim of correlating the phenomena occurring at the surface and in the bulk. Special attention was given to the effect that crystallographic structure has on blister morphology. Experiments were performed by exposing single crystals samples to hydrogen plasma with the aim of analyzing how blister growth is affected by crystallographic orientation without the effect of grain boundaries.

**Chapter 4** is dedicated to experiments performed with tungsten. This material is analyzed by exposing textured polycrystalline samples and single crystals to specific plasma conditions and studying different aspects of blister formation and growth as well as their morphology. This chapter enables to study the crystal symmetry that complement the results obtained with single crystal aluminum samples. This gives a global picture of the effect cubic crystal systems have on blister morphology.

**Chapter 5** presents the basic principles and main results obtained with a Macroscopic Rate equations (MRE) model used to simulate hydrogen retention in material. Simulations including hydrogen dynamics and bubble growth were performed with aluminum under different incident ion energies. The aluminum case was compared with beryllium. Finally, bubble growth was simulated for tungsten under different temperatures with the aim of studying the experimental conditions for bubble formation in this material.

Finally, **Chapter 6** summarizes the main results obtained in this thesis and presents a global picture on the material changes that occur during hydrogen charging. Based on the obtained results, we also provide an outlook on possible further investigations and perspectives on this subject.

# Chapter 1

## **Theoretical background of the thesis: Fundamentals of Plasma Physics, Materials Science and Plasma Surface Interactions in the frame of fusion plasmas**

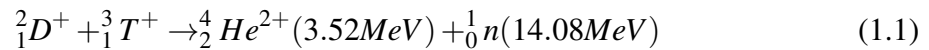
The main objective of this chapter is to introduce the main phenomena involved in plasma surface interactions, such as hydrogen implantation and retention in solids, and material modifications. Some of these phenomena are responsible for fuel retention in thermonuclear fusion reactors and for the degradation of material performance, which limits the lifetime of the plasma facing components (PFC's). At the present time there are no materials available to withstand the conditions found in fusion reactors. Nevertheless, beryllium and tungsten were proposed as PFC materials for ITER, the world's largest fusion reactor which is expected to be operational in the near future. These materials are the most suitable ones given their physical and chemical properties. In this Chapter the properties of both of these materials are presented and the use of aluminum as a proxy for beryllium is discussed. Nonetheless, in order to understand material modifications of metals when exposed to hydrogen plasma, it is imperative to understand the basic principles of material structure and their characteristics. Therefore, this chapter is organized as follows:

- Section 1.1 gives an introduction to the basis of nuclear fusion and the principles of magnetic confinement thermonuclear fusion reactors.

- Section 1.2 focuses on the physics occurring in plasmas at the interface between plasmas and a solid surface.
- Section 1.3 details the main phenomena occurring at the surface of materials when they interact with plasma.
- Section 1.4 introduces the basic principles of metals such as crystal systems, crystallographic directions and planes, polycrystalline and single crystal materials as well as defects found in solid materials.
- Section 1.5 presents the basic phenomena that occur when hydrogen ions interact with a solid surface; focusing on its implantation, retention and release.
- Section 1.6 describes the different phenomena that affect surface modifications caused by volume defects such as bubble formation in metals. In particular, the different theories used to describe bubble formation are described in this section.
- Section 1.7 introduces the basic physical and chemical properties of ITER relevant materials with the aim of discussing the choice of aluminum as a proxy for beryllium.

## 1.1 Nuclear Fusion and ITER project

Nuclear fusion consists in combining two light nuclei to form a heavier one, releasing a large amount of energy in the process. The most feasible way to achieve nuclear fusion is by using deuterium ( $D$ ) and tritium ( $T$ ) as fuel. This reaction produces helium nuclei ( ${}^4_2\text{He}$ ) and highly energetic neutrons (Chen, 2011):



There are certain conditions that should be met in order to achieve this reaction. Particles must have sufficient energy to overcome the electrostatic repulsion between the nuclei, meaning that they need to be heated up to temperatures of the order of millions of degrees Celsius. They also should be close enough to fuse, however, at higher densities the collisions between nuclei and electrons generate a considerable amount of Bremsstrahlung radiation that lowers the plasma power. Finally, they should be confined a certain time  $\tau_E$  which allows the particles, at a given temperature and density, to fuse. The relationship between the plasma temperature  $T$  the density  $n$  and the confinement time  $\tau_E$  is commonly known as the *Lawson Criterion*. This criterion states that the product of the plasma density  $n$ , the energy confinement time  $\tau_E$  and the plasma temperature  $T$  has to be higher than a certain value in

order to achieve a self-sustaining nuclear fusion reaction. For a D-T plasma, the Lawson criterion is met when (Chen, 2011; ITER, 2017):

$$nT\tau_e > 3 \times 10^{21} m^{-3} keVs \quad (1.2)$$

Due to the high temperatures needed in order to achieve nuclear fusion, plasma must be confined using magnetic fields. Due to the behavior of plasma in magnetic fields, the optimum way of confining it is by using an infinite cylinder. However, this solution is not realistic and a toroidal shaped confinement is used. Up to now, the toroidal confinement that has shown the best experimental results is known as a *tokamak*. This design uses coils to generate the toroidal magnetic field and external currents to generate the poloidal magnetic field. At present, the largest experimental nuclear fusion reactor, known as ITER (International Thermonuclear Experimental Reactor) is being built using the tokamak scheme.

The vacuum chamber of ITER, where the plasma is generated, is expected to have an exhaust system that controls the edge plasma. It is designed to extract heat, helium ash and other impurities from the plasma. The design of this system consists in arranging the coils in such a way that the outermost field lines are diverted far away from the plasma into a region known as the divertor, shown in Fig. 1.1 (Chen, 2011; Conn et al., 1997).

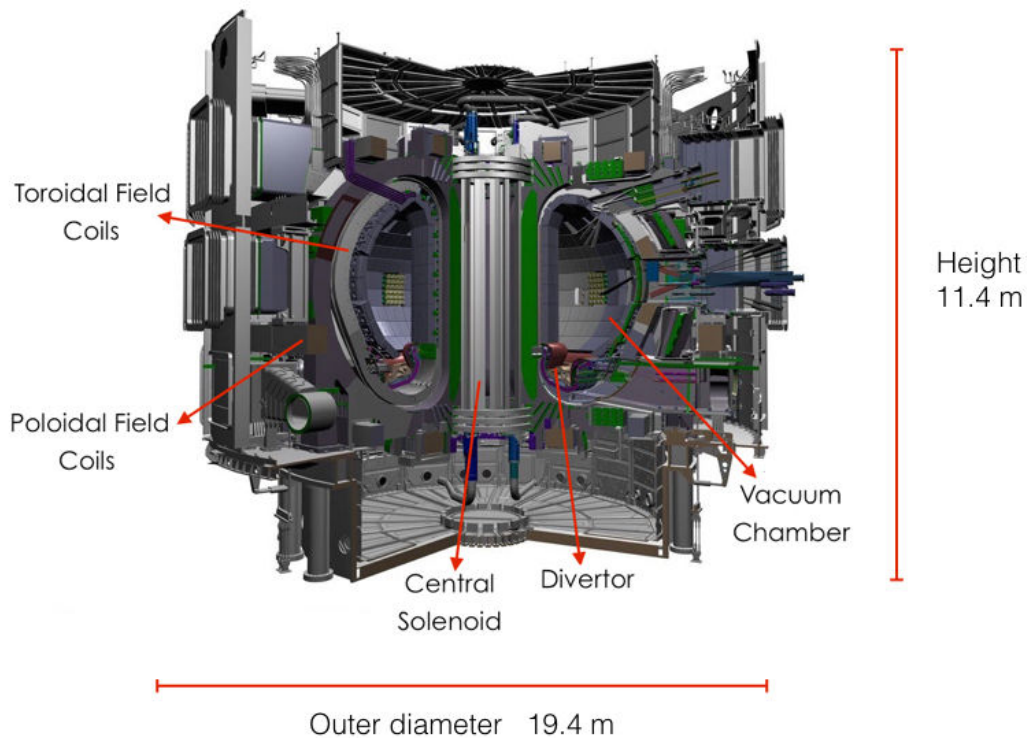


Fig. 1.1 Sketch of ITER and its dimensions (ITER, 2017)

The main characteristics of ITER's first plasmas, expected to take place in 2025, are shown in Table 1.1.

Parameter	Value
Major/minor radius	6.2 m / 2.0 m
Plasma volume	$\sim 850 \text{ m}^3$
Plasma surface area	$\sim 683 \text{ m}^2$
Nominal plasma current	15 MA
Electron density	$0.7 \times 10^{14} \text{ cm}^{-3}$
Volume average temperature	12.9 keV
Toroidal field	5.3 T (at $R = 6.2\text{m}$ )
Fusion power (ignited, nominal)	500 MW
Radiation from plasma core	20 – 50 MW
Transport power loss	50 – 80 MW
Transport energy confinement time $\tau_E$	3.0 s
Burn duration	$\geq 400 \text{ s}$
Available auxiliary heating power	53 – 73 MW
In vessel tritium inventory safety limit	1 kg

Table 1.1 ITER design features and parameters (ITER, 1999, 2017)

### 1.1.1 Plasma facing components in ITER

In ITER the PFC's will be exposed to intense thermal loads (up to  $20 \text{ MW/m}^2$  for the divertor region and  $0.5 \text{ MW/m}^2$  for the first wall), plasma disruptions and high-flux particle bombardment ( $10^{20} - 10^{24}$  ions/ $\text{m}^2\text{s}$ ) (ITER, 1999; Konings, 2012). To minimize the negative effects of these interactions, the vacuum chamber of ITER is foreseen to be composed of different materials. The first wall, which lies closer to the plasma, is expected to be made of beryllium and the divertor and dome region, which lie farther away from the plasma and are subject to energetic ion flux, are expected to be built using tungsten, as seen in Fig. 1.2.

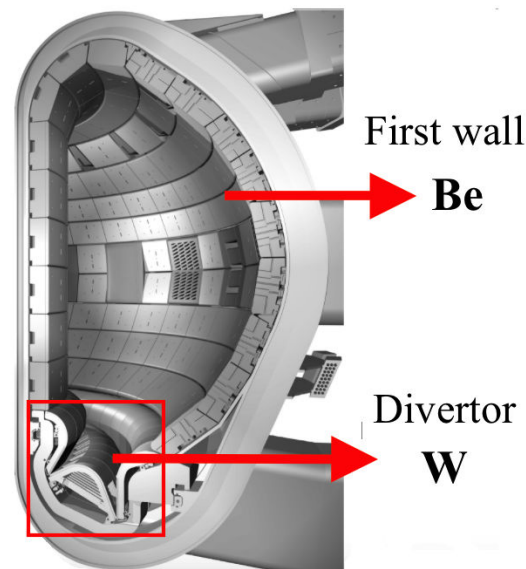


Fig. 1.2 Plasma facing components in ITER (ITER, 2017)

## Tungsten

Tungsten has a strong ability to withstand the harsh conditions present in the divertor area of fusion reactors. It is a refractory metal, which means that it is very resistant to heat due to its high melting temperature (3695 K). It has a high threshold for sputtering with energies of 153, 228 and 457 eV for  $T^+$ ,  $D^+$  and  $H^+$  ions respectively. Consequently, it has a low sputtering yield:  $7 \times 10^{-3}$  atoms/ions for D ions with an incident energy of 1000 eV (Behrish and Eckstein, 2007). Tungsten also presents low vapor pressure:  $1.37 \times 10^{-7}$  Pa at the melting temperature and high thermal conductivity (173 W/mK). It shows no chemical sputtering in H plasma and due to its low tritium retention, the tritium inventory in this material is expected to be small (Federici et al., 2001; ITER, 2017; Philipps et al., 2003).

On the other hand, this material presents certain undesirable characteristics. It is a high Z material ( $Z=74$ ) and therefore even low levels of tungsten contamination in the plasma lead to a strongly enhanced radiative cooling. Tungsten also has a low Ductile to Brittle Transition Temperature DBTT (423 K), which makes it sensitive to thermal shocks. It presents neutron-induced embrittlement, which leads to the generation of radioactive waste (Chen, 2011; ITER, 2017; Philipps et al., 2003). The characteristics of W as a plasma facing component are summarized in Table 1.2.

Strengths of W	Weaknesses of W
High melting point (3695 K)	High Z ( $Z=74$ )
High sputtering threshold	Low DBTT (423 K)
Low sputtering yield	High neutron activation
Low vapor pressure ( $1.37 \times 10^{-7}$ Pa at the melting temperature)	
High thermal conductivity (173 W/mK)	
No chemical sputtering in H plasma	
Low tritium retention	

*Table 1.2 Physical properties of tungsten as a PFC*

These characteristics make tungsten a promising material for the divertor region in ITER. This region is far away from the core plasma, therefore its high Z is not of great concern. Additionally, its high sputtering threshold makes tungsten a strong candidate for the divertor area. In this region a significant flux of hydrogen neutrals, predominantly of low energy, is expected. This leads to a large sputtering and unacceptably short lifetimes for other materials with a lower sputtering threshold, such as beryllium (Federici et al., 2001).

## **Beryllium**

The first wall area in fusion reactors lies closer to the core plasma than the divertor area. Therefore a material low Z is crucial to have lower radiative power losses. Even though it is not a refractory metal, Be fulfills this requirement due to its low Z ( $Z=4$ ). This means that plasma can withstand higher levels of Be contamination. This material has a high thermal conductivity (180 W/mK) and high oxygen gettering ability. Also, it presents a low neutron activation which minimizes the generation of radioactive waste (Conn et al., 1997; Federici et al., 2001; ITER, 2017).

However Be presents a limited thermal shock resistance due to its relatively low melting point (1560 K) and high vapor pressure ( $5 \times 10^{-2}$  Pa). In addition, neutron irradiation causes its embrittlement. Finally, it is a highly toxic material that requires controlled handling procedures. (Chen, 2011; Conn et al., 1997; ITER, 2017). A summary of the strengths and weaknesses of Be as PFC is given in Table 1.3.

Strengths of Be	Weaknesses of Be
Low Z (Z=4)	Limited thermal shock resistance
High thermal conductivity (180 W/mK)	Highly toxic material
Affinity to oxygen	Neutron induced brittleness
Low neutron activation	

Table 1.3 Physical properties of beryllium as a PFC

Tungsten and beryllium are expected to make up the first wall materials of the vacuum chamber in ITER. Both of these materials are foreseen to be subject to heat and particle fluxes from the plasma. The contact between the core plasma and the surface of the material takes place through a sheath region where the electrical neutrality is not fulfilled and the space charge field is very high. This transition region between the plasma and a solid surface is known as a Debye or plasma sheath. The next section describes in more detail this sheath region.

## 1.2 Plasma sheath

The main characteristic of plasmas is their *quasi-neutrality*. In other words, in plasmas the electron density  $n_e$  is approximately equal to the ionic density  $n_i$  ( $n_e \approx n_i$ ). However, all plasma reactors have a transition region from plasma characterized by an intense electric field where plasma *quasi-neutrality* does not hold ( $n_e \neq n_i$ ). This transition region, known as *Debye* or *plasma sheath*, controls the particles fluxes and energy to the limiting materials.

Due to their lower mass, electrons in plasmas are much more mobile than ions. As a consequence, higher electrons fluxes arrive to the wall, which in turn becomes negatively charged with respect to the plasma. The negatively charged wall generates an electric field  $E$  directed towards it that accelerates the ions and decelerates the electrons, resulting in a region with an excess positive charge ( $n_i \gg n_e$ ). The net positive charge density leads to a potential profile that is positive within the plasma and falls sharply to zero near the walls. Fig. 1.3 shows a schematic of the electronic and ionic density as well as the potential  $\Phi$  in the plasma and sheath regions.

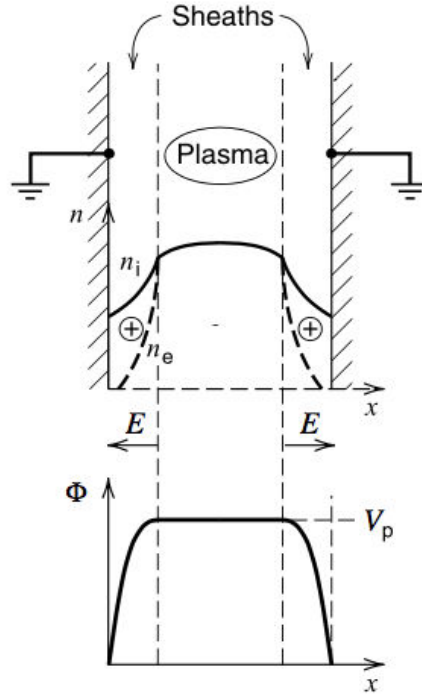


Fig. 1.3 Schematic of the variation of ion and electron density ( $n_i$  and  $n_e$  respectively) and electric potential  $\Phi$  in the plasma between two semi-infinite planes.  $V_p$  denotes the plasma potential with respect to the walls. The thickness of the sheath is amplified for illustration purposes (Lieberman and Lichtenberg, 2005).

Two main regimes may occur at the plasma sheath: non-collisional or collisional. They may be defined by taking into account the ion mean free path, sheath thickness and Debye length. The latter is defined as the maximum distance over which electrons in plasma can move with respect to the ions, against the electrostatic forces if the thermal energy of one degree of freedom  $kT_e/2$  is available.

The ion mean free path is calculated as follows:

$$\lambda_i = \frac{1}{n_g \sigma} \quad (1.3)$$

where  $\sigma$  is the ion-atom scattering cross-section ( $\approx 10^{-14} \text{ cm}^{-2}$ ) and  $n_g$  is the neutral gas density and is defined as  $n_g = P/kT$  with  $k$  being the Boltzmann's constant and  $T$  the gas temperature.

In order for the sheath to exist, ions must be accelerated at the sheath edge to the sound velocity, as follows:

$$v_B = \sqrt{\frac{kT_e}{m_i}} \quad (1.4)$$

where  $v_B$  is known as the Bohm velocity,  $k$  is the Boltzmann constant,  $T_e$  is the electron temperature and  $m_i$  is the ion mass (Lieberman and Lichtenberg, 2005; Stangeby, 2000).

The acceleration of ions to the sound velocity occurs in the residual electric field in the so called pre-sheath region.

The sheath thickness is calculated using Child's law:

$$s = \frac{\sqrt{2}}{3} \lambda_{Ds} \left( \frac{2V_0}{T_e} \right)^{3/4} \quad (1.5)$$

where  $V_0$  is the potential at the plasma-sheath boundary,  $T_e$  the electronic temperature and  $\lambda_{Ds}$  is the electron Debye length at the sheath edge, which is defined as follows:

$$\lambda_{Ds} = \sqrt{\frac{\epsilon_0 T_e^{3/2}}{n_s v_B (Me)^{1/2}}} \quad (1.6)$$

where  $\epsilon_0$  is the permittivity in free space,  $T_e$  the electron temperature,  $n_s$  the ion density at the sheath edge,  $v_B$  the sound velocity and  $M$  the ion mass.

With these parameters, the non-collisional and collisional sheath regimes are identified to occur under the following conditions:

- Non-collisional regime  $\lambda_i \gg s$
- Collisional or strongly coupled sheath  $\lambda_i \ll s$

For a non-collisional regime, the flux is obtained by multiplying this velocity by the ion density:

$$\Gamma_i = n_s v_B \quad (1.7)$$

where  $n_s$  is the ion density at the sheath region and  $v_B$  is the Bohm velocity.

By measuring the ion density and electron temperature, the ion flux can be easily calculated. This allows the calculation of the plasma fluence, as follows:

$$Fluence = \Gamma_i \times t \quad (1.8)$$

Both plasma flux and fluence are useful when analyzing phenomena occurring due to plasma wall interactions and their calculation allows to control the plasma conditions used in each experiment.

The acceleration of ions in the plasma sheath increases the energy of ions impinging the surface, thus affecting interactions with the wall. The principles of these plasma wall interactions are explained in the next section.

### **1.3 Plasma wall interactions**

One of the greatest technical challenges in present day fusion reactors deals with optimizing the interaction between the PFC's and the plasma itself. The magnetic fields are not able to fully confine the ions present in the plasma, so there is always some interaction between the plasma edge and the PFC's. This interaction gives way to diverse and complex phenomena that degrades the lifetime of the PFC's, contaminates the plasma and interferes with the fuel management in fusion reactors. The different phenomena occurring at the plasma edge of fusion reactors are illustrated in Fig. 1.4.

In this section, the different phenomena occurring in the plasma and at the solid material interface are studied in the following order:

- 1.3.1 Chemical Ablation
- 1.3.2 Sputtering
- 1.3.3 Ionization, Multi-wall Interaction and Redeposition
- 1.3.4 Fuel Implantation

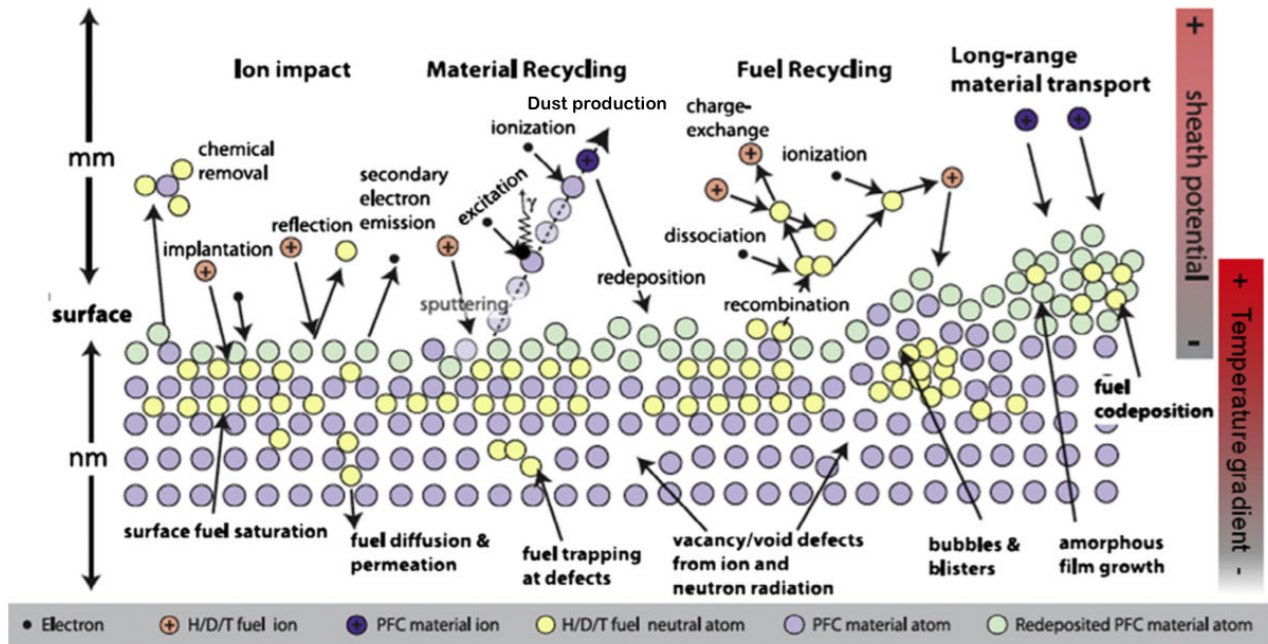


Fig. 1.4 Plasma wall interaction processes present in a fusion reactor (Wirth et al., 2015)

### 1.3.1 Chemical Sputtering

Chemical sputtering takes place when a chemical reaction occurs between the incident ion and an atom of the solid surface. Ions are neutralized during their interaction with the wall and may penetrate into a solid. For some species and values of kinetic energy, a molecule may form with the projectile and a surface atom. This molecule is weakly bounded to the surface and can then be desorbed into the gas phase (Federici et al., 2001).

Chemical sputtering poses a problem in reactors whose PFC's are made of materials that are highly reactive with hydrogen, such as carbon-based materials. Fig. 1.5 shows the chemical sputtering yield as a function of impinging hydrogen ion flux for various beams and tokamak experiments. For comparison purposes, the experimental data are normalized to an impact energy of 30 eV and a surface temperature corresponding to maximum yield. This compilation of data from various experiments indicates a strong flux dependence of the chemical sputtering yield: with increasing incoming hydrogen flux the yield decreases. The maximum chemical erosion yield of 0.8 atoms/ion is achieved at a flux of  $5 \times 10^{19}$  ions/m<sup>2</sup>s.

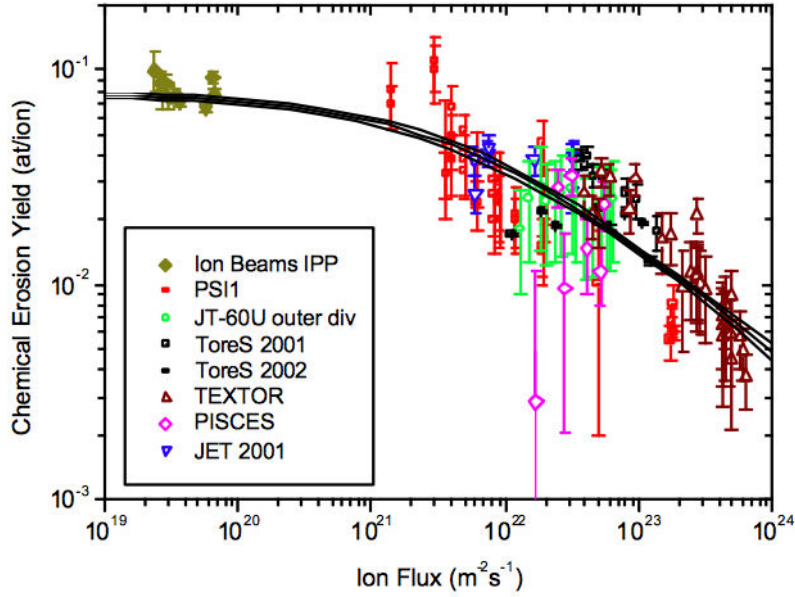


Fig. 1.5 Chemical sputtering yield of Carbon as a function of incident hydrogen ion flux for various beams and tokamak experiments (Roth et al., 2004)

### 1.3.2 Sputtering

Incident particles with sufficient energy are able to transfer enough energy to the material and overcome the surface binding energy  $E_s$  leading to the sputtering of surface atoms. Unlike chemical sputtering, physical sputtering consists solely in the sputtering of atoms from the solid and no chemical reaction takes place. The sputtering yield is proportional to the energy deposited in the elastic collisions within a near surface layer. At low energies, where the transferred energy to surface atoms is comparable with the surface binding energy, the sputtering yield decreases significantly and becomes zero below a threshold energy. As an example, the threshold energy  $E_T$  for physical sputtering at normal incidence may be estimated from (Hotston, 1975):

$$E_T = \frac{(M_1 + M_2)^2}{4M_1M_2} E_s \quad (1.9)$$

where  $E_s$  is the target sublimation energy and  $M_1$  is the molar mass of the target atom and  $M_2$  the colliding ion.

The angle of incidence influences the sputtering threshold energy and the sputtering yield. The angle of incidence  $\alpha_0$  of incident projectiles is defined as the angle between the velocity vector of the projectile and the surface normal vector. Therefore,  $\alpha_0 = 0^\circ$  and  $\alpha_0 = 90^\circ$  represent normal and grazing incidence, respectively. At normal incidence, the sputtering

yield increases with increasing angle of incidence. With more grazing incidence, more energy is deposited near the surface. After reaching a maximum yield  $\alpha_0 \approx 75^\circ$ , the sputtering yield strongly decreases. At these angles reflection of projectiles becomes more important, resulting in less energy available at the surface for sputtering (Ziegler et al., 2010).

The sputtering yield and threshold, *i.e.* the minimum energy needed to sputter a surface atom, for the different materials that make up PFC are presented below:

### Tungsten

The sputtering yields for W when bombarded with H, D,  $^4\text{He}$  and Ar is presented in Fig 1.6 a), b) and c) respectively. In all of these cases, sputtering yield increases with energy until it reaches a maximum. Then, it decreases given that implantation starts to take over. In the image, this decrease is not seen for Ar, however, this could be due to the fact that this decrease occurs at higher energies than those analyzed. In the figure, it is observed that the highest sputtering yield for Ar, D and  $^4\text{He}$  is reached at an energy of 60 keV, 2 keV and 1.5 keV, respectively. The highest sputtering yield values are obtained with Ar whereas the lowest values are obtained with hydrogen.

The sputtering threshold of tungsten for different impinging ions is given in Table 1.4. It is noticed that for hydrogen and deuterium ions the energy needed for sputtering is quite high with values of 458 eV and 229 eV respectively. The lowest sputtering threshold is for Ar, with a value of 27 eV. Energy transfer between the ion and the metal atoms is proportional to their mass ratio. Consequently, for the different incident energies, the fraction of energy transferred from an Ar atom to tungsten is higher than that transferred from H or He to tungsten. As a result, sputtering by Ar is activated at much lower energy, which results in a much lower sputtering threshold.

Ion	Sputtering Threshold (eV)
H	458
D	230
T	154
He	121
Ar	27

Table 1.4 Sputtering threshold of tungsten for different impinging ions (Behrish and Eckstein, 2007)

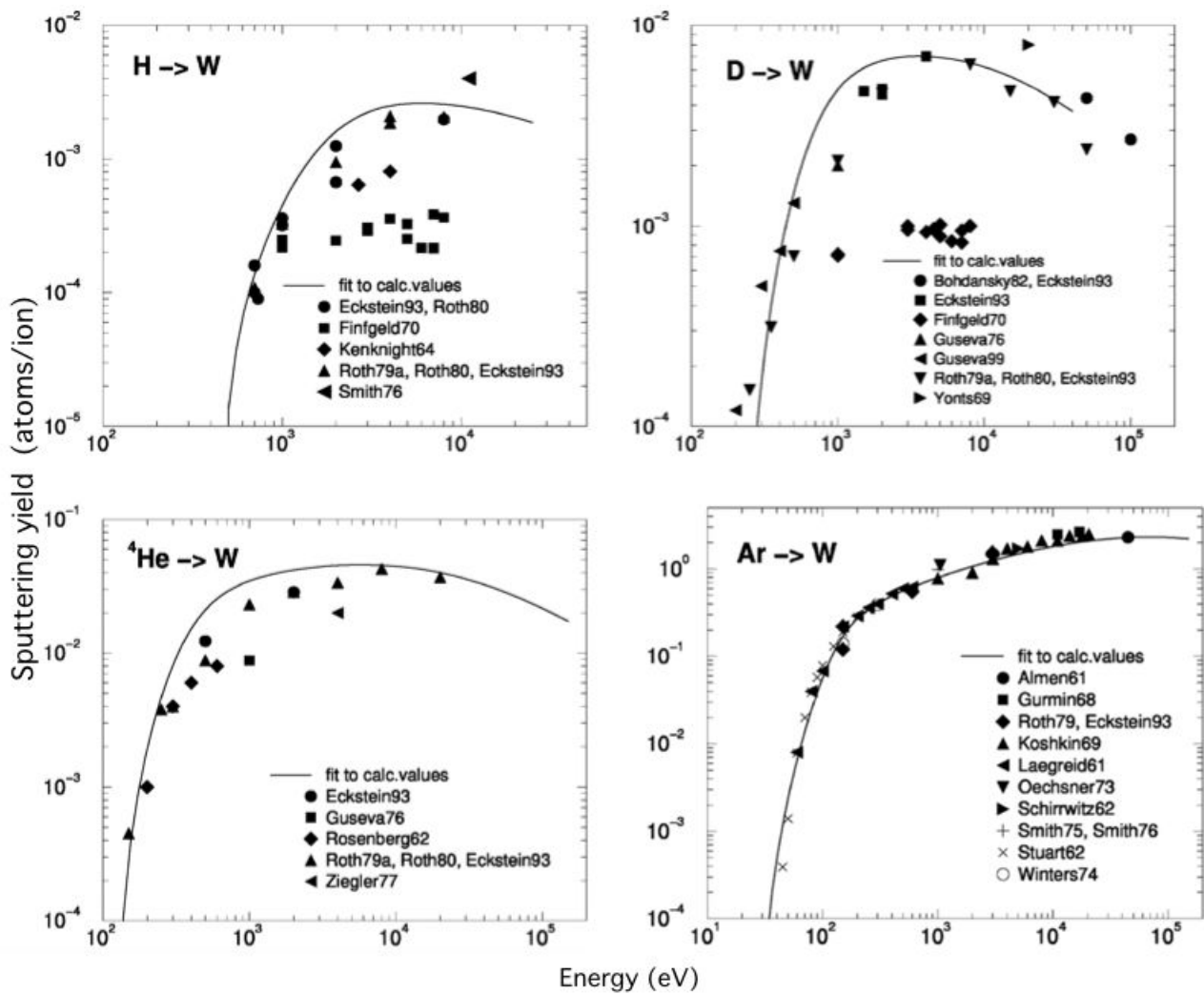


Fig. 1.6 Sputtering yield at normal incidence of W for different ions impacting the surface with different energies (Behrish and Eckstein, 2007)

## Beryllium

The sputtering yield for Be when bombarded with Ar, D and  $^4\text{He}$  ions is presented in Fig 1.7. It is seen that the lowest sputtering yield is obtained with deuterium whereas the highest one with Ar.

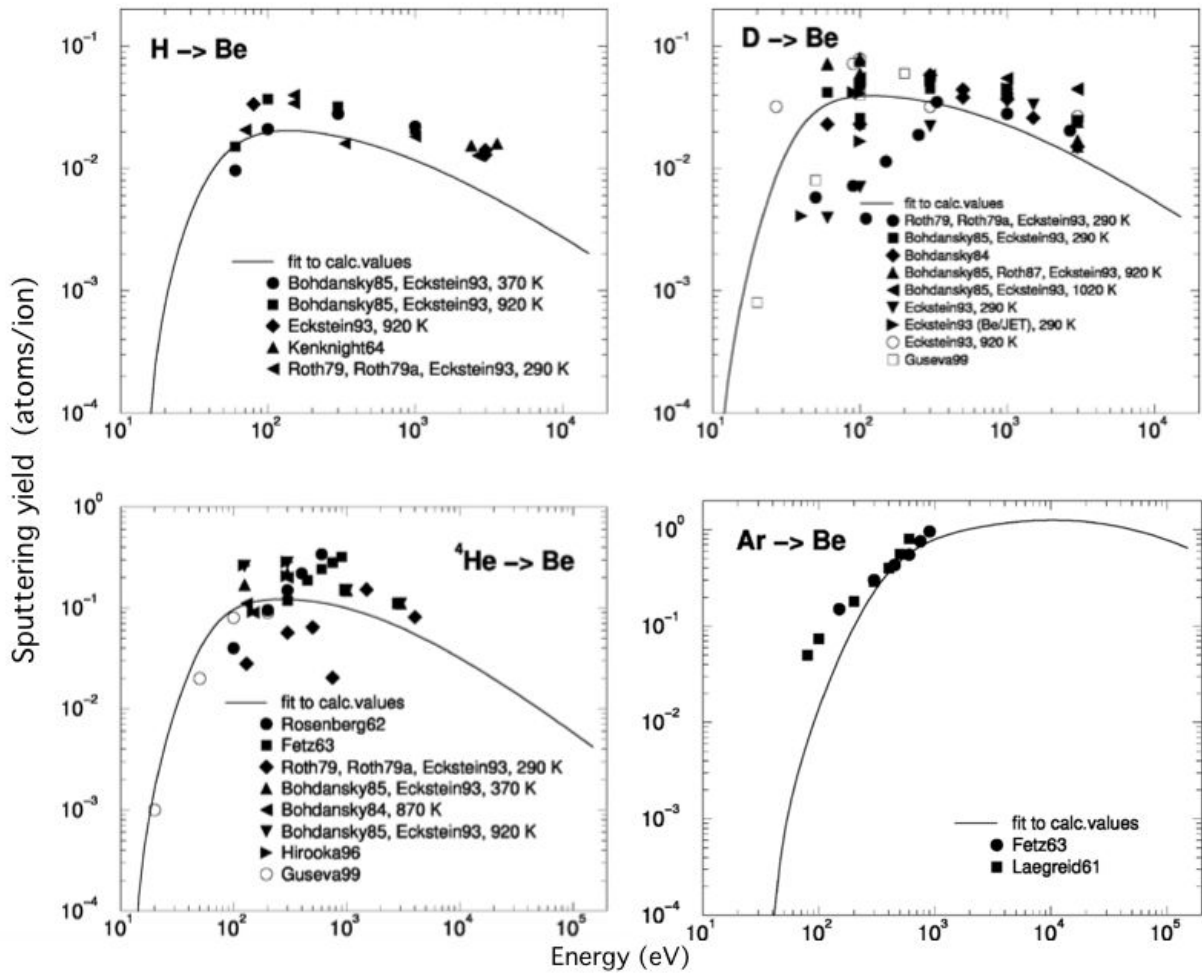


Fig. 1.7 Sputtering yield at normal incidence of different ions impacting the surface with different energies (Behrish and Eckstein, 2007)

The sputtering threshold of beryllium for different incident ions is given in Table 1.5. It is noticed that for hydrogen and deuterium ions the energy needed for sputtering is quite low with values of 14 eV and 10 eV respectively. The highest sputtering threshold is for Ar, with a value of 37 eV. Energy transfer between the ion and the metal atoms are proportional to their mass ratio. Consequently, for the different incident energies, the fraction of energy transferred from a H atom to beryllium is higher than that transferred from H or He to tungsten. As a result, sputtering by H is activated at much lower energy, which results in a lower sputtering threshold.

Ion	Sputtering Threshold (eV)
H	14
D	10
T	9
$^4\text{He}$	12
Ar	37

Table 1.5 Sputtering threshold of beryllium for different incident ions (Behrish and Eckstein, 2007)

### 1.3.3 Ionization, Multi-wall Interaction and Redeposition

Sputtered or eroded material from a surface can be ionized and transported through the plasma. During this process, gas phase molecular growth reactions may also take place leading to dust particle nucleation. In turn, this dust contaminates the plasma core leading to a decrease in plasma temperature and fusion power.

Species and dust particles produced through PSI can be transported into remote regions of the reactor and be redeposited on the surface of different components of the reactor wall. Once re-deposited, they may undergo chemical reactions with the different materials and change the compositions of the PFC's, leading to a change in their thermochemical properties. The combined effect of sputtering, migration and redeposition determines the lifetime of the PFC's (Conn et al., 1997; Konings, 2012; Wirth et al., 2015).

An example of the problematics involved in material redeposition can be given through the analysis of the sputtering yield of mixed-materials of beryllium and tungsten. Fig. 1.8 shows the sputtering yield for beryllium and a mixed material  $\text{Be}_{12}\text{W}$  for different incident ions with different energies. It is noticed that for energies higher than 1000 eV, the sputtering yield with He is higher for the mixed materials rather than for pure beryllium targets. The same is seen for tritium and deuterium, which at energies higher than 1100 and 1500 eV, respectively, the mixed materials show a higher sputtering yield. On the opposite, in the case of incident H ions, the sputtering yield is lower for the mixed material (Mutzke et al., 2015).

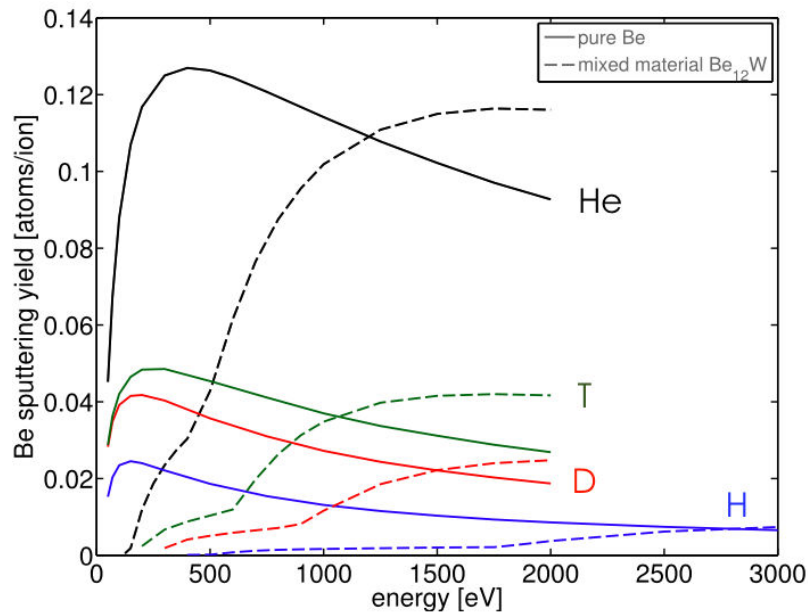


Fig. 1.8 Sputtering yield at normal incidence for Be and Be<sub>12</sub>W for hydrogen, deuterium, tritium and helium ions with different energies (Mutzke et al., 2015).

### 1.3.4 Ion implantation

Ions and neutrals with a sufficiently high energy are implanted in the material and may cause severe damage in its microstructure by strongly displacing atoms from their lattice sites. The threshold energy for defect production can be obtained by using equation 1.9 and substituting the sublimation energy  $E_s$  by the threshold displacement energy  $E_{disp}$  (Broeders and Konobeyev, 2004).

As implanted particles accumulate within the surface layer they start to diffuse from regions of high concentration to regions of low concentration and may reach depths larger than the implantation zone. While implanted particles diffuse inside the bulk they may be trapped in material defects.

Implantation of ions leads to fuel retention and recycling. This process consists in the retention and release of hydrogen isotopes, making the fuel density to vary during a discharge. As a result, the delivered fusion power is affected. Additionally, given that tritium, one of the hydrogen isotopes used as fuel, is radioactive with a half life of 12 years, its inventory is considerably limited in fusion reactors and its retention should be kept as low as possible (Conn et al., 1997; Konings, 2012).

Table 1.6 shows the implantation depth reached by different ions impinging on tungsten and beryllium at normal incidence with different energies. It is seen that the higher the energy, the deeper the ions penetrate in the material. Also, lighter ions penetrate deeper in the material. Deuterium ions with an incident energy of 1000 eV penetrate to a depth of 161 and 25 nm in tungsten and beryllium, respectively. On the other hand, Ar ions with an incident energy of 1000 eV penetrate to a depth of 19 and 3 nm, respectively, in tungsten and beryllium. Although Ar show very efficient sputtering yields, they are not implanted deep in the material. This is due to their greater size with respect to H.

Ion	Energy (eV)	Implantation depth in W (nm)	Implantation depth in Be (nm)
D	50	30	1
	300	79	8
	1000	161	25
$^4He$	50	19	0.7
	300	48	4
	1000	95	12
Ar	100	6	0.8
	500	13	2
	1000	19	3

*Table 1.6 Ion implantation depth at normal incidence in tungsten and beryllium for different ions and implantation energies (Eckstein, 2002)*

Now that the basic principles of PWI's are explained, the main concepts used to describe the microstructures and characteristics of the investigated materials, necessary to explain the phenomena involved when hydrogen interacts with solid surfaces, are presented.

## 1.4 The structure of crystalline solids

Metal solid materials form crystalline structures, that is, their atoms are arranged in periodic arrays over large atomic distances. The simplest repeating unit in this arrangement is the unit cell, which defines the symmetry and structure of the crystal lattice. Crystal systems are organized depending on the shape of their unit cell. A unit cell is defined as the minimal volume that fills up the whole space without overlapping when the following lattice transformation is applied (Manini, 2014):

$$\vec{r}' = \vec{r} + \vec{R} \quad (1.10)$$

with  $\vec{r}$  being a given point in the crystal lattice and  $\vec{R} = n_1\vec{a}_1 + n_2\vec{a}_2 + n_3\vec{a}_3$  where  $n_j$  are arbitrary intergers and  $\vec{a}_j$  three linearly independent vectors (Manini, 2014).

The unit cell is defined by 6 lattice parameters: three edge lengths  $a$ ,  $b$  and  $c$  and three inter-axial angles  $\alpha$ ,  $\beta$  and  $\gamma$ . The seven possible combinations of the lattice parameters represent the different crystal systems: cubic, tetragonal, hexagonal, orthorombic, rhombohedral, monoclinic and triclinic. The different crystal systems are shown in Fig. 1.9 (Calister and Rethwisch, 2010; Kittel, 2005). It may be observed that the greatest degree of symmetry corresponds to the cubic system with  $a = b = c$  and  $\alpha = \beta = \gamma = 90^\circ$ . On the other hand, the lowest degree of symmetry corresponds to triclinic system with  $a \neq b \neq c$  and  $\alpha \neq \beta \neq \gamma \neq 90^\circ$ . Most metals are in the either cubic or the hexagonal crystal systems. More specifically, aluminum and tungsten have cubic crystal systems whereas beryllium has an hexagonal one.

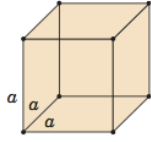
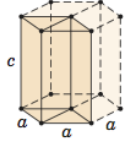
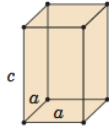
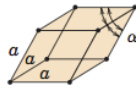
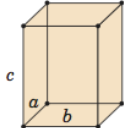
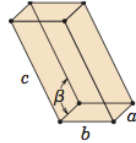
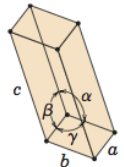
<i>Crystal System</i>	<i>Axial Relationships</i>	<i>Interaxial Angles</i>	<i>Unit Cell Geometry</i>
Cubic Example: W and Al	$a = b = c$	$\alpha = \beta = \gamma = 90^\circ$	
Hexagonal Example: Be	$a = b \neq c$	$\alpha = \beta = 90^\circ, \gamma = 120^\circ$	
Tetragonal	$a = b \neq c$	$\alpha = \beta = \gamma = 90^\circ$	
Rhombohedral (Trigonal)	$a = b = c$	$\alpha = \beta = \gamma \neq 90^\circ$	
Orthorhombic	$a \neq b \neq c$	$\alpha = \beta = \gamma = 90^\circ$	
Monoclinic	$a \neq b \neq c$	$\alpha = \gamma = 90^\circ \neq \beta$	
Triclinic	$a \neq b \neq c$	$\alpha \neq \beta \neq \gamma \neq 90^\circ$	

Fig. 1.9 Lattice parameter combinations and figures of the 7 crystal systems (Calister and Rethwisch, 2010)

Bravais lattices describe the geometric arrangement of the metal atoms on the lattice points. It is defined as an infinite set of points generated by a set of discrete translation operations, shown in equation 1.10. The 14 Bravais lattices achievable by this translational symmetry are: simple cubic, body-centered cubic, face-centered cubic, simple orthorhombic, base-centered, body centered, face-centered orthorhombic, simple triclinic, rhombohedral, hexagonal, simple monoclinic, base-centered monoclinic, simple tetragonal and body-centered tetragonal and are shown in Fig. 1.10. Tungsten is a body-centered cubic metal, aluminum a face-centered cubic and beryllium an hexagonal one.

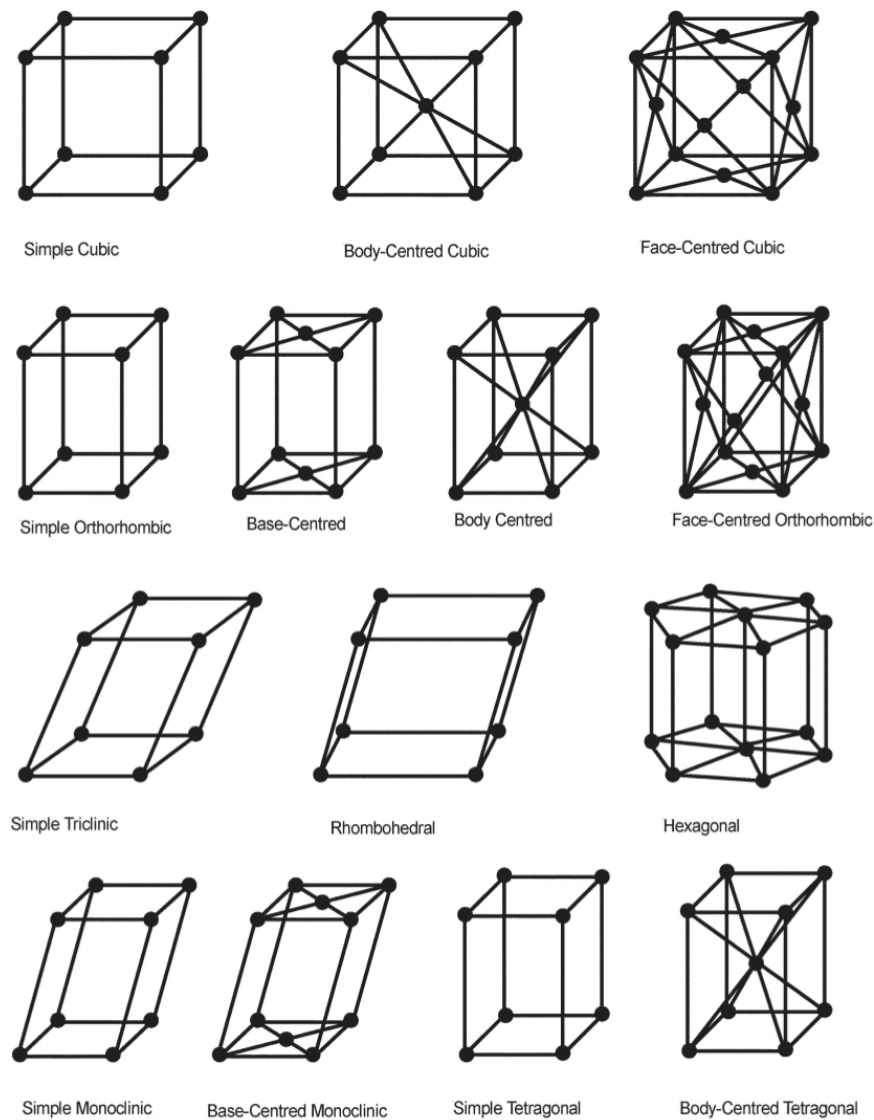


Fig. 1.10 The 14 Bravais lattices classified by crystal system (Flewitt and Wild, 2003)

The PFC materials of ITER are defined using unit cells and their respective Bravais lattices. Tungsten has a body-centered cubic (BCC) crystal structure, hence its lattice constants and inter-axial angles all have that same values. The packing index corresponds to the sphere volumes of all atoms within a unit cell divided by the unit cell volume. For tungsten the packing index is 0.68. Finally its coordination number (*i.e.* the number of nearest-neighbor atoms for each atom in the lattice) is 8. On the other hand, beryllium has an hexagonal closed-packed crystal structure (hcp), hence its lattice constants and inter-axial angles are not the same. The packing index and coordination number for beryllium are 0.74 and 12, respectively. These values are summarized in Table 1.7.

Physical properties	Tungsten	Beryllium
Lattice structure	bcc	hcp
Lattice constants	$a = b = c = 4.06$	$a = b = 2.28 \ c = 3.60$
Inter-axial angles	$\alpha = \beta = \gamma = 90^\circ$	$\alpha = \beta = 90^\circ \ \gamma = 120^\circ$
Packing index	0.68	0.74
Coordination number	8	12

Table 1.7 Physical properties of tungsten and beryllium (Calister and Rethwisch, 2010; Kittel, 2005)

Crystals are also characterized by their crystallographic directions and planes. A crystallographic direction is a geometric line that links atoms, whereas crystallographic planes are geometric planes that link these atoms. These directions and planes are described using integers known as Miller Indices. For cubic crystal systems, Miller indices are expressed as  $(hkl)$  for planes and  $[hkl]$  for directions and are shown in Fig. 1.11 and Fig. 1.12 respectively. A direction  $[hkl] = h\vec{i} + k\vec{j} + l\vec{k}$  and is always perpendicular to a plane  $(hkl)$  of the same indices; however this is not generally true for other crystal systems. Additionally, it is important to notice that  $\{hkl\}$  instead of  $(hkl)$  denotes the set of all planes that are equivalent to  $(hkl)$  by the symmetry of the lattice. Similarly,  $\langle hkl \rangle$  instead of  $[hkl]$  denotes the set of all directions that are equivalent to  $[hkl]$  by symmetry.

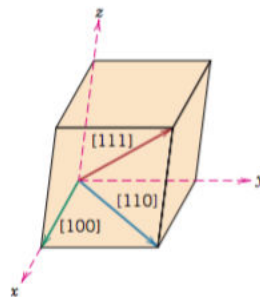


Fig. 1.11 The  $[100]$ ,  $[110]$  and  $[111]$  directions within a cubic unit cell (Calister and Rethwisch, 2010)

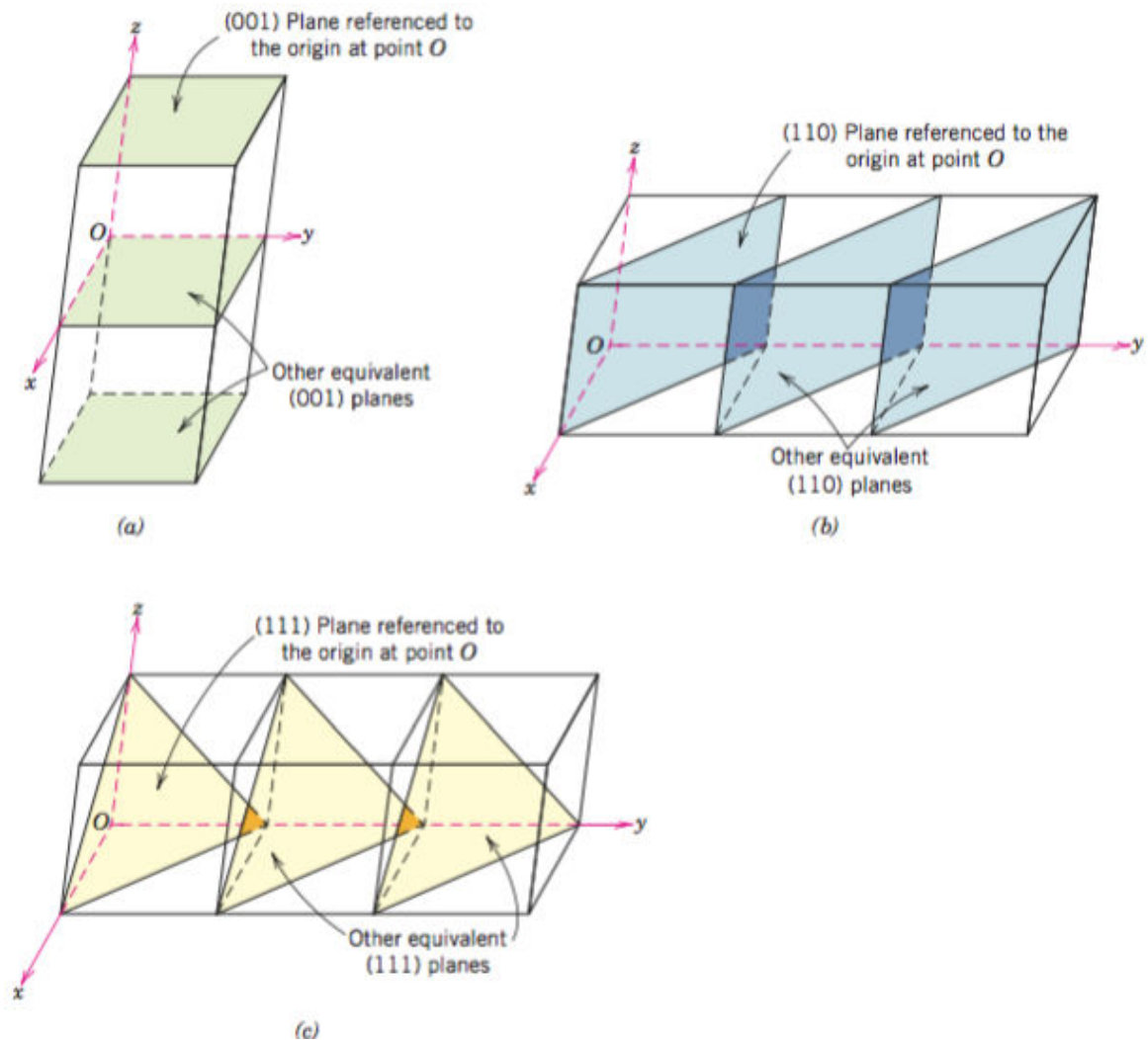
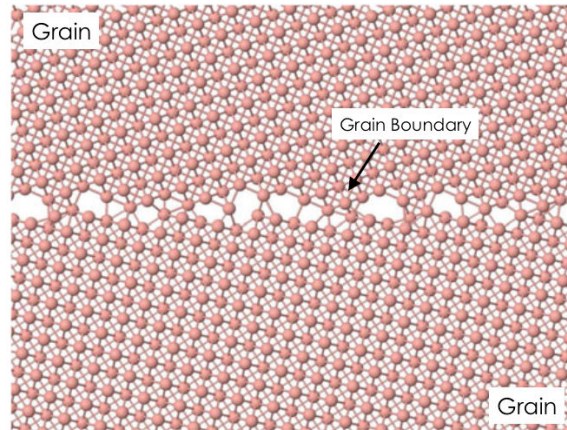


Fig. 1.12 The a) (100), b) (110) and c) (111) planes within a cubic unit cell (Calister and Rethwisch, 2010)

### 1.4.1 Poly-crystalline materials

Poly-crystalline materials are composed of small grains of varying size and orientation. Each grain has a specific periodic structure, that is, they are single crystal like. Grains are separated by narrow linear regions called grain boundaries. Poly-crystal materials may be textured, that is, their surface normal direction (ND) of the grains may be oriented to the same preferred orientation (i.e.  $\langle 100 \rangle$ ,  $\langle 111 \rangle$  or  $\langle 110 \rangle$ ) or may have no preferred orientation (Calister and Rethwisch, 2010).



*Fig. 1.13 Illustration of a grain boundary in a polycrystalline material (Manini, 2014)*

## 1.4.2 Single crystals

Single crystals have a periodic and repeated arrangement of atoms. In other words, they consist in a crystal lattice that is continuous throughout the whole sample. Therefore, there are no grain boundaries and the material has overall the same orientation. They can occur naturally or may be fabricated by a highly controlled and relatively slow crystallization (Callister and Rethwisch, 2010). The absence of the defects associated with grain boundaries give single crystals unique properties that make them useful in a large number of experiments.

## 1.4.3 Defects or imperfections in solids

The arrangement of atoms in crystals is not perfect and hence all solid materials contain large numbers of defects. These defects can be classified according to their geometry or dimension as follows :

### Point Defects

Consists on defects that occur at or around a single lattice points such as vacancies, self interstitials or impurities. All solid materials, regardless of their production method, will have a small percentage of point defects. Fig. 1.14 shows an schematic representation of a vacancy, an interstitial atom in the lattice and an impurity atom.

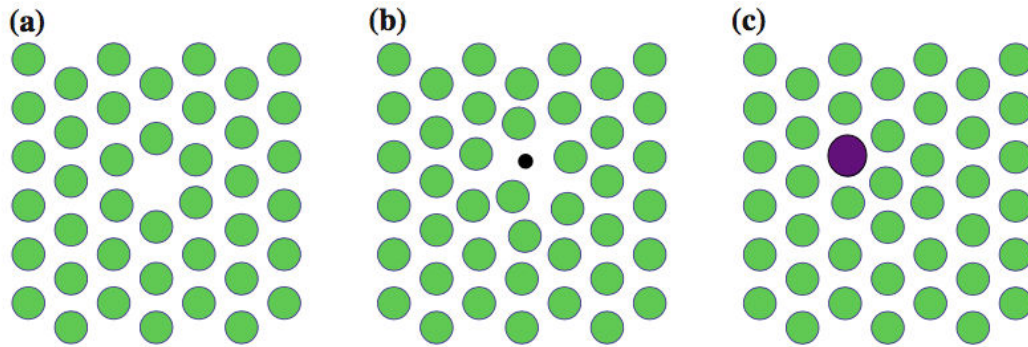


Fig. 1.14 Schematic representation of a) a vacancy b) an interstitial atom and c) an impurity atom (Manini, 2014)

Vacancies are point defects in which an atom is missing from one of the lattice sites, as shown in Fig. 1.14 a). The equilibrium number of vacancies  $N_v$  for a given quantity of material is obtained as follows (Calister and Rethwisch, 2010):

$$N_v = N \exp\left(-\frac{Q_v}{kT}\right) \quad (1.11)$$

where  $N$  is the total number of atomic sites,  $Q_v$  is the energy required for the formation of a vacancy,  $T$  is the absolute temperature and  $k$  is the Boltzmann's constant.

Vacancies may be formed during solidification, plastic deformation or ionic bombardments. These defects are found in all solid materials and they increase the entropy of the crystal. During hydrogen implantation, hydrogen trapped in vacancies lead to a decrease of the configurational entropy of the system. To compensate this decrease, the required energy for vacancy creation is lowered and in turn, these vacancies agglomerate in clusters in order to decrease the total energy of the system. The hydrogen atoms in the vacancy cluster combine into molecules, which stabilizes the cluster. Therefore, vacancies in a material exposed to hydrogen implantation, are able to nucleate other defects such as hydrogen-filled cavities (Ren et al., 2008).

Another type of point defects consists of atoms localized in empty spaces in the crystal lattice. These defects are known as interstitials and may be due either to smaller impurity atoms, such as hydrogen, or self-interstitials. Self-interstitials are atoms displaced from their original lattice site that results in the creation of a vacancy on the original site. These type of defects, in which there are vacancies and interstitials pairs, are known as *Frenkel pairs* (Calister and Rethwisch, 2010). For cubic and hexagonal crystal systems interstitials may be either octahedral or tetrahedrals shown in Fig. 1.15.

Small impurity interstitial atoms such as hydrogen are characterized by the symmetry of the interstitial atom with respect to its nearest lattice atoms. The preferred interstitial sites for hydrogen atoms are the octahedral and tetrahedral sites. Fig. 1.15 shows the octahedral and tetrahedral sites for fcc, hcp and bcc lattices (Fukai, 2005).

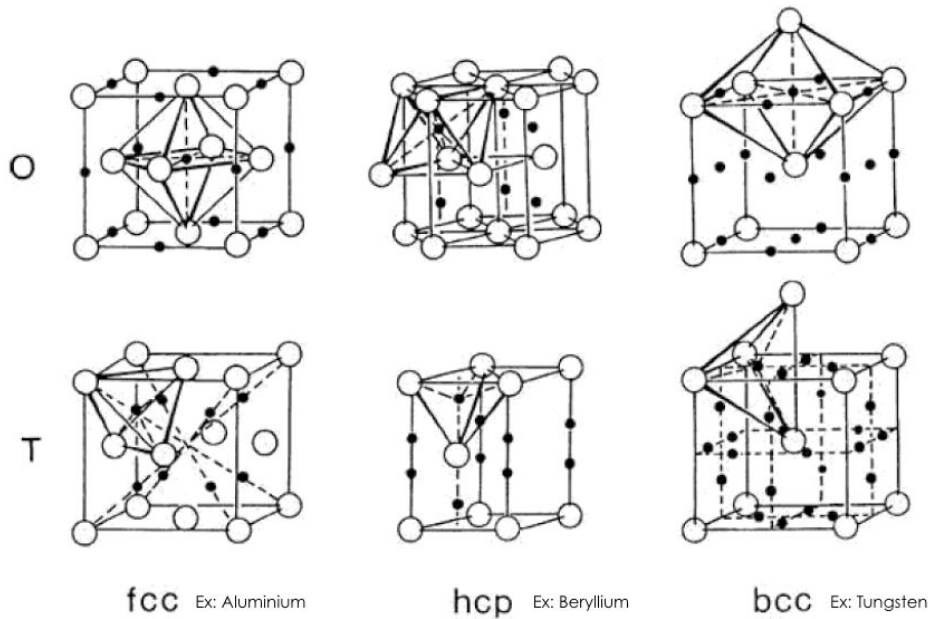


Fig. 1.15 Octahedral (O) and tetrahedral (T) interstitial sites in fcc, hcp and bcc lattices (Fukai, 2005).

Finally, another type of point defects are impurities. They consist in atoms whose size is comparable to those of the lattice and occupy vacant lattice sites, as shown in Fig. 1.14 c). Impurities are always present in materials. Even materials with a purity level of 99.99%, have about  $10^{22} - 10^{23}$  impurity atoms present in one cubic meter of material (Calister and Rethwisch, 2010).

## Linear Defects

Consists of 1-dimensional defects in which some atoms of the crystal lattice are misaligned. They are linear defects in the periodic array of atoms within a crystal and are commonly known as dislocations. These types of defects are characterized by an imaginary vector known as *Burger's vector* that expresses the direction and magnitude of the distortions caused by dislocations. In order to define it, a loop is created around the linear defect that traverses an equal number of lattice steps. The displacement vector that "closes" this loop is defined as the burger's vector.

Fig 1.16 shows a schematic representation of an extra half-plane of atoms, a typical dislocation found in materials, known as edge dislocation. Atoms are distorted around the dislocation: the upper half are compressed by this extra plane (Calister and Rethwisch, 2010; Kittel, 2005).

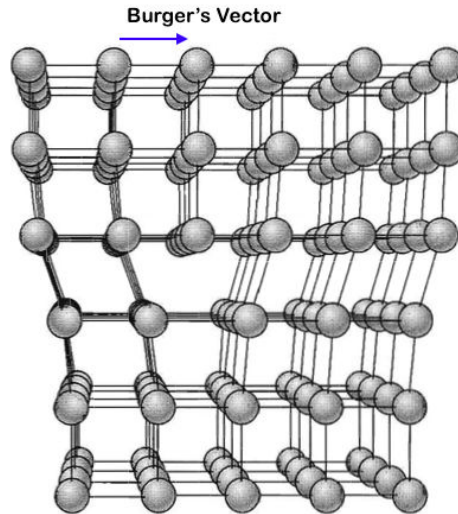


*Fig. 1.16 Schematic representation of an edge dislocation (Calister and Rethwisch, 2010)*

A screw dislocation is formed by a shear stress applied to the material, as shown in Fig. 1.17 a). This stress produces the distortion shown in Fig. 1.17 b). The atomic distortion associated with this dislocation produces a shift of one atomic distance to one side, relative to the bottom portion (Calister and Rethwisch, 2010).

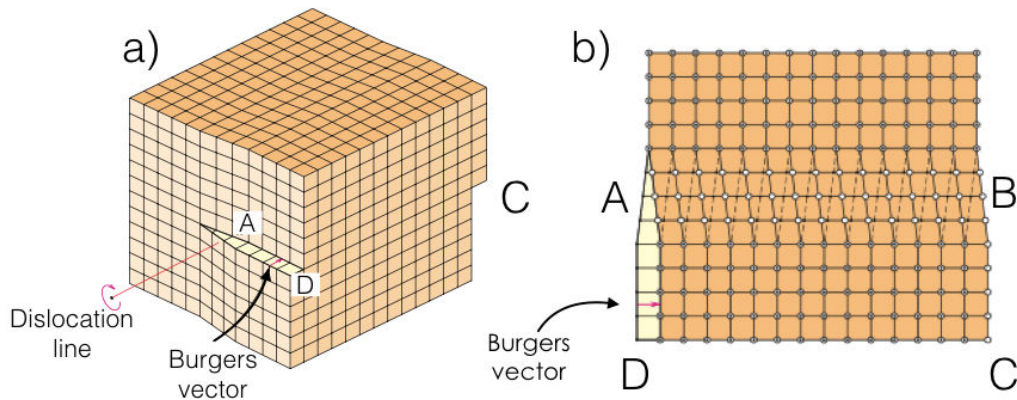


Fig. 1.17 a) Schematic representation of a screw dislocation b) Atom positions along the screw dislocation line (Calister and Rethwisch, 2010)

## Interfacial Defects

Interfacial defects are 2-dimensional defects that arise in the boundary of separate regions of the material. An example of interfacial defects are grain boundaries, in which two different crystallographic directions meet. Grain boundaries are characterized by the misorientation angles between two grains. If this angle is lower than  $15^\circ$  is known as small-angle grain boundary. Similarly, high-angle grain boundaries have a misorientation angle higher than  $15^\circ$ . A schematic representation of grain boundaries is shown in Fig. 1.18. Due to the lower energy with respect to the bulk, grain boundaries also act as sinks for point and linear defects.

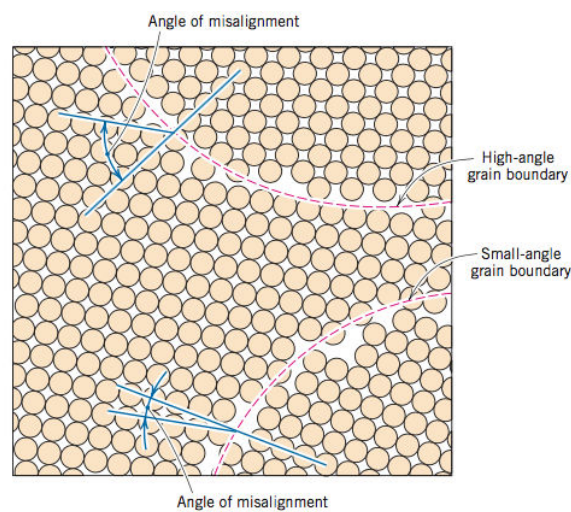


Fig. 1.18 Schematic representation of grain boundaries (Calister and Rethwisch, 2010)

A twin boundary is a special type of grain boundary with a specific symmetry: atoms on one side of the boundary are located in a mirror-image position with respect to the atoms on the other side. Twinning results from applied mechanical shear forces and during heat treatments.

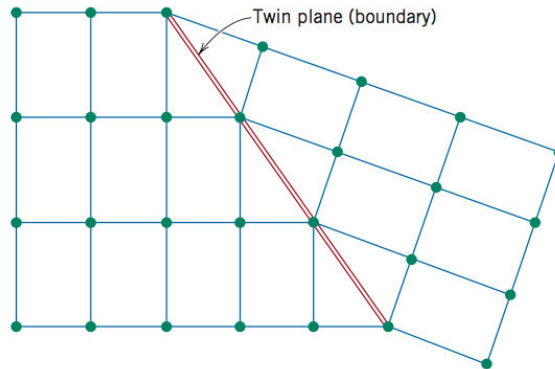


Fig. 1.19 Schematic representation of twin grain boundaries (Calister and Rethwisch, 2010)

### Bulk Defects

These defects are 3-dimensional defects which include vacancy clusters, impurity clusters (*i.e.* precipitates), cavities and cracks. The latter are defined as larger cavities of irregular shape that occur in the bulk of materials. Fig. 1.20 shows an example of cracks and cavities in a material.

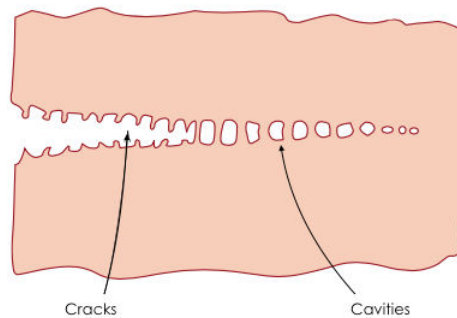


Fig. 1.20 Schematic representation of cracks and boundaries (Calister and Rethwisch, 2010)

This section provided an introduction to the main concepts used to describe the microstructures and characteristics of the investigated materials. The basic principles needed to study and understand the phenomena occurring in solid surfaces after ion implantation were presented. The next section focuses mainly on the implantation of hydrogen ions in solids and describes hydrogen diffusion and solubility in metals.

## 1.5 Hydrogen in metals: solubility and diffusion

### 1.5.1 Solubility

Hydrogen gas may be dissolved in metals by the dissociation of the gas molecule, as follows:



Hydrogen solubility refers to the total amount of hydrogen occupying interstitial sites for a particular exposure pressure. There are two different types of materials as far as solubility is concerned (Causey, 2002; Manhard, 2011; Post and Behrisch, 1986):

- Endothermic material: Energy must be added to introduce hydrogen into solution, that is, the heat of solution has a positive value ( $\Delta H_{sol} > 0$ ). For this type of materials, hydrogen solubility increases with increasing temperature. Usually, endothermic materials have a low affinity for hydrogen. Examples of these materials include Be, W, Al, Zn, Ga, Ge, Cd, In, Sn, Te and Pb. The materials which will be studied in this work, Al, Be and W, are all endothermic materials and hence have a low hydrogen solubility.
- Exothermic material: Releases energy when hydrogen is introduced into solution, *i.e.*,  $\Delta H_{sol} < 0$ . In this case, solubility decreases with increasing temperature. Usually, these materials have a high affinity for hydrogen. Examples of exothermic materials include Ti, Zr, Nb, Ta, Ni, Pd and Mg.

If the gas forms a true solution in the solid, the equilibrium gas constant, which may be also considered as the solubility at unit pressure  $K_s$  is ' given by (Causey, 2002; Serra et al., 1998):

$$K_s = S_o e^{-E_s/kT} \quad (1.13)$$

where  $E_s$  is the heat of solution or enthalpy of the reaction shown in equation 1.12, and  $T$  is the absolute temperature. The hydrogen solubility is then given by Sievert's Law:  $S = k_s \sqrt{p}$  where  $p$  is the hydrogen pressure in Pa.

Fig. 1.22 shows the variation of hydrogen solubility in tungsten and beryllium as a function of the material temperature. Hydrogen solubility is higher in beryllium than in tungsten. In addition, in tungsten it increases by more than 14 orders of magnitude, from  $10^3$  to  $10^{17}$   $\text{mol/m}^3\text{Pa}^{1/2}$  when the temperature increases from 300 K to 800 K. On the other hand, diffusivity in beryllium increases by 13 orders of magnitude from  $10^5$  to  $10^{18}$   $\text{mol/m}^3\text{Pa}^{1/2}$  for the same temperature range.

Solubility determines whether bubbles may form in a material during hydrogen plasma exposure. Low solubility materials such as tungsten and beryllium, are likely to have desorb hydrogen dissolved in defects and thus are more likely to form bubbles and blisters (Causey, 2002).

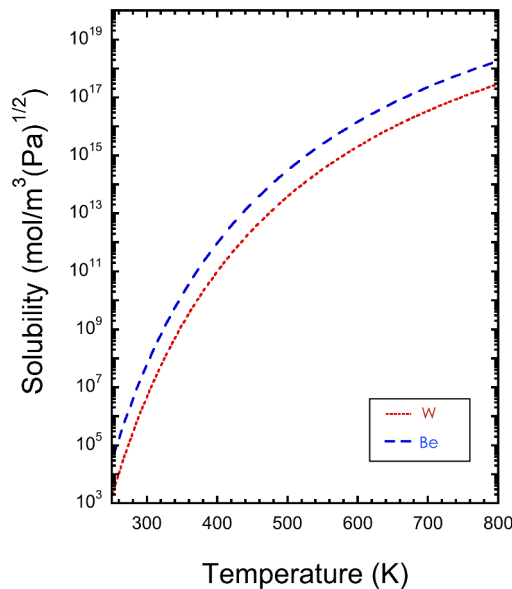


Fig. 1.21 Solubility of hydrogen in tungsten and beryllium as a function of temperature (Serra et al., 1998)

## 1.5.2 Diffusion

Hydrogen ions reaching the surface are neutralized during their interaction with the wall. Neutrals with sufficient energy are able to be implanted in the material. Diatomic  $H_2$  molecules interacting with the surface of a transition metal tend to dissociate and create strong atomic-surface interactions forming Van der Waals bonds. This state of hydrogen in which it resides in the surface is known as *adsorption* (Buzi, 2015).

On the other hand, hydrogen atoms may be trapped in the bulk during a process known as *absorption*. Hydrogen atoms trapped in the material reside in interstitial or solute sites occupying either octahedral or tetrahedral positions. As implanted particles accumulate within the surface layer they start to diffuse from regions of high concentration to regions of low concentration. Due to diffusion, the atoms reach depths larger than the implantation zone. While implanted particles diffuse inside the bulk they may be trapped in material defects such as vacancies. These traps have a higher binding energy  $E_b$  than a regular solute site ( $E_b > E_m$ ) and may be inherent to the material itself or created by radiation damage. Atoms with enough energy may diffuse back to the surface, recombine with another atom and be released as molecules (Manhard, 2011; Post and Behrisch, 1986).

Diffusivity can be derived from the model of random walk, *i.e.* random jumps from one solution site to an adjacent one after thermal activation, and is defined by an Arrhenius-form expression:

$$D(T) = D_0 \cdot e^{-\frac{E_m}{kT}} \quad (1.14)$$

where  $D_0$  may be described as the probability that a hydrogen atom makes a successful jump from one solution site to the next one (Causey, 2002), and  $E_m$  is the activation energy for diffusion.

Hydrogen diffusion in metals is very fast and in particular at low temperatures (lower than 300 K) it is strongly influenced by quantum-mechanical effects in which quantum tunneling processes are involved. As the temperatures increase above 300 K, thermally activated classical jumps between adjacent sites take place (Fukai and Sugimoto, 1985; Maksimov and Pankratov, 1975). In the case of tungsten and beryllium, these jumps occur between tetrahedral interstitial sites (Heinola and Ahlgren, 2010; Zhang et al., 2012). Fig. 1.22 shows the variation of hydrogen diffusivity in tungsten and beryllium with the material temperature. Hydrogen diffusivity is higher in tungsten than in beryllium. In addition, diffusivity in tungsten increases by more than 4 orders of magnitude, from  $10^{-13}$  to  $10^{-8}$  m/s<sup>2</sup> when the temperature increases from 300 K to 1200 K. On the other hand, diffusivity in beryllium increases by 3 orders of magnitude from  $10^{-13}$  to  $10^{-10}$  m/s<sup>2</sup> for the same temperature range.

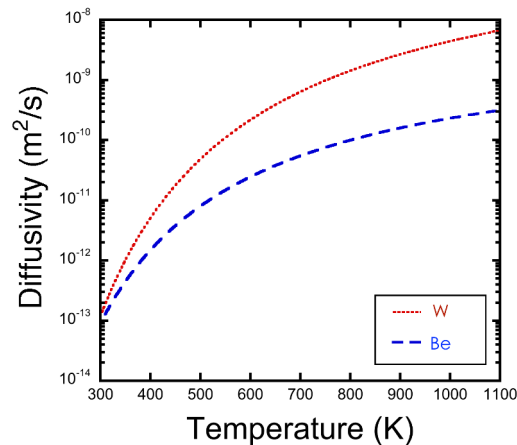


Fig. 1.22 Diffusivity of hydrogen in tungsten and beryllium as a function of temperature (Abramov et al., 1990; Serra et al., 1998)

Hydrogen diffusion is affected by the presence of grain boundaries. Studies have shown an enhanced diffusion along the grain boundaries on samples with grain sizes so large they are almost single crystals. On the other hand, samples with smaller grain sizes suppress hydrogen mobility. This is due to the presence of nodes or junctions of grain boundary that act as traps for the hydrogen atoms (Ichimura et al., 1991).

As hydrogen molecules reach a material they dissociate and their behavior is determined by the nature of the material. Exothermic materials usually have a high hydrogen solubility and hence hydrogen atoms may form hydrides with the atoms from the material. On the other hand, endothermic materials have a low hydrogen solubility and when exposed to hydrogen fluxes are prone to nucleating bubbles and blisters.

It is possible to achieve extremely high local concentrations of hydrogen in the materials when implantation flux densities are sufficiently high. In the case of implanted hydrogen ions on endothermic materials, once hydrogen reaches concentrations far above the solubility limit, molecular hydrogen forms. This is known as the *saturation limit*. At this saturation limit, hydrogen precipitates in the form of gaseous bubbles (Behrish, 1983; Kreter et al., 2014). Bubble formation in materials is of great concern in PFC's since it changes the material properties and favors hydrogen retention. Therefore, the next section will be devoted to the presentation of the different mechanisms of bubble formation.

## 1.6 Bubble formation and material modifications

### 1.6.1 Introduction

Many studies have been conducted on bubble formation in metals and the different parameters that influence their formation have been analyzed (Behrish, 1983). In the present work, bubbles are referred to quasi-spherical shaped cavities in the bulk of the material whereas blisters consist of dome-shaped deformations of the surface layer of the material with mostly circular, sometimes irregular circumference. Underneath blisters one may find a spherical shaped bubble, a lenticular cavity or cracks (Behrish, 1983; Shu et al., 2007). Fig. 1.23 shows blisters and cracks on an aluminum sample after hydrogen plasma exposure at LSPM.

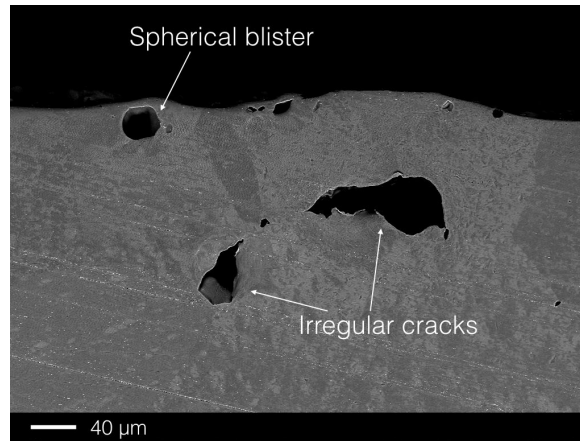


*Fig. 1.23 Blisters and cracks on an aluminum sample after exposure to  $H_2$  plasma with flux of  $1.6 \times 10^{20}$  ions/ $m^2$ , fluence of  $3.3 \times 10^{24}$  ions/ $m^2$  and incident ion energy of 320 eV*

The main difficulty in describing bubble and blister formation comes from the fact that it is influenced by a large number of parameters, summarized in Table 1.8.

#### Projectile related parameters

Parameters such as flux, fluence (integrated flux over time), type of incident ion and its energy, influence bubble and blister formation. The change in tungsten surface morphology when exposed to gas flux depends on the chemical nature of the gas particles. When exposed to pure D plasma they develop blisters all over the surface whereas when exposed to deuterium plasma with a low He content the formation of blisters is suppressed (Roth and Schmid, 2011). Blister formation after plasma exposure is also affected by plasma fluence. Studies performed by implanting Be foils with 1.5 keV deuterium ions at fluences ranging between  $3 \times 10^{21}$ - $1.2 \times 10^{22}$  D/ $m^2$  at 300 K and showed that when the fluence is increased by a factor four, blister density increases by a factor two (Touhouche and B.Terreault, 1994).

Projectile related parameters	Projectile nature Fluence Flux density Energy Angle of incidence
Target related parameters	Method of production and pre-treatment Temperature Target material and composition Bulk structure: crystal grain size, damage concentration and crystallographic orientation Surface roughness
Gas-solid related parameters	Solubility Diffusivity

*Table 1.8 Parameters that influence gas-ion induced surface structures (Behrish, 1983)*

### Target related parameters

The method of production of a material influences its crystal size and damage concentration. As a result, bubble and blister formation are affected by the method of production of the sample. They determine the amount of traps available in the material, which influence hydrogen retention. It was shown that single-crystal tungsten has a higher deuterium retention in comparison with polycrystalline tungsten when exposed to  $10^{22}$  D/m<sup>2</sup> at 300 K due to an enhanced ion-induced trap creation in single crystal materials (Ogorodnikova et al., 2003).

Another parameter that affects bubble formation is the pre-treatment of the material. Nishijima et al. (Nishijima et al., 2005) exposed samples with a different roughness to deuterium plasma with 80 eV ions at a fluence of  $7.6 \times 10^{26}$  D/m<sup>2</sup> at 500 K. The sample with the lowest roughness showed an enhanced blister formation. Other studies reached a similar conclusion: blisters were not detected on rough surfaces. Nonetheless, hydrogen retention in these samples is higher than in polished tungsten samples (Manhard, 2011).

Studies show that some crystallographic directions are preferential for blister growth. Experiments performed with tungsten samples exposed to deuterium plasma with a flux ranging from  $10^{22}$  to  $10^{25}$  ions/m<sup>2</sup>s, a fluence of  $10^{26}$  ions/m<sup>2</sup> an ion energy of 38 eV and a sample temperature range of 573 – 943 K showed that blisters form more promptly on grains with directions close to [111] (Jia et al., 2015, 2016).

These parameters along with exposure temperature, solubility and diffusivity impact the depth at which the damage will most likely occur and the surface morphology of the samples (Behrish, 1983). The next section describes the different mechanisms proposed in literature to explain blister and bubble formation in materials.

## 1.6.2 Mechanisms of bubble nucleation and growth

### Bubble nucleation

Two main theories have been proposed as mechanisms of bubble growth: **the single bubble induced pressure model** and **the interbubble fracture generated crack model**. These two models agree that bubbles nucleate due to a collection of hydrogen-vacancy complexes. This hydrogen vacancy clustering (*i.e.*  $H_2 - v$  clusters) can occur at temperatures higher than  $T_m/4$  (with  $T_m$  being the melting temperature) given that vacancies have enough energy to be mobile and agglomerate into clusters (Post and Behrisch, 1986). At lower temperatures vacancies can agglomerate into clusters in the presence of high concentrations of hydrogen in the material.

Hydrogen trapped as interstitials induce strains and changes in the electronic structure leading to an increase in the energy of the system. To compensate for this energy increase, the formation energy of vacancies decreases, which in turn leads to the creation of more vacancies. This effect is known as hydrogen induced superabundant vacancy concentration. If further vacancies are created, there is an additional energy increase in the system. To counteract this energy increase vacancies tend to organize into clusters, as shown in Fig. 1.24 (Condon and Schober, 1993; Ren et al., 2008).

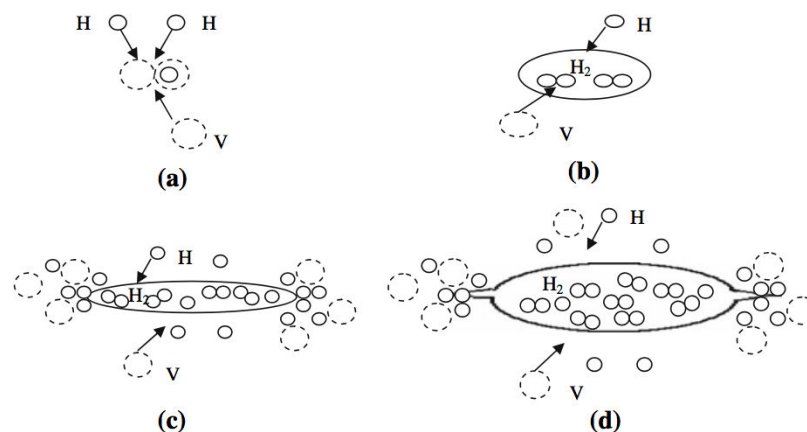


Fig. 1.24 Schematic representation of the vacancy clustering model: a) Superabundant vacancies or thermal vacancies accumulate in a cluster. b) Hydrogen atoms form molecules. c) The void continues to grow by collecting additional vacancies. d) As the pressure inside the bubble reaches a certain value, cracks may form in the wall (Ren et al., 2008)

The energy decrease by the aggregation of interstitial hydrogen atoms into spherical hydrogen clusters without any external stresses may be estimated by taking the energy decrease due to the aggregation of hydrogen in the bubbles minus the increase in energy of

the system due to the creation of a dislocation loop (*i.e.* punching of dislocation loops out of a bubble due to excess pressure). The energy decrease may be expressed as follows (Fujita, 1976; Ren et al., 2008):

$$\Delta E = -\frac{\pi r^3 \varepsilon}{\Omega} - \frac{Gb^2 r \ln(r/r_0)}{2(1-\nu)} \quad (1.15)$$

where  $r$  is the radius of the vacancy cluster in cm,  $\varepsilon$  is the binding energy of a solute hydrogen atom to a cluster in eV,  $\Omega$  is the atomic volume of hydrogen in the cluster in  $\text{cm}^3$ , that is the volume one mole of an element occupies at room temperature,  $G$  is the modulus of rigidity in dynes/ $\text{cm}^2$ ,  $b$  is the Burgers vector in cm,  $\nu$  is the Poisson's ratio and  $r_0$  is the dislocation core radius in cm.

Once the  $H_2 - \nu$  cluster is formed it is able to grow if the work done by the hydrogen pressure does not exceed the total binding energy of a newly created vacancy to an existing cluster. The pressure at which this occurs is the critical pressure under which bubbles can grow in the material. The critical pressure is given by (Ren et al., 2008):

$$P = \frac{E_t}{\Delta V} \quad (1.16)$$

where  $E_t$  is that total energy of binding an existing cluster to a newly created vacancy (*i.e.* the formation energy of a vacancy plus the binding energy of a vacancy to a cluster) and  $\Delta V$  is the change in volume which in this case corresponds to the volume of a vacancy.

Once clusters are formed, hydrogen atoms combine into molecules inside the  $H_2 - \nu$  cluster (Fig. 1.24 b) and c)), releasing energy into the system (Ren et al., 2008):



This chemical reaction has a dissociation energy of  $-4.5$  eV at 300 K. Once hydrogen molecules are formed, it is very difficult for them to dissociate.

Once the bubble is formed and exposure to hydrogen flux continues, the pressure continues to increase. For increasing pressures, cracks may form on the bubble wall and propagate as shown in Fig. 1.24 d) (Ren et al., 2008).

## Bubble growth

### Single bubble induced pressure model

This model proposes that vacancies (inherent to the material or produced by the incident ion beam) act as traps for hydrogen during implantation (Fig. 1.25 a)). Above a certain concentration of hydrogen, there is an increase in size and density. This increase is due to the internal gas pressure, in the order of GPa, which punches the interstitial loops out of one side of the bubble in a process known as interstitial loop punching. The interstitial will then rapidly glide away from the bubble along the direction of its Burgers vector (Fig. 1.25 b)). Once the elastic limit is reached the wall of the cavity is deformed (Behrish, 1983; Condon and Schober, 1993; Jacques, 1983).

At the high pressures required to generate dislocation loops, intermolecular repulsions become more important and the values of pressure and fugacity deviate from each other. The stresses, due to high fugacity in the bubbles, are able to deform the material around the bubble. Depending on the material's ability to deform plastically, bubbles can have spherical shape (Jacques, 1983) or a terraced structure (Kolasinski et al., 2011)

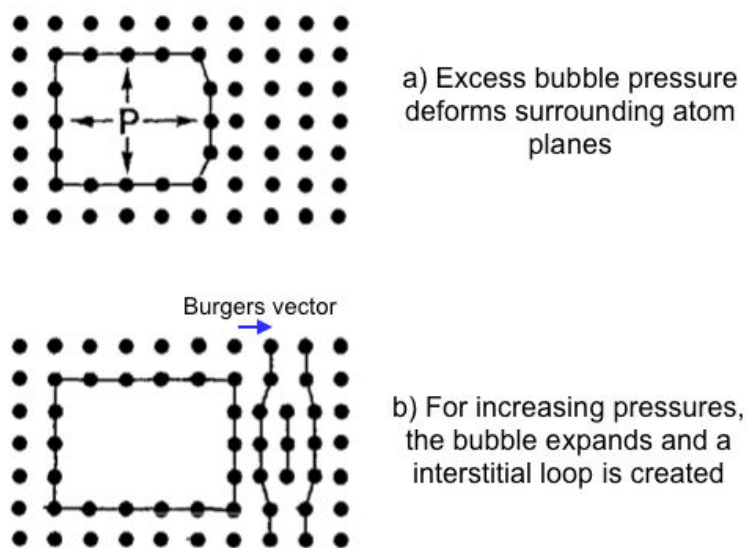


Fig. 1.25 Schematic representation of the loop punching process due to an excessive pressure: a) Hydrogen accumulates at vacancies b) After a certain pressure is achieved, interstitial loops are punched out of one side of the bubble or blister (Behrish, 1983; Evans, 1977)

### Interbubble fracture generated crack model

Another proposed mechanism of bubble formation is the interbubble fracture generated crack model. This model assumes that small bubbles with a high pressure nucleate in the implanted layer of the material (Fig 1.26 a)). Due to the high pressure of the bubbles, there are tensile stresses in the material. As the pressure increases, cracks are produced along the bubbles (Fig 1.26 b)). These cracks are large when compared to the initial bubble size. As more bubbles break into the cavity, a flat cavity is formed (Fig 1.26 d)). This flat cavity develops in a bubble (Fig 1.26 f)). Afterwards, two bubble growth mechanisms are proposed: **loop punching due to the high pressure inside the bubble, and acquisition of vacancy clusters** (Behrish, 1983; Evans, 1977; Jacques, 1983).

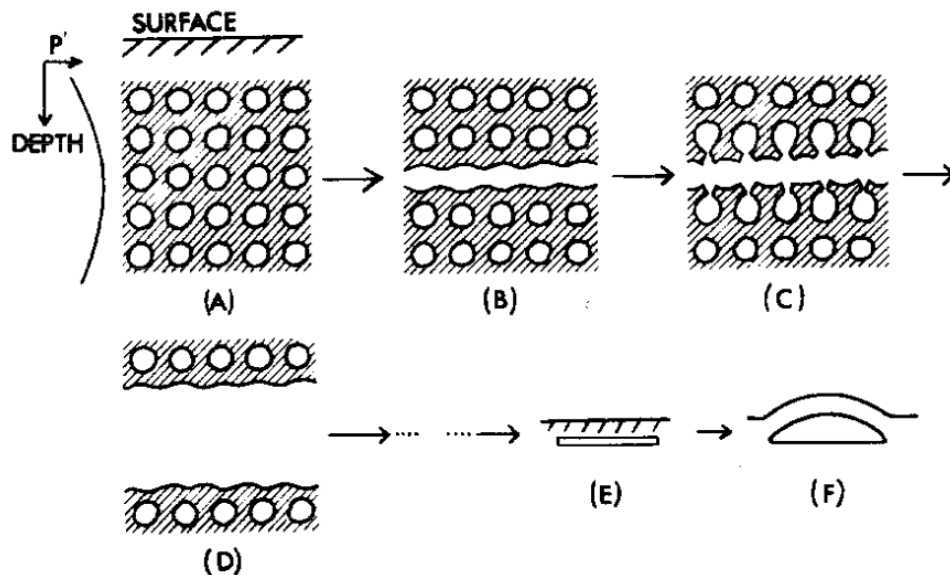


Fig. 1.26 Schematic representation of the interbubble or crack fracture model. a) Bubbles form in the lattice. b) Tensile stresses due to the high pressures inside the bubble results in the formation of cracks. c-d) The cracks continues to grow. e-f) a flat cavity forms which then develops in a bubble (Evans, 1977)

These theories provide two different mechanisms for bubble growth. However, both of them agree on the fact that at **high pressures bubbles grow by dislocation loop punching**.

This section provided a brief introduction of the different mechanisms involved in bubble nucleation and growth. This information, along with the other described topics (*i.e.* plasma sheath, PWI, structure of crystalline solids and hydrogen in metals) provide the basic tools to study bubble and blister formation. The main concepts described in the previous section are summarized in Fig. 1.27.

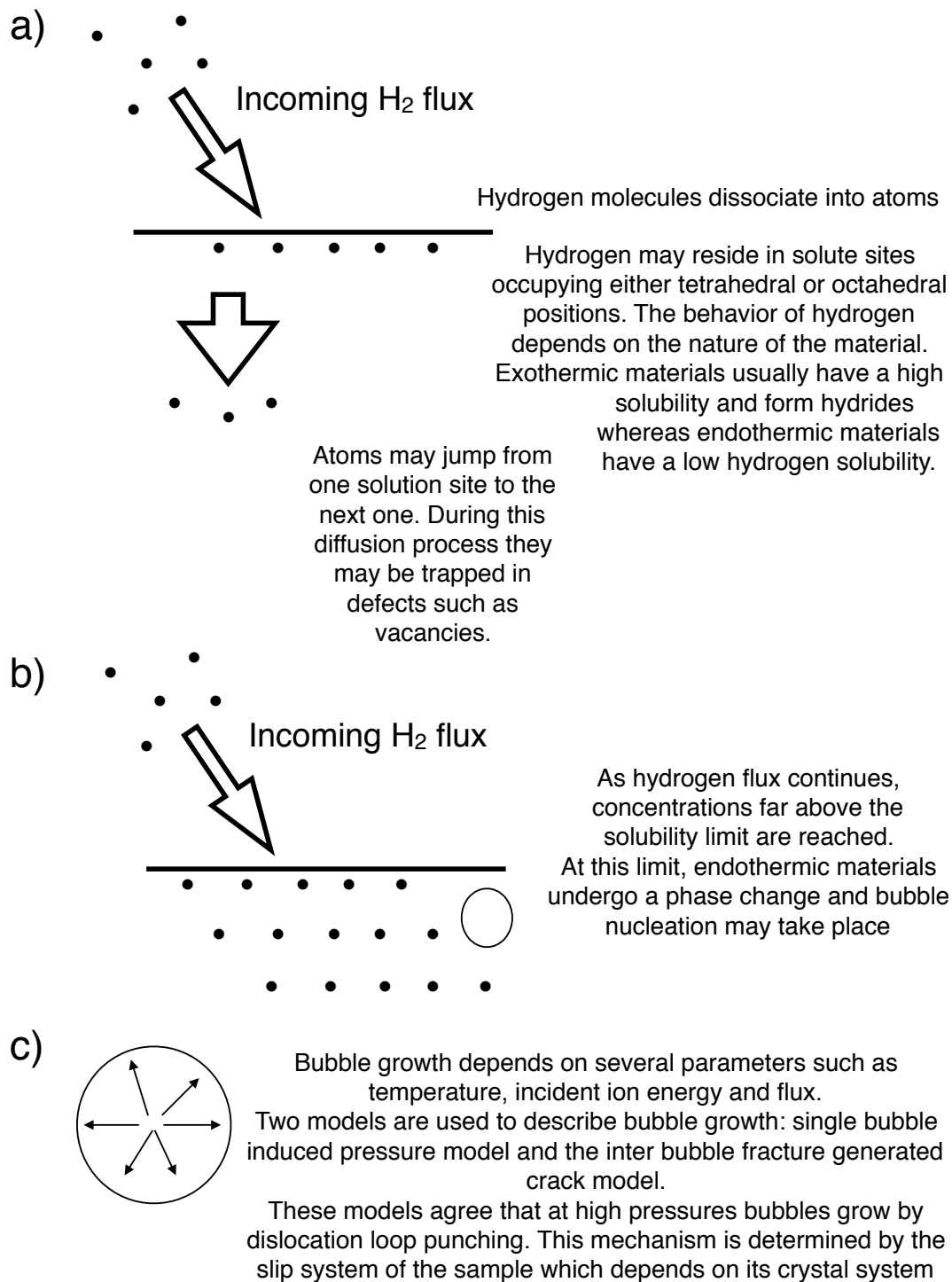


Fig. 1.27 Brief summary of a solid material exposed to hydrogen flux.

However, one aspect remains to be analyzed. In order to study bubble and blister formation in PFC's, analysis must be performed using beryllium samples. Nevertheless, due to the toxicity of beryllium, aluminum was proposed as a proxy for this material. The next section focuses on describing the main differences and similarities between these two materials.

## 1.7 Aluminum as a possible proxy for Beryllium

The main constraint when performing experiments with beryllium is due to its high toxicity. Inhalation of beryllium dust can lead to a disease known as chronic beryllium disease (CBD), a lung disease whose symptoms include shortness of breath, fatigue, chest and joint pain among others (Jr. and Krieger, 2001). LSPM is not authorized to handle this material due to its toxicity. The European Union has classified this material as category 1 carcinogen and is subject to a decree known as CMR (Carcinogen, mutagen and reprotoxic) by the french legislation (CMR 2001-97 of February 1<sup>st</sup> 2001) (Legifrance, 2001).

Both magnesium and aluminum have been proposed as proxy for beryllium (Marot et al., 2013). Aluminum and beryllium share some similarities: They both develop grass or cone-like structures when exposed to high fluence (in the order of  $1.2 \times 10^{26} \text{m}^{-2}$ ) deuterium plasma, as shown in Fig. 1.28 (Kreter et al., 2014). After implantation at lower fluences (in the order of  $10^{20}$ - $10^{24}$  ions/ $\text{m}^2$ ) both Al and Be show the formation of bubbles and interconnecting channels or tunnel structures (Anderl et al., 1992; Kamada, 1989; Markin et al., 1996). Finally, Buckhovets *et al.* (Bukhovets et al., 2015) analyzed ion sputtering of Al and Be in a low pressure DC discharge in  $D_2/O_2$  mixtures and determined that the chemical nature of sputtering in aluminum and beryllium has a similar behavior.

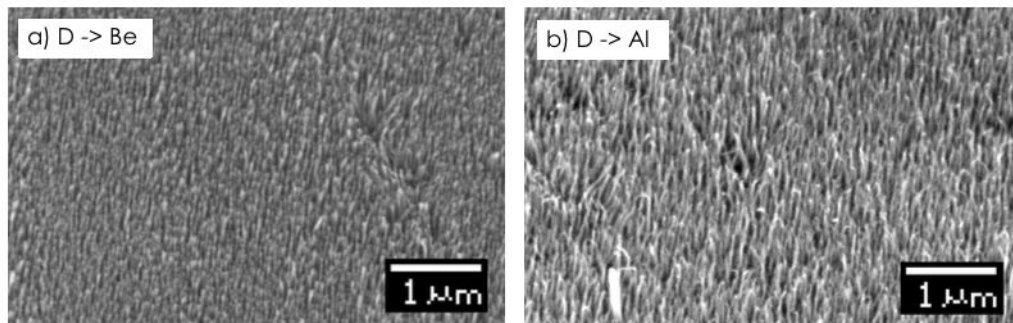


Fig. 1.28 SEM micrographs of a) Be and b) Al exposed to D plasma (Kreter et al., 2014)

Several experiments were performed using Al as a surrogate for Be. Eren *et al.* (Eren et al., 2013) performed experiments on first mirror materials exposed to tungsten and aluminum impurities. These experiments concluded that Al deposits on the mirror surface as oxides. Since Be and Al form similar types of oxides, it is expected for Be to be deposited as oxide on the mirror surfaces in ITER. Additionally, De Temmerman *et al.* (Temmerman et al., 2013) used Al with the aim of analyzing droplet ejection and melt layer motion under ITER-relevant plasma conditions. Al was used as a proxy for Be given that it is a metal with a lower melting point than tungsten. Finally, Wisse *et al.* (Wisse et al., 2013) performed cleaning experiments on stainless steel coated with mixtures of carbon, tungsten and aluminum. In this case Al was used as a stand in for Be given that it is expected to form mixed alloys with tungsten.

As proposed by Marot et al. (Marot et al., 2013) aluminum is a non-toxic proxy material to Be regarding its formation of hydrides, oxides and alloys with tungsten. All these different physical and chemical properties of Be and Al are analyzed in further detail in the following sections.

### 1.7.1 Physical properties of Al and Be

The physical properties of Be and Al are shown in Tab. 1.9. The melting temperature for Be is 1560 K, almost twice as high as for Al. Melting temperature determine the recrystallization temperature in which materials hardness and resistance are decreased. Also, it is seen that the yield or elastic modulus of Be is four times higher than for Al. This modulus measures the materials ability to deform elastically, which means that under similar conditions, Be will not be as elastic as Al. Even though Be is less ductile than Al, beryllium is able to withstand larger stresses than Al before rupture. This is determined by the tensile strength of both materials, which is more than 10 times higher for Be than for Al. Both the yield modulus and tensile strength influence bubble and blister formation, given that during these processes, materials are elastically deformed. Hence, this difference may be of importance when analyzing these phenomena.

In addition, these two materials have a different lattice structure: Be crystallizes in hcp while Al in fcc. Nevertheless, these two structures share numerous similarities. Both patterns have the highest possible density of nodes and consequently, their packing index is the same, they have the same number of nearest-neighbor atoms (coordination number) and the nearest-neighbor distance is almost the same for both cases (Kittel, 2005; Manini, 2014). Nonetheless, their slip systems are not the same (Calister and Rethwisch, 2010). The latter affects the slipping of dislocations when samples are subject to stresses. As a result, their blister morphology is expected to be different.

Physical properties	Beryllium	Aluminum
Melting point K	1560	933
Elastic Modulus (GPa)	287	70
Tensile strength (MPa)	370	30
Lattice structure	hcp	fcc
Lattice constants	$a = b = 2.28$ $c = 3.60$	$a = b = c = 4.06$
Inter-axial angles	$\alpha = \beta = 90^\circ$ $\gamma = 120^\circ$	$\alpha = \beta = \gamma = 90^\circ$
Packing index	0.74	0.74
Coordination number	12	12
Nearest-neighbor distance (nm)	0.222	0.286
Number of Atoms per unit cell	6	4

Table 1.9 Physical properties of beryllium and aluminum (Behrish and Eckstein, 2007; Calister and Rethwisch, 2010; Kittel, 2005; Marot et al., 2013)

Both Al and Be have octahedral and tetrahedral sites for interstitial hydrogen atoms. Both hcp and fcc materials have the same number of available interstitial sites per atom of material and both have the same maximum sphere radius to be accommodated in interstitial space formed by target-atom spheres (Fukai, 2005). The octahedral and tetrahedral interstitial sites for fcc and hcp lattices are shown in Fig. 1.29

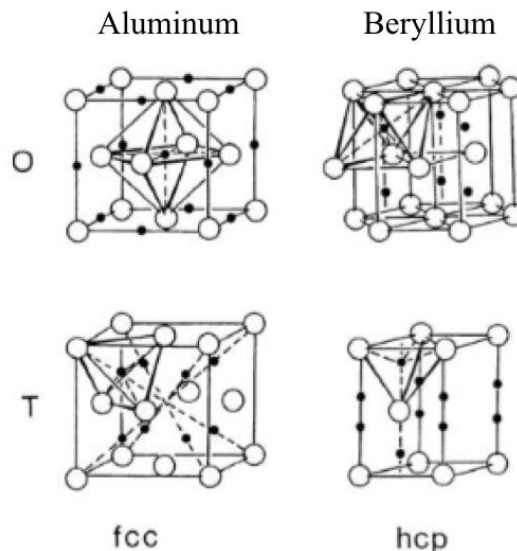


Fig. 1.29 Octahedral (O) and tetrahedral (T) interstitial sites in fcc (Al) and hcp (Be) lattices (Fukai, 2005)

Fig 1.30 shows the sputtering yield as a function of incident ion energy for both Be and Al when bombarded with Ar, D and  $^4\text{He}$  ions. It is seen that the sputtering yield shows a similar behavior for different energies. For Ar, D and He ions they both have a maximum

sputtering yield value at 1100 eV, 500 eV and 800 eV respectively. For higher energies, sputtering yield decreases and ion implantation becomes dominant. The main difference is that Al has a higher sputtering yield than Be. For 1000 eV Ar, D and He ions the sputtering yield values for Al 1 atoms/ions, 0.04 atoms/ions and 0.16 atoms/ions, respectively. For Be the sputtering yield values are 0.5 atoms/ions, 0.027 atoms/ions and 0.12 atoms/ions, respectively.

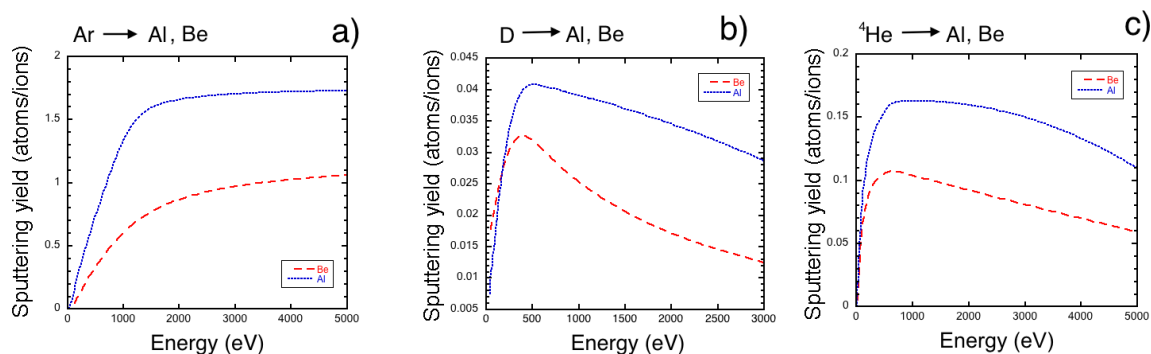


Fig. 1.30 Sputtering yield at normal incidence of Be and Al for a) Ar b) D and c) <sup>4</sup>He ions impacting the surface with different energies at normal incidence (Eckstein, 2002)

Tab. 1.10 shows the sputtering threshold values of both Be and Al, for different incident ions. In the case of H and D ions, the sputtering threshold for Al is almost two times higher than for Be with values of 30 eV and 14 eV respectively. The opposite is seen for Ar, in which its sputtering threshold is 22 eV for Al and 37 eV for Be. With Ar ions, the sputtering threshold is lower for Al due to the mass ratio of Ar with Al and Be. The fraction of energy transferred from an Ar atom to an aluminum is higher than that transferred to beryllium. As a result, sputtering by Ar is activated at much lower energy in aluminum, which results in a lower sputtering threshold. Finally, with He the sputtering threshold is quite similar for both materials with values of 12 eV for Be and 14 eV for Al.

Ion	Sputtering Threshold (eV) for Be	Sputtering Threshold (eV) for Al
H	14	30
D	10	18
T	9	14
4He	12	14
Ar	37	22

Table 1.10 Sputtering threshold of beryllium and aluminum for different impinging ions (Behrish and Eckstein, 2007)

Table 1.11 shows the ion implantation depth for D, Ar and He ions in Be and Al. The implantation depth for both materials are quite similar. Its values for 1000 eV D, He and Ar ions is, respectively, 25, 12 and 3 nm for both Be and Al.

Ion	Energy (eV)	Implantation depth (nm) for Be	Implantation depth (nm) for Al
D	40	1	2
D	300	8	9
D	1000	25	25
He	50	0.7	1
He	300	4	5
He	1000	12	12
Ar	100	0.8	0.5
Ar	500	2	1
Ar	1000	3	3

Table 1.11 Ion implantation depth at normal incidence for different ions and implantation energies in Al and Be (Eckstein, 2002)

Fig 1.31 shows the variation of hydrogen diffusivity in Al and Be as a function of the material temperature. For temperatures lower than 450 K, beryllium has a higher diffusivity when compared to aluminum. In addition, diffusivity in beryllium increases by 3 orders of magnitude, from  $10^{-13}$  to  $10^{-10}$  m/s<sup>2</sup> when the temperature increases from 300 K to 1100 K. On the other hand, diffusivity in aluminum increases by more than 6 orders of magnitude from  $10^{-15}$  to  $10^{-9}$  m/s<sup>2</sup> from 300 K to 900 K (melting temperature for aluminum).

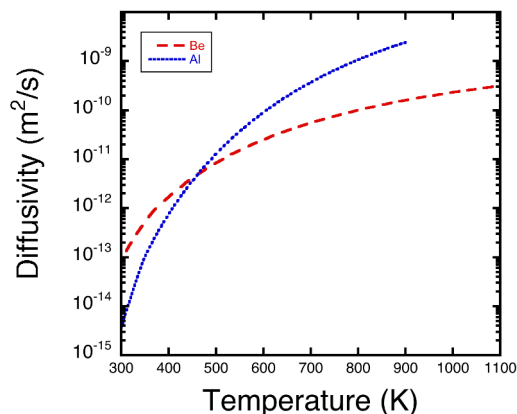


Fig. 1.31 Diffusion of hydrogen ions in Al and Be as a function of temperature (Abramov et al., 1990; Young and Scully, 1998)

Fig. 1.32 shows the variation of hydrogen solubility in tungsten and beryllium as a function of the material temperature. Both of them increase exponentially with increasing temperature, an expected behavior of endothermic materials. Endothermic materials have the characteristic that their solubility is extremely low (Causey, 2009; Serra et al., 1998). Hydrogen solubility is higher in aluminum than in beryllium; however this difference decreases for increasing temperature. In addition, solubility in beryllium increases by more than 13 orders of magnitude, from  $10^5$  to  $10^{18}$   $\text{mol/m}^3 \sqrt{\text{Pa}}$  when the temperature increases from 300 K to 800 K. On the other hand, solubility in aluminum increases by 7 orders of magnitude from  $10^{11}$  to  $10^{19}$   $\text{mol/m}^3 \sqrt{\text{Pa}}$  for the same temperature range.

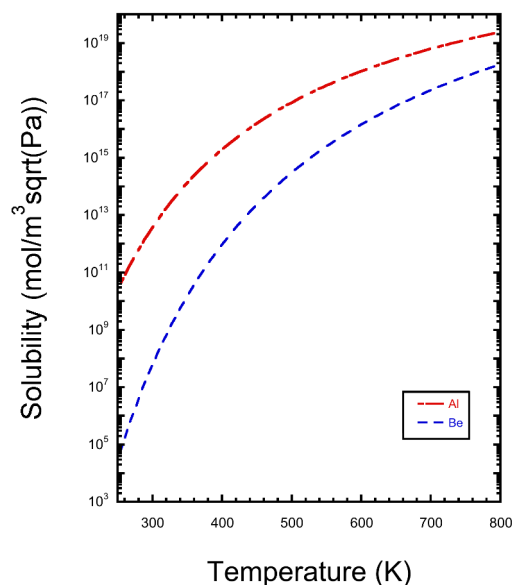


Fig. 1.32 Solubility of hydrogen ions in Al and Be as a function of temperature (Serra et al., 1998)

One main difference between beryllium and aluminum is related to their hydrogen retention mechanisms. The thermal desorption spectra (TDS) for aluminum and beryllium exposed to high fluence ( $1.2 \times 10^{26}$  ions/m<sup>2</sup>) deuterium plasma are shown in Fig. 1.33. TDS experiments consist in heating a sample with a controlled evolution of temperature and measuring quantitatively the partial pressures of atoms and molecules that are desorbed from the sample (Schroeder and Gottfried, 2002). The measured TDS profiles and their relation with the heating temperature ramp and heating rate are used to obtain information on the trapping energy and desorption mechanisms of the materials. In the case of beryllium and aluminum, their hydrogen desorption peaks occur at different temperatures and aluminum has just one desorption peak whereas beryllium has two desorption peaks (Kreter et al., 2014). Consequently, it is seen that these materials have different trapping energies and desorption mechanisms. This result is not surprising since both materials have a different crystal structure and hence their hydrogen retention dynamics should differ as well.

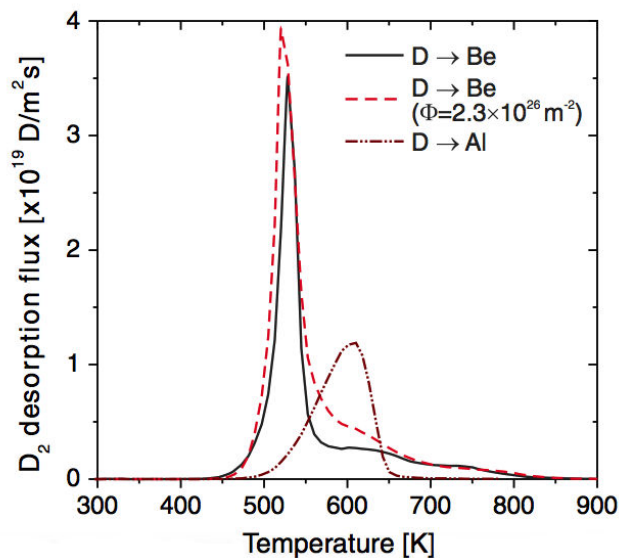


Fig. 1.33 TDS spectra of Be and Al exposed to D plasma (Kreter et al., 2014)

Fig. 1.34 shows the Al-H phase diagram at 0.1 MPa for atomic hydrogen in the range of 0 – 0.01 atomic percent hydrogen. Our main interest is to study hydrogen dissolved in solid aluminum, that is, the section below 660°C (red square). It is seen that the solubility of H in solid Al is very small at atmospheric pressure (0.1 MPa). At 400°C it has a value of  $5.6 \times 10^{-6}$  atoms/m<sup>3</sup> (red arrow) increasing to a value of  $1.16 \times 10^{-4}$  atoms/m<sup>3</sup> (blue arrow) for increasing temperature. The dashed line denotes the observed limit of H solubility (green arrow). Nevertheless, this dashed line does not denote the boundaries of equilibrium phases

and hence at hydrogen concentrations higher than this limit, hydrogen does not necessarily precipitates in bubbles.

Studies show that for low concentrations of hydrogen in Al, there is no formation of hydrides. The  $AlH_3$  phase is formed at hydrogen concentrations of 75% (San-Martin and Manchester, 1992).

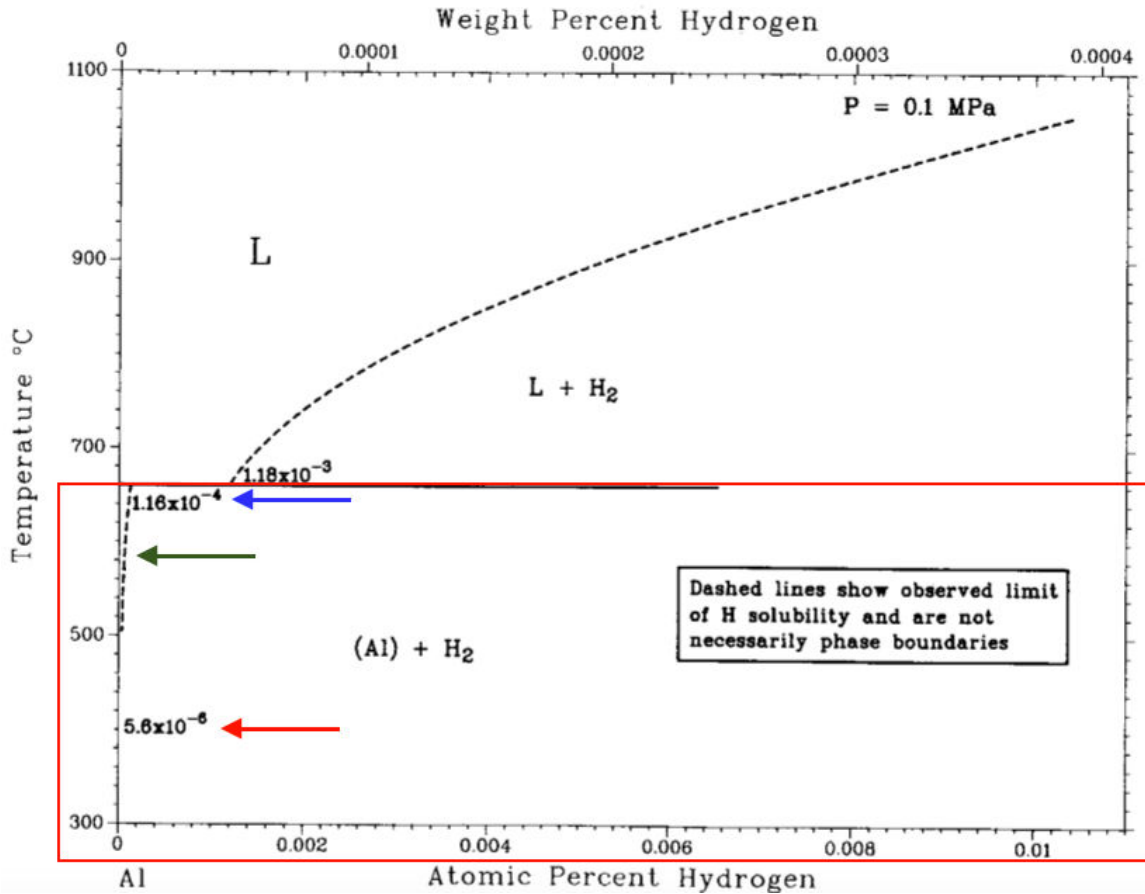


Fig. 1.34 Al-H phase diagram at 0.1 MPa (San-Martin and Manchester, 1992)

## 1.7.2 Chemical properties of Al and Be

The different chemical properties for both elements are shown in Table 1.12. Beryllium and aluminum are both metals belonging to the alkaline earth family and boron family respectively. This means that they have different electronic configuration and thus different number of valence electrons. Additionally, their ionization energies are different and thus, their chemical properties are different. However, their electronegativity, which describes the tendency of an atom to attract electrons, are quite similar. Therefore it is expected that they form similar compounds.

Chemical properties	Beryllium	Aluminum
Atomic number	4	13
Atomic weight (amu)	9.012	26.98
Electron configuration	$1s^2 2s^2$	$1s^2 2s^2 2p^6 3s^2 3p^1$
Oxidation states	+2	+3
Atomic radius (nm)	0.114	0.143
Ionic radius (nm)	0.035	0.053
Ionization energies (eV)	1st : 9.32 2nd : 27.53	1st : 5.98 2nd : 24.80
Electronegativity (Pauling scale)	1.57	1.61

Table 1.12 Chemical properties of beryllium and aluminum (Calister and Rethwisch, 2010; Marot et al., 2013; NIST, 2016)

Tab. 1.13 summarizes different chemical compounds formed by Be and Al. It can be seen that both Al and Be form hydrides with covalent bonds.  $BeH_2$  usually presents an amorphous appearance with a density of  $0.62 - 0.65 \text{ g/cm}^3$  and it can also form in an hexagonal crystalline form with a higher density ( $0.77 - 0.78 \text{ g/cm}^3$ ). The most stable phase of  $AlH_3$ ,  $\alpha$ -Alane forms a rhombohedral or trigonal crystal structure (Brendel et al., 1978; Ojwang et al., 2009).

Both of these elements form oxides with ionic bonds, due to the similarity in their electronegativity values. These two oxides have a high melting point and a similar density.  $BeO$  forms a wurtzite or hexagonal structure while  $Al_2O_3$  has a trigonal structure (Marot et al., 2013; Rado and Suhl, 1963; Zalkind et al., 1997). Both of these elements have a natural affinity with oxygen, therefore they easily form a thin ( $\sim 10 \text{ nm}$ ), stable, passivating oxide layer even under vacuum conditions (Federici et al., 2012; Palik, 1998a).

Both beryllium and aluminum form compounds with nitrogen (Jeffrey et al., 1956; Oberkofler and Linsmeier, 2010).

Finally, the vacuum chamber is subject to cross-contamination from the PFC's, beryllium and tungsten, so it is important to analyze the interaction between Be and W and its similarities with Al and W. Studies have shown that both Be and Al form compounds with W as shown in Table 1.13 (Baldwin et al., 2007; Effenberg and Ilyenko, 2005).

Compounds	Beryllium	Aluminum
Hydride	$(BeH_2)_x$ Covalent bond Melting point: 523 K Crystal system: amorphous or hexagonal	$(AlH)_x$ Covalent bond Melting point: 423 K Crystal system: Trigonal
Oxide	$BeO$ Ionic bond Melting point: 2780 K Density: 3.01 g/cm <sup>3</sup> Crystal system: Wurtzite	$Al_2O_3$ Ionic bond Melting point: 2345 K Density: 3.95 – 4.01 g/cm <sup>3</sup> Crystal system: Trigonal
Nitride	$Be_3N_2$ Crystal system: Cubic	$AlN$ Crystal system: Wurtzite
Alloys with W	$Be_2W, Be_{12}W$ $Be_{22}W$	$Al_4W, Al_5W, Al_6W$ $Al_{12}W, Al_{50}W_{50}$

Table 1.13 Chemical compounds of Be and Al relevant for ITER (Calister and Rethwisch, 2010; Marot et al., 2013; NIST, 2016)

## 1.8 Context of this PhD project

The "Plasma Surface Interaction" research group at LSPM (Laboratoire des Sciences des Procédés et des Matériaux) was developed in 2005 within the team MP4 (Milieux PolyPhasiques et Procédés Plasma). It was created with the aim of studying plasma wall interactions related to fusion reactors by simulating some of the phenomena involved in edge plasmas in fusion reactors. In order to fulfill this objective the team is supported by the FR-FCM (Fédération de Recherche-Fusion par Confinement Magnétique) relying on a network combining the CEA (Commissariat à l'énergie atomique), the CNRS (Centre National de la Recherche Scientifique) in addition to several universities. The mission of this federation is to coordinate the research conducted in France in the field of magnetic fusion related to the ITER project and accompanying framework supported by Europe (Eurofusion).

The reactor CASIMIR I (Chemical Ablation, Sputtering, Ionization, Multi-wall Interaction and Redeposition) was developed at LSPM in 2006 supported by the ANR (Agence Nationale de la Recherche). It was designed to study the interactions between a hydrogen (or deuterium) plasma and a solid material (carbon or tungsten). Then, in the frame of a second project supported by the ANR CRWTH (Carbon-Tungsten Ternary compounds with hydrogen for fusion reactor walls) the CASIMIR II reactor was developed in 2011. The objective

was to improve the erosion and pulverization performances of CASIMIR I and reach more relevant densities and plasma fluxes. A third reactor, called Mono-source, was developed mainly to study dust formation in edge plasma environments. Initially, these reactors were used to study and analyze the behavior of carbon in plasma edge environments (Delacqua, 2012). However ITER withdrew its decision to use carbon as a PFC and hence studies were afterwards focused on PSI's with tungsten (Ouaras, 2016). The experimental results obtained with these reactors are then used to develop and validate computational models developed in our team by X. Bonnin, C. Sang and A. Michau. These codes are: the Hydrogen Isotope Inventory Processes Code (HIIPC), which simulates hydrogen retention in ITER relevant materials and another model in charge of analyzing the kinetics of ions and neutrals in a magnetized plasma environment.

## 1.9 Research proposal

Beryllium is the proposed material for the first wall in ITER and performing analysis on this material is of paramount importance. In the continuity of the research performed at LSPM on the field of PWI for fusion reactors, analysis should be performed with beryllium. However, this material is highly toxic and its manipulation should be done under strictly controlled conditions in order to evacuate its dust properly and avoid its inhalation. These conditions are not met at LSPM and therefore a proxy should be used to perform the experiments. Aluminum was recently proposed in the fusion community as a surrogate for Be and was used as a proxy for beryllium by different research teams in diverse experiments. Nonetheless, this material has a large number of differences with beryllium and under certain conditions is not a suitable proxy. Regardless of this fact, analyses performed with aluminum aid in the understanding of blister and bubble dynamics due to hydrogen plasma exposure in materials with a low hydrogen solubility. Another important aspect has to do with the fact aluminum and beryllium have a different crystallographic structure: aluminum crystallizes in fcc whereas beryllium in hcp. In other words, beryllium has a more complex crystal system than aluminum. Experiments performed in endothermic cubic systems, such as a fcc crystal, provide a suitable background to understand phenomena related to crystallographic structure. It is also a pre-requisite for the investigation of more complex hexagonal systems such as beryllium.

This thesis work focuses mainly on performing experiments with aluminum and tungsten samples. Specifically, analyzing surface modifications after hydrogen plasma exposure. The experiments consist in analyzing the influence different parameters such as incident ion energy, plasma fluence and material micro-structure have on material modifications. Special

attention is given to surface morphology after plasma exposure and how it is affected by the crystallographic orientation of the material. To fulfill this objective, two materials with a cubic crystal systems are analyzed: aluminum and tungsten that crystallize in fcc and bcc structures, respectively.

The results obtained during this work allow to acquire an overall picture of blister dynamics in materials with a low hydrogen solubility. Additionally, the results obtained with aluminum and tungsten provide a suitable background of the effect cubic crystal systems have on blister morphology. These results provide the necessary tools for analyzing more complex, hexagonal crystal systems such as beryllium. As a result, a new proxy may be proposed in order to fully understand blister growth and morphology in beryllium.

# Chapter 2

## Materials, Methods and Plasma Characterization

The main focus of this chapter is to give an overview of the tools used during this thesis work, as well as the characterization of the samples and the plasma used in the experiments. Three kinds of tools were used during this work: plasma devices, plasma characterization tools and material characterization tools. To cover these topics, this chapter is divided as follows:

- Section 2.1 presents the different plasma devices used to perform the experiments.
- Section 2.2 describes the different tools used to characterize the samples used in the experiments.
- Section 2.3 focuses in describing the basic procedures used to obtain fully characterized samples regarding their microstructure.
- Section 2.4 through Section 2.7 detail the measurements performed to obtain different plasma parameters (*i.e.* plasma potential and electron temperature and density) and describe the steps followed to calculate the ion flux and fluence in our experimental conditions. These sections also give an overview of the spectroscopic measurements and the main results obtained by collecting aluminum dust particles in our experimental conditions.

### 2.1 Experimental set-up

Two reactors were used to perform the different hydrogen loading experiments: CASIMIR and the mono-source reactor. Both of these devices were designed with the objective of achieving high atomic, ionic and electronic densities in order to simulate and study plasma surface interactions. In our case, they are used to simulate some of the phenomena occurring

in the edge plasma of thermonuclear fusion reactors. CASIMIR works with a magnetized plasma which relies on the Electron Cyclotron Resonance (ECR) principle whereas the mono-source reactor can work with either magnetized or non-magnetized plasma. Due to its high density and volume, CASIMIR is more suited to perform experiments to analyze surface modifications and hydrogen retention after plasma exposure. The mono-source reactor is mainly used for the synthesis of dust due to its adjustable settings and geometry that allows easy access to perform plasma diagnostics. It has several windows to perform spectroscopic analysis and laser measurements. Furthermore, its plasma sources can be adjusted to work under pressures as low as 0.1 Pa or as high as 100 Pa. Its geometry allows to polarize the sample to high voltages ( $-5$  kV) and the distance between the plasma source and the sample can be easily adjusted ( $\pm 5$  cm).

Both of these reactors were developed using microwave sources given that they present a large number of advantages with respect to other plasma sources. Some of these benefits are (Lacoste et al., 2002):

- Contamination risk is small given that there is not sputtering of the antenna material.
- They are compact sources that produce high density, isotropic plasmas.
- They have a high excitation frequency and hence the discharge is almost continuous for both ions and electrons.
- There is a decrease in wall loading effects with respect to other plasma sources due to the fact that very few electrons arrive at the surfaces.
- The density of the ions produced in the discharge does not depend on the energy they have when they arrive on a substrate. As a result, the energy of these ions can be easily controlled by polarizing the target while keeping a constant flux.

Microwaves also present some disadvantages. In particular the non-uniformity of the discharges and the difficulty of obtaining larger-sized discharges. However, it is possible to overcome these drawbacks by arranging the microwave sources in specific ways to achieve uniform and large discharges.

### 2.1.1 Mono-source

A schematic of this reactor, along with a picture of the device and its components are shown in Fig. 2.1. This reactor consists of a single source, which can deliver a maximum power of 180 W and generate plasmas with a maximum density of  $10^{11}$  cm<sup>-3</sup>. It works either in low pressure (0.1 – 1 Pa) with a dipolar ECR source or at high pressures (10 – 100 Pa) without a permanent magnet. In the case of ECR source, the electron cyclotron resonance is met at 875 G for an excitation frequency of 2.45 GHz. The plasmas sources used in

this reactor are Boreal Plasma DP10 180 W sources supplied by a SAIREM microwave generator (2.45 GHz). The microwaves are transmitted by a coaxial cable connected to a circulator with a water charge adapted to absorb the reflected power. This reactor allows the polarization of samples at either low or high voltage. In the low polarization regimes, a continuous voltage of up to  $-600$  V with a current of  $1$  A is applied to the sample by a SEFELEC high voltage supply. For a higher polarization, a pulsed voltage reaches the sample holder by a coaxial high voltage cable. The system consists of a high supply voltage TECHNIX SR5-N-600 and an EFFITECH AHTPM5 supply modulator. The duration of the pulses and their frequency are parameters which can be adjusted in the range of  $1 - 100$   $\mu$ s and  $0 - 10$  kHz respectively. The current and voltage can be adjusted respectively in the range of  $0 - 120$  mA and  $0$  to  $-5$  kV.

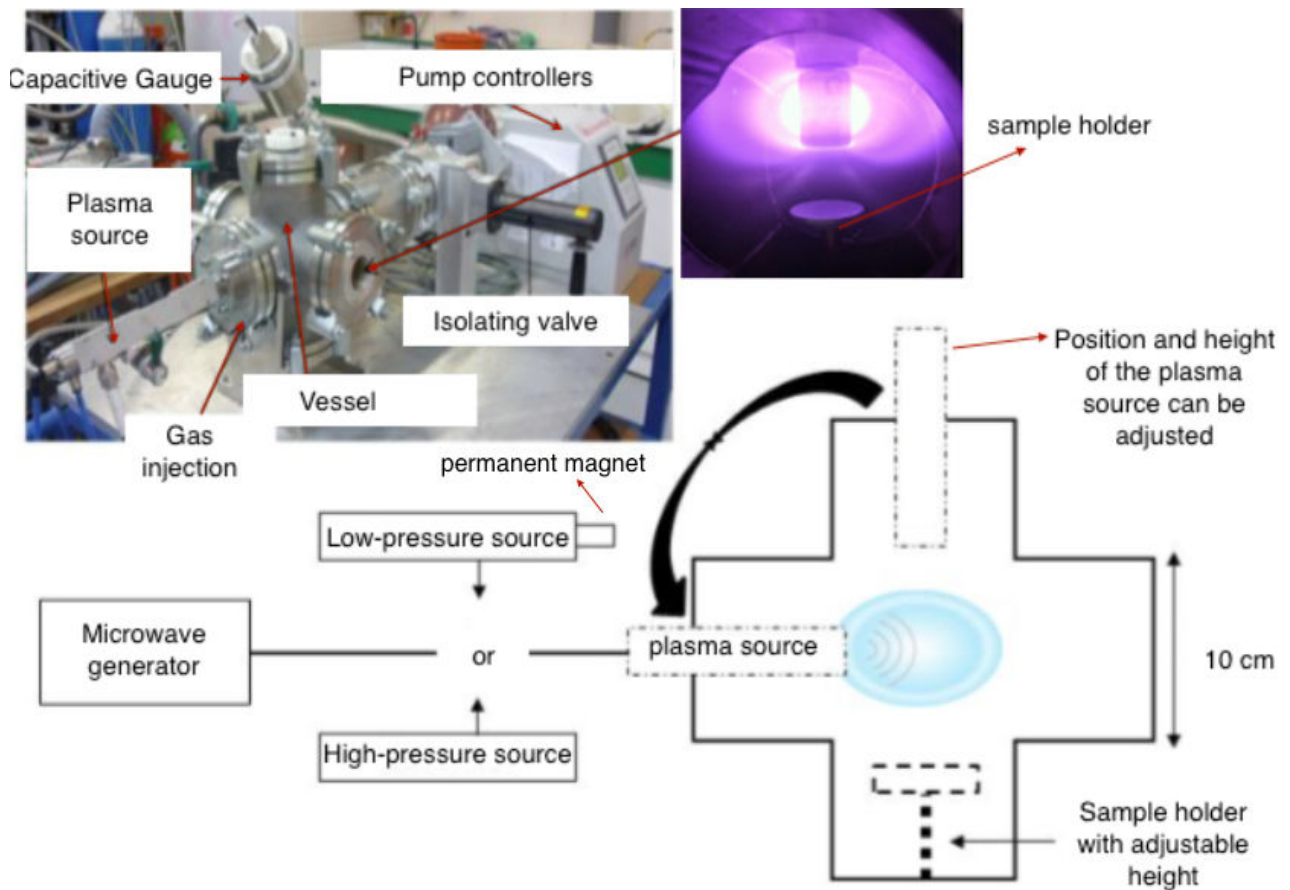


Fig. 2.1 a) Monosource plasma reactor b) Argon plasma in the monosource

The mono-source reactor consists of a cross-shaped stainless steel vessel with a total volume of 5.12 L. It has 6 ports or openings which have multiple uses: one of these ports is used for the pumping system, the second one for the sample holder and another one for the plasma sources. As a result, three ports are available to perform spectroscopic and laser measurements. The sample holder has an adjustable height ( $\pm 5$  cm). It is made of stainless steel and isolated with a ceramic piece. It was designed in such a way to allow the application of high voltage to the sample.

The vacuum systems allows reaching a maximum vacuum of  $5 \times 10^{-4}$  Pa. The system is composed of two pumps: a primary dry pump and a turbo-molecular pump. The pressure is measured by a MKS capacitive gauge (range 100 Pa). The reactor has a manual valve in front of the pumping system that allows to isolate the reactor when needed.

The gas is introduced into the reactor at flows controlled by Bronkhorst flowmeters. Each flowmeter is calibrated for the gas it controls (from 10 to 100 sccm standard cubic centimeter per minute  $\text{cm}^3/\text{min}$ ).

The mono-source reactor has been used mostly for the study of carbon and tungsten dust formation and dynamics. This is due to the fact that its design allows using several diagnostics that aid in the study of dust dynamics. This reactor has a single source, whereas the CASIMIR reactor has 16 sources. The CASIMIR reactor, due to its configuration, does not allow the use of the same number of diagnostics as the mono-source reactor. Additionally, it presents a higher electronic and ionic density and hence a higher plasma flux. As a result, this reactor is more suitable for studies focusing on material modifications after plasma exposure.

### 2.1.2 CASIMIR

CASIMIR stands for Chemical Ablation, Sputtering, Ionization, Multi-wall Interaction and Redeposition. This reactor, shown in Fig. 2.2, consists of 16 dipolar plasma sources close enough together to ensure a homogeneous plasma density ( $10^{10} - 10^{12} \text{ cm}^{-3}$ ) over a large volume. It relies on the ECR principle, has a large injected power, up to 3 kW, and works at low pressures (0.1 – 1 Pa). In order to have the same injected power, each source is connected to the generator by a microwave power divider. Additionally, the reflected microwaves are directed to 16 water cooled circulators. The main characteristic of this reactor is its high plasma exposed surface to reactor volume ratio of the order of  $22.6 \text{ m}^{-1}$ .

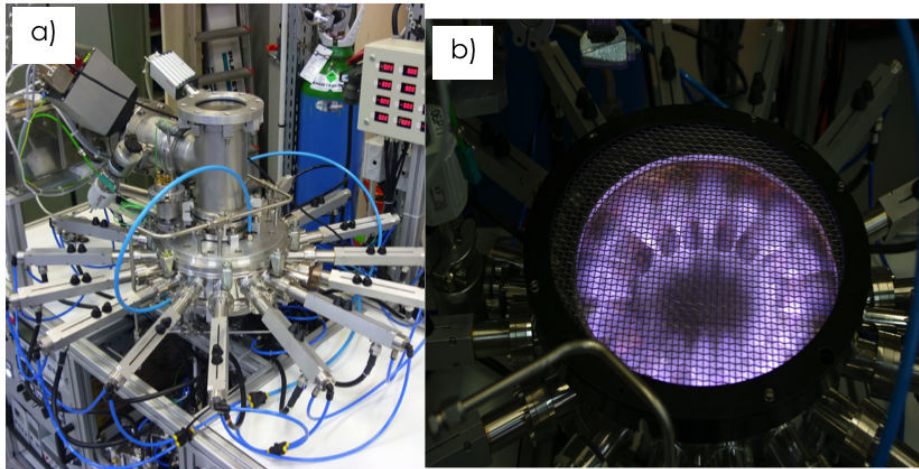


Fig. 2.2 a) CASIMIR II plasma reactor b) Hydrogen plasma in the CASIMIR

The reactor is made of stainless steel and its vessel has a diameter of  $d = 26.1$  cm and a height of  $h = 6$  cm; for a total volume of 3.2 L. It has a double water cooled wall to sustain the high temperatures during the discharges. The vessel is composed of austenitic steel due to its non-magnetical properties and its high chemical resistance. It has 16 opening for the plasma sources and 2 small openings used for optical spectroscopy measurements. The sample holder is located in the center of the chamber and is isolated by a ceramic piece. This sample holder has a bias system that allows the application of high voltage to the sample. Fig. 2.3 shows a schematic representation of this vessel.

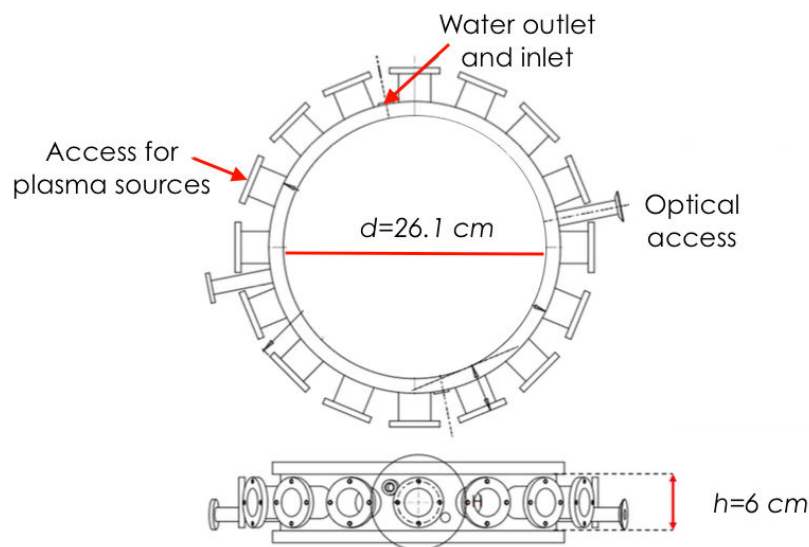


Fig. 2.3 Schematic representation of the CASIMIR vessel

CASIMIR has two pumps: a dry one (Alcatel ACPA15) (0.1 – 1 Pa) and a turbo-molecular one (Pfeiffer) with a pumping rate of 250 L/s that allows reaching a vacuum limit of 0.001 Pa. Additionally, a gauge system allows measuring the pressure in the reactor: a combined Penning-Pirani (model Ionivac, Leybold) and a capacitive gauge with a range of 100 Pa (model Ceravac, Leybold). The gas is introduced through 3 openings in the lower wall. The gas flow is controlled by 3 Bronkhorst flow-meters specifically calibrated for each gas. A schematic of this reactor is shown in Fig. 2.4

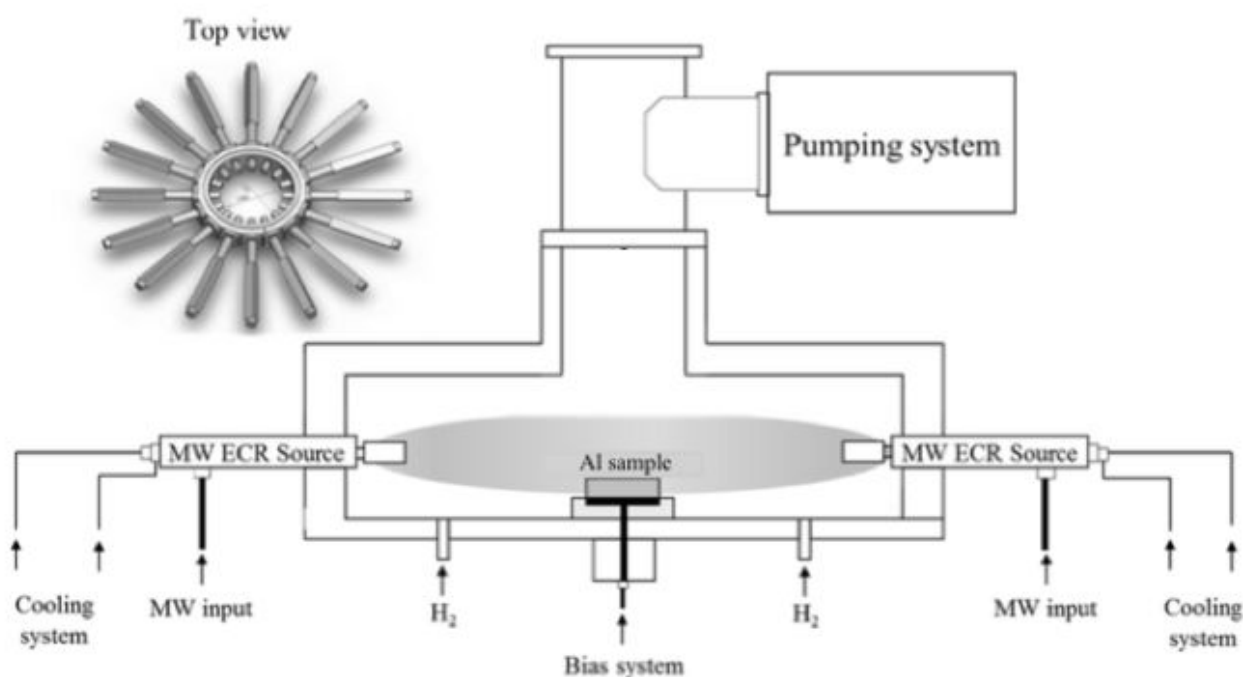


Fig. 2.4 Schematic of the CASIMIR plasma reactor

## 2.2 Sample characterization tools

This section describes the different tools used to characterize the samples before and after plasma exposure. Furthermore, the polishing procedures and heat treatments used for both tungsten and aluminum are discussed.

### 2.2.1 Scanning Electron Microscopy

Scanning electron microscopes (SEM's) are useful tools used to obtain high resolution images of a given sample as a result of the interaction of an electron beam with the atoms of

this sample. The sample is scanned by an electron beam that emits different signals that give different information on the material. The most common SEM mode is the detection of secondary electrons emitted by the atoms that are excited by the electron beam. This detection mode allows obtaining information on the surface topography (Goldstein et al., 2012; Ruste, 2016). Therefore, it is an important tool for analyzing the surface morphology of the samples before and after plasma exposure as well as the dust collected during the dust synthesis experiments. Fig. 2.5 shows a typical SEM micrograph obtained for our Al samples exposed to  $H_2$  plasma. The topography of the sample is clearly seen and two spherical and a square-shaped deformation of a few  $\mu\text{m}$  in size can be distinguished.

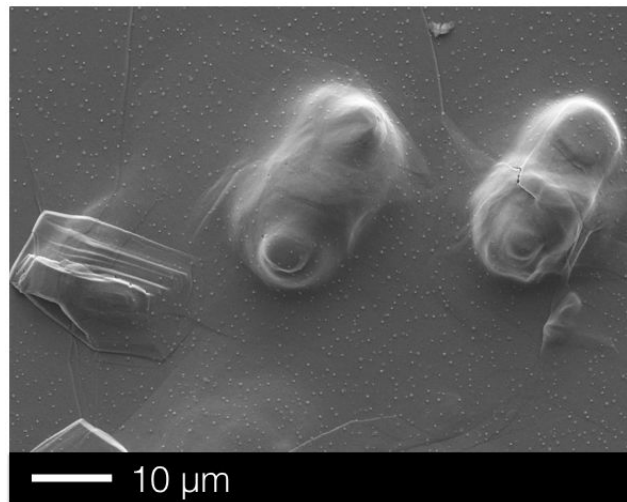


Fig. 2.5 Typical SEM micrograph

Another detection mode available in SEM is the measurement of back-scattered electrons, which are sensitive to the phase composition of the material. It is possible to associate these back-scattered electrons to several parameters, which allow the measurement of the crystal phase and orientation of the material within the electron interaction volume (Pouchou, 2002). This technique is known as electron back-scatter diffraction (EBSD) and is used to obtain grain morphology of the samples during different steps of the experiments. Fig. 2.6 shows a typical EBSD measurement for our Al samples. It can be seen that each crystallographic direction has a specific color assigned by an inverse pole figure (*i.e.* grains whose surface normal direction (ND) is oriented to the  $\langle 100 \rangle$  direction are portrayed with a red color). Grains with an orientation closely in common are represented by similar colors. Two grains may be distinguished from each other by their misorientation angle. For our case, this misorientation angle is set to have a value higher than  $15^\circ$  degrees. Dislocations, on the other

hand, are considered as those misorientations having angles above  $2^\circ$  degrees and below  $15^\circ$  degrees.

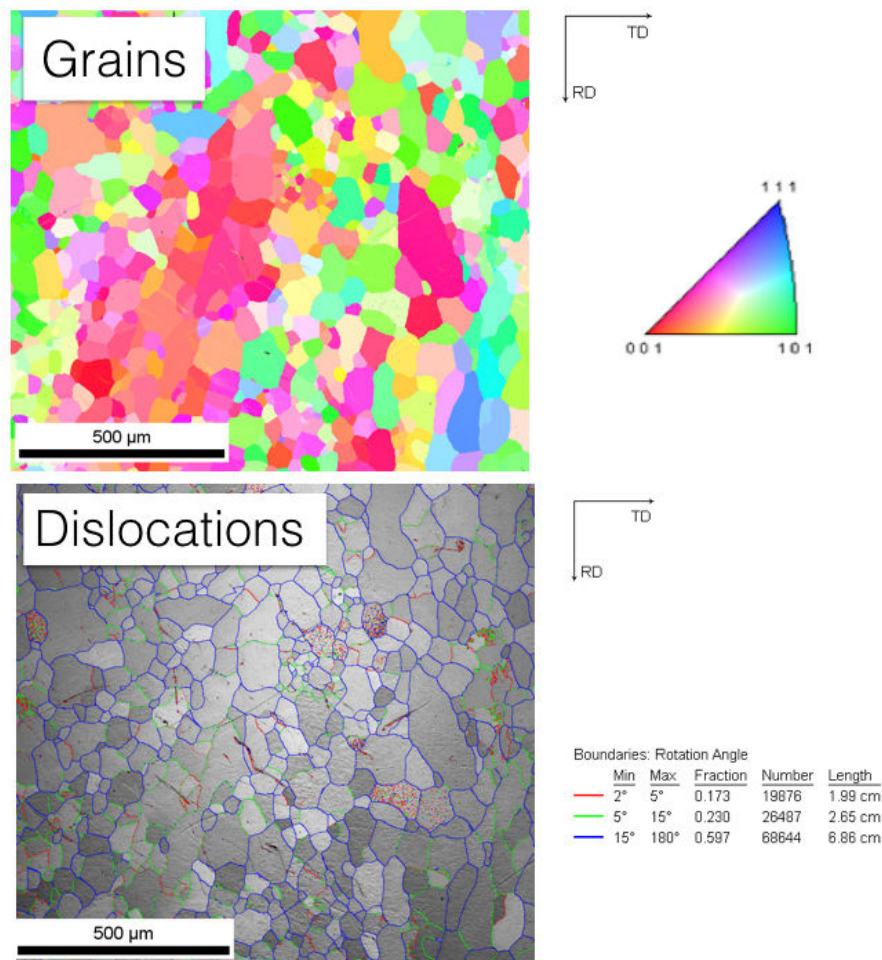


Fig. 2.6 Typical EBSD measurement obtained for Al samples used in this work

SEM's can be equipped with an energy-dispersive spectroscopy X-ray spectroscopy system (EDS), which is used to characterize the elemental composition of the analyzed sample. It relies on the ability to detect X-rays generated when a sample is bombarded with high-energy electrons in a SEM. These X-rays are measured with an energy-dispersive spectrometer that are able to separate X-rays with different energy levels; thus revealing which elements are present in a particular specimen (Goldstein et al., 2012). The results obtained with EDS measurements are a unique set of peaks like the one shown in Fig. 2.7, which was obtained for Al dust collected on Si samples. Three peaks are seen: Si, Al and O. The latter peak corresponds to the oxidation of aluminum.

During this work two different SEM's were used:

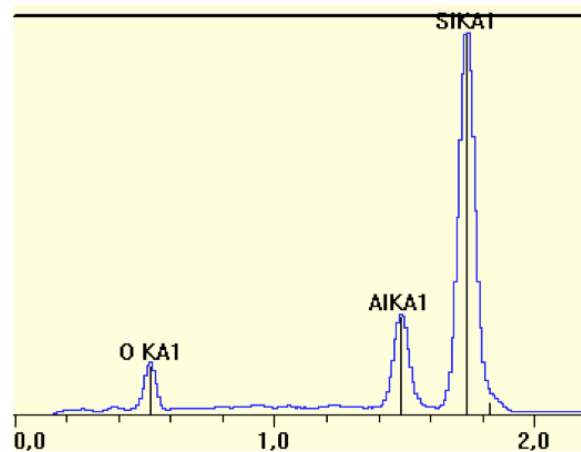


Fig. 2.7 EDS spectrum obtained for aluminum dust collected on Si samples

- A Field emission gun (FEG)-SEM SUPRA 40 VP provided by CARL ZEISS. It has a field emission cannon type Schottky (W/ZrO filament heated at 1800 K). This microscope is equipped with a fast electron back-scatter diffraction (EBSD) camera (HJELEN UF300, 305 points/s).
- SEM S440 with a tungsten filament, it was provided by LEICA and is equipped with an EDS system.

## 2.2.2 Confocal microscopy

Confocal microscopy is used to reconstruct three-dimensional structures from sets of images obtained at different depths within a sample. The principle of this microscope is to use a point illumination source focused on a small spot within the specimen. Light emitted from this spot is focused by the objective lens to a small spot at the image plane. Therefore, a point source of light is in conjugate focus at the sample and the image plane. A small pinhole aperture allows only the light coming from the focal point of the sample to pass to the detector and the out of focus signal is eliminated, *i.e.* light coming from above and below the focal plane (see Fig. 2.8). The name *confocal* is actually derived from this configuration. As only light produced by fluorescence very close to the focal plane can be detected, the image's optical resolution, particularly, the sample depth, is much better than common microscopes. In order to acquire full details across the plane of the sample, the spot is scanned across the image and the image information collected sequentially. Given that a great percentage of the light is diffracted at the pinhole, the increased resolution is at the cost of a decreased signal intensity. To counteract this drop in signal at the pinhole, the light intensity is detected by a sensitive detector that transforms light signal into an electrical one (Price and Jerome, 2011).

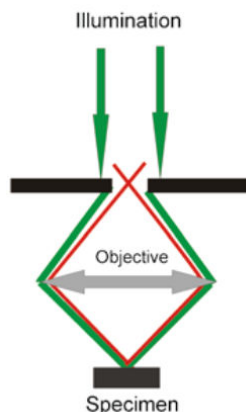


Fig. 2.8 Pinhole aperture in Confocal microscopy that allows only the light from the focal point of the sample to pass to the detector (Price and Jerome, 2011)

The microscope used in the present work is a Keyence VK-9700 Laser Scanning Confocal Microscope. Fig. 2.9 shows a measurement made with the Confocal microscope of an aluminum sample with several blisters on its surface. The measured surface has an area of  $6600 \mu\text{m}^2$ . In addition, the outline of one blister was obtained allowing the measurement of its height. The height of this blister is  $3 \mu\text{m}$ . The parameters used to take this image allowed obtaining a lateral resolution of  $150 \mu\text{m}$  and a vertical resolution of  $10 \text{ nm}$ .

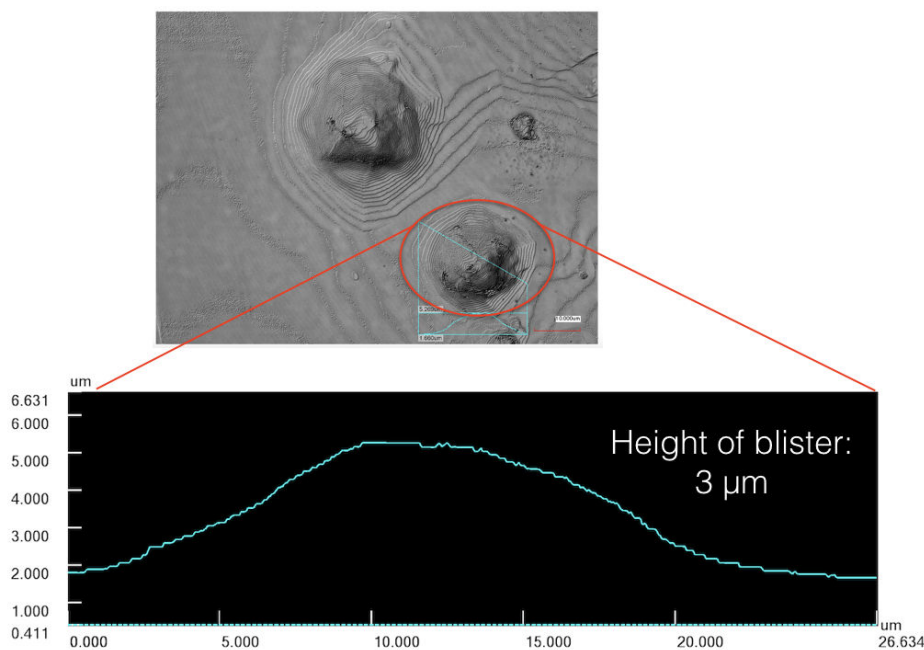


Fig. 2.9 Confocal measurements on blisters in an Al surface

### 2.2.3 X-Ray Diffraction

X-Ray diffraction is based on the constructive interference of monochromatic X-rays and a crystalline sample. The x-rays are generated by a cathode ray tube, filtered to produce monochromatic radiation, collimated and directed towards the sample. Atoms scatter X-rays mainly through the atom's electrons (Cullity and Stock, 2014). These scattered waves cancel out in most directions through destructive interference, however, they add constructively in a few directions given by Bragg's Law. In this law the difference in the optical path is an interger multiple of the wavelength, which gives (Bragg and Bragg, 1913):

$$2d\sin\theta = n\lambda \quad (2.1)$$

where  $d$  is the spacing between diffracting planes,  $\theta$  is the incident angle,  $n$  is called the order of diffraction and may take any interger value and  $\lambda$  is the wavelength of the incoming beam. This equation is illustrated in Fig. 2.10.

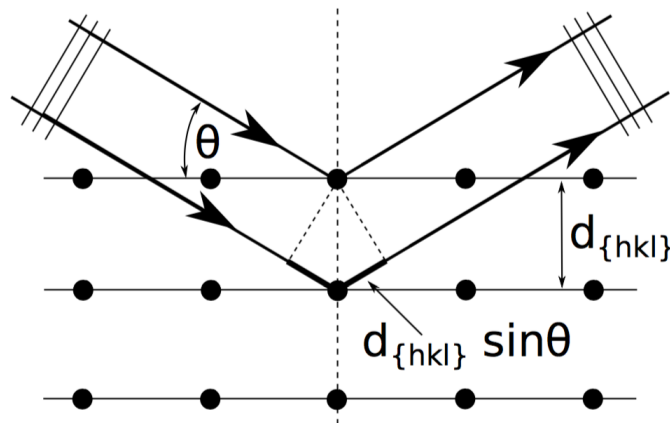


Fig. 2.10 X-ray diffraction on a crystal according to Bragg's law (Cullity and Stock, 2014)

### Crystallographic Texture

Usually, polycrystalline materials have different crystallographic directions of the individual grains. However, there are *textured polycrystalline materials* in which the grains have a preferential crystallographic direction (Calister and Rethwisch, 2010). In this work, X-Ray diffraction was used to determine the crystallographic texture of the samples.

All planes in the crystal can be represented by a set of plane normals radiating from one specific point within the crystal. By taking a reference sphere around this point, the plane normals will intersect the surface of the sphere in a set of points called poles (Cullity and

Stock, 2014). This representation is known as stereographic projection and is as shown in Fig. 2.11. The angle  $\chi$  outlines the azimuth of the pole, where  $\chi = 0^\circ$  is the north pole of the unit sphere, and the angle  $\phi$  represents the rotation of the pole around the polar axis, starting from a specified reference direction. ND is typically chosen to be in the north pole of the sphere, so that  $\chi = 0^\circ$  and the rotation angles  $\phi = 0^\circ$  for the rolling (or longitudinal) direction RD or the transverse direction TD (Engler and Randle, 2010). These directions correspond to a macroscopic reference to the crystal coordinate system.

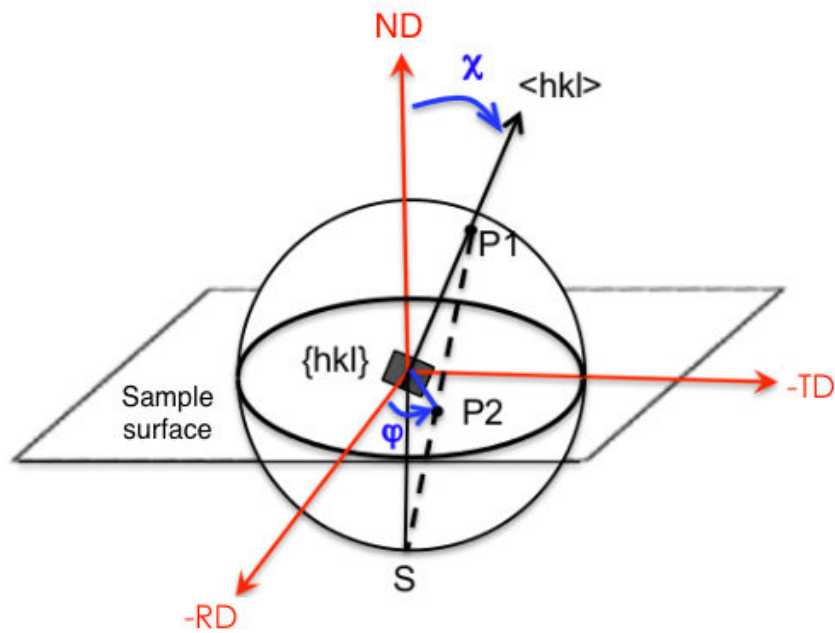


Fig. 2.11 Stereographic projection of the normal to  $\{hkl\}$  (Dufrenoy, 2016)

The principal poles of a cubic crystal projected on the  $\{001\}$  plane of the crystal, that is, the standard  $\{001\}$  stereographic projection is shown in Fig. 2.12. Furthermore, Fig 2.13 and Fig 2.14 show the stereographic projection of a  $\{011\}$  and a  $\{111\}$  cubic crystal, respectively. It is seen that for each specific direction, the pole is at the center of the figure. In other words, the pole  $\{001\}$  is located at the center of the projection in Fig. 2.12 as is the case of  $\{011\}$  in Fig. 2.13 and of  $\{111\}$  in Fig. 2.14.



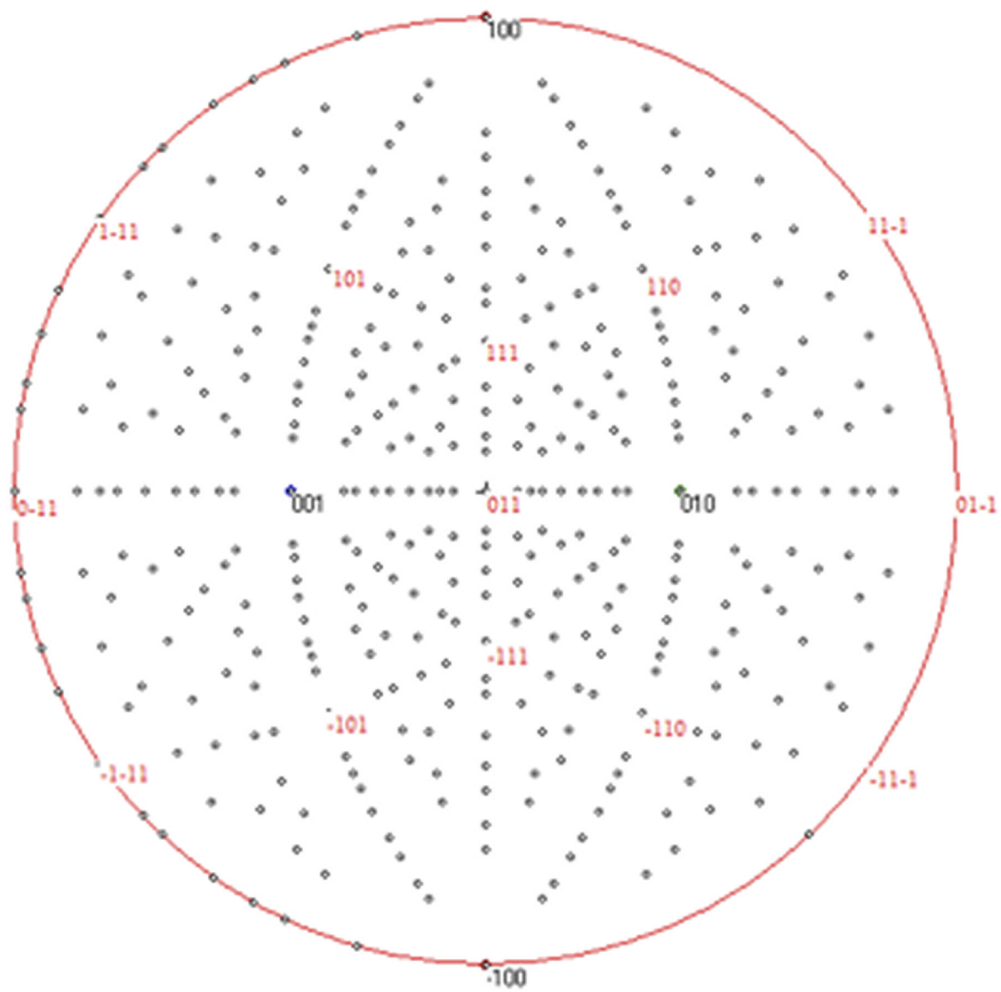


Fig. 2.13 Standard projection of a {011} cubic single crystal

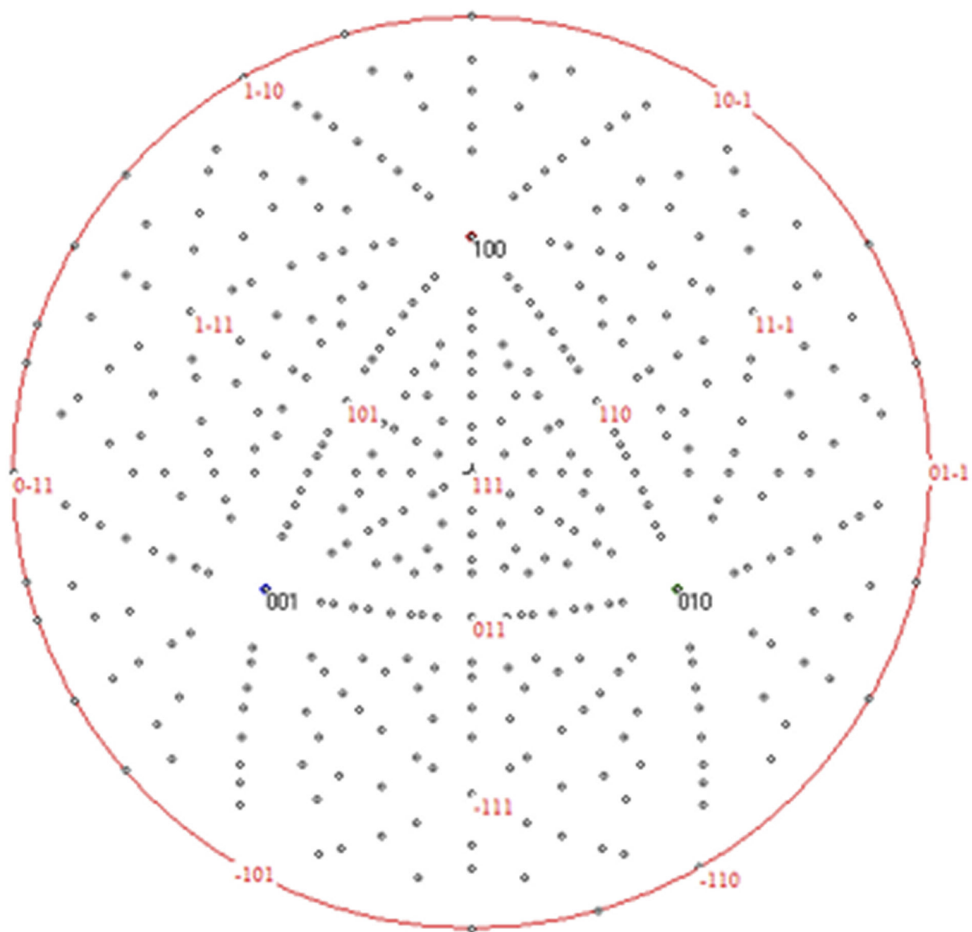


Fig. 2.14 Standard projection of a)  $\{111\}$  cubic single crystal

X-Ray diffraction experiments (XRD) for textures analysis were carried out on Al and W samples. A direct macroscopic reference system (ND, RD and TD) has been attached on the analyzed faces. Texture data was collected using an Inel<sup>TM</sup> four circles goniometer in Bragg-Brentano geometry with a point focus X-Ray source having a CoK $\alpha$  radiation ( $\lambda = 0.17902 \text{ nm}$ ). The measurement consisted first of the determination of the Bragg angles  $\{111\}$ ,  $\{200\}$ ,  $\{220\}$  reflections for Al samples;  $\{110\}$ ,  $\{200\}$ ,  $\{211\}$  reflections for W samples) and then the acquisition of the corresponding pole figures. After corrections of the experimental pole figures (background, defocusing and normalization), the determination of the orientation distribution functions was performed in order to determine the complete pole figures  $0^\circ \leq \chi \leq 90^\circ$ .

X-Ray diffraction was used to analyze the texture of the aluminum and tungsten samples used in the experiments. The measurements performed on aluminum samples are explained in this section. These samples consisted mainly of large grains which made it difficult to obtain the desired statistic for the measurements. Therefore, for each analyzed sample, three measurements were performed on different areas of the sample. On the other hand, the tungsten case is explained in detail in Chapter 4. This chapter describes how these measurements were used to cut the samples and obtain different textured samples.

Fig. 2.15 shows the pole figures obtained for a textured aluminum sample. The first thing to notice when analyzing pole figures is the presence of intensity poles in the center of the figure. In this case, there is an intensity pole in the center of the  $\{200\}$  figure. This pole indicates a strong  $\{200\}\langle 200 \rangle$  texture component. The other intensity poles in this pole figure should coincide with the  $\langle 100 \rangle$  directions in the  $\{001\}$  stereographic projection. These directions are marked with a red cross in the  $\{200\}$  pole figure, as shown in Fig. 2.15. It may be observed that the intensity poles coincide with the  $\langle 100 \rangle$  directions from the  $\{001\}$  stereographic projection. This supports the assumption that this sample presents a strong  $\{200\}\langle 200 \rangle$  texture component

In addition, the intensity poles found in the  $\{111\}$  and  $\{220\}$  pole figures should coincide with their respective directions in the  $\{001\}$  stereographic projection, which are marked with a red cross in Fig. 2.15. In other words, the intensity poles in the  $\{111\}$  pole figure should coincide with the  $\langle 111 \rangle$  directions seen in the  $\{001\}$  stereographic projection. Similarly, the intensity poles in the  $\{220\}$  pole figure should coincide with the  $\langle 110 \rangle$  directions seen in the  $\{001\}$  stereographic projection. Since these poles correspond to their respective directions in the  $\{001\}$  stereographic projection it can be determined that the observed textures correspond to recrystallized samples with a so called cube texture component  $\{200\}\langle 200 \rangle$ .

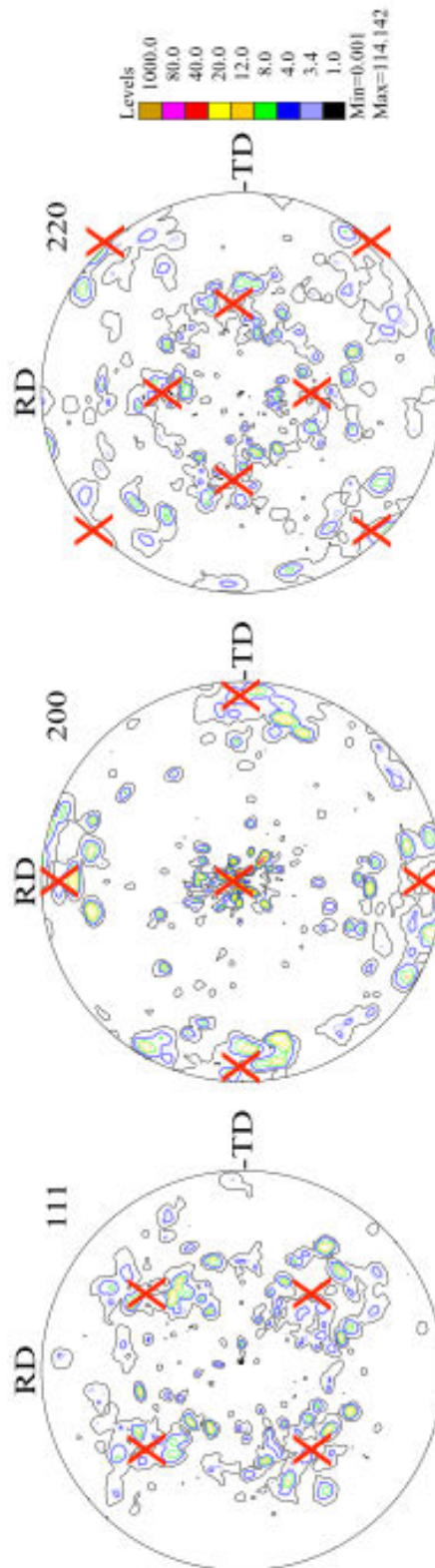


Fig. 2.15 Pole figures measured for an aluminum sample with a cube texture component {200} <200>

Fig. 2.17 shows the pole figures obtained for another aluminum sample. In this case, none of the figures have an intensity pole in their center. Therefore, in this case the sample does not present a defined texture.

However, there are some intensity poles in Fig. 2.17 that coincide with their respective directions in the  $\{001\}$  stereographic projection. More specifically, some of the intensity poles in the  $\{220\}$  pole figure coincide with the  $\langle 110 \rangle$  directions seen in the  $\{001\}$  stereographic projection. Similarly for the  $\{001\}$  and  $\{111\}$  pole figures. These directions are marked with red crosses in Fig. ???. Since some intensity poles coincide with their respective directions in the stereographic projection, it may be concluded that there is a cube texture component but with a low intensity.

One can see that there are other  $\{hkl\}\langle hkl \rangle$  components present in the sample. These components could be determined but this does not provide significant results for our work.

The experimental device used to perform the different XRD measurements is shown in Fig. 2.16.



*Fig. 2.16 Experimental device used to perform XRD measurements*

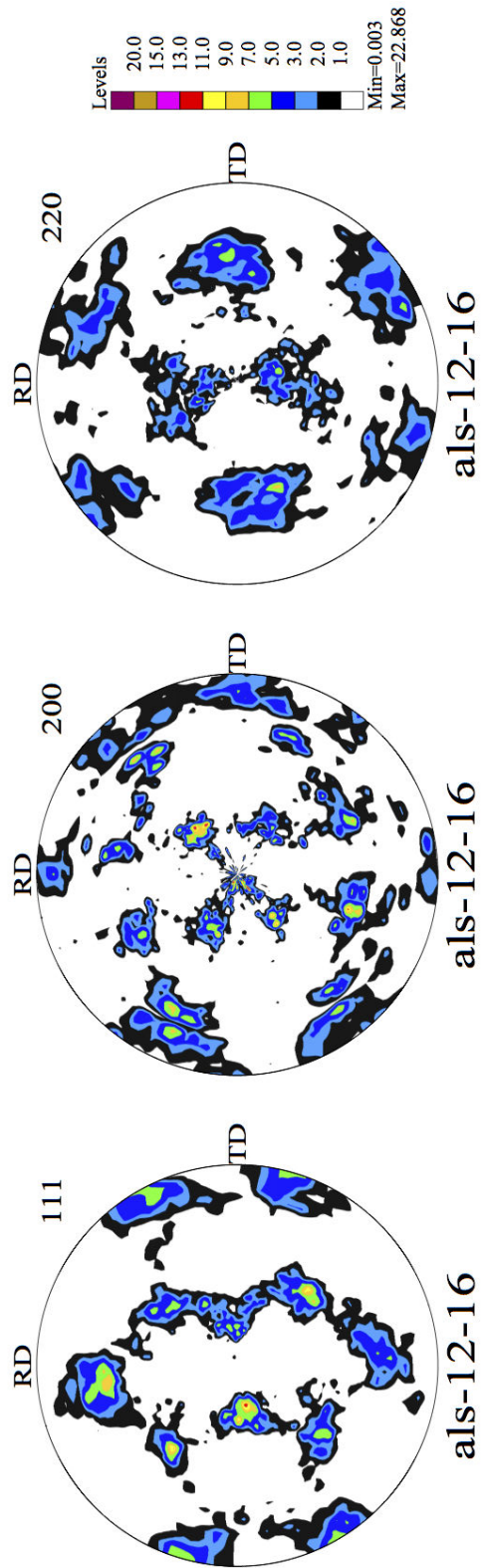


Fig. 2.17 Pole figure of a non-textured aluminum sample

## 2.3 Sample preparation and characterization

In order to perform a thorough analysis of the microstructural modifications in a material surface, it is important to work with a well-defined low-roughness base material. To do this, the materials used had a 99.98 w.t % purity and were subject to the same polishing procedure and EBSD, SEM, and X-Ray measurements in order to characterize the samples.

### 2.3.1 Polishing procedure

A general polishing procedure consists of two main steps:

- A first step consists of a mechanical polishing with an abrasive fine-grained silicon carbide (SiC) grinding paper. This step is usually performed using water as a lubricant; however, for samples with a tendency to oxidize, it can be performed using ethanol. The grinding steps may be followed by polishing with diamond suspensions of various sizes (3  $\mu\text{m}$ , 1  $\mu\text{m}$ , etc) depending on the hardness and characteristics of each sample. Mechanical polishing is performed with the aim of obtaining a flat surface with a low roughness.
- The second step consists of a chemo-mechanical process performed using an active oxide polishing suspension (OPS) which uses Coloidal Silicia ( $\text{SiO}_2$ ) as an abrasive. The OPS is composed of fine silica particles ( $\sim 30 \text{ nm}$ ) in a alkaline solution. The polishing step with OPS is performed with a sheet of type OP-CHEM.
- The chemo-mechanical step may be replaced by an electrochemical or electropolishing procedure performed by immersing the sample in a temperature-controlled bath of electrolyte and passing a current through the sample. As a result, the metal surface is oxidized and dissolved in the electrolyte. It is performed with the objective of obtaining polished samples with a low roughness. This step was not performed for the aluminum or tungsten samples in this work due to the fact that favorable results were obtained using the chemo-mechanical procedure. Additionally, analysis performed with tungsten samples show that reliable and effective results are obtained by following the mechanical and chemo-mechanical steps (Manhard et al., 2013). Similarly, the polishing procedure recommended for pure aluminum samples consists in following a mechanical polishing procedure followed by a chemo-mechanical one (Struers, 2016).

The combination of abrasion and chemical attack allows obtaining a flat, mirror-like surface free of scratches and deformations. In some cases in the course of the polishing procedure, i.e., after grinding, after polishing with diamond paste, the samples were analyzed with an optical microscope in order to check the quality of the sample. According to measurements made with AFM and Confocal microscopy, the surface roughness of the samples

after polishing is approximately 10 nm.

The procedure used to polish aluminum sample with a diameter of 5 mm is shown in Table 2.1. Aluminum is a relatively soft material that quickly oxidizes, even under high vacuum conditions. This oxide layer is both adherent and impermeable. Once formed it protects the material from further oxidation (Palik, 1998b). Consequently, caution must be taken during polishing. The final polishing steps should be done with ethanol instead of water. Additionally, the samples were kept in sealed jars with ultra-pure ethanol in order to avoid oxide formation on the surface.

Steps	Duration (min)
<i>P1000</i>	1
<i>P1200</i>	5
<i>P2400</i>	15
<i>P4000</i>	20
Diamond paste of $\frac{1}{4}\mu\text{m}$	5
OPS	10

*Table 2.1 Polishing procedure for Aluminum*

Fig. 2.18 a) and b) shows the polished surface and cross-section of an aluminum sample prior to plasma exposure. The cross-section was obtained by cutting the sample using a diamond wire saw and polishing the obtained surface. Fig. 2.18 shows that the surface as well as the cross-section are almost free of defects such as voids or cracks. There are however a few small cavities or voids of a few nanometers on both the surface and the cross-section. The cross-section also presents some thin cracks whose width and height are, respectively, 10  $\mu\text{m}$  and 500 nm. The small voids and cracks may be due to the cutting and polishing process or may occur during material processing. Note that similar defects, whose size do not surpass the above mentioned dimensions, were seen in other analyzed virgin samples.

Tungsten is a very hard material and hence its polishing procedure differs from that of aluminum. Longer time is devoted to each step and more steps should be included in the procedure. This should start by a rough grinding paper, such as *P800* and, after mechanically polishing several smaller size grinding papers, different diamond pastes are used to ensure the sample achieves a mirror-like finish with the OPS. Table 2.2 shows the polishing procedure used for rectangular tungsten samples with a dimensions of 1.5  $\times$  0.5 cm.

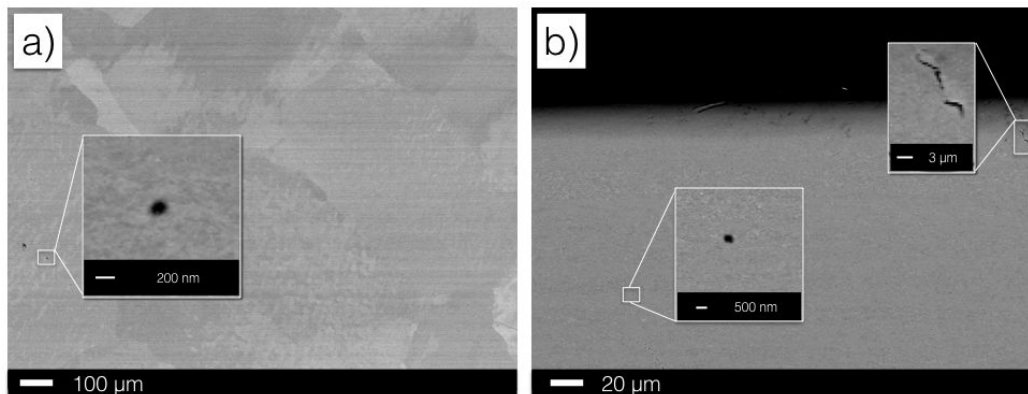


Fig. 2.18 SEM micrograph of a polished Al a) surface and b) cross section

Steps	Duration (min)
P800	5
P1000	10
P1200	15
P2400	40
P4000	50
Diamond paste of $3\mu\text{m}$	5
Diamond paste of $1\mu\text{m}$	5
Diamond paste of $\frac{1}{4}\mu\text{m}$	5
OPS	10

Table 2.2 Polishing procedure for Tungsten

### 2.3.2 Heat treatment

After surface polishing and cleaning in ultrasonic baths with ethanol and acetone, the specimens were subject to a heat treatment. This treatment, known as annealing, consists in heating a sample to a desired temperature, maintaining it for a specific period of time and then cooling the sample down to room temperature. Annealing is performed in order to selectively obtain samples with well-defined grains and defect structures, to reduce the number of dislocations and to relief stress. Depending on the annealing temperature, different processes may occur: recovery, recrystallization and grain growth. During recovery there is an enhanced atomic diffusion in the crystal lattice and the number of dislocation decreases. Recrystallization occurs when a new set of strain-free and equiaxed grains (*i.e.* having equal dimensions in all directions) is formed in the material. These grains have low dislocation densities. For metals, the recrystallization temperature is usually  $0.4T_m$  where  $T_m$  is the melting temperature (Calister and Rethwisch, 2010).

The recommended recrystallization temperature for aluminum is 350 K (Calister and Rethwisch, 2010). However, the sample temperature during plasma exposure at our specific

conditions is of 620 K. In order to ensure the stability of the material microstructure during the plasma discharge, the sample is annealed at a higher temperature. Therefore, annealing for aluminum was performed under vacuum conditions ( $10^{-4}$  Pa) at 673 K during 2 hours. Fig. 2.19 a) and b) show, respectively, an Al sample before and after annealing. It is clearly seen that after annealing grains are larger in size and dislocations are greatly reduced. Prior to annealing, this sample was completely deformed and had no defined grains.

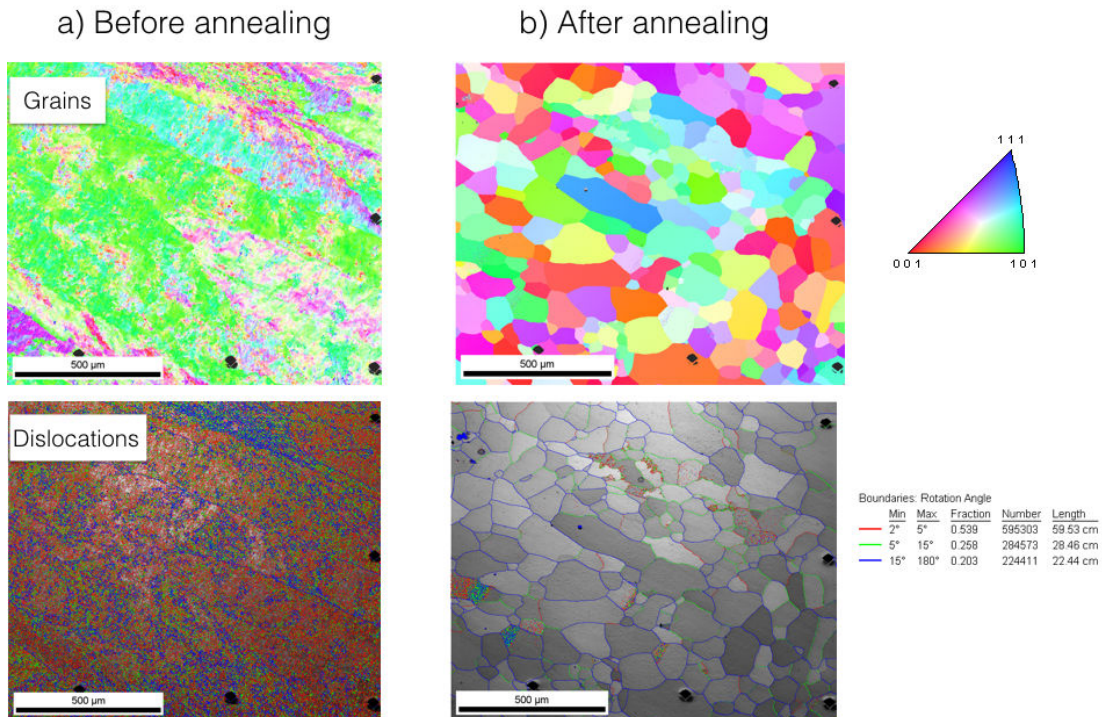


Fig. 2.19 EBSD measurements of an aluminum sample a) before and b) after annealing

Tungsten, on the other hand, has to be annealed at much higher temperatures. The recommended recrystallization temperature is 1500 K. Analysis performed by Manhard (Manhard, 2011) determined that at this temperature there is a partial recrystallization of the material whereas the full recrystallization is obtained at temperatures of 1700 K. However, the maximum achievable temperature in our vacuum furnace is 1373 K. Therefore, tungsten samples were annealed at 1373 K for 1 hour at a vacuum of  $10^{-4}$  Pa. Fig. 2.20 a) and b) show, respectively, a W sample before and after annealing. It is seen that prior to annealing, grains were not visible whereas after annealing grains are clearly discernible, some with sizes larger than  $10\ \mu\text{m}$  and some smaller ones with sizes of approximately  $1\ \mu\text{m}$ .

EBSD measurements were performed after annealing to verify that the samples have a small percentage of dislocations. It can be seen in Fig. 2.21 that the density of dislocations in the sample is small. In fact, it corresponds to approximately 8% of the whole surface.

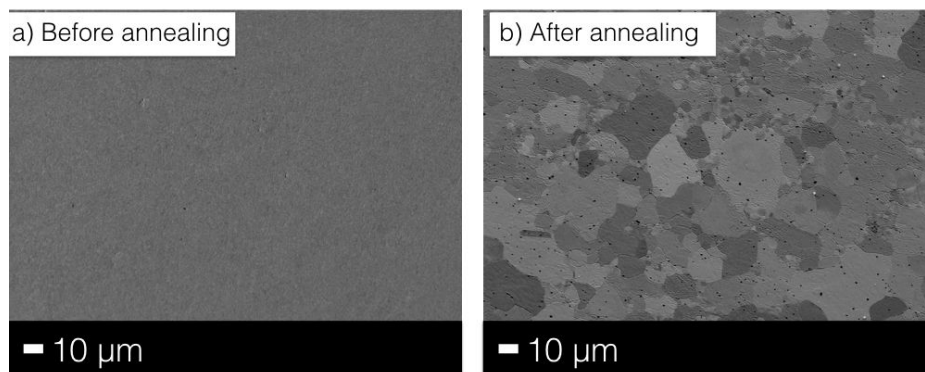


Fig. 2.20 SEM micrographs of a tungsten sample a) before and b) after annealing

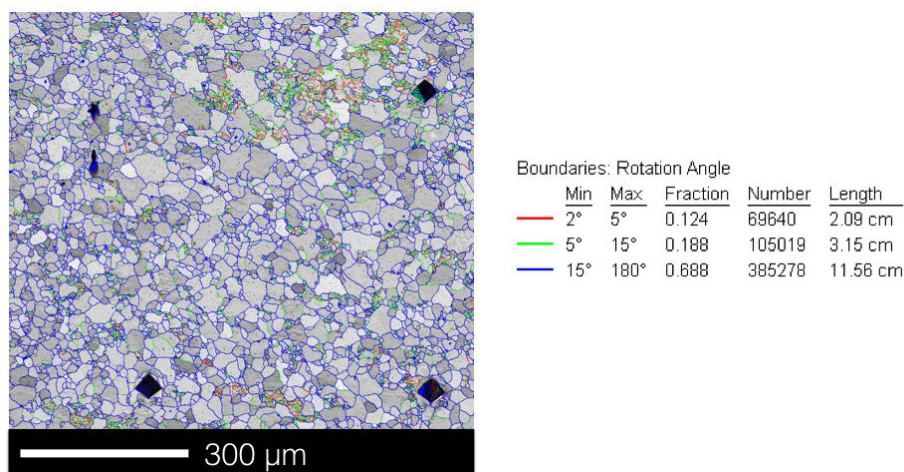


Fig. 2.21 Dislocations on a W sample after annealing

## 2.4 Plasma Characterization

In order to perform the different plasma exposure experiments with aluminum and tungsten samples, it is necessary to characterize the plasma. Plasma characterization allows the measurement of different parameters such as ion and electron density and plasma potential. In turn, these parameters allow the calculations of the incident ion energy, plasma flux and plasma fluence needed to characterize the experiments.

The different parameters were measured by using a Langmuir probe in different plasma discharges in the CASIMIR reactor. The probe was placed in one of the apertures instead of a plasma source and the different parameters were measured along the trajectory of the probe (see Fig 2.22). The measurements were made every 5 mm, starting from the plasma center (0 cm position) and reaching the magnet (12 cm position).

This section gives a brief overview of the different parameters measured in order to characterize the plasma.

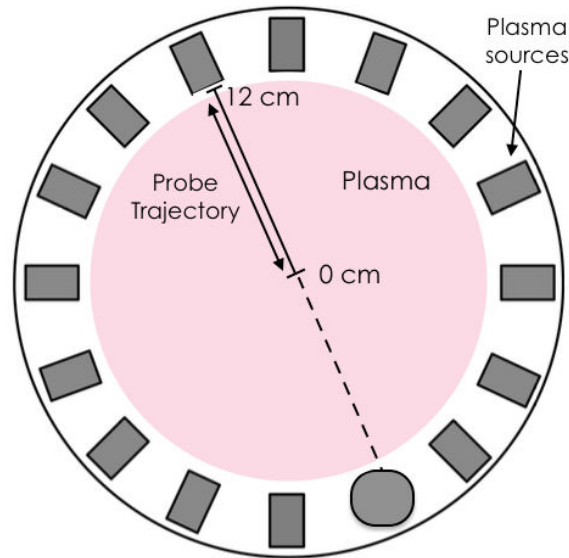


Fig. 2.22 Schematic of the trajectory followed by the Langmuir probe in the CASIMIR reactor

### 2.4.1 Plasma potential

The plasma potential profiles  $V_p$  for different injected microwave powers are shown in Fig. 2.23 b). It can be seen that for a given microwave power, the plasma potential is almost constant over the reactor. Due to the symmetry of the reactor, it can be assumed that the plasma potential is homogeneous in the whole plasma volume. Finally, it is seen that the plasma potential increases for increasing microwave power. The plasma potential corresponding to the experimental conditions (2 kW of microwave injected power) used during this work is 20 V.

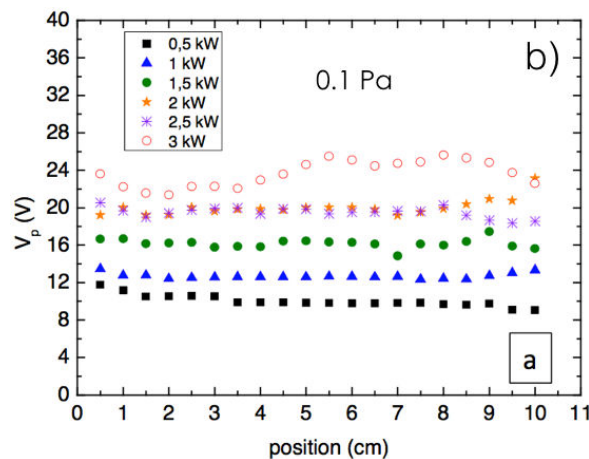


Fig. 2.23 Radial profiles of the plasma potential in CASIMIR for different microwave powers and a pressure of 0.1 Pa for hydrogen plasmas in the CASIMIR reactor (Delacqua, 2012)

## 2.4.2 Electron temperature and density in a hydrogen plasma

The electron temperature and density were measured using the Langmuir probe and their radial profiles are shown in Fig. 2.24 a) and b) respectively. Both the electron temperature and density increase for increasing microwave powers. The electron temperature for the plasma conditions used during this work (2 kW of microwave injected power) is 2 eV and the electronic, and hence ion, density is  $1 \times 10^{11} \text{ cm}^{-3}$ .

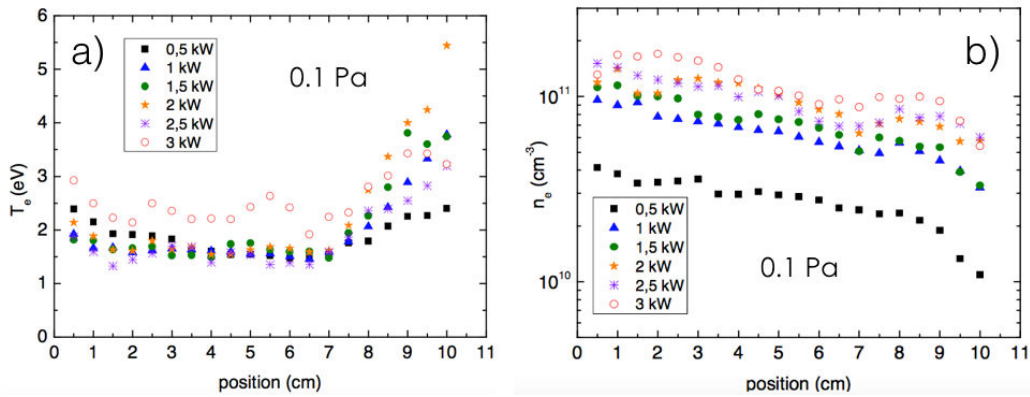


Fig. 2.24 Electron a) temperature and b) density in CASIMIR for different microwave powers and a pressure of 0.1 Pa (Delacqua, 2012)

Both the electron temperature and density show a different behavior as the Langmuir probe approaches the plasma sources. In order to perform the measurements, the Langmuir probe has to be placed perpendicular to the magnetic field. Since the plasma sources are magnetized, the Langmuir probe measurements in their vicinity are not performed perpendicular to the magnetic field. As a result, closer to the walls there is a non-monotonous deviation in the measurements.

## 2.5 Flux and fluence in a hydrogen plasma

The experimental conditions used during this work are: an injected microwave power of 2 kW and a pressure 0.1 Pa. The electron temperature in these conditions is of 2 eV and the ion velocity can be calculated by using this value in equation 1.4 ( $v_B = \sqrt{kT_e/m_i}$ ).

In order to determine the plasma flux, the ion density in the sheath region  $n_s$  has to be calculated. The relationship of this value with the ion density at the plasma center  $n_0$  is complicated due to the ambipolar diffusion of ions and electrons. This depends on several parameters such as: the plasma length and radius, and the system pressure. Our conditions

correspond to a low pressure and low aspect ratio system, that is, the plasma radius is larger than the plasma length. In this case,  $n_s$  and  $n_0$  are related by (Lieberman and Lichtenberg, 2005):

$$\frac{n_s}{n_0} = 0.5 \quad (2.2)$$

For our plasma conditions, the ion density at the plasma center is  $1 \times 10^{11} \text{ cm}^{-3}$ . Hence the ion density in the sheath edge is  $5 \times 10^{10} \text{ cm}^{-3}$ .

The flux is calculated by using equation 1.7 ( $\Gamma_i = n_s v_B$ ), that is, by multiplying the ion Bohm velocity by the ion density at the sheath edge. Using this equation the plasma flux used throughout the experiments is calculated and has a value of  $1.6 \times 10^{20} \text{ ions/m}^2\text{s}$ .

The fluence is calculated by multiplying the flux by the exposure time, that is:

$$Fluence = \Gamma_i \times t \quad (2.3)$$

Since the analyzed sheath regions during the experiments are non-collisional, the ion energies  $E$  were determined by taking into account the applied voltage to the sample, as follows:

$$E = -e(V - V_p) \quad (2.4)$$

where  $V$  is the applied voltage and  $V_p$  is the plasma potential.

The plasma parameters calculated in this section allow us performing experiments under strictly controlled conditions. In fact, these parameters will be used as variables during the experiments.

The next section gives a brief overview of aluminum dust collection experiments performed at LSPM in the field of PWI. These experiments consisted mostly in studying dust dynamics in plasma environments.

## 2.6 Optical spectroscopy and dust collection of aluminum dust containing plasmas

Different measurements were performed in CASIMIR and the monosource reactor in order to verify the presence of aluminum dust during the plasma discharges. In other words, in order to verify that under our plasma conditions it is possible to generate aluminum dust and further analyze their formation mechanisms, density and morphology.

Optical spectroscopy measurements were performed and two atomic aluminum lines were identified: 394.4 and 396.21 nm. Fig. 2.25 shows both of these lines for hydrogen and argon plasma at two different applied voltages. It is seen that for an applied voltage of  $-100$  V, in the case of hydrogen plasma, these two lines can be easily identified whereas for argon plasmas they are imperceptible. Both of these lines increase with the applied voltage in both hydrogen and argon plasmas.

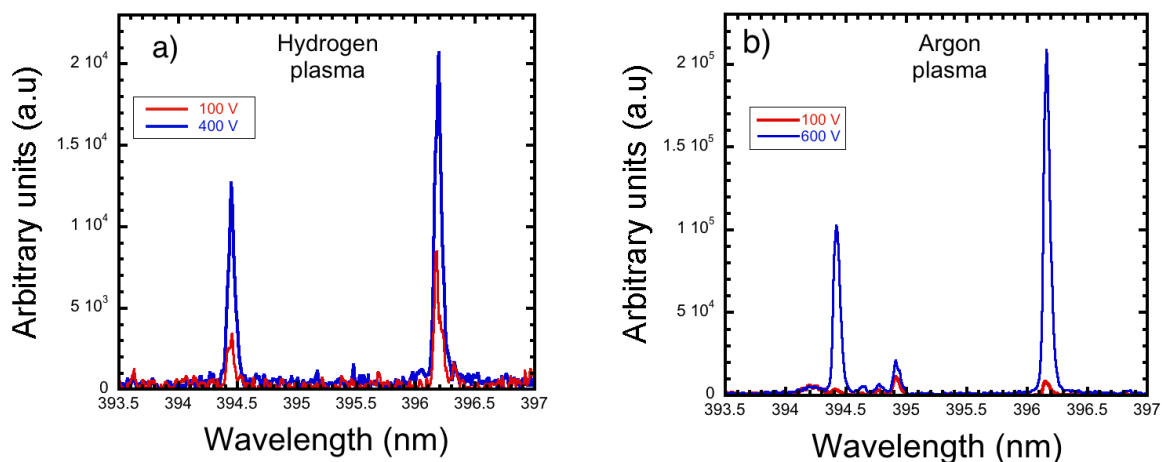


Fig. 2.25 The optical spectroscopy aluminum lines located at 394 and 396 nm in a) hydrogen and b) argon plasma

Fig. 2.26 shows the optical emission spectroscopy intensity of the 394 and 396 nm lines as a function of applied voltage in hydrogen and argon plasma. It is seen that as the voltage increases, the intensities of the line increase, specially in the case of Ar plasma. This result is expected given that the sputtering yield in Al is higher for Ar ions than H ions. For increasing Ar ions energies, more atoms will be sputtered from the aluminum sample and hence the intensity of its line tends to increase.

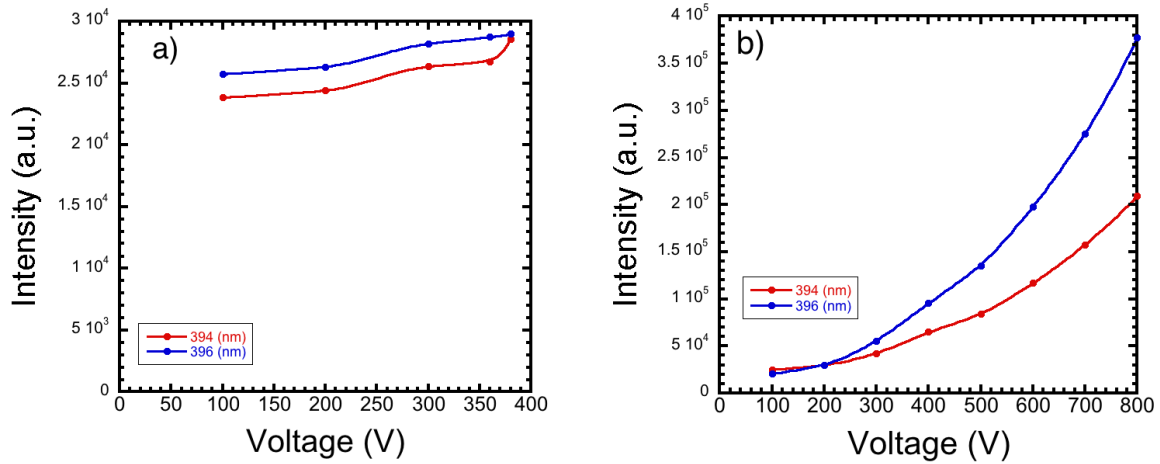


Fig. 2.26 Evolution of the 394 and 396 nm line intensities for increasing applied voltages in a) hydrogen and b) argon plasma

For the above mentioned applied voltages, the current per sample area was calculated for a sample of  $0.35 \text{ m}^2$ . Fig. 2.27 shows the intensity of the 394 and 396 nm lines with respect to the current per sample area for hydrogen and argon plasma. It is seen that for hydrogen plasmas the line intensities remain almost constant whereas for argon plasmas the line intensities increase for increasing current.

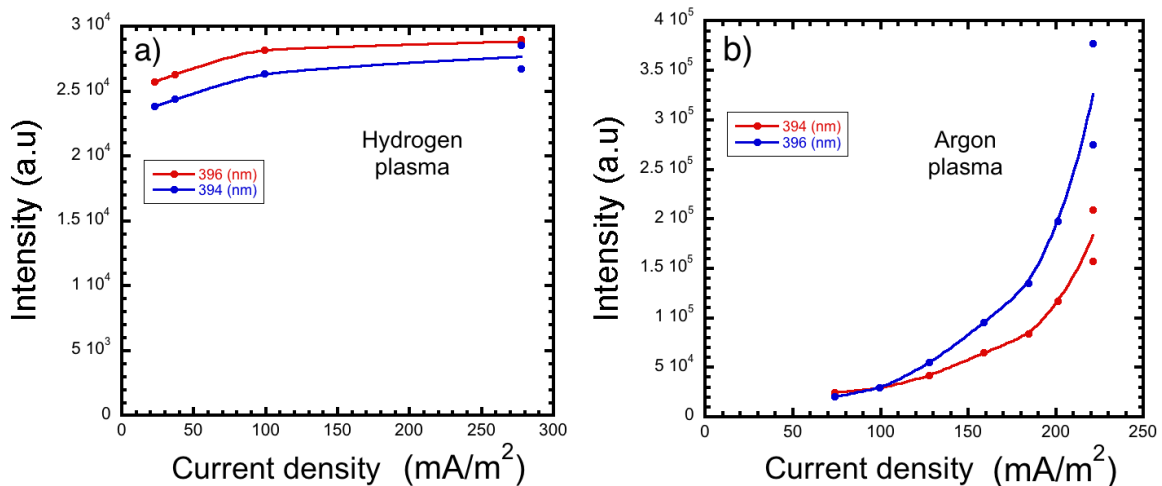


Fig. 2.27 Evolution of the 394 and 396 nm line intensities with respect to the current density in a) hydrogen and b) argon plasma

It may be observed in Fig. 2.26 b) and in Fig. 2.27 b) that the aluminum line intensity in argon plasmas increases with increasing voltage and current density. These two parameters are related with the ion energy, therefore, as the voltage and current density increase so does the incident ion energy. This phenomenon represents the typical behavior of physical

sputtering systems. Since the sputtering yield is proportional to the energy deposited in the elastic collisions within a near surface layer, it increases for increasing incident ion energies. On the other hand, Fig. 2.26 a) and in Fig. 2.27 a) show that in hydrogen plasmas, the aluminum line intensity remains constant with increasing voltage and current density. However, as observed in Fig. 2.25, the two atomic aluminum lines are detected even at low incident ion energies. This may be due to the chemical sputtering of aluminum submitted to hydrogen plasmas.

Finally, Fig. 2.28 shows the evolution of the current density with respect to voltage in hydrogen and argon plasmas. It may be observed that the current density increases with voltage in both hydrogen and argon plasmas. It is worthy to mention that in the mono-source reactor, the highest achievable current density is approximately  $300 \text{ mA/m}^2$ . At higher current density values the plasma becomes unstable. Therefore, the analysis were performed for up to  $-400 \text{ V}$  for hydrogen plasmas and  $-800 \text{ V}$  for argon plasmas.

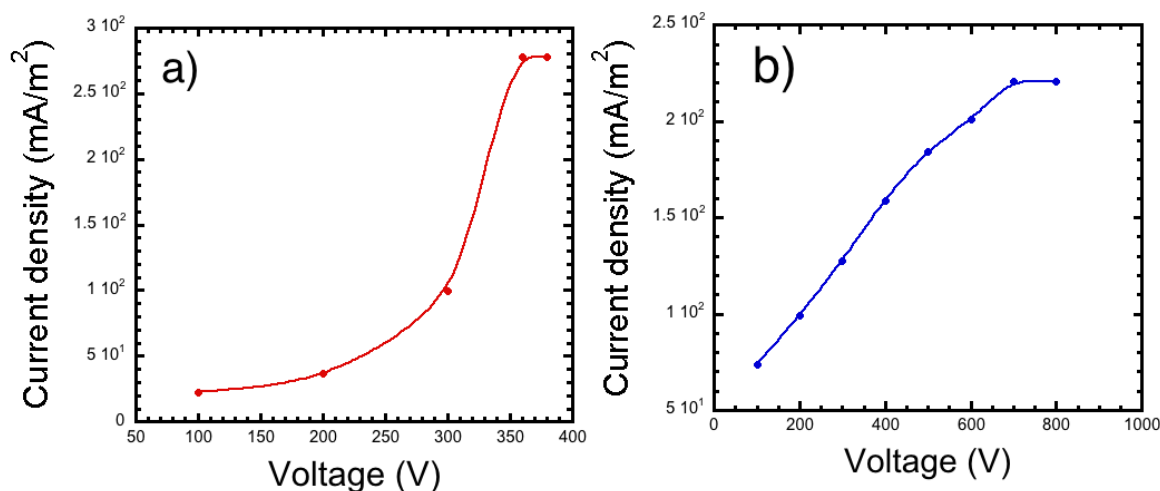


Fig. 2.28 Evolution of the current density with respect to voltage in a) hydrogen and b) argon plasma

## 2.7 Aluminum dust formation

Given that the presence of aluminum was confirmed by optical spectroscopy measurements, experiments were performed under different conditions in order to verify if it is possible to form and collect aluminum dust particles for our plasma conditions. Dust particles were collected in the lower wall of the reactor at either low (1 Pa) or high pressure (50 Pa) and using hydrogen or argon plasma and high pulsed voltage. The latter was optimized to obtain the highest possible dust density by varying the pulse time  $t_p$  and pulse frequency  $F$ .

In both hydrogen and argon plasma, spectroscopic measurements were performed in order to confirm the presence of dust in either the plasma or the collected dust samples. During the plasma discharges, the two aluminum lines of 394.4 nm and 396.21 nm were observed, as shown in Fig. 2.29 a). These lines were seen for all the conditions in which aluminum dust particles were collected in hydrogen and argon plasma. Additionally, after the dust was collected it was verified by Energy dispersive X-ray spectroscopy to corroborate the presence of aluminum. Fig. 2.29 b) shows the usual spectra obtained for the analyzed samples. The presence of three elements was identified: aluminum, oxygen and silicon. The former is present due to the rapid oxidation of aluminum dust particles whereas the latter is present given that the dust particles were collected on Si samples.

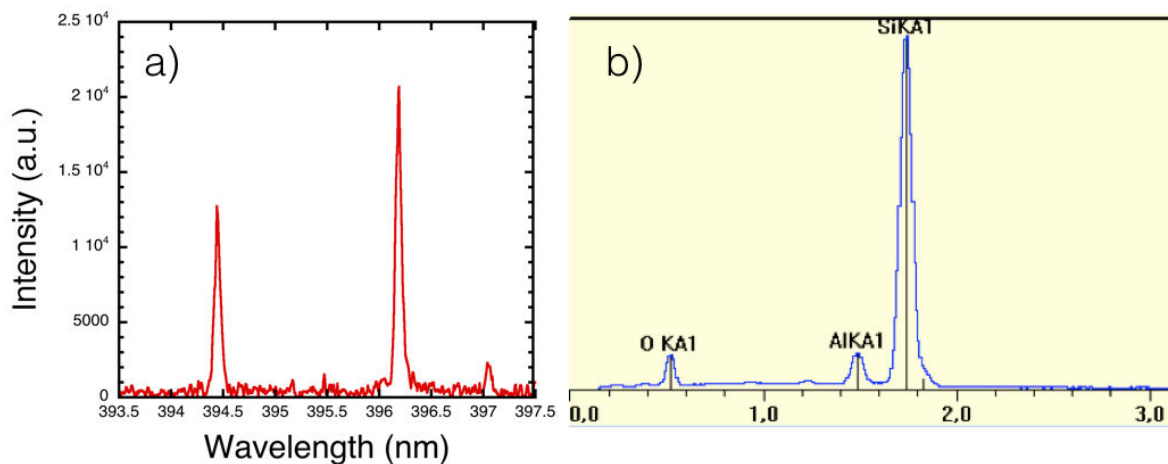


Fig. 2.29 a) Optical emission spectroscopy measurements for Al and b) Energy dispersive X-ray spectroscopy measurements for Al dust particles

### 2.7.1 Aluminum dust formation using argon plasma

Fig. 2.30 shows the dust particles collected using argon plasma under different conditions. The different parameters for voltage  $V$ , pulse time  $t_p$  and frequency of pulses  $F$  are also shown in the image. In both cases micro and nanometric dust particles are seen, however their density is not significant. In the high pressure case, dust particles are mostly spherical whereas for the low pressure case they appear to have a toroidal shape.

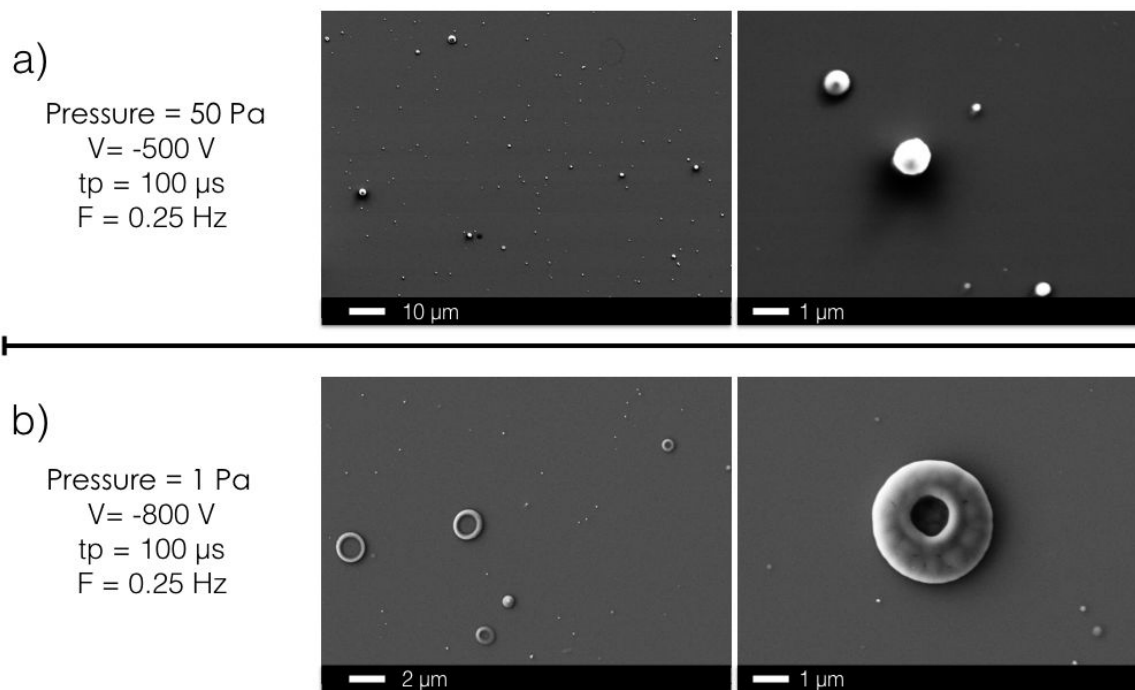


Fig. 2.30 Dust collected using argon plasma at a pressure of a) 50 Pa and b) 1 Pa

Further analysis showed that the toroidal shape is in fact an spheroidal shape, as shown in Fig 2.31. This spheroidal shape may be due to the electrical arcs present during the discharge that alters the dust growth mechanisms. Spheroidal dust particles were found in the ASDEX upgrade tokamak. The particles were made up of either boron or tungsten or a mixture of both elements. It is believed that the W spheroids are droplets produced during arcing (Balden et al., 2014).

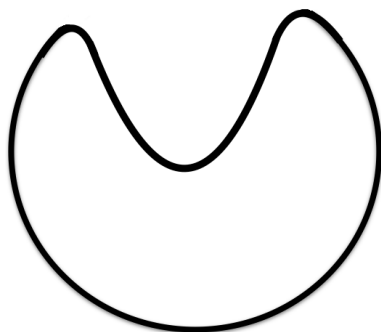


Fig. 2.31 Sketch of an spheroidal dust particle collected in argon plasma

### 2.7.2 Aluminum dust formation using hydrogen plasma

Fig. 2.32 shows the dust particles collected using hydrogen plasma under different conditions along with the different parameters used to control the pulsed high voltage. Both cases show a low dust density with a spherical shape and sizes of a few nanometers and a few micrometers.

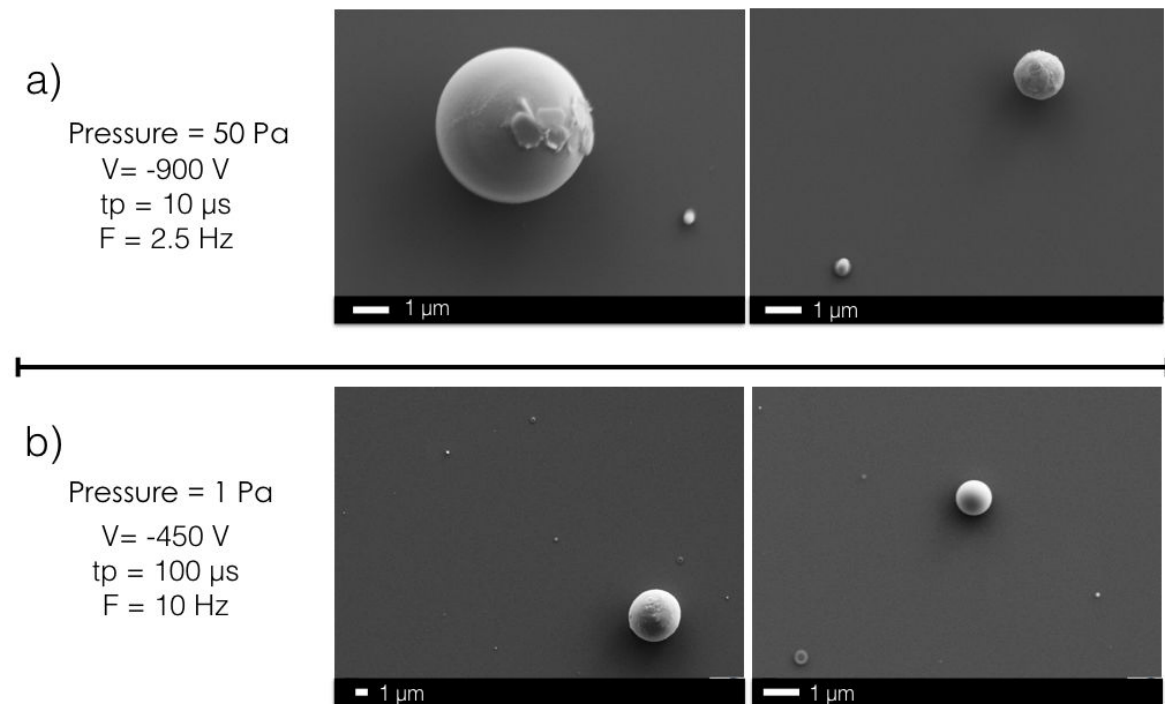


Fig. 2.32 Dust collected using hydrogen plasma at a pressure of a) 50 Pa and b) 1 Pa

This chapter focused in describing the experimental and characterization tools used in the experiments. It also presented the basic procedures used to obtain fully characterized samples. This process is very important in the experiments, because it allows to control the initial state of the sample prior to the experiments. The last part of the chapter was devoted to plasma characterization and spectroscopic analysis. It described the measurements performed to obtain the plasma potential and electron temperature and density. These parameters allowed calculating the ion flux and fluence for our experimental conditions. Finally, this section gave an overview of the spectroscopic measurements and the main results obtained by collecting aluminum dust particles in our experimental conditions. However, the collected density of aluminum dust particles was not enough to perform significant analysis regarding dust formation dynamics. As a result, this thesis work mainly focuses on the material modifications caused by plasma wall interaction processes. The next two chapters

show the results obtained by exposing aluminum and tungsten to hydrogen plasma under different conditions.

## Chapter 3

# Plasma surface interaction between hydrogen plasma and an aluminum target

The main objective of this chapter is to determine how surface morphology and bulk structure in aluminum are affected when a sample is exposed to non-equilibrium hydrogen plasmas. More specifically, experiments are performed in order to understand the different mechanisms involved in bubble and blister formation. A more in depth study on this subject allows understanding blister growth dynamics in materials with a low hydrogen solubility.

Aluminum is not of direct interest for fusion applications. However, the study of bubble growth dynamics (specifically through loop punching and plastic deformation) for cubic materials, such as aluminum, should help in setting up the methodology for studying similar effects in more complex hexagonal systems. An example of a relevant material with an hexagonal system is beryllium, which has a real interest for fusion applications.

For this purpose, several questions arise regarding bubble and blister formation among which we address the following:

- What is the effect of the material microstructure on blister growth?
- What is the link between the crystallographic structure and surface modifications, such as bubble formation, under hydrogen charging?
- How do the discharge conditions affect blister formation in aluminum?

In order to answer these questions various experiments were performed. These experiments consisted in analyzing the surface modifications in an aluminum surface after being submitted to hydrogen plasmas with variable parameters, such as incident ion energy, fluence, microstructure and crystallographic orientation when exposing aluminum to hydrogen

plasma. The results obtained along with the conclusions are discussed in this chapter, which is organized as follows:

- Section 3.1 gives a brief introduction on the nature of the surface modifications occurring on aluminum when exposed to hydrogen plasma.
- Section 3.2 describes how bubble and blister growth is affected by incident ion energy.
- Section 3.3 analyzes how blister and bubble formation are affected by the plasma fluence. This was studied by using two different experimental procedures: continuous and cyclic plasma exposure. The former was performed by exposing several samples continuously to the desired fluence whereas the latter was implemented by performing several cycles of plasma exposure followed by *ex-situ* SEM and optical microscope analysis until the desired fluence was reached.
- Section 3.4 describes the effect the polishing procedure, *i.e.* surface finish, has on blister formation.
- Section 3.5 illustrates the effect grain boundary misorientation have on blister formation. In order to do this, the behavior of textured and non-textured samples after hydrogen plasma exposure was studied.
- Section 3.6 focuses on analyzing aluminum single crystals with the aim of studying blister growth and morphology without the effect of grain boundaries.
- Section 3.7 summarizes the different results and gives the main conclusions that may be drawn from this chapter.

## 3.1 Introduction

Hydrogen exposure of aluminum samples leads to different surface modifications on its surface and bulk. Fig. 3.1 a) and b) show, respectively, the surface and the cross-section of an Al sample after being exposed to hydrogen plasma at a fluence of  $1.3 \times 10^{24}$  ions/m<sup>2</sup>. It can be observed in Fig. 3.1 a) that there is a high density of blisters on the Al surface, with sizes in the range 2-30  $\mu\text{m}$ . These blisters are located either at the grain boundaries, *i.e.* *intergrain blisters* or within the grains, *i.e.* *intragrain blisters*. The surface shows a slight swelling in many regions of the sample. Fig. 3.1 b) shows large irregular cavities and circular bubbles in the bulk of the sample. For the analyzed conditions bubbles are formed at a maximum depth of 80  $\mu\text{m}$  whereas irregular cavities were mostly located at the grain boundaries and at depths of up to 90  $\mu\text{m}$ .

It is worthy to mention that the difference between bubbles, blisters, cracks, cavities and voids is not always clear in literature. During this work the term bubbles refers to quasi-spherical shaped cavities in the bulk of the material whereas blisters consist of dome-

shaped deformations of the material surface with mostly circular, but sometimes, irregular circumference (see Fig. 3.1 a)). Underneath blisters one may find a spherical shaped bubble, a lenticular cavity or a crack (see Fig. 3.1 b)).

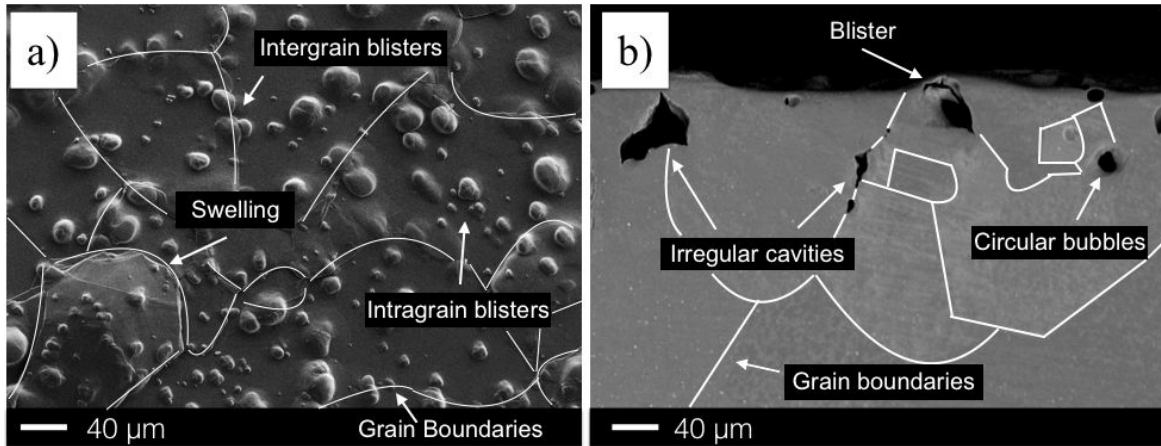


Fig. 3.1 a) Blisters, b) bubbles and cavities in an aluminum sample after hydrogen plasma exposure with flux of  $1.6 \times 10^{20}$  ions/m<sup>2</sup>s, fluence of  $4.7 \times 10^{24}$  ions/m<sup>2</sup> and incident ion energy of 320 eV

Blister depth is measured from the surface to the center of the cavity. Therefore, the depth of a blister formed due to a spherical bubble located just underneath the surface would be of the same order of magnitude as the blister cap.

During this work, the smallest blister detected using Image J software (NIH, 2017) has a radius of approximately 100 nm. It is important to emphasize that this value is far above the radius of vacancy clusters, which should be of a few nm. Therefore the term blister appearance should not be confused with blister nucleation.

Before discussing the detailed results obtained by exposing different aluminum samples to various discharge conditions, we would like to describe the major observed changes observed when an aluminum sample is exposed to hydrogen plasma.

### 3.1.1 Major observed surface modifications

Fig. 3.2 shows an example of intergrain blisters in an aluminum sample after plasma exposure. Impurity atoms, such as hydrogen, tend to segregate along the grain boundaries. In other words, hydrogen concentration tends to be greater in the grain boundaries than in the matrix. Since atoms in the grain boundaries are not bonded to the maximum number of nearest neighboring atoms, the material is mechanically more ductile in this area. As a result blistering is easier to occur than in the matrix (Calister and Rethwisch, 2010; Ren et al., 2008). Intergrain blisters result from hydrogen trapping at the grain boundaries and hence

they are always located within two or more grains. They have circular or irregular shapes with a radius ranging from 100 nm to more than 15  $\mu\text{m}$ .

Another phenomenon that occurs to aluminum samples after plasma exposure is the swelling of the grains, as shown in Fig. 3.2. This swelling consists in the upward deformation of a large fraction or the whole grain. Since the samples have large grains of about 10-40  $\mu\text{m}$ , grain swelling covers a more important surface area than blisters. The height of swollen blisters, as measured using the confocal optical microscope, is between 0.5 and 10  $\mu\text{m}$ . Compared to other modifications, such as blistering, grain swelling presents a much larger area (*i.e.* the whole grain area) and a significantly lower height.

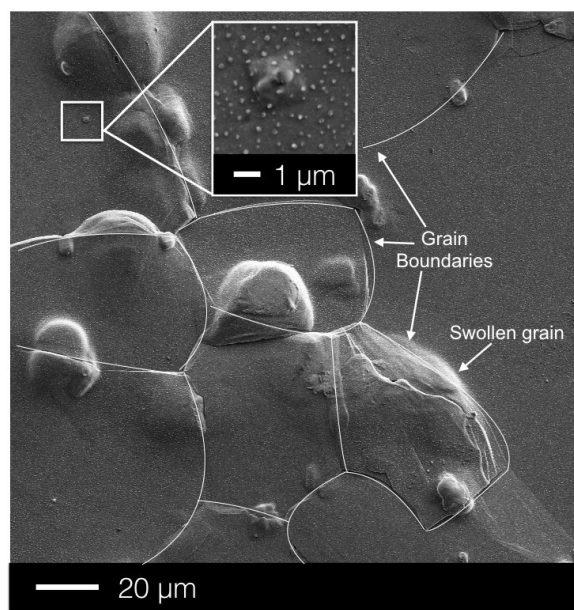


Fig. 3.2 Intergrain blisters and swollen grains on an aluminum sample exposed to  $\text{H}_2$  plasma with flux of  $1.6 \times 10^{20}$  ions/ $\text{m}^2\text{s}$ , fluence of  $1.7 \times 10^{24}$  ions/ $\text{m}^2\text{s}$  and incident ion energy of 320 eV

Fig. 3.3 shows an example of intragrain blisters in an aluminum sample after plasma exposure. Intragrain blisters grow solely within the grains and have mostly circular shapes. During hydrogen implantation, hydrogen is trapped in defects such as vacancies. Due to the presence of hydrogen, the vacancy-hydrogen complexes tend to organize in clusters. These clusters are further stabilized by the formation of molecular hydrogen in the hydrogen-vacancies cluster induced cavity. This process represents the initial nucleation mechanism for bubbles that may generate intragrain blisters (Condon and Schober, 1993; Ren et al., 2008).

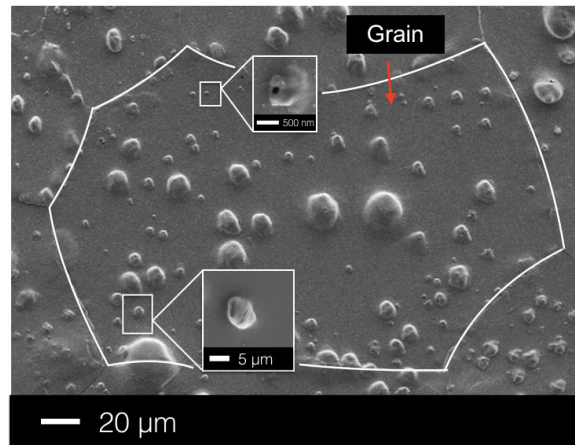


Fig. 3.3 Intragrain blisters on an aluminum sample exposed to  $H_2$  plasma with flux of  $1.6 \times 10^{20}$  ions/ $m^2s$ , fluence of  $2.2 \times 10^{24}$  ions/ $m^2s$  and incident ion energy of 320 eV

The situation may be more complex since a secondary blister nucleation may take place. This effect corresponds to either the formation of small blisters on the top of larger ones or the formation of large blisters underneath smaller ones (see Fig. 3.4). Secondary blistering may also take place through the formation of small blisters on swollen grains (see Fig. 3.4).

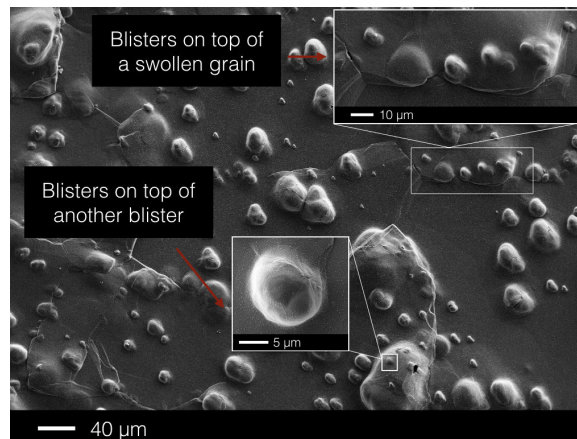


Fig. 3.4 Secondary blister growth on an aluminum sample exposed to  $H_2$  plasma with flux of  $1.6 \times 10^{20}$  ions/ $m^2s$ , fluence of  $2.2 \times 10^{24}$  ions/ $m^2s$  and incident ion energy of 320 eV

We also observe that large blisters may form by the coalescence of smaller ones (see Fig. 3.5). This image shows several examples of blisters close enough to each other and about to coalesce. This phenomenon leads to the increase in blister size and the decrease in blister density. Therefore coalescence represents another growth mechanism besides loop punching and vacancy clustering mechanisms that were previously discussed in Chapter 1 Section 1.6.2.

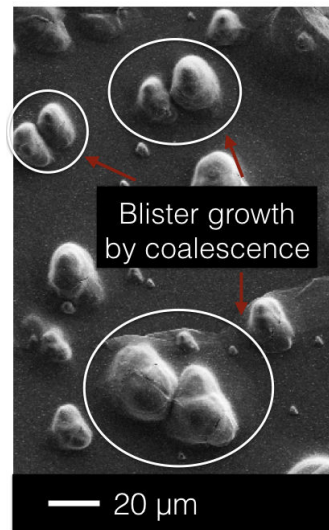


Fig. 3.5 Blister growth by coalescence on an aluminum sample exposed to  $H_2$  plasma with flux of  $1.6 \times 10^{20}$  ions/ $m^2s$ , fluence of  $2.2 \times 10^{24}$  ions/ $m^2s$  and incident ion energy of 320 eV

Besides blister formation and grain swelling, nanostructures of a few nm size form all over the surface after 30 min of hydrogen plasma exposure with the following plasma conditions: fluence of  $3.0 \times 10^{23}$  ions/ $m^2$ , incident ion energy of 320 eV, temperature of 618 K and a plasma flux of  $1.6 \times 10^{20}$  ions/ $m^2s$ . Fig. 3.6 shows an example of these nanostructures.

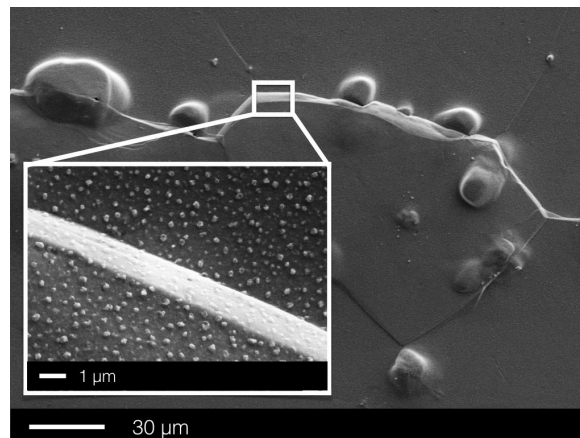


Fig. 3.6 Nanostructures on an Al sample exposed to  $H_2$  plasma with flux of  $1.6 \times 10^{20}$  ions/ $m^2s$ , fluence of  $3.0 \times 10^{24}$  ions/ $m^2$  and incident ion energy of 320 eV

After 3 h of plasma exposure (fluence of  $1.7 \times 10^{24}$  ions/m<sup>2</sup>), these nanostructures have a triangular shape with sharp edges and their density depends on the grain orientation, as shown in Fig. 3.7. Blister density is similar on  $\langle 100 \rangle$  and  $\langle 111 \rangle$  grains, with a value of 1.5 nanostructures/ $\mu\text{m}^2$ . On the other hand,  $\langle 110 \rangle$  grains have the lowest density, with a value of 0.7 nanostructures/ $\mu\text{m}^2$ . These nanostructures were seen all over the surface of the sample, including on the top of blisters. This indicates that their depth is less important than that of blisters.

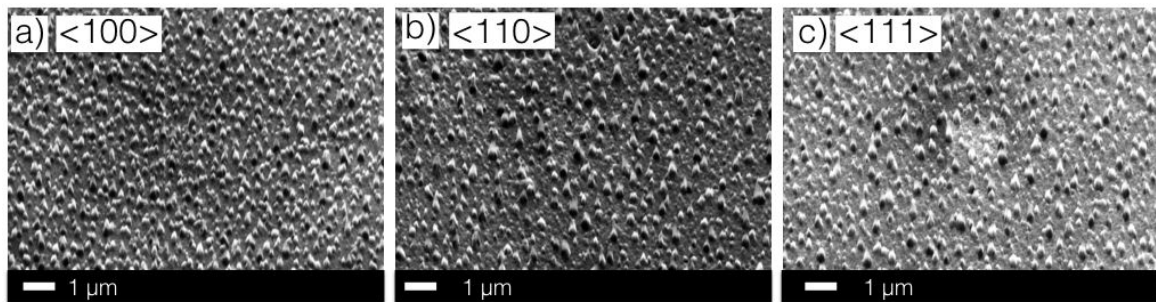


Fig. 3.7 SEM micrographs of nanostructures on grains whose surface normal is perpendicular to the a)  $\langle 100 \rangle$  b)  $\langle 110 \rangle$  and c)  $\langle 111 \rangle$  directions on an Al sample exposed to H<sub>2</sub> plasma with flux of  $1.6 \times 10^{20}$  ions/m<sup>2</sup>s, fluence of  $1.7 \times 10^{24}$  ions/m<sup>2</sup> and incident ion energy of 320 eV. Images taken with the samples tilted 70° degrees with respect to the electron beam.

The formation of nanostructures was already observed in tungsten exposed to high flux (*i.e.*  $10^{24}$  ions/m<sup>2</sup>s), deuterium plasma at different surface temperatures and an incident ion energy of 38 eV. Their formation mechanisms have not been documented yet. However, it is believed that these nanostructures form due to the fact that, at high fluxes, the kinetics of hydrogen loading at the near surface region surpasses the diffusion rate. As a result, hydrogen can accumulate and agglomerate into clusters. This allows the formation of high pressure bubbles. Due to the high pressures, aluminum atoms at the bubble wall may be pushed out of their position. This leads to the generation of dislocation loops, which results in the formation of nanostructures at the surface of the material (Xu et al., 2014).

### 3.1.2 Experimental conditions used in the experiments

The formation of blisters, bubbles and their interrelated phenomena is influenced by several parameters such as incident flux, fluence, ion energy and bulk structure of the material. Furthermore, the probability of hydrogen bubble formation is enhanced for low hydrogen solubility materials, low sample temperatures and high fluences (Condon and Schober, 1993). In our case two of these conditions will be fulfilled: a material with a low hydro-

gen solubility, aluminum, will be exposed to high fluence hydrogen plasma (in the order  $10^{23} - 10^{24}$  ions/m<sup>2</sup>).

The parameters that are modified in our experiments are: **ion energy, fluence, microstructure, surface finish** and **crystallographic orientation**. There are some parameters that remain constant throughout the experiments: all samples consisted of 99.99% pure aluminum, polished to a mirror-like finish (except when investigating the surface finish experiments), annealed for 2 hours at 673 K at a pressure of  $10^{-4}$  Pa and exposed at a temperature of 618 K with a flux of  $1.6 \times 10^{20}$  ions/m<sup>2</sup>s.

During the analysis, blister density and size were measured by taking into account blisters with radius larger than 100 nm and heights of approximately 0.5  $\mu$ m. In addition, primary and secondary blisters, and blister coalescence were taken into account. Grain swelling was considered as a different phenomenon and hence was not taken into account for the statistical analysis of blister population characteristics.

## 3.2 Influence of incident ion energy

Four experiments were performed in order to study the influence incident ion energy has on blister and bubble formation. Aluminum samples were exposed to the following experimental conditions: incident ion flux of  $1.6 \times 10^{20}$  ions/m<sup>2</sup>s, sample temperature of 618 K, fluence of  $3.3 \times 10^{24}$  ions/m<sup>2</sup> and four different incident ion energies of 20 (which corresponds to the sample at the floating potential  $V_f$ ), 120, 220 and 320 eV. The energy values were chosen based on the threshold for ion induced defect production, which is 195 eV for  $H^+$  ions (Broeders and Konobeyev, 2004; Hotston, 1975) The two lowest energy values,  $V_f$  and 120 eV, are smaller than the energy needed for vacancy production. The energy value of 220 eV, is close to the ion defect generation value and the energy value of 320 eV lies above the threshold for ion induced defect production.

The implantation depth for the analyzed ion energies was calculated using SRIM (Ziegler et al., 2010). Fig 3.8 shows the implantation profile for the different energy values. Each profile has a Gaussian shape with a relatively small average implantation range with values between 1.6 and 8 nm for the analyzed energy range.

The ion back-scattering or reflection yield values were also calculated by SRIM (Ziegler et al., 2010). For the different analyzed energies this value is only slightly affected by the incident energy and ranges between 14 and 32% (Ziegler et al., 2010). The highest reflection yield corresponds to the lowest energy  $V_f$ .

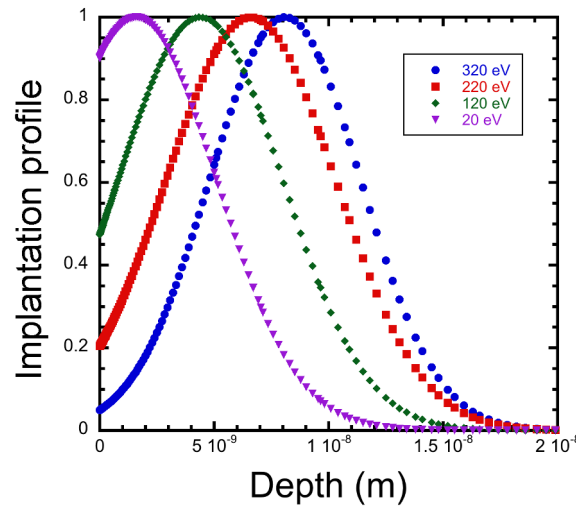


Fig. 3.8 Implantation profiles showing the implantation depth of hydrogen ions impinging in an aluminum surface at different energies

### 3.2.1 Blister formation

After plasma exposure, for incident ion energies above 120 eV, samples show circular blisters distributed all over the surface. Experiments performed at a floating potential  $V_f$  showed no signs of blistering. Fig 3.9 shows the changes in surface morphology for increasing incident ion energies. The sample exposed to hydrogen plasma with incident ion energy of 120 eV shows the lowest blister density and size (Fig 3.9 a)). Both blister density and size increase for increasing incident ion energy. The sample exposed to hydrogen plasma with incident ion energy of 320 eV shows blisters that cover most of the surface (Fig 3.9 c)).

Fig 3.9 also shows a more detailed image of the sample surface. It is seen that the samples exposed to incident ion energy higher than 220 eV develop nanostructures on their surface. These nanostructures are distributed all over the surface, even on the top of the blisters and have a height of a few nanometers. It may then be concluded that a minimum incident ion energy is required for nanostructures formation. This threshold energy is higher than that required for blister formation.

Additionally, Fig 3.9 c) shows the image of a small blister with a radius of approximately 100 nm. These small blisters are observed in the samples exposed to incident ion energy of 120, 220 and 320 eV and were the smallest blisters measured in the samples.

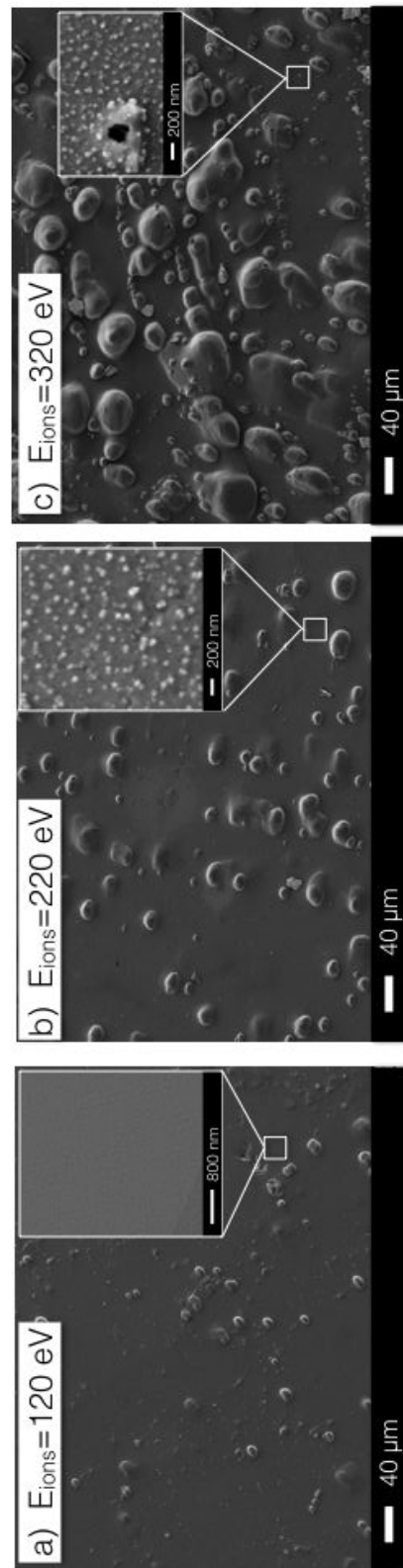


Fig. 3.9 SEM micrograph of Al samples exposed to  $\text{H}_2$  plasma with flux of  $1.6 \times 10^{20} \text{ ions/m}^2\text{s}$ , fluence of  $3.3 \times 10^{24} \text{ ions/m}^2$  and an incident ion energy of a) 120 eV, b) 220 eV and c) 320 eV

Fig. 3.10 shows the statistics of blister formation for different energies. To obtain these values, both inter and intragrain blisters were taken into account. This is due to the fact that for the analyzed conditions, blisters growth was observed all over the surface, both in the grains and at the grain boundaries. It can be observed, in Fig. 3.10, that blister density and average radius vary linearly with energy. Blister density and average radius increase from 160 blisters/mm<sup>2</sup> to 750 blisters/mm<sup>2</sup> and from 4.5 μm to 10 μm, respectively.

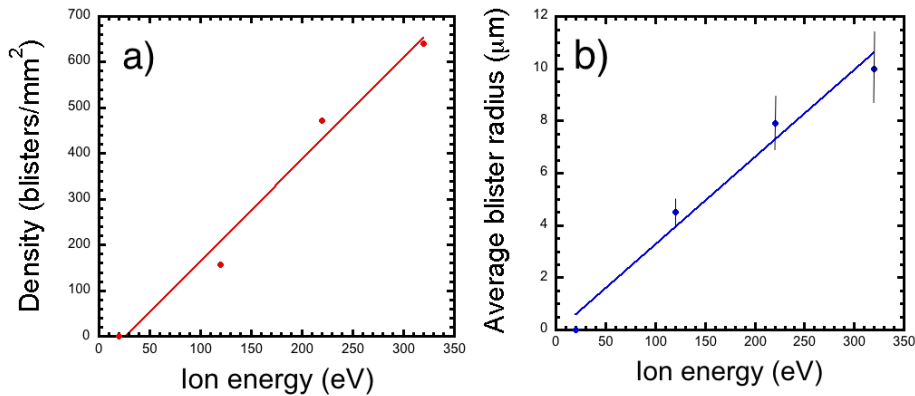


Fig. 3.10 Statistics of blisters in Al samples exposed to H<sub>2</sub> plasma with flux of  $1.6 \times 10^{20}$  ions/m<sup>2</sup>s, fluence of  $3.3 \times 10^{24}$  ions/m<sup>2</sup> at different incident ion energies

The increase in blister density may be attributed to different factors: at higher energies more ions are implanted in the material (*i.e.* less ions are reflected back to the plasma). As energy increases, ions are implanted deeper in the material and for sufficiently high energies, ion induced defects are created in the material. The reflection yield of hydrogen ions in aluminum does not change substantially for the analyzed energies. The percentage of implanted ions for the studied energy range lies between 68% and 82%. Therefore the increase in blister density cannot be attributed solely to ion back-scattering. Ion implantation, on the other hand, remains in the nanometric scale (between 1.5 – 8 nm), suggesting that this parameter is not responsible for the increase in blister density.

As a matter of fact, bubble nucleation rates are at least partly determined by the level of induced defects in the material. In addition to the enhancement of defect production at larger incident ion energies, the presence of hydrogen in the material decreases the formation energy for vacancies and promotes the formation of hydrogen vacancy complexes (Ren et al., 2008). Therefore there is a cooperation effect between an increased defect production and hydrogen vacancy clustering. This leads to an increase in blister density that is much larger than what would be suspected on the basis of a simple back-scattering effect. In other words, implantation with incident ion energies high enough to create defects allows the nucleation of a higher blister density in the surface of the material. For this reason, as the incident energy

increases, blister density increases. However, it is also important to notice that blisters are able to nucleate at conditions where the incident ion energy is lower than the value required to create defects in aluminum.

Fig. 3.11 shows the size distribution of blisters for the considered energies. The size distribution was obtained by measuring the blister size of 100 blisters from each sample. The first thing to notice is that there is a smaller fraction of blisters at smaller incident ion energies. As incident ion energy increases, the blister size distribution shifts towards larger sizes and gets wider.

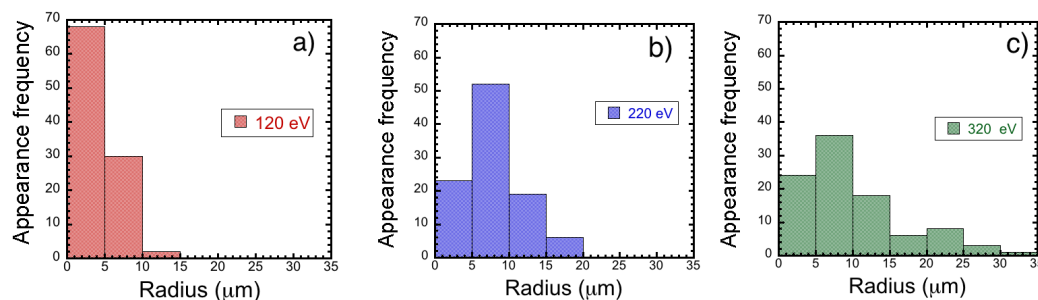


Fig. 3.11 Statistics of blisters in Al samples exposed to  $H_2$  plasma with flux of  $1.6 \times 10^{20}$  ions/ $m^2s$ , fluence of  $3.3 \times 10^{24}$  ions/ $m^2$  and different incident ion energies

Additional investigation of the sample may be performed by analyzing the phenomena occurring in the bulk. Therefore the next section focuses on studying the cross section of the samples exposed at different incident ion energies.

### 3.2.2 Cross section

Defects in the material bulk may be divided in three groups: blisters, bubbles and cracks. Blisters are cavities or bubbles close to the surface, usually with a circular shape and are able to deform the material surface. Bubbles lie deeper in the material. They also have a circular shape but are not responsible for surface deformation (Condon and Schober, 1993). Finally, cracks are larger cavities, which occur deeper in the material and are usually located at grain boundaries.

The cross-sections of the Al samples exposed to different incident ion energies were analyzed in order to correlate the surface modifications to the change and damage in the bulk of the material. Fig. 3.12 a), b) and c) show a SEM micrograph of the cross section of the samples exposed to hydrogen plasma with ions having an energy of 120, 220 and 320 eV respectively.

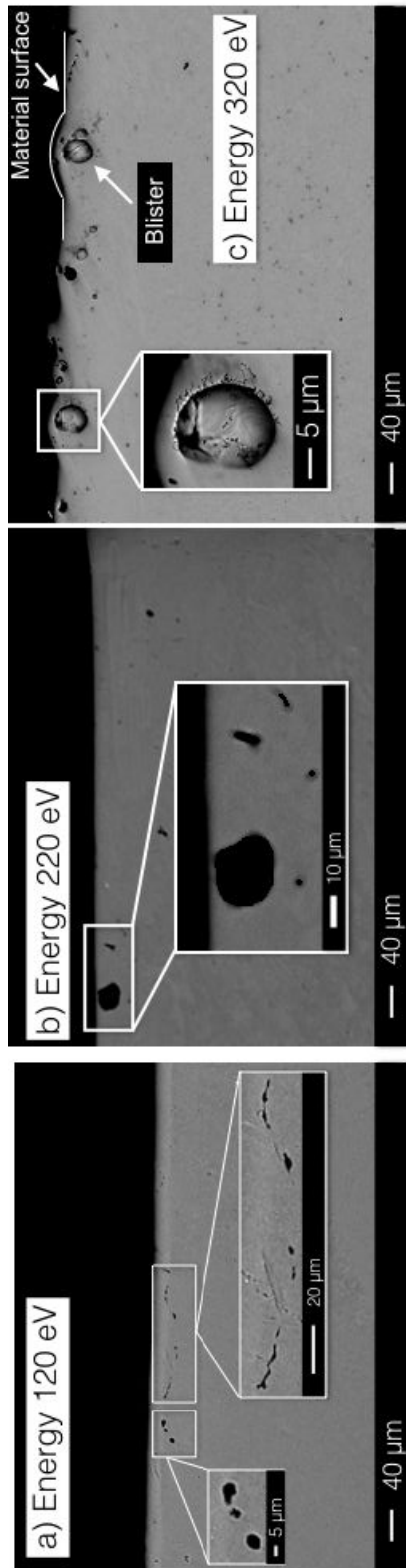


Fig. 3.12 Cross-section of Al samples exposed to H<sub>2</sub> plasma with flux of  $1.6 \times 10^{20}$  ions/m<sup>2</sup>-s, fluence of  $3.3 \times 10^{24}$  ions/m<sup>2</sup> and an incident ion energy of a) 120 eV, b) 220 eV and c) 320 eV

For the sample exposed to incident ions energies of 120 eV there is no major damage in the bulk, as shown in Fig. 3.12 a). There are some bubbles with a radius of a few micrometers and some cracks of approximately 20  $\mu\text{m}$  in length and a few micrometers wide. Note that it was previously determined that the samples may have cracks that are either inherent to the material itself or caused by the cutting process used to obtain the cross-section. These cracks may have a few micrometers in length and a few nanometers wide. When the sample is exposed to  $H_2$  flux these cracks may act as traps for hydrogen in the material. As hydrogen accumulates in the crack, pressure increases and may cause the crack to grow further in size resulting in wider cracks than those seen in the virgin samples. Due to its dimensions, the crack observed in Fig. 3.12 a) is an example of an inherent crack that grows due to excess hydrogen pressure.

Fig. 3.12 b) shows the cross section of a sample exposed to a hydrogen plasma with ions having an energy of 220 eV. A few bubbles with a radius ranging between 1 and 10  $\mu\text{m}$  are observed. Even though the bubbles are close to the material surface, no blisters were observed to be induced by the presence of this bubble. The bubbles observed in this sample are larger than those observed for an incident ion energy of 120 eV.

Fig. 3.12 c) shows the cross section of a sample exposed to hydrogen plasma with ions having an energy of 320 eV. Blisters with a radius ranging between 5-15  $\mu\text{m}$  are observed close to the surface. Additionally, some bubbles with a radius of up to 7  $\mu\text{m}$  are also observed in the cross section. In this case, the material bulk is more damaged than in the lower energy cases. This is because ions impinging with an energy of 320 eV are able to produce more defects that may diffuse in the material bulk.

Table. 3.1 also shows the radius of blisters and bubbles and the length of cracks for the analyzed energies. It is observed that the size of the cavities increases for increasing incident ion energy. For the analyzed cases, ions with an energy of 120 eV are not able to induce defects in the materials whereas ions with an energy of 220 eV and higher can induce such defects. Induced defects such as vacancies act as trap for hydrogen. These vacancies and vacancy hydrogen complexes may diffuse deeper in the material and tend to combine in hydrogen-filled clusters (*i.e.*  $H_2 - v$  clusters). Inside the  $H_2 - v$  clusters hydrogen recombines into molecules and hence these clusters act as the initial nucleation mechanisms for bubbles. The probability of bubbles nucleation increases if a higher density of vacancies are present in the material. As a result, bubble nucleation is enhanced in a highly damaged material. Therefore, more bubbles are able to grow in the sample exposed to the highest incident ion energy.

One aspect noticed in Fig. 3.12 is that the defects lie at a depth of a few micrometers. This depth is deeper than the implantation depth, which is of a few nanometers for the different analyzed incident ion energies. The reason these defects lie deeper than the implantation depth is due to hydrogen diffusion from regions of high concentration to regions of low concentration during implantation (Manhard, 2011; Post and Behrisch, 1986). In addition,  $H_2 - v$  complexes may also diffuse in the material and recombine into  $H_2 - v$  clusters at depths deeper than the implantation depth. As a result, hydrogen atoms reach depths larger than the implantation zone and defects may nucleate and grow deeper in the material. Table 3.1 shows the depth of blisters, bubbles and cracks for the different analyzed energies. The depth of the cavities increase for increasing incident ion energy.

Energy (eV)	120 eV	220 eV	320 eV
Average blister depth	Not observed	Not observed	20.5 $\mu\text{m}$
Average blister radius	Not observed	Not observed	11.5 $\mu\text{m}$
Average bubble depth	32 $\mu\text{m}$	78 $\mu\text{m}$	92 $\mu\text{m}$
Average bubble radius	3 $\mu\text{m}$	6 $\mu\text{m}$	6.7 $\mu\text{m}$
Average cracks depth	2 $\mu\text{m}$	34.6 $\mu\text{m}$	82 $\mu\text{m}$
Average cracks length	22 $\mu\text{m}$	24 $\mu\text{m}$	30 $\mu\text{m}$

Table 3.1 Values of depth, radius and length of blisters, bubbles and cracks of an Al sample exposed continuously to  $H_2$  plasma at different incident ion energies with flux of  $1.6 \times 10^{20}$  ions/ $\text{m}^2\text{s}$ , a fluence of  $3.3 \times 10^{24}$  ions/ $\text{m}^2$  and different incident ion energies

Analysis of the cross section of the sample exposed to plasma with 320 eV hydrogen ions allows analyzing bubble growth dynamics. As a matter of fact, Fig 3.13 shows two different phenomena found in the cross-section and related to the bubble growth kinetics.

Fig 3.13 a) shows a blister with microcracks on one side of the blister wall. These microcracks have a length of a few micrometers and a width ranging from 0.3 to 1.5  $\mu\text{m}$ . These microcracks are located on the wall closer to the surface. The first question that arises when observing these cracks is: how are they formed? One possible explanation would be due to the high pressures inside the bubble, which are able to generate cracks in the material. Another possible explanation is that the incoming hydrogen flux leads to a higher hydrogen concentration in the near surface region. More  $H_2-v$  clusters are able to form, which decreases the tensile strength in this region of the material. The stress from the high pressures inside the bubble are able to rupture the weakened material leading to microcrack formation.

Fig 3.13 b) shows another phenomenon related to bubble growth. This image shows four bubbles with clear signs of coalescence. This occurs when a bubble grows to a size where they are able to coalesce with a neighboring bubble. Although bubble coalescence has not been thoroughly studied in literature, it has also been observed experimentally in tungsten exposed to deuterium plasma (Xu et al., 2016).

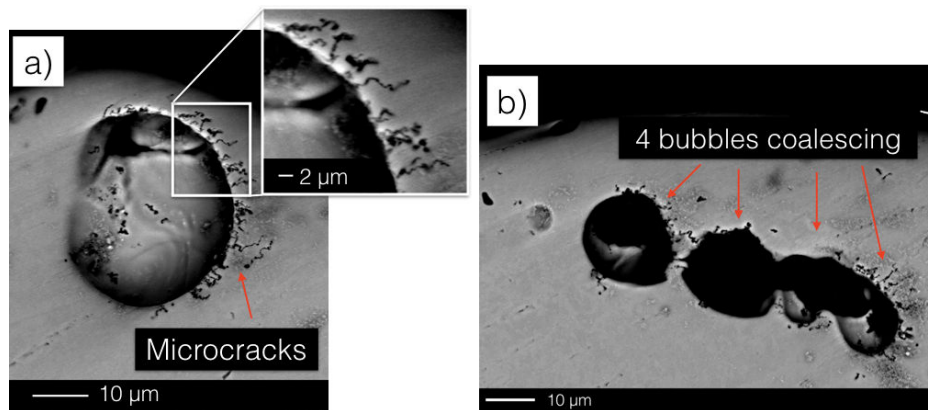


Fig. 3.13 Examples of a) a bubble with microcracks and b) bubble coalescence found in the cross section of an Al sample exposed to  $H_2$  plasma with a flux of  $1.6 \times 10^{20}$  ions/ $m^2s$ , fluence of  $3.3 \times 10^{24}$  ions/ $m^2$  and incident ion energy of 320 eV

*Conclusion:* In this section, an analysis of how blister and bubble growth is affected by incident ion energy was performed. The main conclusions reached are:

- Blister density and size increase with increasing ion energy at constant fluence. Similarly, bubble density and size increase for increasing energy. In addition, the bubbles are formed much deeper in the material for higher energies. This may be attributed to the fact that at higher energies, larger quantity of defects are created in the material. This enhances blister nucleation and growth.
- The results obtained in these experiments may be interpreted by invoking two possible growth models simultaneously: diffusion followed by clustering of  $H_2$ -v complexes, and bubble coalescence.

Besides the effect of ion energy, surface modifications also depend on plasma fluence. The next section focuses on the study of bubble growth dynamics when the samples are exposed to different amounts of hydrogen.

### 3.3 Influence of fluence

The experimental conditions chosen to perform an analysis of the effect fluence has on blister and bubble formation were the following: incident ion flux of  $1.6 \times 10^{20}$  ions/m<sup>2</sup>s and a sample temperature of 618 K. The incident ion energy at the biased target was kept constant at 320 eV since previous investigations showed that blisters nucleate more promptly at this condition; thus facilitating the analysis of fluence and blister formation.

A SEM micrograph and EBSD measurements of the sample before plasma exposure are shown in Fig. 3.14 a). The EBSD scans show large equiaxed grains with sizes of a few  $\mu\text{m}$ , typical of a recrystallized sample. Fig. 3.14 b) shows the sample after 1h of plasma exposure, corresponding to a fluence of  $5.4 \times 10^{23}$  ions/m<sup>2</sup>. It can be observed that blisters start to nucleate on the Al surface and are mainly located at the grain boundaries with a misorientation angle higher than 15° degrees. There are no blisters within the grains. Blisters tend to nucleate in the grain boundaries given that impurity atoms tend to segregate in this area. Additionally, the atoms in this area are not bonded to the maximum number of nearest atoms. As a result, grain boundaries are more ductile than the matrix, and it is easier for blisters to grow in this area through loop punching and plastic deformation.

Fluence plays a key role in the evolution of surface morphology in materials. According to the literature, at lower fluences (in the range of  $10^{18} - 10^{21}$  ions/m<sup>2</sup>) hydrogen is trapped in already existing defects or extrinsic ones created by ion impact. Since hydrogen atoms diffuse in the material, at low fluences there is a low local hydrogen concentration in the material. As the fluence increases (in the range of  $10^{21} - 10^{24}$  ions/m<sup>2</sup>), so does the local hydrogen concentration. This leads to the formation and diffusion of  $H_2$ -v complexes, which eventually combine into  $H_2$ -v clusters. As a result, there is a higher blister nucleation and growth (Behrish, 1983; Condon and Schober, 1993; Ren et al., 2005). Investigation of fluence effects on surface morphology remains essentially qualitative in nature. In this section a detailed study on the effect fluence has on blister growth dynamics is presented.

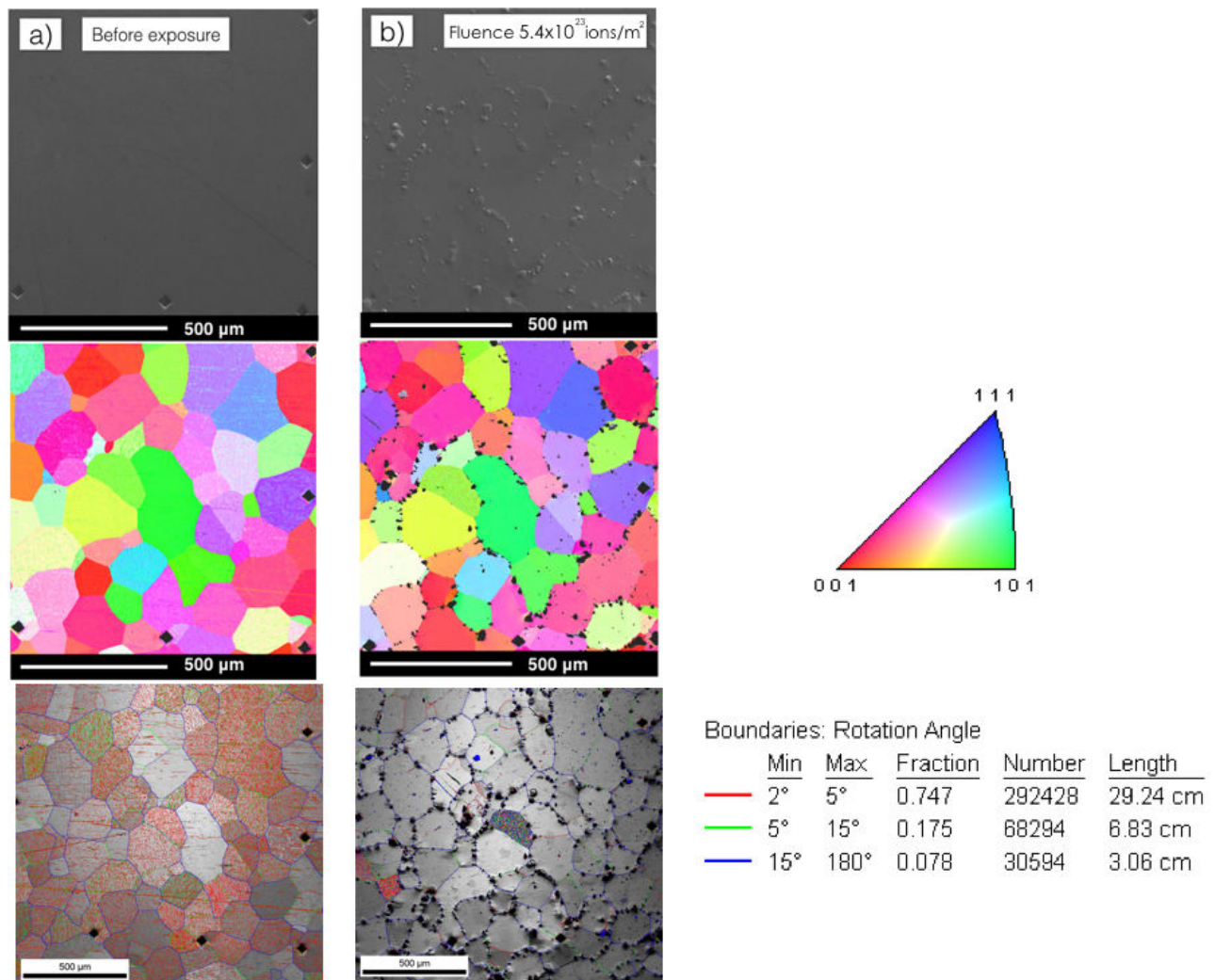


Fig. 3.14 SEM micrograph and EBSD measurements of an Al sample a) before and b) after plasma exposure with a flux of  $1.6 \times 10^{20}$  ions/m<sup>2</sup>s, incident ion energy of 320 eV and a fluence of  $5.4 \times 10^{23}$  ions/m<sup>2</sup>

The effect of fluence was investigated for two different discharge regimes: continuous and cyclic plasma exposure. In the first case, the sample is continuously submitted to hydrogen plasma until the desired fluence value is reached. In the second case, the desired value is reached by a series of experiments where the sample is submitted to hydrogen plasma for periods of 1 hour. At the end of each experiment the sample is analyzed *ex-situ* by SEM and Confocal optical microscopy. Afterwards, the sample is submitted again to hydrogen plasma for 1 h. This cycle is repeated until the desired fluence is reached. In this procedure, the sample is subject to hydrogen charging, stress, thermal cooling and relaxation between experiments. Analyzing the case of cyclic plasma exposure enables us to examine **the effects**

**stress, relaxation and cooling have on bubble and blister formation given that current plasma reactors work in cycles instead of continuous plasma exposure.**

The fluences used in the experiments are summarized in Table 3.2.

Exposure time	Fluence (ions/m <sup>2</sup> )
1 h	$5.4 \times 10^{23}$
2 h	$1.3 \times 10^{24}$
3 h	$1.7 \times 10^{24}$
4 h	$2.2 \times 10^{24}$
5 h	$2.8 \times 10^{24}$
6 h	$3.3 \times 10^{24}$
7 h	$4.0 \times 10^{24}$
8 h	$4.7 \times 10^{24}$

Table 3.2 Different fluences used in the experiments with an incident ion energy of 320 eV

### 3.3.1 Surface morphology after continuous plasma exposure

Fig. 3.15 shows the surface morphology for increasing fluences of different Al samples exposed continuously to  $H_2$  plasma. The sample exposed to a fluence of  $1.7 \times 10^{24}$  ions/m<sup>2</sup> (*i.e.* 3 h of plasma exposure) shows essentially intergrain blisters, as seen in Fig. 3.15 a). For increasing fluences intragrain blisters start to nucleate and intergrain blisters increase in size. Intragrain blisters have a mean radius that varies between  $3.2 \mu\text{m}$  for a fluence of  $2.2 \times 10^{24}$  ions/m<sup>2</sup> to  $6.5 \mu\text{m}$  for a fluence of  $4.7 \times 10^{24}$  ions/m<sup>2</sup>. This increase in average size is also accompanied by a decrease in blister density, which may be an indication of blister coalescence.

Both Fig. 3.15 and Fig. 3.14 show that intergrain and intragrain blisters present a different behavior. Intragrain blisters appearance requires a higher fluence than intergrain blister appearance. Therefore, these two cases are analyzed separately.

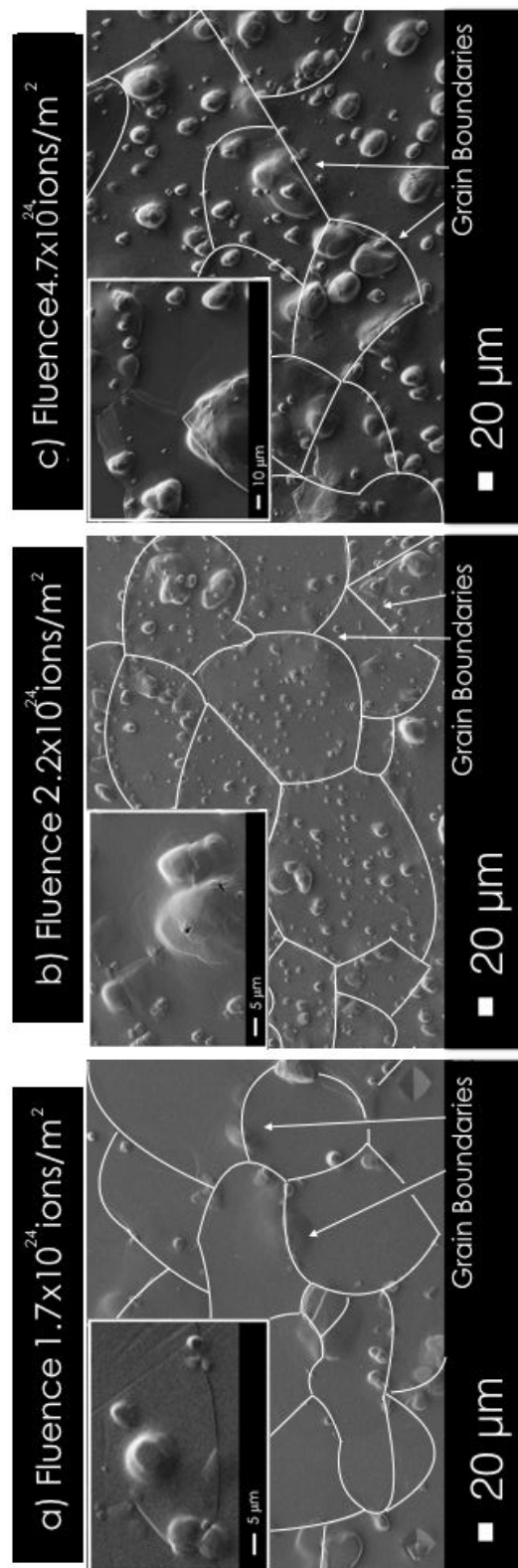


Fig. 3.15 SEM micrographs of different Al samples exposed continuously to H<sub>2</sub> plasma with flux of  $1.6 \times 10^{20}$  ions/m<sup>2</sup>s, incident ion energy of 320 eV and a fluence of a)  $1.7 \times 10^{24}$  ions/m<sup>2</sup> b)  $2.2 \times 10^{24}$  ions/m<sup>2</sup> and c)  $4.7 \times 10^{24}$  ions/m<sup>2</sup>

### Evolution of intergrain blisters with fluence subject to continuous plasma exposure

Intergrain blisters, as shown in Fig. 3.14, are the first ones to nucleate after 1 h of plasma exposure. Therefore, a study of shorter exposure times was performed in order to determine the threshold fluence for blistering. Table 3.3 shows the additional fluences used to analyze intergrain blisters.

Exposure time	Fluence (ions/m <sup>2</sup> )
15 min	$1.4 \times 10^{23}$
20 min	$1.9 \times 10^{23}$
25 min	$2.4 \times 10^{23}$
30 min	$2.8 \times 10^{23}$

Table 3.3 Additional fluences used in the experiments to analyze intergrain blisters

Fig. 3.16 a) shows the evolution of blister density with time, defined as blisters/mm of grain boundary. The threshold fluence for intergrain blistering in our experimental conditions is  $1.2 \times 10^{24}$  ions/m<sup>2</sup>, which corresponds to 15 minutes of plasma exposure. It is worthy to mention that blister growth is not a progressive phenomenon. In fact, it is a critical phenomenon defined by a situation where no blisters are observed prior to 15 minutes of plasma exposure. After this time period, blisters are observed in the surface with sizes ranging from 100 nm to a few  $\mu\text{m}$ . Therefore, at the threshold fluence the average blister size is 1.2  $\mu\text{m}$ .

Intergrain blister density increases for increasing fluence, reaching a maximum at 1 h of plasma exposure, as shown in Fig. 3.16 b). Afterwards, blister density remains rather constant. The average radius of intergrain blisters shows a similar behavior, however, it continues to slightly increase for increasing fluences. The radius increases from 1.4  $\mu\text{m}$  at lower fluences to around 7  $\mu\text{m}$  for higher fluences.

The linear coverage of blisters, that is the percentage of grain boundary length covered with blisters, increases with fluence. For 15 minutes of plasma exposure, this value is close to zero; then it continues to increase very rapidly, reaching 30% percent of linear coverage for 1 h of plasma exposure. For increasing time periods, the linear coverage increases more slowly reaching 60% of linear coverage after 8 h of plasma exposure.

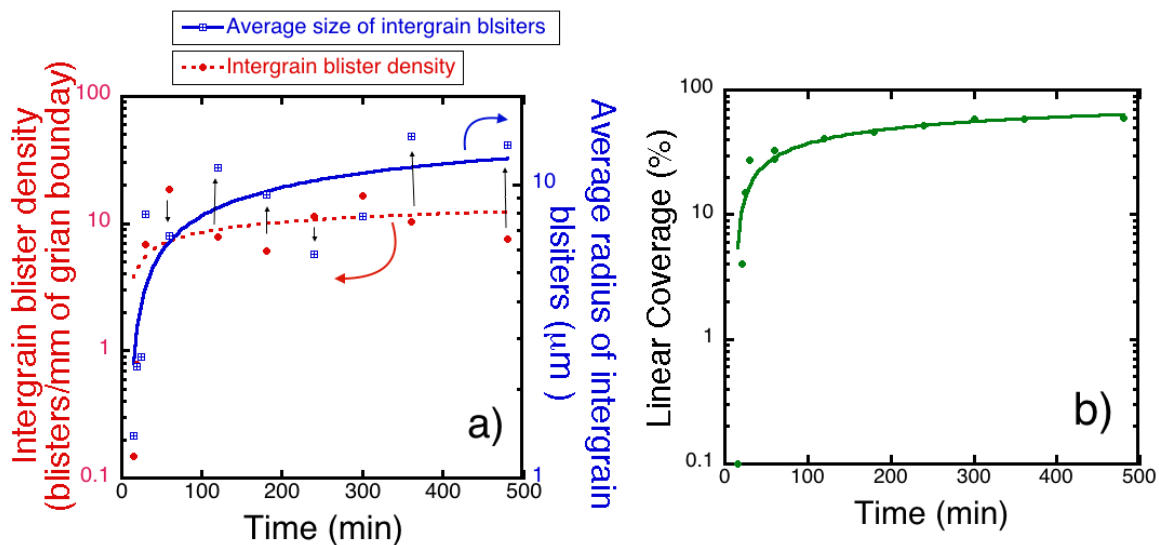


Fig. 3.16 a) Blister density (red circles), radius (blue squares) and b) linear coverage of intergrain blisters for different fluences for Al samples exposed to H<sub>2</sub> plasma continuously with a flux of  $1.6 \times 10^{20}$  ions/m<sup>2</sup>s and incident ion energy of 320 eV

There are different phenomena occurring at the sample surface during plasma exposure at different fluences. The first one is the coalescence of small blisters (sizes of a few μm) into larger ones, shown in Fig 3.17 a). This blister coalescence is consistent with the fact that although time variation shows fluctuations in the blister density and radius, these fluctuations are consistent: high density values correspond to smaller sized blisters, as shown by the arrows in Fig 3.17 a).

A second phenomenon is the presence of a secondary blister growth. As mentioned in Section 3.1.1, this phenomenon consists of smaller blisters, with a radius of approximately 100 nm to a few μm, that either nucleate on already existing blisters or a large blisters that nucleate underneath the smaller blisters. Secondary blister growth is shown in Fig 3.17 b). The smaller blisters might be difficult to recognize due to the rough blistered surface or might have their lids eroded, as shown in Fig 3.17 c).

These effects lead to a fairly significant statistical error as far as blister density measurements is concerned. This explains the observed non-monotonous changes in density observed in Fig. 3.16 a).

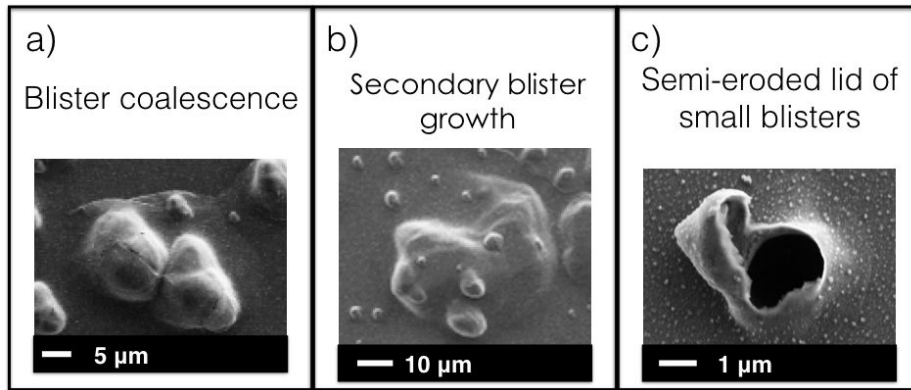


Fig. 3.17 a) Blister coalescence, b) secondary blister growth and c) semi-eroded blister caps

It is also important to notice that for fluences lower than  $1.4 \times 10^{23}$  ions/m<sup>2</sup> no blisters were found. A minimum concentration of hydrogen must be present in the material in order for blisters to nucleate, a condition which is not met for fluences lower than  $1.4 \times 10^{23}$  ions/m<sup>2</sup>. This fluence is higher than the one used by Kamada *et al* (Kamada, 1989), where he found bubbles and blisters by implanting 15 keV hydrogen ions at 300 K with fluences as low as  $4 - 5 \times 10^{21}$  ions/m<sup>2</sup>. This difference in threshold fluence may be attributed to the large difference in incident ion energy and sample temperature, since blistering phenomena not only depends on fluence. It is important to keep in mind that both hydrogen solubility and diffusion in aluminum increase for increasing temperature (Serra et al., 1998; Young and Scully, 1998). At 618 K, hydrogen in the material diffuses quicker than at 300 K. This leads to a lower local concentration of hydrogen in the material. As a result, higher fluences are required to achieve hydrogen solubility limits for blistering at higher sample temperatures. In addition,  $H_2$  solubility is enhanced at higher temperatures, which means that the hydrogen in the material is less likely to precipitate into bubbles.

An important phenomenon occurring in the samples exposed to increasing fluences, is grain swelling. Fig. 3.18 shows the behavior of grains for increasing fluences. Swelling starts after 20 minutes of plasma exposure at a fluence of  $1.9 \times 10^{23}$  ions/m<sup>2</sup> and it continues to occur for increasing fluences. After being exposed to a fluence of  $4.7 \times 10^{24}$  ions/m<sup>2</sup>, the height of this swelling ranges between 3 and 10 μm. Grain swelling eventually leads to a rupture at the grain boundaries.

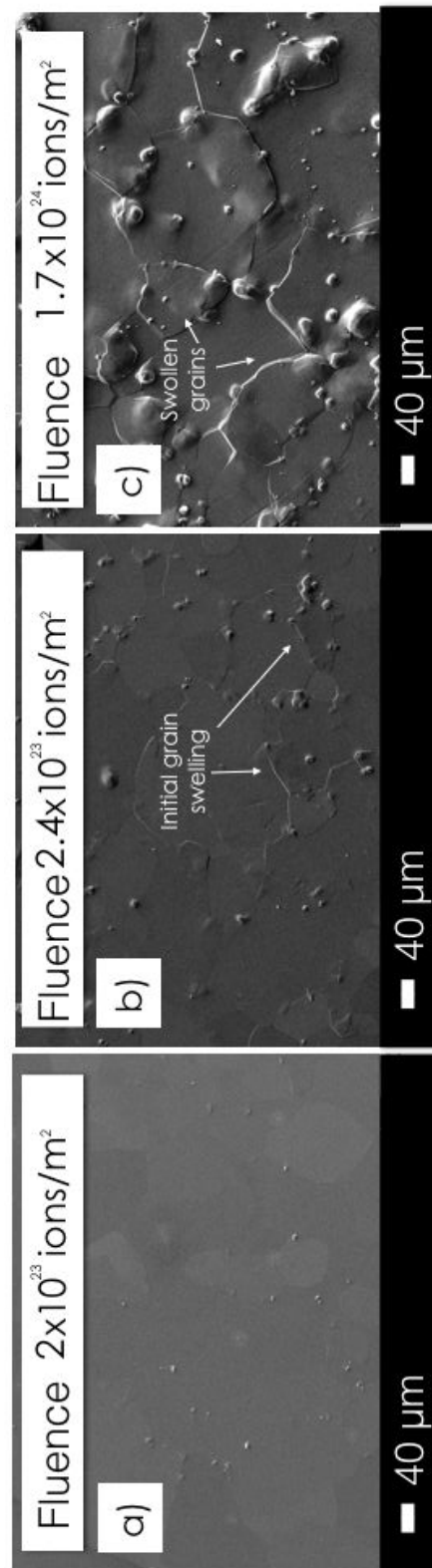


Fig. 3.18 Grain swelling in Al samples exposed continuously to  $\text{H}_2$  plasma with a flux of  $1.6 \times 10^{20} \text{ ions/m}^2\text{s}$ , incident ion energy of  $320 \text{ eV}$  and a fluence of a)  $2 \times 10^{23} \text{ ions/m}^2$  b)  $2.4 \times 10^{23} \text{ ions/m}^2$  and c)  $1.7 \times 10^{24} \text{ ions/m}^2$

*Conclusion:* This section described the most relevant results obtained for the analysis of the evolution of intergrain blisters with increasing fluence for continuous plasma exposure. We showed that for the investigated plasma conditions (*i.e.* incident ion flux of  $1.6 \times 10^{20}$  ions/m<sup>2</sup>s, sample temperature of 618 K and incident ion energy of 320 eV) **the threshold fluence for intergrain blistering is  $5.4 \times 10^{23}$  ions/m<sup>2</sup>**. For increasing fluences two different phenomena are observed in the surface of the aluminum samples. First, larger blisters seem to result from the coalescence of smaller ones. Second, the swelling of grains is observed in the material. The results obtained in this section were for intergrain blisters and their behavior for increasing fluences. The next section focuses on the analysis of intragrain blisters and their evolution with increasing fluence.

### Evolution of intragrain blisters with fluence subject to continuous plasma exposure

Fig. 3.19 a) and b) show respectively the intragrain blister density, average radius and surface coverage as a function of time for aluminum samples exposed continuously to hydrogen plasma. When the sample treatment time reaches 1 h, corresponding to a fluence of  $5.4 \times 10^{23}$  ions/m<sup>2</sup>, Fig. 3.19 a) shows there are no intragrain blisters in the sample surface. On the other hand, at this fluence there is an important intergrain blister density in the aluminum sample, as was shown in Fig. 3.16. This indicates that intragrain blister nucleation kinetics is much slower than intergrain blister kinetics. Therefore, for our plasma conditions, intragrain blister appearance requires a higher fluence. The threshold fluence for intragrain blister appearance is  $1.3 \times 10^{24}$  ions/m<sup>2</sup>, corresponding to 2 h of plasma exposure.

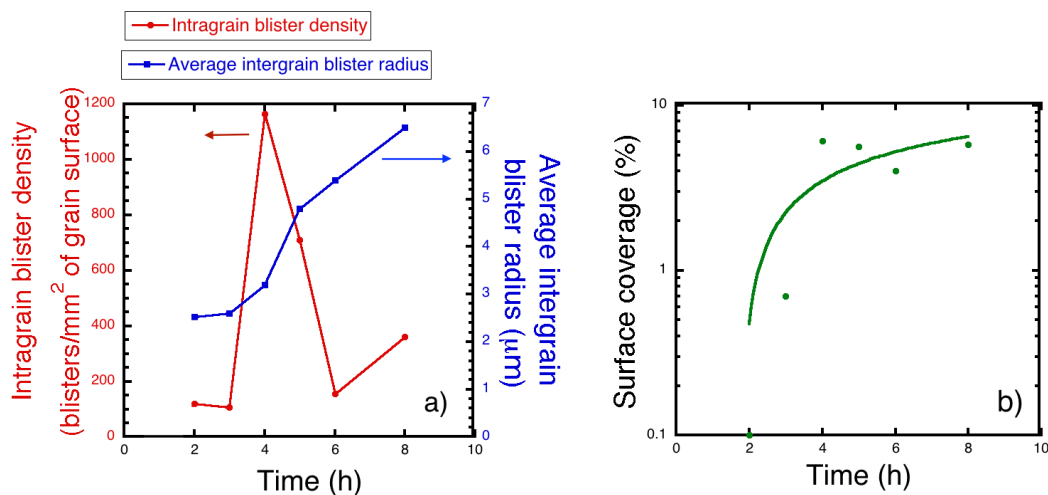


Fig. 3.19 a) Density (red circles), radius (blue squares) and b) surface coverage of intragrain blisters for different fluences for Al samples exposed to H<sub>2</sub> plasma continuously with a flux of  $1.6 \times 10^{20}$  ions/m<sup>2</sup>s and incident ion energy of 320 eV

The blister density is shown in Fig. 3.19 a). The area occupied by grain boundaries was not excluded from the measurements since grains are very large (90-300  $\mu\text{m}$ ) and the influence of grain boundaries on the measurements can be neglected. Intragrain blister density increases a factor of 8, from 150 blisters/ $\text{mm}^2$  to 1200 blisters/ $\text{mm}^2$ , when the discharge duration increases from 2 h to 4 h of plasma exposure. This increase can be easily appreciated in the image shown in Fig. 3.15 a) and Fig. 3.15 b) that corresponds to SEM micrographs at lower and higher fluence, respectively.

Also, Fig. 3.19 a) shows that for a time duration above 4 h, the blister density decreases to 300 blisters/ $\text{mm}^2$ . This decrease in intragrain blister density is accompanied by an increase in the average blister radius, which varies from 3  $\mu\text{m}$  for 4 h of plasma exposure to 6.6  $\mu\text{m}$  for 8 h of plasma exposure. The decrease in blister density and increase in blister size may be observed in Fig. 3.15 b) and c) and can be attributed to blister growth due to coalescence. It is worthy to mention that this non-monotonous change in blister density, with a maximum value at 4 h, was confirmed by repeating the experiments.

Blister coalescence is confirmed by observing a more detailed SEM micrograph where blister size is seen to increase after 4 h of plasma exposure (Fig. 3.20 a)) and after 8 h of plasma exposure (Fig. 3.20 b)). A decrease in blister density may also be appreciated in this image. These experiments clearly show that blister coalescence is an additional mechanism that governs blister growth dynamics, along with the previously mentioned: blister nucleation and growth by loop punching.

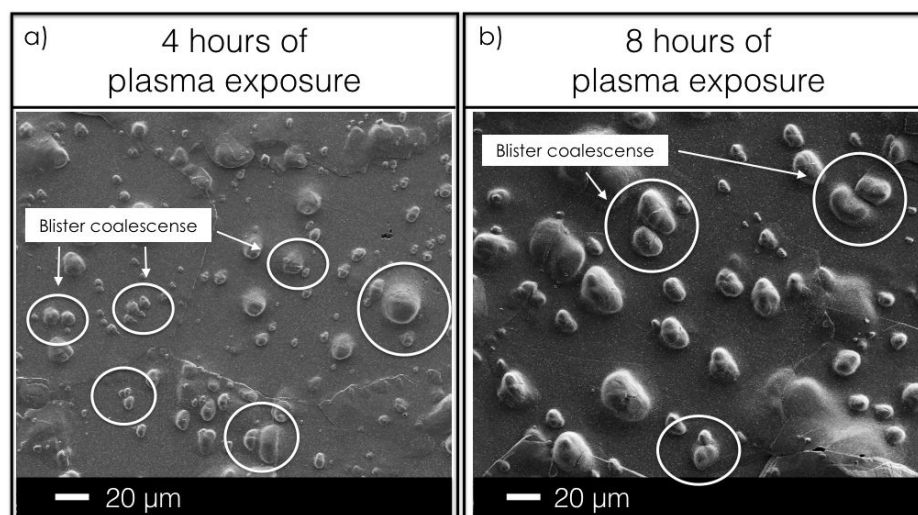


Fig. 3.20 SEM micrographs of Al samples exposed to  $\text{H}_2$  plasma continuously with a flux of  $1.6 \times 10^{20}$  ions/ $\text{m}^2\text{s}$  and incident ion energy of 320 eV during a) 4 h and b) 8 h.

The surface coverage, shown in Fig. 3.19 b) is seen to rapidly increase once blisters start to nucleate. After 4 h of plasma exposure, the increase in surface coverage is slower. It appears that a large nucleation of blisters takes place for time period between 3 and 4 hours, while it seems that nucleation is quenched for longer time periods. During longer time periods it appears that only coalescence takes place. As a result, blister density decreases for time periods greater than 5 hours. After 8 h of plasma exposure, corresponding to a fluence of  $2 \times 10^{25}$  ions/m<sup>2</sup>, the surface coverage of intragrain blisters is less than 10%.

In order to verify if intragrain blister size and density are affected by grain size, the number of blisters were analyzed separately for each grain and fluence value. Fig. 3.21 a) shows the number of blisters with respect to grain area and Fig. 3.21 b) the average radius of blisters with respect to grain area for a sample exposed to a fluence of  $2.2 \times 10^{24}$  ions/m<sup>2</sup> (*i.e.* 4 h of plasma exposure). It can be observed that larger grains have a higher number of blisters, whereas their average radius is the same regardless of the grain area. Also, the average blister number increases linearly with grain area. This means that, at the studied fluences and grain sizes, the average blister density does not depend on grain size. This behavior was observed for all the sample exposed to different fluences, however, only the ones corresponding to 4 h of plasma exposure are shown here.

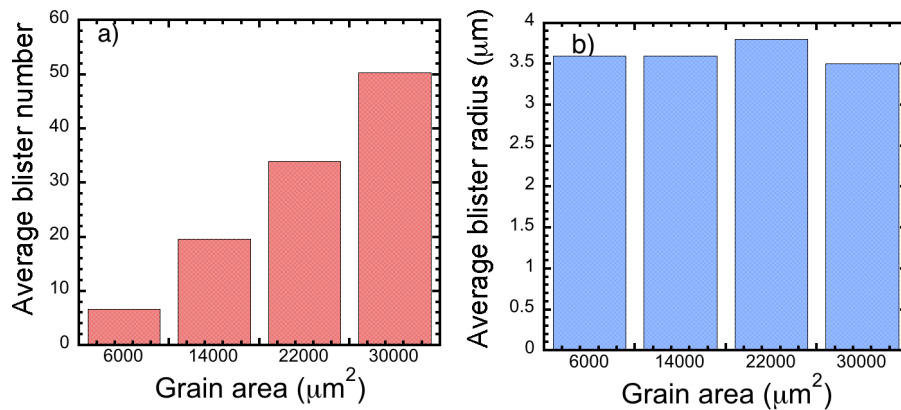


Fig. 3.21 a) Number of blisters and b) average radius per grain size for an Al sample exposed continuously to H<sub>2</sub> plasma with a flux of  $1.6 \times 10^{20}$  ions/m<sup>2</sup>s, incident ion energy of 320 eV and fluence  $2.2 \times 10^{24}$  ions/m<sup>2</sup>

**Conclusion:** This section described the most relevant results obtained for the analysis of the evolution of intragrain blisters with increasing fluence for continuous plasma exposure. We showed that for the investigated plasma conditions (*i.e.* incident ion flux of  $1.6 \times 10^{20}$  ions/m<sup>2</sup>s, sample temperature of 618 K and incident ion energy of 320 eV) **the threshold fluence for intragrain blistering is  $1.3 \times 10^{24}$  ions/m<sup>2</sup>**. The experiments shows

that blister coalescence is an additional mechanism that governs blister growth dynamics. The results obtained in this section were for intragrain blisters and their behavior for increasing fluences. The next section focuses on the analysis of the surface morphology when exposing the samples to high plasma fluences.

### **Surface morphology evolution at high fluences subject to continuous plasma exposure**

This section focuses on analyzing blister surface morphology evolution at high fluences. The objective is to analyze the precursors of grass-like structures, such as those reported for Be and Al under high fluence exposure (Doerner et al., 2013, 2014; Kreter et al., 2014). The samples were exposed continuously to hydrogen plasma up to a fluence of  $1.7 \times 10^{25}$  ions/m<sup>2</sup> with the same plasma conditions used throughout this section.

Fig. 3.22 a) shows the sample surface after an exposure to high fluence. A rough and completely blistered surface can be observed. Blister size ranges between 10 and 100  $\mu\text{m}$ , most of them having already burst. It may be remarked that there are single and multiple burst blisters. These multiple burst blisters corresponds to blisters produced by secondary nucleation, which burst during plasma exposure.

Fig. 3.22 b) shows the aluminum sample tilted 70° degrees in order to better appreciate the blistered topography. This image shows that the topography seen in the sample surface consists in fact of cone-shaped microstructures with a height ranging between 20 and 80  $\mu\text{m}$ . These cone-shaped microstructures are scattered non-uniformly over the surface with a density of approximately 800 cones/mm<sup>2</sup>. It has been reported in literature that cone-like structures appear at much higher fluences than those required for blister formation. This phenomenon is due to local variation in the sputtering yield of the material. High fluences of ion bombardment (*i.e.* higher than  $10^{23}$  ions/m<sup>2</sup>) are able to generate imperfect or rough areas in the material surface. These imperfections may cause changes in the projectile stopping power and atom binding energies to the surface, resulting in variations in the sputtering yield (Behrish, 1983). As a result, structures such as the cone-like structures observed in Fig. 3.22 b) may develop in the material surface.

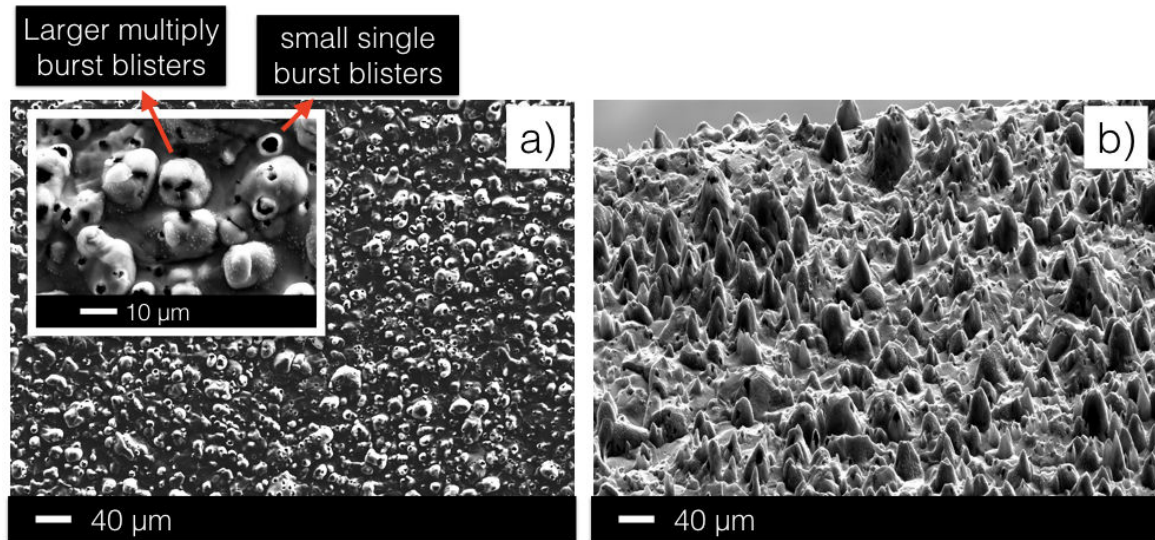


Fig. 3.22 SEM micrographs of the surface a) normal to the electron beam and b) tilted  $70^\circ$  of an Al exposed to  $H_2$  plasma continuously with a flux of  $1.6 \times 10^{20}$  ions/ $m^2s$ , incident ion energy of 320 eV and a fluence of  $1.7 \times 10^{25}$  ions/ $m^2$

**Conclusion:** This section focused on the analysis of the evolution of intragrain blisters for increasing fluence. It was shown that **the threshold fluence for intragrain blistering is higher than for intergrain blistering**. During plasma exposure at different fluences it was determined that the observed **blister density and size is governed by three processes: appearance (nucleation), blister growth by loop punching and blister growth by coalescence**. At higher fluences, cone-like structures start to develop at the sample surface.

So far, both intergrain and intragrain blisters were studied for continuous plasma exposure. The next subsection focuses on studying blister growth dynamics that takes place under cyclic plasma exposure.

### 3.3.2 Surface morphology after cyclic plasma exposure

Fig. 3.23 shows the surface morphology for increasing fluences of a single Al sample exposed cyclically to hydrogen plasma. The sample exposed to a fluence of  $1.3 \times 10^{24}$  ions/ $m^2$  (*i.e.* 2 h of plasma exposure) shows mostly intergrain blisters, as seen in Fig. 3.23 a). For increasing fluences intragrain blisters start to nucleate existing blisters increase in size. During cyclic plasma exposure the average radius of both inter and intragrain blisters remains fairly constant with values of 6 and  $4.5 \mu m$ , respectively. It is observed in Fig. 3.23 that blister density increases for increasing fluences.

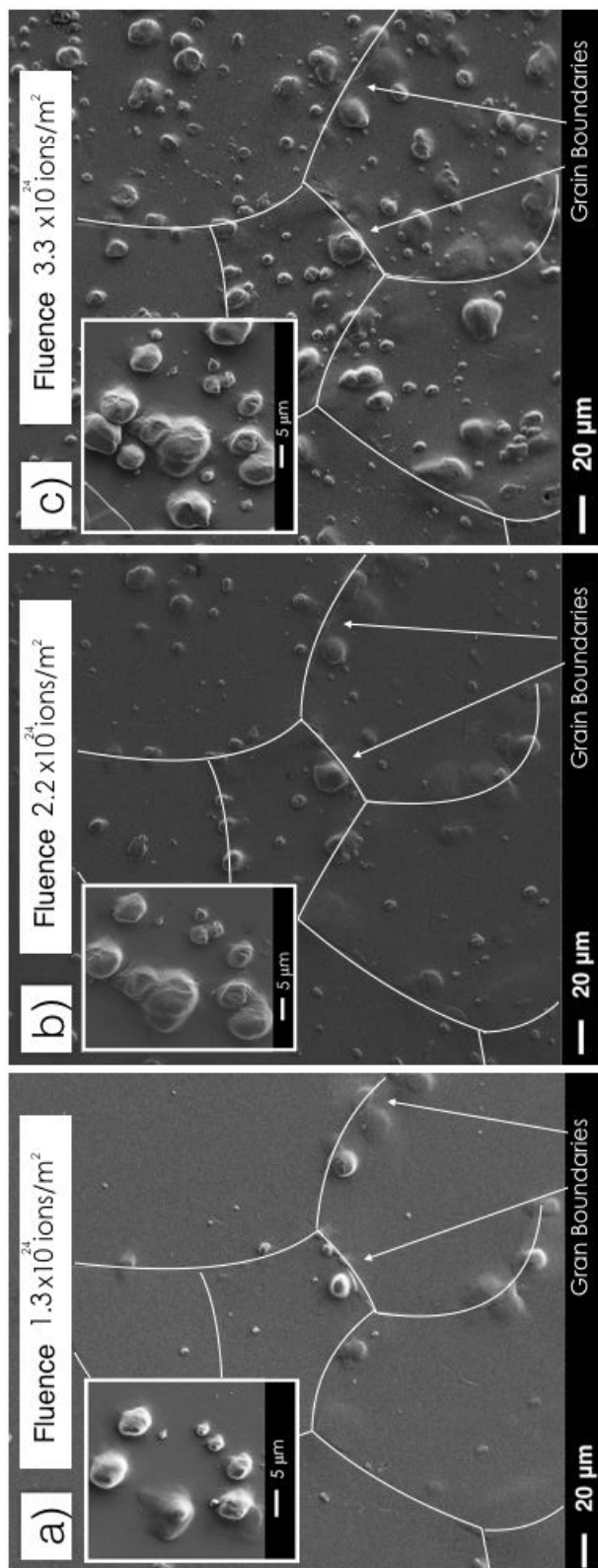


Fig. 3.23 SEM micrographs of a single Al sample exposed cyclically to H<sub>2</sub> plasma with flux of  $1.6 \times 10^{20}$  ions/m<sup>2</sup>-s, incident ion energy of 320 eV and a fluence of a)  $1.3 \times 10^{24}$  ions/m<sup>2</sup> b)  $2.2 \times 10^{24}$  ions/m<sup>2</sup> and c)  $3.3 \times 10^{24}$  ions/m<sup>2</sup>

### Evolution of intergrain blisters with fluence subject to cyclic plasma exposure

Fig. 3.24 a) depicts the density increase of intergrain blisters with time. It is seen that intergrain blister density (blisters/mm of grain boundary) increases linearly from 40 blisters/mm of grain boundary, after 1 h of plasma exposure, to 90 blisters/mm of grain boundary after 8 h of plasma exposure. The radius of these blisters, shown in Fig. 3.24 b), reaches a value of  $6 \mu\text{m}$  after 2 h of plasma exposure and remains constant for increasing fluences. It may be concluded during the first hour of plasma exposure that there is blister appearance and growth. Above the one hour treatment, existing blisters stop growing and further hydrogen flux leads to the appearance of new blisters that grow up to a size of approximately  $6 \mu\text{m}$ .

The size distribution is almost the same for all the analyzed time periods. An example at 8 h of plasma exposure, corresponding to a fluence of  $4.7 \times 10^{24}$  ions/m<sup>2</sup>, is shown in Fig. 3.24 c). This figure shows that after 8 h of plasma exposure most of the blisters have radius between 4 and 8  $\mu\text{m}$ .

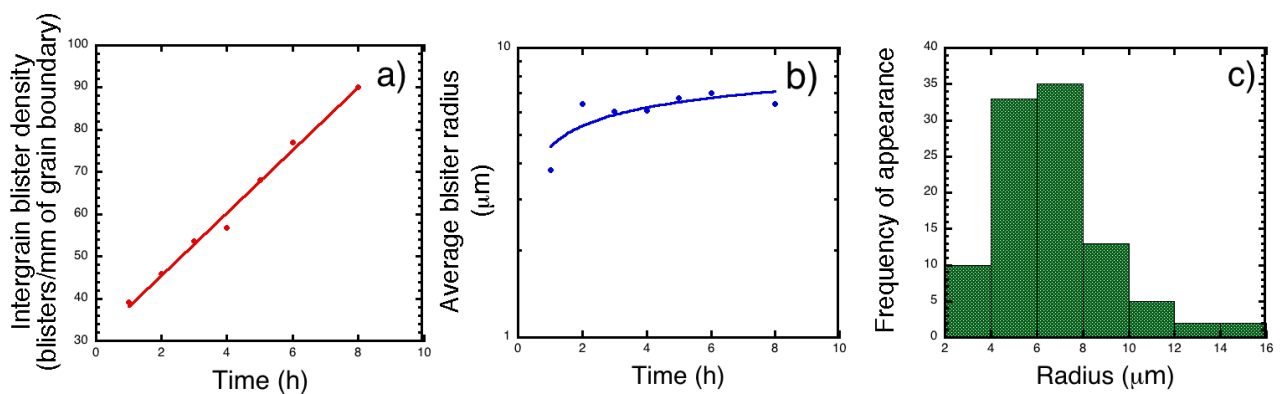


Fig. 3.24 a) Density b) radius and c) size distribution of intergrain blisters as function of time for an Al sample exposed to  $\text{H}_2$  plasma cyclically with a flux of  $1.6 \times 10^{20}$  ions/m<sup>2</sup>s and incident ion energy of 320 eV

During cyclic plasma exposure, certain grains are seen to swell for increasing fluences. Fig. 3.25 shows an evolution of a grain for increasing fluences. It is observed that at fluences lower than  $2.8 \times 10^{24}$  ions/m<sup>2</sup> there is no grain swelling. For fluences higher than  $2.8 \times 10^{24}$  ions/m<sup>2</sup> grains begin to swell in the material. Fig. 3.25 c) shows an image a swollen grain with a height of  $0.7 \mu\text{m}$ , after being exposed at a fluence of  $4.7 \times 10^{24}$  ions/m<sup>2</sup>. In this case, grain swelling is observed in fewer grains and reaches lower heights than in the samples exposed continuously to plasma.

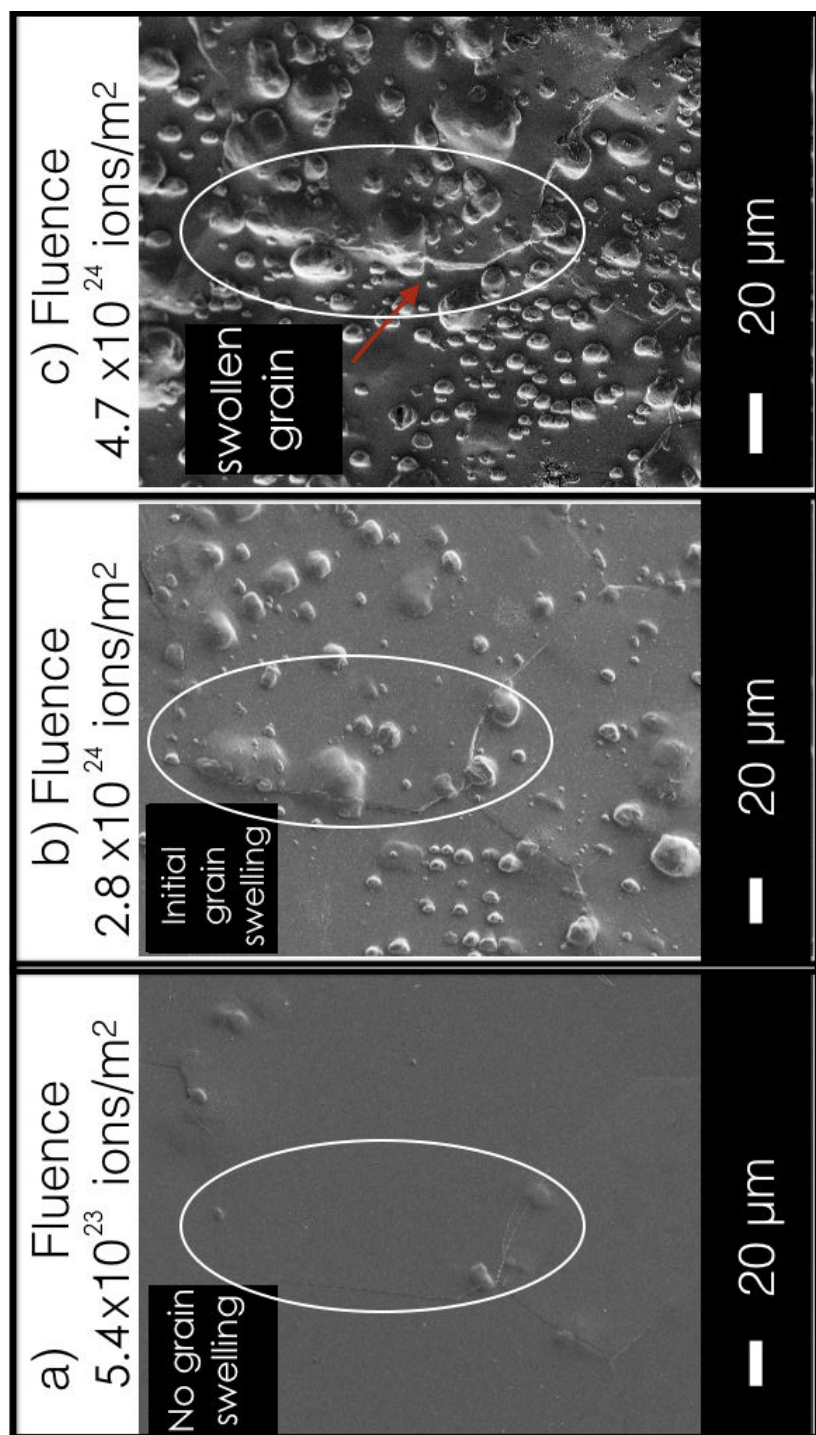


Fig. 3.25 Grain swelling at different fluences in Al samples exposed continuously to  $\text{H}_2$  plasma cyclically with a flux of  $1.6 \times 10^{20}$  ions/m<sup>2</sup>s, incident ion energy of 320 eV and a fluence of a)  $5.4 \times 10^{23}$  ions/m<sup>2</sup>, b)  $2.8 \times 10^{24}$  ions/m<sup>2</sup> and c)  $4.7 \times 10^{23}$  ions/m<sup>2</sup>

One interesting aspect is that the Al sample exposed cyclically to  $H_2$  plasma shows a significant percentage of burst blisters. Fig. 3.26 shows the percentage of burst intergrain blisters for increasing fluences along with an image of the typical blister burst occurring at the grain boundaries. For cyclic plasma treatment, intergrain blister burst leads ultimately to a crack formation. It is also possible for cracks to form directly without proceeding from blister burst. It is worthy to mention that previous studies showed that blister burst is one of the mechanisms that lead to tungsten nanoparticle formation through hydrogen plasma surface interaction with tungsten (Ouaras et al., 2016). The results obtained here would therefore indicate that for cyclic plasma exposure, larger fluences lead to an enhanced intergrain blister burst and hence a higher probability for nanoparticle formation. A comparison with the continuous plasma exposure case is given in section 3.3.4.

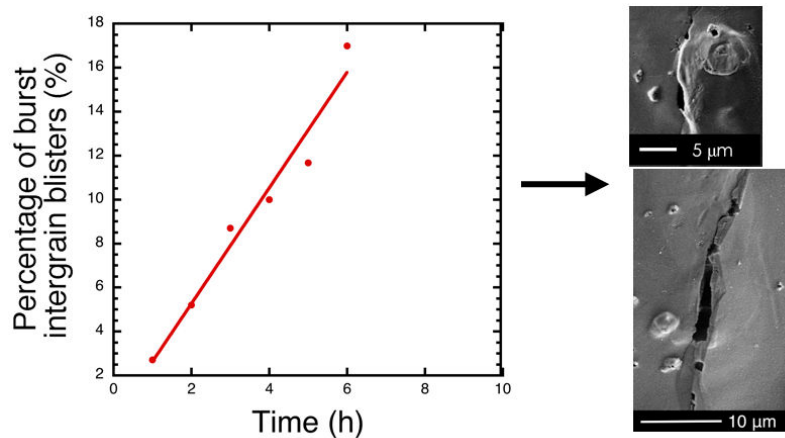


Fig. 3.26 Percentage of intergrain burst blisters at different fluences exposed cyclically to  $H_2$  plasma with a flux of  $1.6 \times 10^{20}$  ions/ $m^2s$  and incident ion energy of 320 eV

*Conclusion:* For cyclic plasma exposure, intergrain blister density increases linearly with increasing fluence however their radius remains fairly constant with fluence. This means that for cyclic hydrogen treatments, blisters form, grow up to an average radius of  $5 \mu m$ . Further hydrogen accumulation would lead to an increase in the internal pressure of the bubble, which eventually leads to burst. In addition, during cyclic plasma treatments, the height of swollen grains is smaller than in the continuous case. Grain swelling eventually leads to a crack formation along the grain boundaries.

### Evolution of intragrain blisters with fluence subject to cyclic plasma exposure

Fig. 3.27 shows the statistics of intragrain blisters for increasing fluence of samples exposed cyclically to plasma. It can be seen, in Fig. 3.27 a), that intragrain blisters take a longer

time to nucleate than intergrain blisters. They start to appear (nucleate) at a fluence of  $1.3 \times 10^{24}$  ions/m<sup>2</sup>, corresponding to 2 h of plasma exposure. Hence for a cyclic plasma exposure, the threshold fluence for blistering remains the same as in the case of continuous plasma exposure. Intragrain blister density (blisters/mm<sup>2</sup>) increases linearly for increasing fluences, reaching a value of 3500 blisters/mm<sup>2</sup> after 8 h of plasma exposure.

The average intragrain blister radius is almost constant for increasing fluences, as shown in Fig. 3.27 b). The size distribution is almost the same for all the analyzed time periods. An example at 8 h of plasma exposure, corresponding to a fluence of  $4.7 \times 10^{24}$  ions/m<sup>2</sup>, is shown in Fig. 3.27 c). This figure shows that after 8 h of plasma exposure 80% of the blister population has radius between 0.1 and 4  $\mu$ m. The average blister radius is small because after each plasma cycle new blisters appear on the sample. Even though the radius of some existing blisters increase after each exposure, this is not enough to counteract the appearance (nucleation) of new, smaller blisters. As a result, the radius is almost constant with an average value of 4  $\mu$ m.

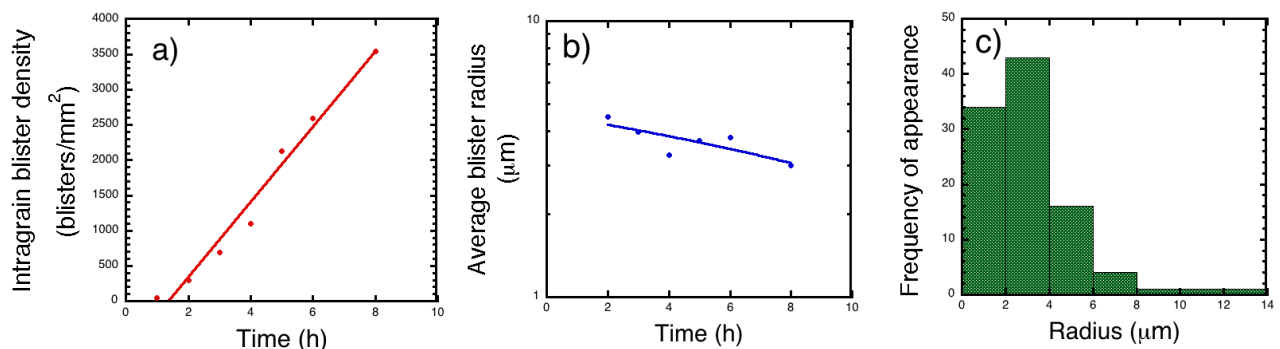


Fig. 3.27 a) Density b) radius and c) size distribution of intragrain blisters for different fluences for an Al sample exposed to H<sub>2</sub> plasma cyclically with a flux of  $1.6 \times 10^{20}$  ions/m<sup>2</sup>s and incident ion energy of 320 eV

Fig. 3.28 shows the percentage of burst intragrain blisters along with an image of the typical blister burst occurring in the grains. The percentage of burst blisters increases linearly with fluence. Intragrain blisters may burst at both small and large sizes ranging from 100 nm to a few  $\mu$ m. It appears therefore that blisters burst does not depend on blister size. This means that the fracture limit may be reached either at sizes as low as 100 nm or at larger sizes of a few  $\mu$ m. It may be concluded that the sample exhibits two types of blisters. A first type for which the fracture limit is reached before a significant plastic deformation and a second type corresponding to those blisters than have the ability to plastically deform and are therefore characterized by large fracture strains.

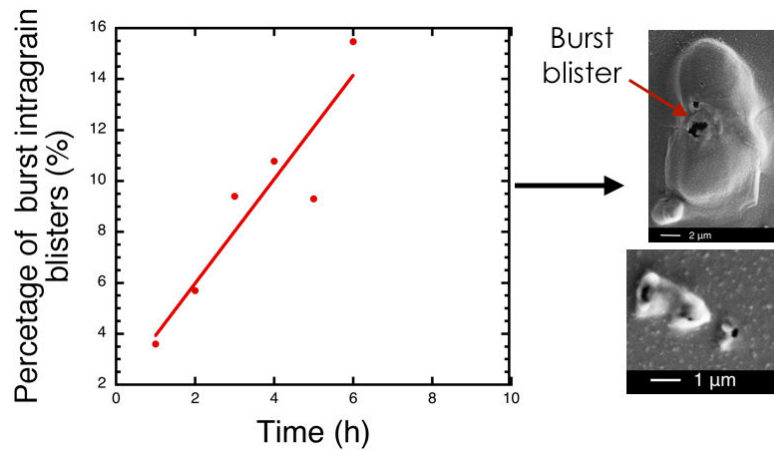


Fig. 3.28 Percentage of intragrain burst blisters at different fluences exposed cyclically to  $H_2$  plasma plasma cyclically with a flux of  $1.6 \times 10^{20}$  ions/ $m^2s$  and ion energy of 320 eV

The volume evolution of 10 randomly chosen blisters was analyzed after each exposure in order to better understand their development with increasing fluences. The volume was calculated by using the projected area inferred from SEM micrographs and the height of each blister measured by confocal optical microscopy. Fig. 3.29 shows the height evolution of the 10 blisters as a function of time. It can be seen that the observed blisters show a different behavior as far as their volume evolution is concerned. In most cases blister volume increases and then decreases after 6 h of plasma exposure whereas in three cases, blister volume keeps increasing for increasing fluences. The increase in volume is due to the ability of the material around the blister to undergo plastic deformation. So, as the pressure exerted by the hydrogen inside the blisters stays at a reasonable value, the blister will increase in size by undergoing plastic deformation. The volume decrease seen in some blisters for higher fluences may be due to different factors. First, after 6 h of plasma treatment, grain swelling is observed, as shown in Fig. 3.25. It is believed that the observed blister volume decrease is a direct consequence of this grain swelling, which results in an underestimated value for the measured heights. Another reason for this volume decrease may be due to hydrogen desorption from the sample. During the measurement cycles, hydrogen could desorb from the sample. In the case of blisters which were not fully elastically deformed, this gas release may lead to a partial relaxation of the blister. This phenomenon was already reported for deuterium blisters in tungsten (Balden et al., 2011).

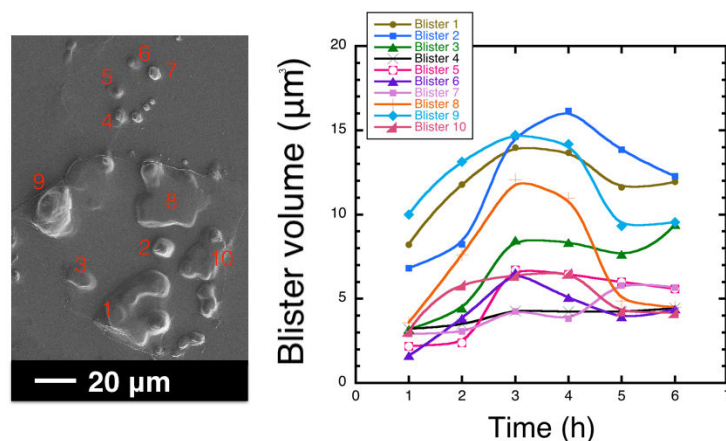


Fig. 3.29 Volume evolution of blisters on an Al sample exposed cyclically to  $H_2$  plasma for an Al sample exposed to  $H_2$  plasma cyclically with a flux of  $1.6 \times 10^{20}$  ions/ $m^2s$  and ion energy of 320 eV

*Conclusion:* For cyclic plasma exposure, intergrain blister density increases linearly with increasing fluence. However, their radius remains fairly constant with fluence. This is due to the fact that during cyclic plasma treatments blister appearance (nucleation) dominates over blister growth. Also, there is a much larger fraction of burst blisters at larger fluences. **Blister burst was seen in small blisters where the fracture limit is reached before a significant deformation and in larger blisters where there is a significant deformation prior to reaching the fracture limit.**

The next subsection focuses on the analysis of the cross-section of an aluminum sample exposed to hydrogen plasma to a fluence of  $4.7 \times 10^{24}$  ions/ $m^2$ . Since the essential features observed on the cross-section of the samples exposed continuously and cyclically to plasma are similar, we will restrict ourselves to discussing the case of continuously exposed samples.

### 3.3.3 Cross-section of Al samples after continuous plasma treatment

Blisters observed at the surface are in fact consequences of hydrogen retention and bubble and void formation in the bulk of the material. This may be indeed observed on the cross section of the sample exposed continuously to a fluence of  $4.7 \times 10^{24}$  ions/ $m^2$  in Fig. 3.30. It can be observed that there is a large number of bubbles in the vicinity of the sample surface. Some of these bubbles are able to induce deformation at the sample surface and result in blister formation. Other bubbles do not induce such deformation despite their proximity with the surface. Basically, blister size is similar to the size of the bubble that induces the blister. The cross-section also reveals very large cracks located in the sample volume, very far from

the surface. These cracks may also induce small height deformations. It is believed that grain swelling is the ultimate deformation induced by such large cracks.

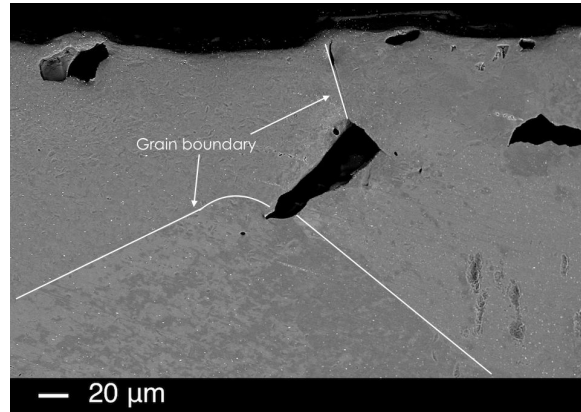


Fig. 3.30 Cross section of an Al sample exposed continuously to  $H_2$  plasma with flux of  $1.6 \times 10^{20}$  ions/ $m^2s$ , incident ion energy of 320 eV and a fluence of  $4.7 \times 10^{24}$  ions/ $m^2$

The statistics of the different cavities found in the cross-section were analyzed. Fig. 3.31 a), b) and c) show respectively the statistics of blisters, bubbles and voids as function of depth of an Al sample exposed continuously to  $H_2$  plasma. It can be seen in Fig. 3.31 a) that smaller blisters are generated by bubbles located closer to the surface while larger ones are generated by bubbles located deeper in the material. This is appreciated in Fig. 3.30 where there is a large blister and smaller blisters, closer to the surface. Blisters are located closer to the surface than the other cavities and have an average depth of 12  $\mu m$ . The majority of the blister population lies between 1 and 10  $\mu m$  with a size of approximately 5  $\mu m$ . Bubbles that are not able to deform the surface of the material are located farther away from the surface at an average depth of 68  $\mu m$ . Bubbles have a smaller radius than blisters with average values of 6  $\mu m$  and 8  $\mu m$  respectively. This result is expected given that close to the surface the material deforms more easily than in the bulk. As a result, bubbles are allowed to reach larger sizes than in the bulk (Condon and Schober, 1993). Finally, cracks are located far away from the surface with an average depth of 80  $\mu m$ .

It can be concluded that there are two scale surface deformation in the material. Large scale deformations, such as cracks, that result in large area, limited height deformations. The ultimate stage of this deformation is grain swelling in the surface of the material. The second type of deformation is the small scale deformations located in the vicinity of the surface. This results in larger heights and limited deformation area.

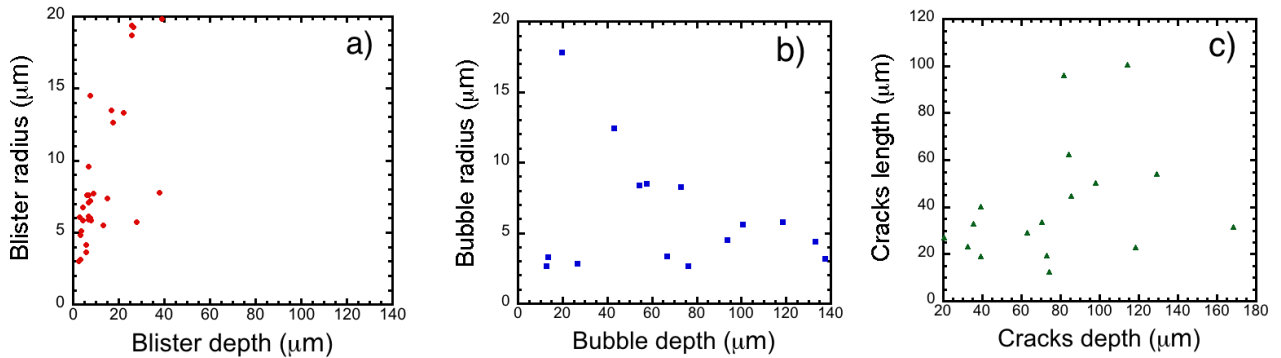


Fig. 3.31 Statistics of a) blisters b) bubbles and c) cracks of an Al sample exposed continuously to  $H_2$  plasma with flux of  $1.6 \times 10^{20}$  ions/ $m^2s$ , incident ion energy of 320 eV and a fluence of  $4.7 \times 10^{24}$  ions/ $m^2$

Cavities and bubbles in the bulk give information of the phenomena occurring at the surface of the material. Fig. 3.32 a) shows two cavities related to two blisters on the surface. This confirms the fact that smaller blisters are located close to the surface than larger blisters.

Fig. 3.32 b) shows two cavities underneath a single blister. The cavities are not spherical and are believed to have coalesced, resulting in a larger blister at the surface of the sample.

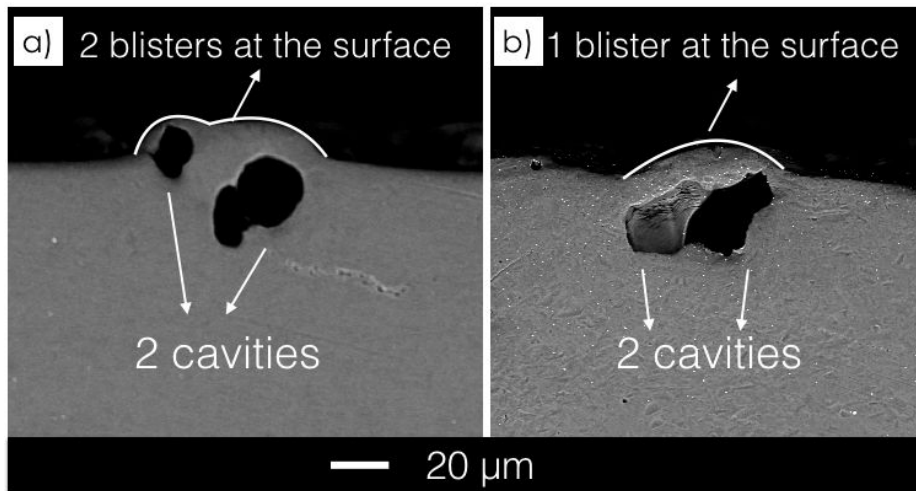


Fig. 3.32 Two cavities corresponding to a) two blisters b) one blister in the surface of an Al sample exposed continuously to  $H_2$  plasma with flux of  $1.6 \times 10^{20}$  ions/ $m^2s$ , incident ion energy of 320 eV and a fluence of  $4.7 \times 10^{24}$  ions/ $m^2$

Fig. 3.33 shows some small bubbles with a radius of approximately  $3 \mu m$  and a larger one with a radius of approximately  $8 \mu m$ . This larger bubble has a crack along the wall. The excessive pressure inside the bubble is able to plastically deform the material. As the

pressure increases, the fracture limit of the material may be reached. As a result, blisters may burst or cracks may start to propagate in the bulk.

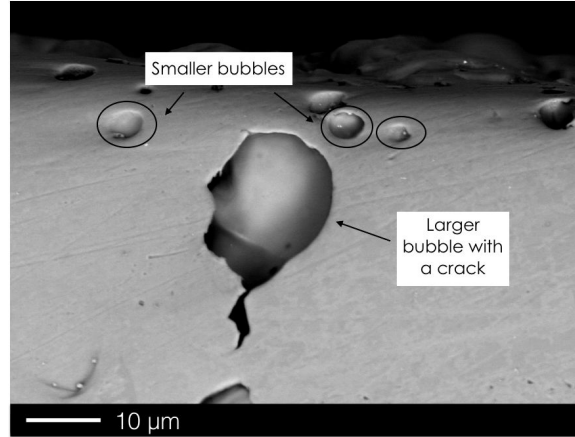


Fig. 3.33 Bubble with a crack in the cross section of the continuously to  $H_2$  plasma with flux of  $1.6 \times 10^{20}$  ions/ $m^2s$ , incident ion energy of 320 eV and a fluence of  $4.7 \times 10^{24}$  ions/ $m^2$

Before crack formation, high pressures in blisters allows the punching of dislocation loops out of the bubble, allowing the bubble to grow. This internal pressure  $p$  inside the blisters, before the cracks initiate, can be estimated analytically by the following equation (Ren et al., 2008):

$$p = \frac{K_{IC}\sqrt{\pi}}{2M(a/h)\sqrt{a}} \quad (3.1)$$

where  $K_{IC}$  is the fracture toughness ( $K_{IC}=24 \text{ MPam}^{1/2}$  for aluminum) (Skinn et al., 1994),  $a$  is the radius of the bubble,  $h$  is the bubble depth and  $M(a/h)$  is a function that equals 1.37 when  $a/h = 1$ .

Using this equation and assuming that the blister has a radius of the same order of magnitude as its depth, one obtains  $p = 8.9 \text{ GPa}$  for a  $3 \mu\text{m}$  bubble and  $p = 5.9 \text{ GPa}$  for a  $7 \mu\text{m}$  bubble. In both cases, the pressure greatly exceeds the value of the yield and tensile strength of aluminum:  $0.035 \text{ GPa}$  and  $0.09 \text{ GPa}$  respectively (Calister and Rethwisch, 2010). The yield strength measures the stress at which a materials begins to deform plastically and the tensile stress corresponds to the maximum stress that can be sustained by a structure before its fracture. Therefore, at these high pressures, the bubble in the bulk of the material is likely to induce plastic deformation of the surrounding area and cracks may form along the bubble wall.

### 3.3.4 Comparison between continuous and cyclic plasma exposure

Results show many differences between samples exposed continuously and cyclically to plasma. First, during continuous plasma treatment, blister density and size is governed by three processes: blister appearance, blister growth by loop punching, and blister coalescence. Blister appearance and coalescence affect both blister size and density whereas blister growth by loop punching affects only blister size. On the other hand, during cyclic plasma treatment, blister appearance dominates over blister growth. As a result, blisters are smaller compared to continuous plasma case but their density is larger. It is worthy to mention that no blister coalescence was observed in samples exposed to a cyclic plasma treatment.

The difference between the two plasma treatments is appreciated in the SEM micrographs. Fig. 3.34 a) and b) depicts the Al samples exposed, respectively, continuously and cyclically, to  $H_2$  plasma with flux of  $1.6 \times 10^{20}$  ions/m<sup>2</sup>s and incident ion energy of 320 eV and a fluence of  $4.7 \times 10^{24}$  ions/m<sup>2</sup>. It can be noticed that the sample exposed to a continuous plasma treatment has fewer but larger blisters.

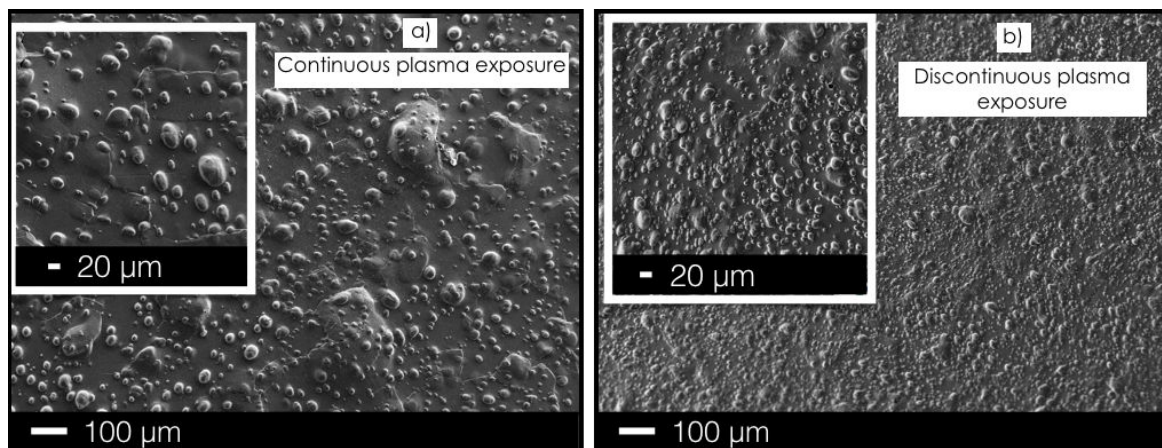


Fig. 3.34 Al samples exposed a) continuously and b) cyclically with flux of  $1.6 \times 10^{20}$  ions/m<sup>2</sup>s, incident ion energy of 320 eV and a fluence of  $4.7 \times 10^{24}$  ions/m<sup>2</sup>

Table 3.4 summarizes the statistics related to blister density, average radius and height as inferred from the SEM and optical microscope. The samples exposed to a continuous plasma treatment have lower intergrain and intragrain blister density; however blisters are larger in size and height. This difference is explained by considering that the samples submitted to continuous plasma treatment are subject to fairly constant stress that induces continuous plastic deformation through loop punching. As a result, blisters are able to grow continuously during the plasma treatment. On the other hand, samples exposed to a cyclic plasma treatment, experience cycles of stress and relaxation that results in cyclic deformation of blisters during plasma exposure.

Besides, this cyclic deformation is also associated with hydrogen desorption from the sample during the relaxation process. As reported in the literature (Valiev et al., 2002), such cyclic deformation leads to a local hardening in the blistered area. Consequently, blister growth during subsequent hydrogen exposure remains quite limited. Existing blisters still act as hydrogen traps during plasma treatment; however blisters tend to grow or appear in areas that are easier to deform. In other words, blisters tend to grow in areas that have not been subject to hardening. As a result, blister density is higher in the sample exposed cyclically to plasma.

Parameter	Continuous plasma exposure	Cyclic plasma exposure
Intergrain blister density (blisters/mm of grain boundary)	8	90
Average intergrain blister radius ( $\mu\text{m}$ )	14	5
Intragrain blister density (blisters/ $\text{mm}^2$ )	360	3500
Average intragrain blister radius ( $\mu\text{m}$ )	7	3
Maximum blister height ( $\mu\text{m}$ )	40	20

Table 3.4 Different parameters for Al samples exposed continuously and cyclically to  $\text{H}_2$  plasma with flux of  $1.6 \times 10^{20}$  ions/ $\text{m}^2\text{s}$ , incident ion energy of 320 eV and a fluence of  $4.7 \times 10^{24}$  ions/ $\text{m}^2$

Another major difference between these two cases comes from the fact that there are almost no burst blisters in the sample exposed continuously to hydrogen plasma whereas the sample exposed cyclically has a significant percentage of burst blisters. Once again, this phenomenon can be explained by the fact that the sample exposed cyclically endures cycles of stress and relaxation which result in a cyclic deformation of the sample. Such cyclic deformation leads to a decrease in ductility of the material in the blistered areas (Valiev et al.,

2002). As the samples are subject again to stress during plasma treatment, blister growth is locally inhibited and existing blisters tend to burst due to their enhanced fragility.

Even though the sample cross-section of samples exposed to different discharge regimes show similar structures, they have differences with respect to their size and depth. Table 3.5 summarizes the statistics related to average cavity depth and radius as inferred by SEM and the optical microscope for the two different cases. During continuous plasma treatment, a large hydrogen flux is constantly imposed to the sample surface, which leads to an enhanced hydrogen diffusion inside the samples. This enables bubble formation very deep in the bulk. As a result, cavities in the material are formed at larger depths in the samples exposed to a continuous plasma treatment than in the case of the cyclic plasma treatment, as shown in Table 3.5.

The average size of cavities is smaller for the samples exposed cyclically to hydrogen plasma. As in the case of blisters, cavity size in the near surface area and in the bulk is influenced by the continuous character of the discharge. Samples exposed to a cyclic plasma treatment experience cycles of stress and relaxation that lead to a local strength increase (*i.e.* hardening) in the blistered area. Therefore, the growth of cavities is quite limited during subsequent blister growth and blister burst is favored.

	Continuous plasma exposure	Cyclic plasma exposure
Average blister depth	12 $\mu\text{m}$	6 $\mu\text{m}$
Average blister radius	8.6 $\mu\text{m}$	4.5 $\mu\text{m}$
Average bubble depth	68 $\mu\text{m}$	21.8 $\mu\text{m}$
Average bubble radius	6.2 $\mu\text{m}$	5.6 $\mu\text{m}$
Average cracks depth	78 $\mu\text{m}$	40.6 $\mu\text{m}$
Average cracks length	41 $\mu\text{m}$	11.6 $\mu\text{m}$

Table 3.5 Values of depth, radius and length of blisters, bubbles and cracks of an Al sample exposed continuously and cyclically to  $\text{H}_2$  plasma with flux of  $1.6 \times 10^{20}$  ions/ $\text{m}^2\text{s}$ , incident ion energy of 320 eV and a fluence of  $4.7 \times 10^{24}$  ions/ $\text{m}^2$

**Conclusion:** This section focused on analyzing the effect the plasma fluence has on blister growth dynamics. Different aluminum samples were exposed to different fluences of hydrogen plasma either continuously or cyclically. Surface and volume modifications were seen in all the analyzed fluences. However, the density and size of the defects depended on the discharge regime. In addition, it seems that blister dynamics is not coupled and intergrain blister kinetics is faster than intragrain blister kinetics.

Another parameter that affects bubble growth kinetics is the surface finish of the material. Therefore, the next section analyzes the results obtained by exposing samples with a different surface finish to hydrogen plasma.

### 3.4 Influence of surface finish

In order to prepare the samples for SEM analysis, they are usually polished to a mirror-like finish with a measured roughness of a few nm. This is performed with the objective of obtaining a scratch-free surface and remove all traces of deformation from each grinding and polishing steps (Bramfitt and Benscoter, 2002). In other words, samples that undergo mechanical polishing and are not polished to a mirror-like finish, have a deformed surface with a larger number of defects.

With the aim of understanding the effect the surface finish of a sample has on blister formation, two different surface roughness were chosen to perform the experiments: one sample polished to a mirror like finish with roughness of a 10 nm and another one only mechanically polished with a roughness of a 1  $\mu\text{m}$ . A SEM micrograph of both samples before plasma exposure is shown in Fig. 3.35. In order to assure they have a similar microstructure these samples were cut from an initial larger sample by using a diamond wire.

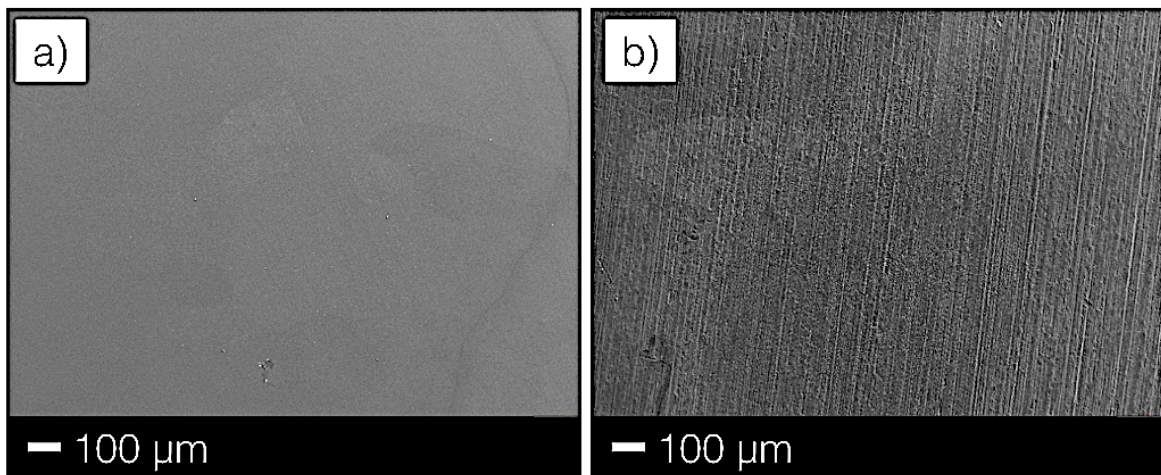


Fig. 3.35 SEM micrographs of an Al sample a) polished to a mirror-like finish and b) mechanically polished

These samples were exposed to hydrogen plasma with the following conditions: an incident ion flux of  $1.6 \times 10^{20}$  ions/m<sup>2</sup>s, pressure of 0.1 Pa, sample temperature of 618 K, fluence of  $2.4 \times 10^{23}$  ions/m<sup>2</sup> and incident ion energy to the biased sample of 320 eV.

Fig. 3.36 a) and b) shows, respectively, the SEM micrographs of the Al with a roughness of 10 nm and 1  $\mu$ m after plasma exposure. It can be clearly observed that blister formation is hindered in the mechanically polished sample. Blister density in the sample polished to a mirror-like finish is of approximately 525 blisters/mm<sup>2</sup> with an average radius of 2.5  $\mu$ m. On the other hand, the sample polished mechanically has a blister density of approximately 175 blisters/mm<sup>2</sup> with an average radius of 5  $\mu$ m. It is important to remark that the mechanically polished surface is deformed up to a depth of 3  $\mu$ m. This leads to an increase in the sample roughness and the defect density in the 3  $\mu$ m layer. Due to this layer, there is a decrease in the diffusion of hydrogen,  $H_2 - v$  complexes and  $H_2 - v$  clusters in the material. Since  $H_2 - v$  clusters are considered as the initial bubble nucleation mechanism, a decrease in their diffusion would lead to a lower concentration of nucleation centers in the sample. As a result, the mechanically polished sample has a lower blister density. Similar results concerning blister suppression were obtained for tungsten exposed to deuterium plasma (Nishijima et al., 2005).

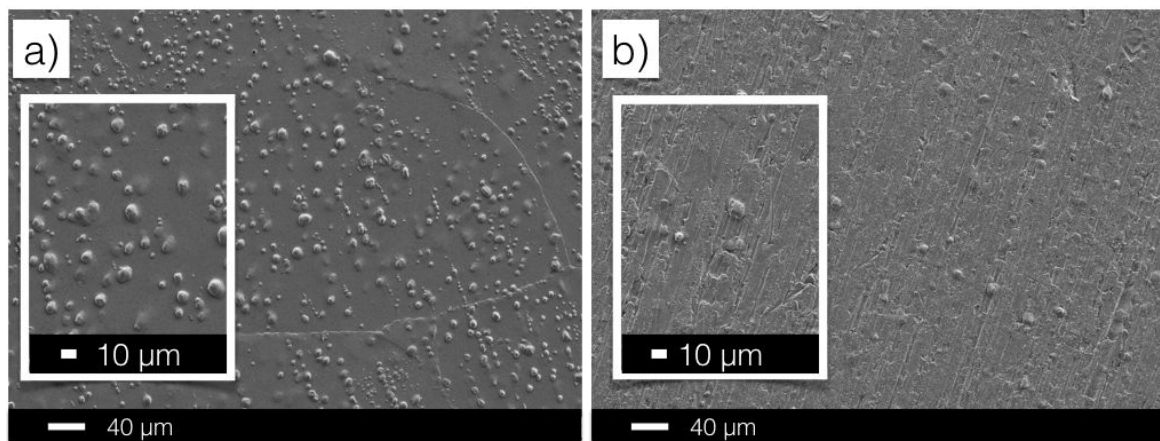


Fig. 3.36 SEM micrographs of Al samples with a roughness of a) 10 nm and b) 1  $\mu$ m exposed to  $H_2$  plasma with flux of  $1.6 \times 10^{20}$  ions/m<sup>2</sup>s, fluence of  $3 \times 10^{23}$  ions/m<sup>2</sup> and ion energy of 320 eV

The experiments performed up to this point were carried out using non-textured aluminum samples. During previous analysis it was determined that intergrain blister kinetics is much faster than intragrain blister kinetics. However, it is important to understand the role grain boundaries play in blister growth kinetics. Therefore, the next section describes the effect

grain boundary misorientation has on blister growth by analyzing textured samples, *i.e.* samples with a grain misorientation of less than  $15^\circ$ .

### 3.5 Influence of grain boundary misorientation

To perform this study two samples were analyzed: a non-textured sample and a  $\langle 100 \rangle$  textured sample. Both samples were exposed to a continuous plasma treatment with the following conditions:  $H_2$  plasma with an incident ion flux of  $1.6 \times 10^{20}$  ions/ $m^2s$ , sample temperature of 618 K, fluence of  $2.8 \times 10^{24}$  ions/ $m^2$  and an incident ion energy to the biased sample of 320 eV.

Fig. 3.37 a) and b) show respectively SEM micrographs of a non-textured and a textured Al sample exposed to  $H_2$  plasma. Several differences may be appreciated between both samples. First, the non-textured sample shows a lower blister density than the textured sample. However, blister size is larger in the non-textured case. This is confirmed by performing statistical measurements: the non-textured sample has a blister density of 160 blisters/ $mm^2$ , with an average radius of  $8 \mu m$  whereas the textured sample has a blister density of 5000 blisters/ $mm^2$  with an average radius of  $2.5 \mu m$ .

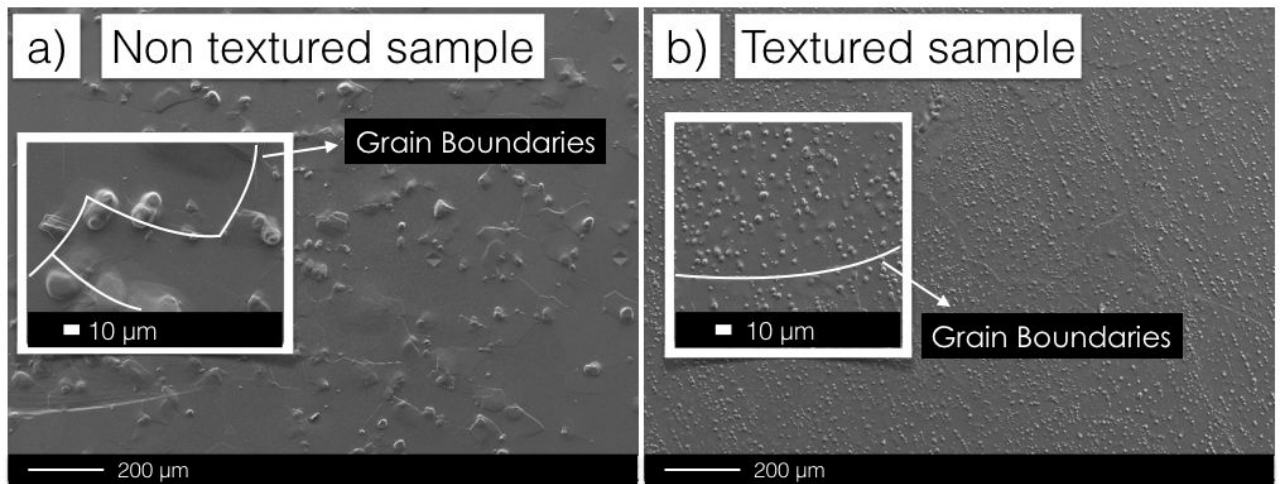


Fig. 3.37 SEM micrographs a) non-textured and b) textured Al samples exposed to  $H_2$  plasma with flux of  $1.6 \times 10^{20}$  ions/ $m^2s$ , fluence of  $2.8 \times 10^{24}$  ions/ $m^2$  and incident ion energy of 320 eV

Another different is the fact that for the analyzed fluences blister growth in the textured samples occurs in the grains (*i.e.* intragrain blisters) whereas blister growth in the non-textured sample occurs mainly at the grain boundaries (*i.e.* intergrain blisters). Grain

boundaries act as traps for hydrogen and since they are not bonded to the maximum number of atoms, it is easier for blisters to grow in this area through loop punching and plastic deformation. However it appears that the misorientation angle between adjacent grain boundaries plays a key role in blister appearance. As the misorientation angle between adjacent grain boundaries decreases, so does the dislocation centers at the grain boundaries. As a result, for smaller misorientation angles it is harder for blisters to grow in this area through loop punching and plastic deformation.

*Conclusion:* The previous sections focused on the analysis of the effect that different plasma parameters have on blister growth dynamics. To perform these studies, different aluminum polycrystalline samples were used. However, in this section it was determined that the material microstructure has an important influence on blister growth dynamics. *It was shown that in non-textured samples blistering kinetics is much faster at the grain boundaries whereas the opposite is observed in textured samples.* Therefore, it is important to analyze single crystal aluminum samples with the aim of further understanding blister growth. Studying single crystals allows analyzing the samples without the effect of grain boundaries. Consequently, phenomena such as loop punching and the effect crystallographic orientation have on blister growth and morphology may be further investigated. Therefore, the next section focuses on the analysis of aluminum single crystals exposed to hydrogen plasma.

### 3.6 Influence of crystallographic orientation

In order to analyze the effect crystallographic orientation has on blister nucleation, experiments were performed on three aluminum single crystal (ASC) samples respectively named  $\langle 100 \rangle$ ,  $\langle 110 \rangle$  and  $\langle 111 \rangle$  ASC. These samples were purchased at Goodfellow and their dimensions are: 1 cm in diameter and a thickness of 2 mm

Fig. 3.38 shows the EBSD measurements for these samples. It can be observed that their surface normal directions (ND's) are parallel to the  $\langle 100 \rangle$ ,  $\langle 110 \rangle$  and  $\langle 111 \rangle$  directions and perpendicular to the  $\{100\}$ ,  $\{110\}$  and  $\{111\}$  planes. An analysis of grain orientation and pole figures of the samples was performed by EBSD. A direct macroscopic reference ( $x_1$ ,  $x_2$ ,  $x_3$ ) is attached on the analyzed face, where  $x_3$  is the normal direction, and  $x_1$  and  $x_2$  are the complementary directions lying on the surface.

Prior to plasma exposure the samples were polished to a mirror-like finish. Afterwards they were exposed to  $H_2$  plasma with an incident ion flux of  $1.6 \times 10^{20}$  ions/m<sup>2</sup>s, sample

temperature of 618 K, fluence of  $2 \times 10^{23}$  ions/m<sup>2</sup> and incident ion energy to the biased sample of 320 eV.

After plasma exposure the samples were analyzed with a confocal optical microscope given that it has a higher height resolution than the SEM. This allows analyzing blister morphology in greater detail.

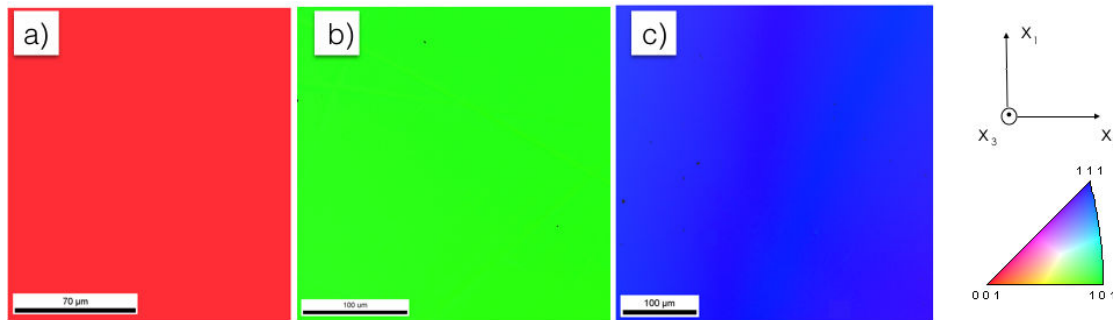


Fig. 3.38 EBSD measurements of the a)  $\langle 100 \rangle$ , b)  $\langle 110 \rangle$  and c)  $\langle 111 \rangle$  ASC samples

### Surface morphology of aluminum single crystals after continuous hydrogen plasma exposure

After hydrogen plasma exposure, the sample surface shows the growth of blisters with a different morphology and size depending on the crystallographic direction of the sample, as shown in Fig. 3.39. The  $\langle 100 \rangle$  ASC shows blisters with a square-like morphology, the  $\langle 110 \rangle$  ASC shows ellipsoidal-shaped blisters and the  $\langle 111 \rangle$  ASC shows mostly triangular blisters. As for blister size, the  $\langle 111 \rangle$  ASC sample shows the smallest blisters with an average radius of  $3.0 \mu\text{m}$  and average height of  $4.2 \mu\text{m}$ , the  $\langle 100 \rangle$  ASC sample shows blisters with an average radius of  $5.3 \mu\text{m}$  and average height of  $8.4 \mu\text{m}$ , and the  $\langle 110 \rangle$  ASC sample shows blisters with an average radius of  $15.2 \mu\text{m}$  and average height of  $47.1 \mu\text{m}$ .

It is worthy to mention that in crystalline materials plastic deformation occurs by the motion of dislocations in a process called slip. Dislocations do not move freely in every crystallographic direction. They usually have a preferred plane, known as slip plane. In this slip plane there are specific directions, known as slip directions, along which dislocation motion is possible. The combined system consisting of the slip plane and the slip direction is referred to as slip system (Calister and Rethwisch, 2010).

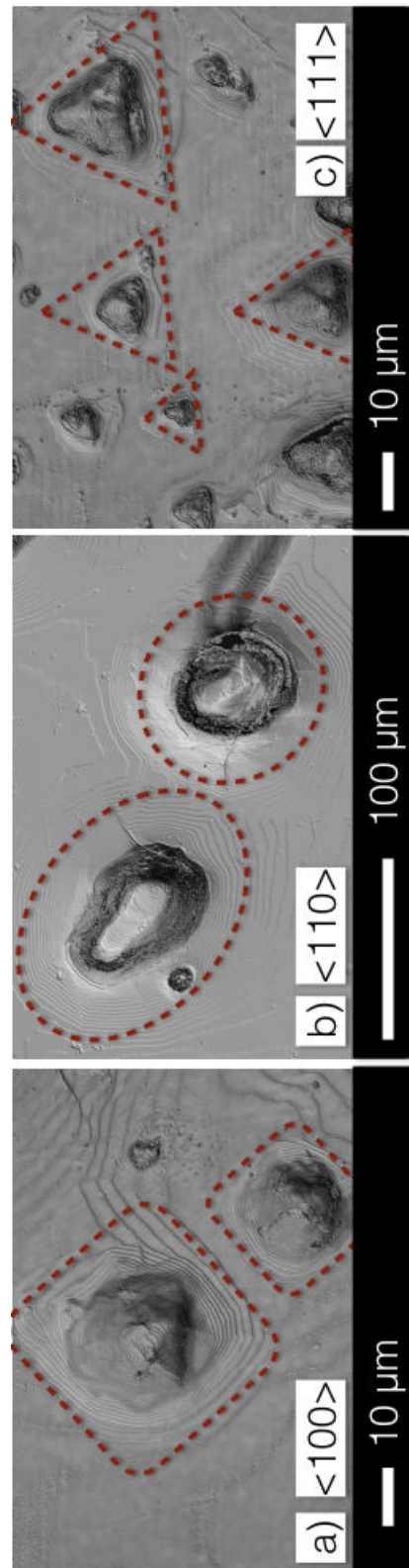


Fig. 3.39 Confocal images of the a) <100>, b) <110> and c) <111> ASC samples exposed continuously to  $H_2$  plasma with an incident ion flux of  $1.6 \times 10^{20}$  ions/ $m^2 \cdot s$ , sample temperature of 618 K, incident ion energy of 320 eV and fluence of  $2 \times 10^{23}$  ions/ $m^2$ . The scale is not the same in every image.

One important aspect to notice in Fig. 3.39 is the fact that blisters have terraces and steps. If the loop punching mechanism is valid, the plastic deformation experienced by blisters during growth should lead to the emergence of slip planes at the sample surface. As a result, blisters should have the terraced structure seen in Fig. 3.39. This terraced structure and hence the obtained blister morphology should be coherent with the slip system of the sample. Blister morphology should correspond to the macroscopic traces of the atomic scale crystallographic planes. In the case of a fcc material, such as aluminum, the slip systems correspond to the slip direction  $\langle 110 \rangle$  and the slip plane  $\{111\}$ . This means that during plastic deformation of a fcc material the activated slip planes are the  $\{111\}$  planes. These planes are able to move in the  $\langle 110 \rangle$  directions belonging to this plane. For each  $\{111\}$  slip plane, there are three  $\langle 110 \rangle$  slip directions (Calister and Rethwisch, 2010).

The next subsections focus on analyzing the blister morphology in three different ASC samples whose surface ND is parallel to the  $\langle 100 \rangle$ ,  $\langle 110 \rangle$  and  $\langle 111 \rangle$  directions. In each case, the corresponding slip plane should be identified.

#### **$\langle 100 \rangle$ Aluminum single crystal**

If the terraces shown in Fig. 3.39 a) correspond to the macroscopic traces of the atomic scale crystallographic planes then the steps seen in the blister shown in Fig. 3.39 a) should be perpendicular to the  $\langle 111 \rangle$  directions shown in the associated stereographic projection for cubic crystals. In order to verify this, the first step consists in tilting the stereographic projection around the  $x_3$  axis so that it coincides with the  $x_1$  and  $x_2$  directions of the analyzed ASC sample. Fig. 3.40 shows the associated stereographic projection for cubic crystals where the blue circles correspond to the  $\langle 111 \rangle$  directions.

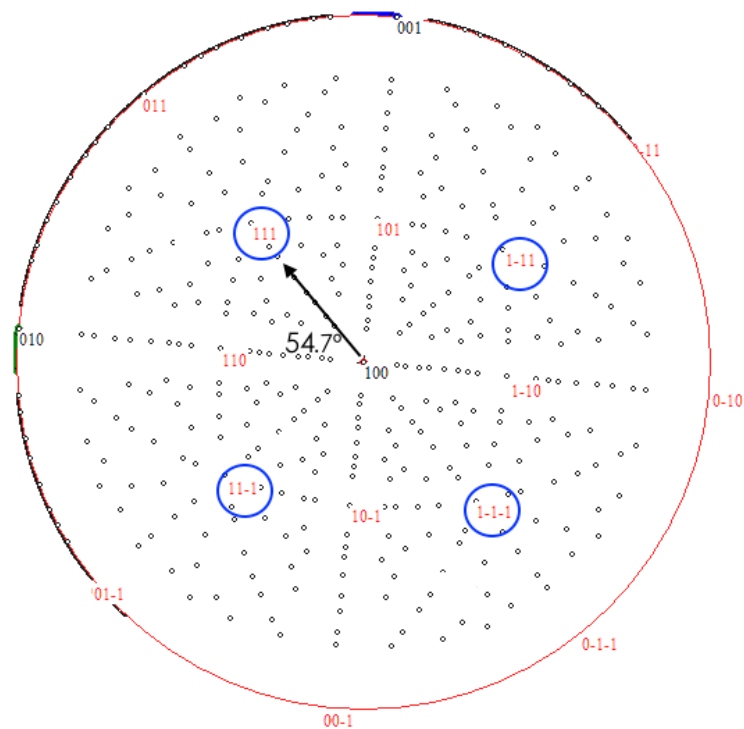


Fig. 3.40  $\{100\}$  stereographic projection for cubic crystals tilted to coincide with the analyzed direction of the ASC sample

The second step consists in determining the angle the surface ND (*i.e.* the direction located in the center of the stereographic projection) forms with the  $\langle 111 \rangle$  direction. This angle may be determined by using an Wulff diagram based software. In this case, the theoretical angle between the  $\langle 100 \rangle$  and the  $\langle 111 \rangle$  directions is  $54.7^\circ$  degrees. Therefore, the angle between the surface ND and the direction normal to the steps should be  $54.7^\circ$ .

The steps are measured with an outline of the blister steps obtained by confocal optical microscopy, as shown in Fig. 3.41. The averaged measured angle between the surface normal and the direction normal to the steps is  $50.5^\circ$ . This value is fairly close to  $54.7^\circ$  and its deviation may be due to uncertainties that may arise during the measurements such as precision of the confocal measurements and accuracy in reproducing the steps oriented exactly towards the  $\langle 111 \rangle$  directions.

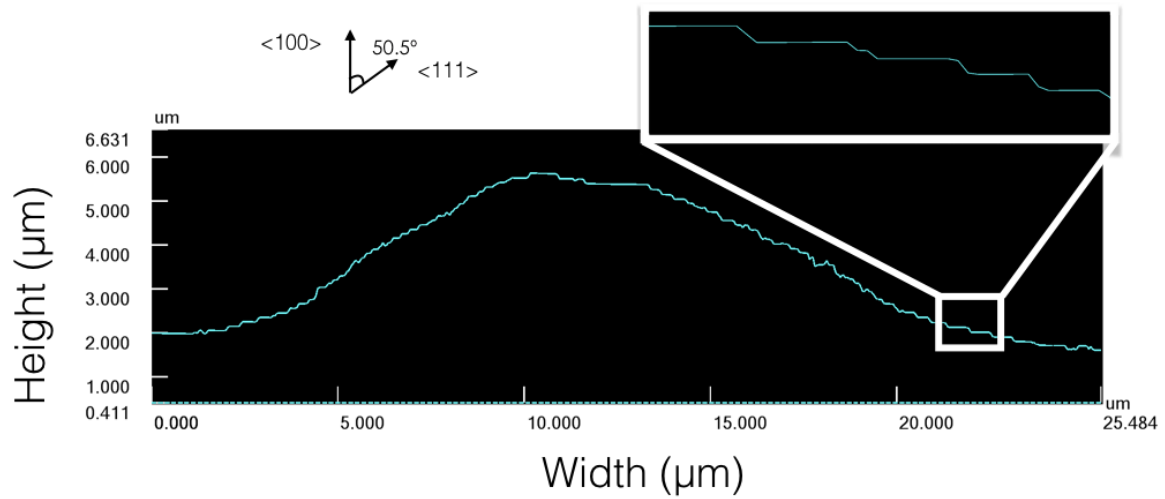


Fig. 3.41 Outline of blister steps of the  $\langle 100 \rangle$  ASC measured by a confocal optical microscope

Fig. 3.42 a) shows two square-like blisters on a  $\langle 100 \rangle$  ASC sample. These blisters have steps with a  $54.7^\circ$  angle inclination with respect to the surface and are perpendicular to the  $\langle 111 \rangle$  direction, as can be seen from the associated stereographic projection shown in Fig. 3.42 b), where only the  $\langle 111 \rangle$  directions that have  $54.7^\circ$  angle with the surface ND ( $\langle 100 \rangle$ ) are reported.

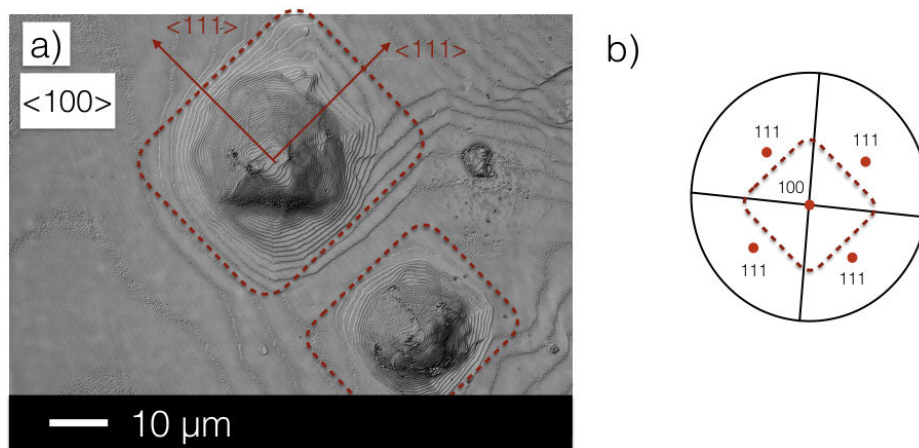


Fig. 3.42 a) Blister morphology on the  $\langle 100 \rangle$  ASC surface and b) the associated stereographic projection containing only the  $\langle 111 \rangle$  directions with a  $54.7^\circ$  degree angle to the surface

An outline of the type of blisters found in a  $\langle 100 \rangle$  ASC is shown in Fig. 3.43.

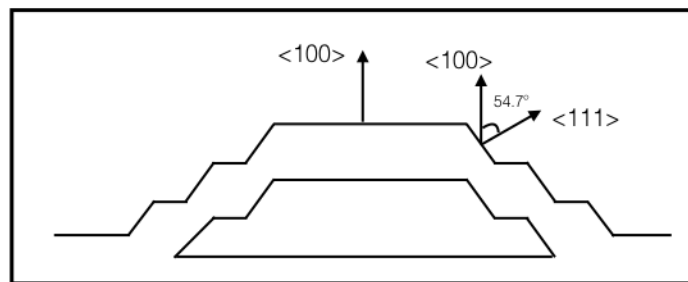


Fig. 3.43 Blister steps with directions having a 54.7° degree angle with the direction normal to the surface

### **<math>\langle 110 \rangle</math> Aluminum single crystal**

In this case, the steps seen in the blister shown in Fig. 3.39 b) should be perpendicular to the  $\langle 111 \rangle$  directions shown in the associated stereographic projection for cubic crystals. In order to verify this, the stereographic projection is tilted around the  $x_3$  axis so that it coincides with  $x_1$  and  $x_2$  directions of the analyzed ASC sample, as shown in Fig. 3.44. It can be appreciated that there are six  $\langle 111 \rangle$  directions. Therefore, the blisters shown in Fig. 3.39 b) should outline an hexagonal shape instead of the spheroidal shape.

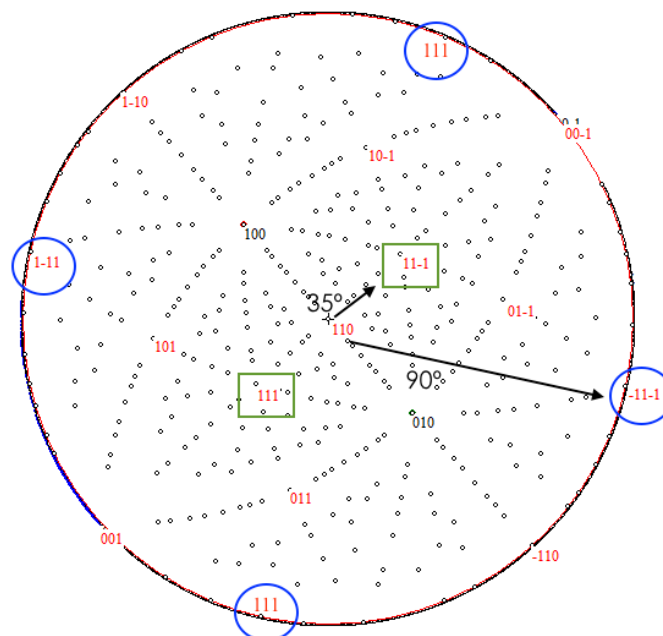


Fig. 3.44  $\{110\}$  stereographic projection for cubic crystals tilted to coincide with the analyzed direction of the ASC sample

The angles between the  $\langle 110 \rangle$  and the  $\langle 111 \rangle$  direction are either  $35^\circ$  or  $90^\circ$  degrees, marked respectively with green squares and blue circles in Fig. 3.44. Therefore, some steps should be perpendicular to the surface whereas other steps should form a  $35^\circ$  angle with the sample surface.

The steps are measured with the outline of the blister steps obtained by confocal optical microscopy. Fig. 3.45 shows an example of the outline obtained for the  $90^\circ$  degree case. The averaged measured angle between the surface normal and the direction normal to the steps is fairly close to  $90^\circ$  for the steps oriented to the  $\langle 111 \rangle$  direction perpendicular to the ND whereas the steps oriented towards the  $[111]$  and  $[1\bar{1}1]$  directions, have an average angle of  $42.3^\circ$ . The latter value is fairly close to theoretical value of  $35^\circ$ .

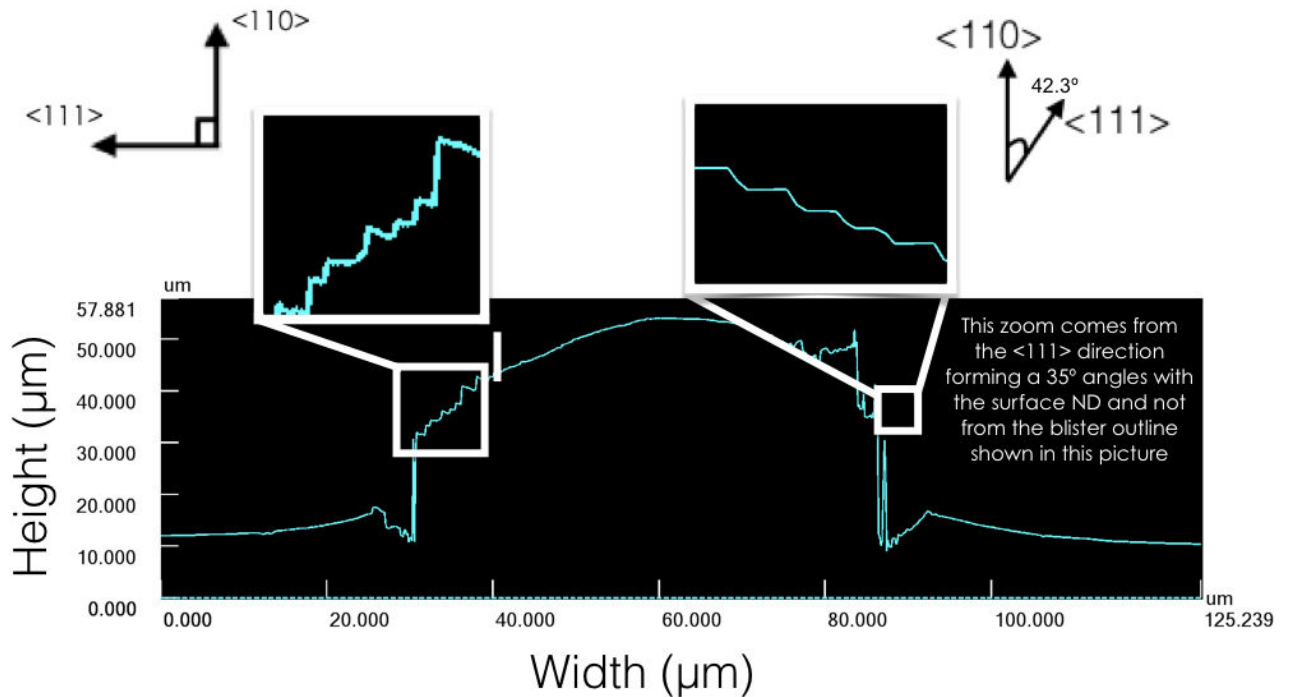


Fig. 3.45 Outline of blister steps of the  $\langle 110 \rangle$  ASC measured by a confocal optical microscope

A blister on a  $\langle 110 \rangle$  ASC surface is shown in Fig. 3.46 a) where the steps can be clearly appreciated. The blister should have a hexagonal shape, however, due to the plastic deformation there is an overlap of slip planes, which makes the hexagonal harder to recognize.

By comparing the blister steps with the associated stereographic projection containing the  $\langle 111 \rangle$  directions seen in Fig. 3.46 b), it is observed how the edges of the terraces are perpendicular to the  $\langle 111 \rangle$  directions.

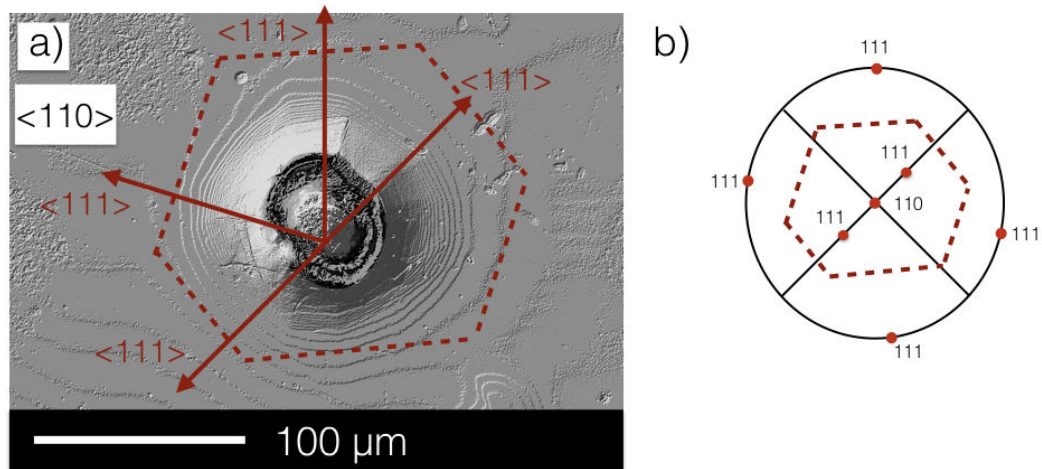


Fig. 3.46 a) Blister morphology on the <110> ASC surface and b) the associated stereographic projection containing only the <111> directions

An outline of the type of blisters observed in an <110> ASC is shown in Fig. 3.43.

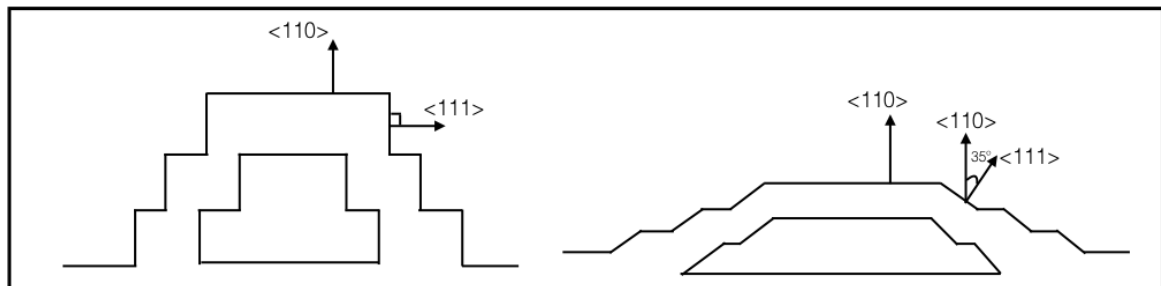


Fig. 3.47 Blister steps with directions a) perpendicular and b) forming a 35° degree angle with the direction normal to the surface

**<111> single crystal aluminum**

In this case, the steps seen in the blister shown in Fig. 3.39 c) should be perpendicular to the <111> directions shown in the associated stereographic projection for cubic crystals. In order to verify this, the stereographic projection is tilted around the  $x_3$  so that it coincides with the  $x_1$  and  $x_2$  directions of the analyzed ASC sample, as shown in Fig. 3.48.

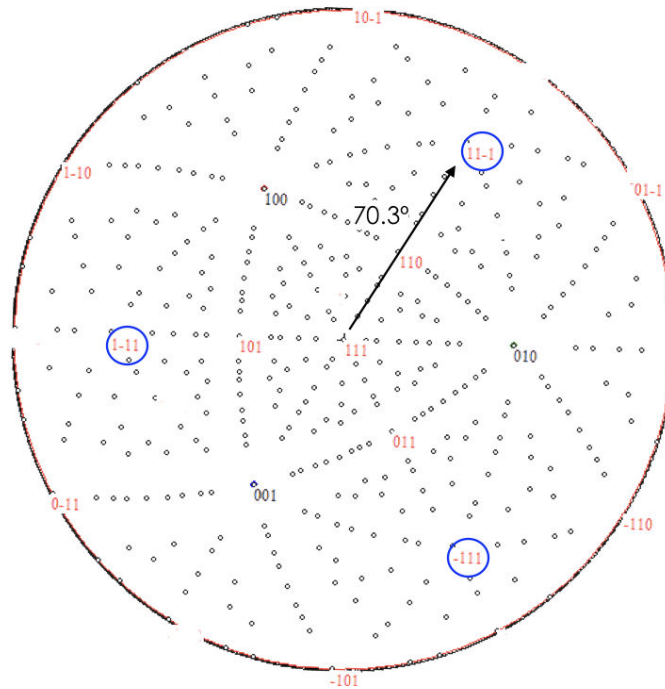


Fig. 3.48 {111} stereographic projection for cubic crystals tilted around the  $x_3$  axis so that it coincides with  $x_1$  and  $x_2$  directions of the ASC sample

The angle between the <111> directions is  $70.3^\circ$  degrees. The <111> directions are marked with blue circles in Fig. 3.48. As a result, the angle between the surface ND and the direction normal to the steps should be  $70.3^\circ$  degrees. The steps are measured with the outline of the blister steps obtained by confocal optical microscopy shown in Fig. 3.49. The averaged measured angle between the surface normal and the direction normal to the steps is  $68.5^\circ$ . This value is fairly close to the theoretical value of  $70.3^\circ$ .

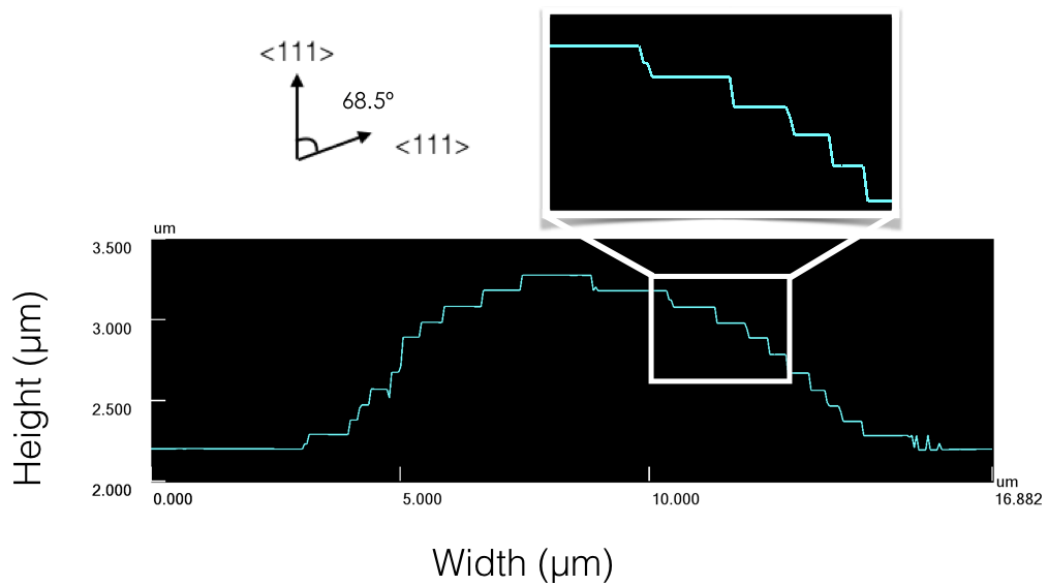


Fig. 3.49 Outline of blister steps on the  $\langle 111 \rangle$  ASC measured by a confocal optical microscope

Fig. 3.50 a) shows several triangular shaped blisters in the  $[111]$  ASC surface with several terraces or steps. By comparing these steps with the stereographic projection shown in Fig. 3.50 b), it is seen that the steps are perpendicular to the  $[111]$  directions. These steps have a surface normal that forms a  $70.3^\circ$  degree angle with the surface ND of the sample. This figure also shows a second family of planes on top on the blister. It is observed that secondary blister growth is also determined by the slip system of the sample and hence their morphology is the same as in primary blister growth.

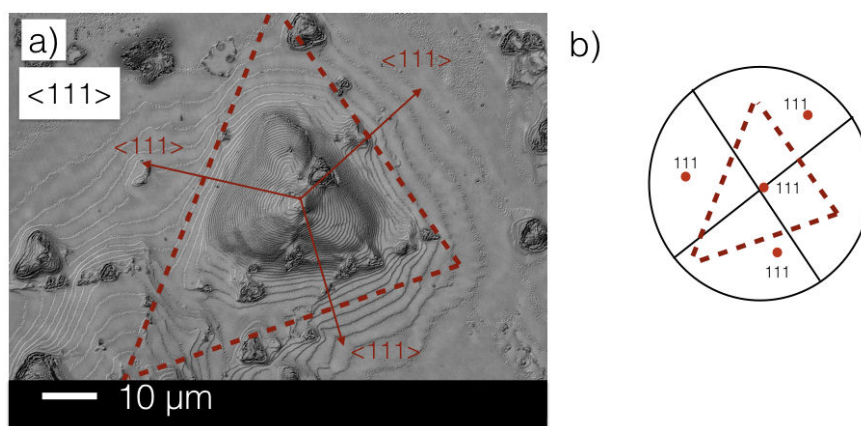


Fig. 3.50 a) Blister morphology on the  $\langle 111 \rangle$  ASC surface and b) the associated stereographic projection containing only the  $\langle 111 \rangle$  directions with a  $70.3^\circ$  degree angle to the surface

An outline of the type of blisters observed in a  $\langle 111 \rangle$  ASC is shown in Fig. 3.51.

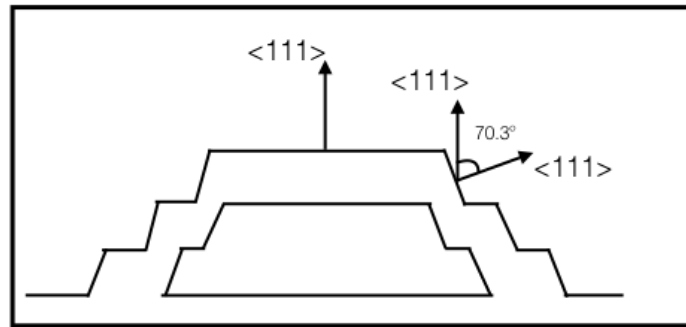


Fig. 3.51 Blister steps with directions having a  $70.3^\circ$  degree angle with the direction normal to the surface

### Discussion

The exposure of ASC to hydrogen plasma showed that blister growth is affected by the crystallographic structure of the material:  $\langle 100 \rangle$  ASC samples shows somewhat square-like shaped blisters,  $\langle 110 \rangle$  ASC samples show mostly spheroidal blisters and finally  $\langle 111 \rangle$  ASC samples show mainly triangular-shaped blisters. It was determined that spheroidal blisters in the  $\langle 110 \rangle$  ASC should actually have an hexagonal shape, however there is a slip plane overlapping due to the plastic deformation experienced by the material.

Plastic deformation in crystalline materials occurs by the motion of dislocations in the slip system of the material. Therefore, the plastic deformation during blistering leads to the emergence of slip planes at the sample surface. The step or terraced structure observed in blisters is a consequence of the punching of dislocation loops during the growth process. These steps correspond to the slip plane of the material and their ND forms a well-defined angle with the surface ND. This angle may be estimated using the corresponding stereographic projection for each sample. The experiments performed with aluminum single crystals confirm that the angles are consistent with the values given by the stereographic projection. Thus confirming that blister growth is due to loop punching and that in fact, blister steps correspond to the macroscopic traces of the atomic scale crystallographic planes of the sample.

A sketch of the different blisters found in the ASC samples is shown in Fig. 3.52. This figure shows that under stress, plastic deformation occurs in the directions determined by the slip planes. As a result, in the case of a  $90^\circ$  degree angle between the slip direction and the sample surface, growth perpendicularly to the surface is enhanced. Therefore, blisters in the  $\langle 110 \rangle$  sample are able to grow higher whereas blisters in the  $\langle 111 \rangle$  sample reach the smallest heights.

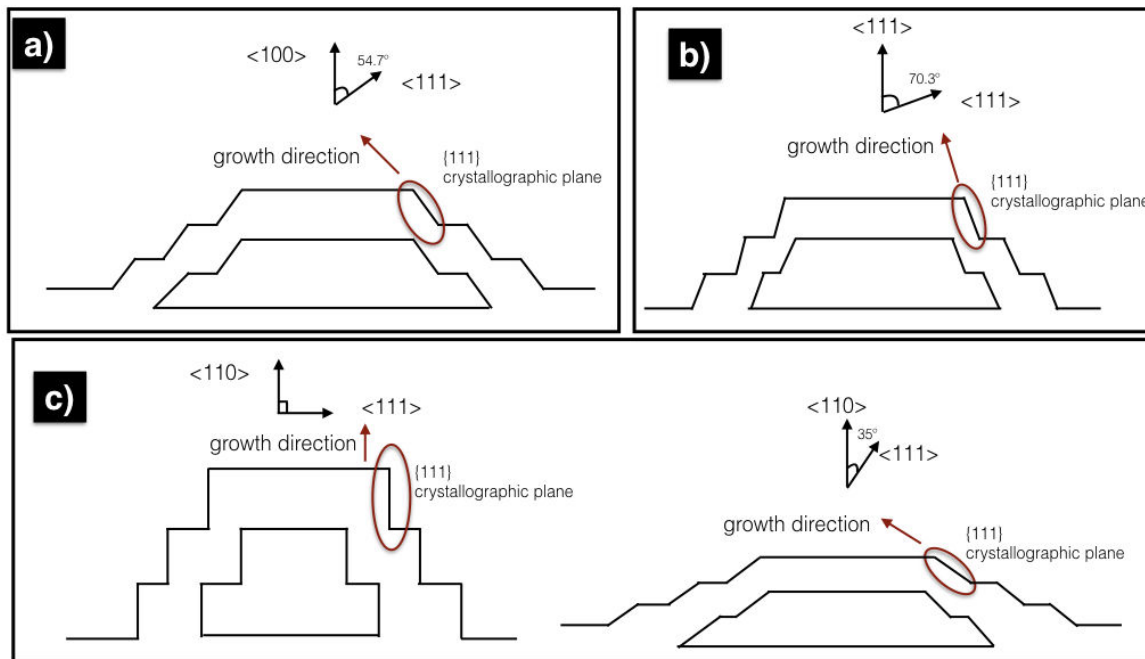


Fig. 3.52 Blister steps with directions having a)  $54.7^\circ$  b)  $74.3^\circ$  c)  $90^\circ$  and  $35^\circ$  degree angle with the direction normal to the surface

### 3.7 Summary and discussion

Aluminum samples exposed to hydrogen plasma are subject to high energy ion implantation. Once implanted in the material the ions diffuse and agglomerate in defects such as vacancies, cracks or grain boundaries. At high fluences, as is the case in our experimental conditions, along with the low hydrogen solubility in aluminum (Serra et al., 1998), hydrogen concentration is able to reach high levels in the near surface regions. Hydrogen trapped in the material is able to agglomerate into  $H_2 - v$  clusters, which marks the initial nucleation mechanism for bubbles.

Experimental studies on  $H_2 - v$  clusters is not a trivial task. In literature, detection of  $H_2 - v$  clusters is performed mainly under cryogenic conditions. During this work,  $H_2 - v$  clusters were not detected, however their existence was inferred by analyzing the effect incident ion energy has on blister formation. At high enough incident ion energies, defects may be induced in the material. In addition the presence of hydrogen in the material decreases the formation energy for vacancy creation. This presence of hydrogen promotes the formation of hydrogen-vacancy clusters. The combination of these two phenomena contribute to blister nucleation. There is a cooperation effect between an increased defect production and  $H_2 - v$  clustering. As a result, **implantation with incident ion energies high enough to create**

**defects allows the nucleation of a higher blister density in the surface of the material.** This was clearly observed in the experiments performed in the parametric study of incident ion energy.

Once a  $H_2 - v$  cluster is formed, it has to increase in size to become a bubble. In order for the cluster to grow, the work done by the hydrogen pressure must not exceed the total binding energy of an existing cluster to a newly created vacancy. The critical pressure under which bubbles can grow in the material is determined by equation (1.16),  $P = \frac{E_t}{\Delta V}$ . For hydrogen in aluminum these values are the following: the formation energy of a vacancy is 0.67 eV (Wolverton et al., 2004), the binding energy of a single vacancy to a vacancy cluster is  $-0.5$  eV (Gavini et al., 2007) and the volume of a vacancy is  $6.89 \times 10^{-30} m^3$  (Calister and Rethwisch, 2010). The calculated critical pressure under which a bubble may form in aluminum is 3.95 GPa. However, this value was calculated under the condition that vacancies are at thermodynamic equilibrium at a certain temperature. If vacancies are superabundant, the critical hydrogen pressure decreases drastically given that clusters may grow due to the binding energy. This can be observed by comparing the binding energy of a single vacancy to a vacancy cluster in aluminum ( $-0.5$  eV) with the binding energy of hydrogen atoms to a cluster in aluminum ( $-5$  eV) (Kawamura et al., 2001).

Once an  $H_2 - v$  cluster is formed and stabilized, it is able to increase in size due to the high internal pressures. The high pressure forces are able to punch interstitial loops out of one side of the bubble and plastically deform the material (Behrish, 1983; Calister and Rethwisch, 2010).

Experiments performed on aluminum single crystals show that blisters have a step or terraced structure. This terraced structure is a consequence of the punching of dislocation loops during the growth process. **The blister steps correspond to the macroscopic traces of the atomic scale slip plane of the material and their ND forms a well-defined angle with the surface ND.** These angles are consistent with the values given by the stereographic projection.

In addition to loop punching, other bubble growth mechanisms were observed during the experiments on polycrystalline samples. Samples exposed to different fluences showed signs of blister coalescence. This occurs when bubbles grow and coalesce into larger ones. This phenomenon leads to a decrease in blister density and an increase in the average blister radius. Therefore, **once a cluster is formed and stabilized it can grow by loop punching and blister coalescence.**

Blister growth dynamics is a complex phenomenon that is influenced by a large number of parameters. For our conditions, **the threshold fluence for blistering in single crystals is lower than for polycrystalline samples.** In addition, blister growth in aluminum is

influenced by the sample microstructure. **In non-textured samples, intragrain blister nucleation kinetics occurred much slower than intergrain blister kinetics.** Also, these intergrain blisters were mainly located at the grain boundaries with a misorientation angle higher than  $15^\circ$  degrees. On the other hand, **textured samples showed the opposite behavior. Intragrain blister kinetics occurred much faster than intergrain blister kinetics.** For the analyzed conditions, blisters in textured samples appeared only within the grains.

An important effect observed during the analysis of blister growth dynamics is the occurrence of secondary blister nucleation. This effect corresponds to the formation of small blisters on top of larger ones. It may also correspond to the formation of large blisters underneath smaller ones.

Blister growth dynamics seems to be affected by the discharge regime. **Blister density and size in samples subject to continuous plasma treatment is determined to be governed by three processes: blister appearance, blister growth by loop punching and blister coalescence.** Blister appearance and coalescence affect both blister density and size whereas blister growth by loop punching affects only blister size.

Blister density in samples subject to cyclic plasma treatment increases linearly with increasing fluence whereas their radius remains fairly constant. This is due to the fact that during cyclic plasma treatments blister appearance dominates over blister growth. Furthermore, the samples that followed a continuous plasma treatment are subject to fairly constant stress that induces continuous deformation. As a result, blisters are able to grow continuously during the plasma treatment. On the other hand, samples exposed to a cyclic plasma treatment, experience cycles of stress and relaxation that results in *quasi* cyclic deformation of blisters during plasma exposure. Such cyclic deformation leads to a local hardening and decrease in ductility. Consequently, blister growth during subsequent hydrogen exposure remains quite limited. During subsequent plasma treatments, new blisters tend to nucleate in non-blistered areas and existing blisters tend to burst. It is worthy to notice that secondary blister nucleation was not observed in the samples exposed cyclically to plasma. All the above mentioned phenomena results in a larger blister density but smaller in size in the sample exposed cyclically to plasma when compared to the one exposed continuously.

Cross-sections analysis shows that there are **three different cavities in the bulk: blisters, bubbles and cracks.** Blisters are bubbles or cavities that are able to deform the surface material and hence are located closer to the surface. Bubbles are circular cavities that do not deform the material surface. Cracks are very far from the surface and usually located in grain boundaries. These cavities may be divided by two scale surface deformation in the material. Large scale surface deformation, such as cracks, result in large area, limited height deformations. The ultimate stage of this deformation is grain swelling in the surface of the

material. The second type is the small scale surface deformations located in the vicinity of the surface. This results in limited area deformations with larger heights.

Cavities in the cross-section differ in depth and size in the samples that underwent different plasma treatments. During continuous plasma treatment, a large hydrogen flux is constantly imposed to the sample surface, which leads to an enhanced hydrogen transport inside the samples. This enables bubble formation very deep in the bulk. As a result, **cavities in the material are located at larger depths in the samples exposed to a continuous plasma treatment than the ones exposed to a cyclic one.**



## Chapter 4

# Plasma surface interaction between hydrogen plasma and tungsten

Particle bombardment in ITER leads to the net erosion of the tungsten divertor and formation of surface structures such as fuzz and blisters, which may enhance the uptake of tritium (Philipps, 2011). Therefore tungsten has been widely studied in the fusion community under a large number of conditions. Studies have shown that blisters grow in a temperature range that depends on the plasma fluence and incident ion energy. Tungsten samples exposed to deuterium plasma with a flux of  $10^{21}$  ions/m<sup>2</sup>s, fluence of  $10^{24}$  ions/m<sup>2</sup> and ion energy of 200 eV show blister formation in the temperature range between 300 K and 700 K (Alimov et al., 2009, 2008). Similar experiments performed at higher fluxes and fluences (flux of  $10^{24}$  ions/m<sup>2</sup>s, a fluence ranging from  $8 \times 10^{25}$  to  $1.1 \times 10^{26}$  ions/m<sup>2</sup> and an incident ion energy of 38 eV) show blister formation for sample temperatures as high as 1273 K (Jia et al., 2015).

Recent studies show that crystallographic orientation affects blister growth and morphology. It was observed that  $\langle 111 \rangle$  grains show an enhanced blister nucleation whereas nucleation is hindered for the  $\langle 100 \rangle$  grains (Jia et al., 2015, 2016). This result was attributed to the fact that the slip direction in tungsten is the  $\langle 111 \rangle$  direction. Therefore, when the implanted surface is perpendicular to the slip direction, surface deformation is likely to be perpendicular to the sample surface. This means that the obtained blisters are likely to have a high aspect ratio (Jia et al., 2016). These results show a discrepancy with analysis performed at LSPM in which the preferred direction for blistering was determined to be the  $\langle 100 \rangle$  direction (Ouaras et al., 2016). The main difference between these two experiments is that the former were obtained with annealed samples. During annealing, the number of dislocations is reduced and stress is relieved from the sample. If they do not follow this

process, defects may interfere with the measurements and results. The presence of these defects might explain the discrepancy found in the experimental results.

Several questions arise that require a more thorough study on how tungsten surface modifications are affected by crystallographic orientation:

- How is blister growth affected by crystallographic structure? For example, is there a preferential direction for blistering?
- What is the difference between blistering in a fcc and a bcc material?
- What is the role grain boundaries play in blister formation?

In order to answer these questions, analyses were first performed with polycrystalline samples. This was carried out with the aim of determining the role of grain boundaries and microstructure have on blister formation. A second step in the experiments consisted in using single crystal tungsten samples. The use of single crystals helps in the study of specific crystallographic orientations without the effect of grain boundaries.

Results obtained with tungsten single crystals complement the results obtained with aluminum single crystals. This give a global picture of how blister growth and morphology are affected by crystallographic structure in cubic crystal systems. This sets the basic principles for understanding more complex hexagonal systems, such as beryllium.

To reach these objectives the present chapter is organized as follows:

- Section 4.1 describes the procedure followed to obtain textured polycrystalline tungsten samples and the results obtained with these samples when submitted to hydrogen plasma.
- Section 4.2 focuses on experiments performed with single crystal tungsten samples. Special attention is given to the effect crystallographic structure has on blister morphology.
- Section 4.3 summarizes the different results and gives the main conclusions that may be drawn from this chapter.

## 4.1 Tungsten polycrystalline textured samples

The use of textured samples offers an effective way to analyze the effect crystallographic direction and grain boundaries have on blister formation and morphology in a polycrystalline sample. To perform the experiments, the first option was to buy textured polycrystalline samples from an external supplier. However, it is not easy to buy good-quality textured samples. Therefore other methods to obtain them had to be considered. A practical way of obtaining textured samples with different orientations is by taking a sample textured in a certain direction and cutting it in a specific way. This cutting procedure is performed by analyzing its stereographic projection to obtain the angles and cutting directions. The next subsection describes the different steps followed to obtain textured tungsten samples.

### 4.1.1 Production of textured polycrystalline samples

Fig. 4.1 shows the pole figure for the initial tungsten sample used in this work. It may be observed that there is an intensity pole located close to the center of the pole figure  $\{200\}$  in Fig. 4.1 b). Usually, an intensity pole located in the center of a pole figure indicates a strong texture in the direction corresponding to that pole figure. In this case, this intensity pole could indicate a strong  $\langle 100 \rangle \{100\}$  texture.

To confirm the presence of this texture, we compared the position of the other intensity poles using the stereographic projection shown in Fig. 2.12. From this image, the position of the  $\langle 200 \rangle$  direction may be inferred and are shown as red crosses in Fig. 4.1.

Fig. 4.1 a) shows two intensity poles that coincide with  $\langle 100 \rangle \{100\}$  texture and 5 intensity poles that have a slight deviation from this texture. Fig. 4.1 b) shows that 3 intensity poles coincide with the  $\langle 100 \rangle \{100\}$  texture whereas one intensity pole is far from this texture. Finally, Fig. 4.1 c) shows that all of the poles have a slight deviation with the  $\langle 100 \rangle \{100\}$  texture. The slight deviation from the texture means that the sample is almost textured with most grains having a ND oriented towards the  $\langle 100 \rangle$  crystallographic direction.

There is another texture present in the sample. Using Labotex software (K.Pawlik and P.Ozga, 1999), the other texture was determined to be  $\{11 \ 3 \ 2\} \langle -4 \ 14 \ 1 \rangle$ . The angle between the  $\{200\}$  and  $\{11 \ 3 \ 2\}$  planes is  $18^\circ$ . This angle is small, which means that the plane of the other texture present in the sample has a slight deviation with respect to the  $\{200\}$  plane. As a result, this sample may be considered as having a low intensity

{200}<200> texture.

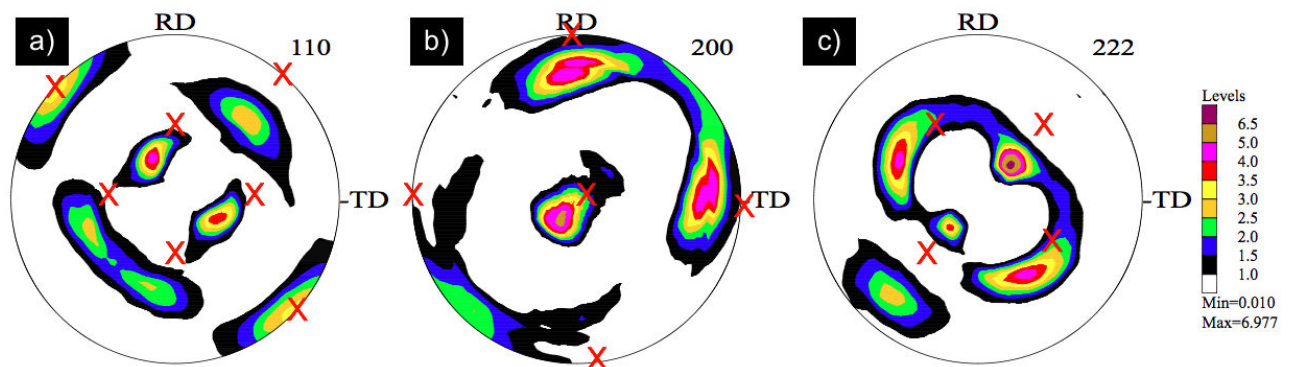


Fig. 4.1 Pole figures obtained for a W sample with the directions corresponding to a {200}<200> texture

Since the initial tungsten sample has a <100> texture, it may be used to obtain samples with surfaces whose ND are oriented close to the <111> and <110> crystallographic directions. To do this, the sample has to be cut in a specific directions and with a certain angle  $\alpha$  determined by the pole figures.

To show the cutting procedures that should end up with textured crystal faces, let's have a look on the geometrical transformation that links two planes with different orientations. All the planes in the crystal are represented by a set of plane normals radiating from a single point within the crystal. By assuming that there is an imaginary sphere around this point, the intensity poles correspond to a 2D projection of the intersection of the plane normals with this sphere (Cullity and Stock, 2014; Engler and Randle, 2010). This procedure, along with its corresponding pole figure, is depicted in Fig. 4.2.

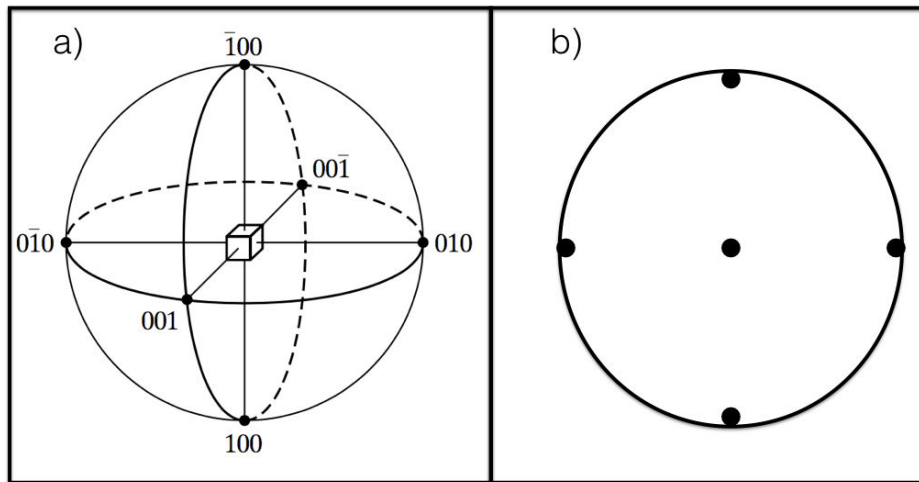


Fig. 4.2 a)  $\{100\}$  poles of a cubic crystal (Cullity and Stock, 2014) b) Example of a pole figure for a  $\{100\}$  cubic crystal

The angle  $\alpha$  between two crystallographic planes (or directions in cubic crystal symmetry) is equal to the angle between their normals, as shown in Fig. 4.3 (Cullity and Stock, 2014). This angle may be measured by using stereographic projections. In fact, the angle  $\alpha$  between two crystallographic planes corresponds to the angles between two intensity poles in their corresponding pole figures.

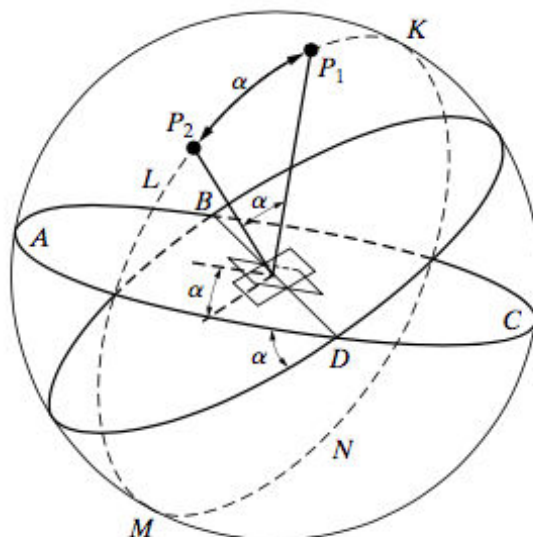


Fig. 4.3 Angle between two crystallographic planes (Cullity and Stock, 2014)

It is important to keep in mind that pole figures are statistical measurements which reflect a distribution of orientations in the sample. The colors found in each intensity pole correspond to the intensity of a given direction, with purple being the highest intensity and black the smallest intensity. In order to cut the samples, these intensity poles will be used as reference to obtain the desired orientations. The objective is to cut the sample in order to obtain the highest possible intensity pole.

Also, it is useful to remember that during X-Ray measurements, macroscopic references to the crystal coordinate system are attached to the samples. These references correspond to the RD (Rolling or longitudinal Direction) and the TD (Transverse Direction) shown in Fig. 2.11.

### **Production procedure for a $\langle 110 \rangle$ textured surface**

The first step to obtain this sample is to determine the angle  $\alpha$  between the  $\{200\}$  and the  $\{110\}$  plane. To do this we must consider the  $\{110\}$  pole figure shown in Fig. 4.4 a). In this pole figure, the angle  $\alpha$  between the macroscopic RD (where one of the  $\langle 100 \rangle$  poles is located) and an intensity pole oriented towards  $\langle 110 \rangle$  is  $47^\circ$ . This means that angle  $\alpha$  between the  $\{200\}$  and the  $\{110\}$  plane is  $47^\circ$ . Therefore, the sample has to be cut at a  $47^\circ$  degree angle from the macroscopic RD, as shown in Fig. 4.4 a).

The fact that this intensity pole is located in the circumference of the pole figure is also an important factor. This means that the  $\{110\}$  plane is perpendicular to the  $\langle 110 \rangle$  direction and hence the cut should be performed perpendicularly. In other words, the sample has to be cut by performing a single rotation of  $47^\circ$  from the macroscopic RD, around the  $\{200\}$  axis, as shown in in. 4.4 b).

Even though there are two other intensity poles with a higher intensity, they would not be used since they required cutting the sample with a vertical inclination. The chosen intensity pole is easily accessible just by cutting the sample perpendicularly and close to the border. In order to obtain a textured sample by using the other intensity poles, the sample has to be cut with specific angles and closer to the center. The sample resulting from such procedure would be too small and thus not useful for obtaining the remaining crystallographic orientation.

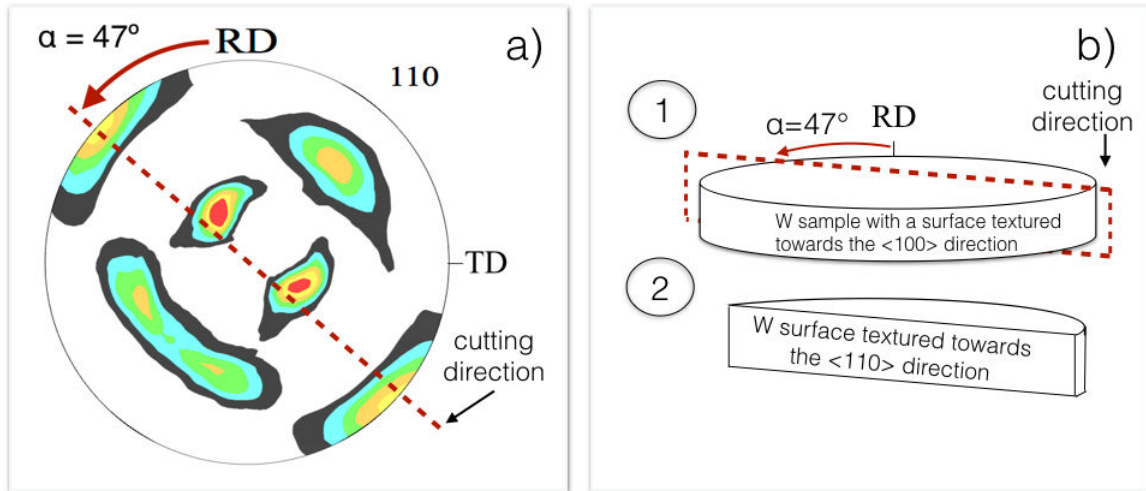


Fig. 4.4 a)  $\{110\}$  Pole figure and cutting angle with the rolling direction b) Sketch of the steps followed to cut the W sample to obtain a textured surface with the ND oriented towards the  $\langle 110 \rangle$  direction

### Production procedure for a $\langle 111 \rangle$ textured surface

The  $\langle 111 \rangle$  surface is more difficult to obtain, since that the intensity poles are not located in the circumference of the pole figure. This means that this plane must be obtained by performing two rotations instead of one. In the  $\{111\}$  pole figure, the angle  $\alpha$  between the RD macroscopic direction and the direction oriented towards  $\langle 110 \rangle$  is  $42^\circ$ , as shown in Fig. 4.5 a). This means that the sample has to be cut at a  $42^\circ$  degree angle from the macroscopic RD, as shown in Fig. 4.5 a).

It may be observed that the chosen intensity pole is not located in the circumference of the pole figure, as in the previous case. As a matter of fact, the angle between the circumference and the local maximum of intensity is  $14^\circ$ . This means that the sample has to be cut, in first instance, at  $42^\circ$  from the RD direction perpendicularly to the initial analyzed surface, as shown in Fig. 4.5 b). Then the obtained cross section must be cut with an inclination angle of  $14^\circ$ . This cut should be performed by taking into account the "B" and "A" sides of the sample, as shown in Fig. 4.5 b).

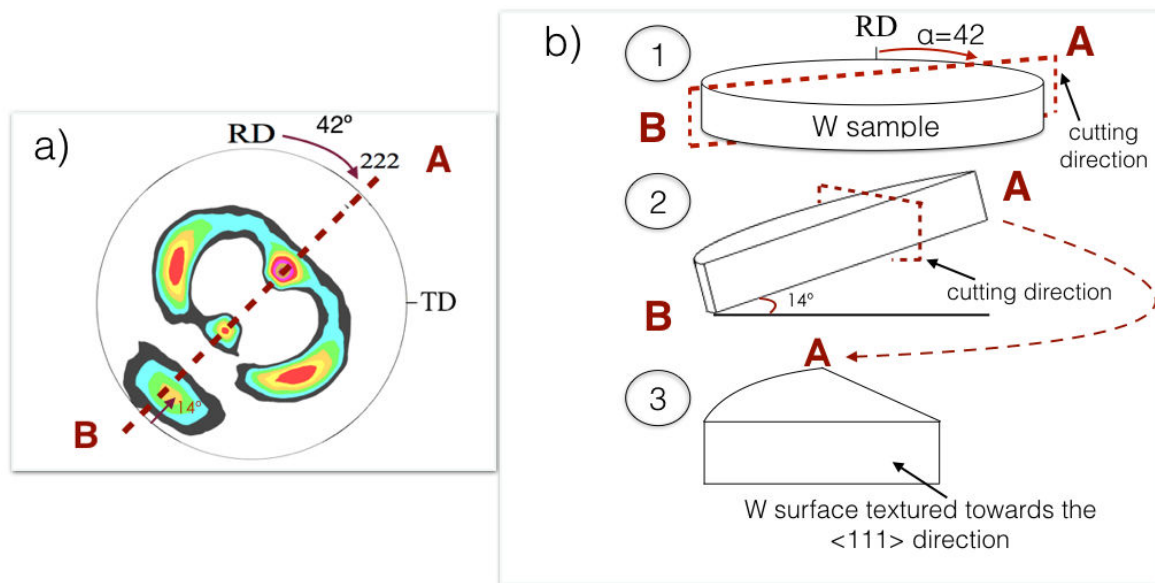


Fig. 4.5 a)  $\{111\}$  Pole figure and cutting angles in order to obtain grains whose ND is oriented towards the  $\langle 111 \rangle$  direction b) Sketch of the steps followed to cut the W sample to obtain a textured surface with the ND oriented towards the  $\langle 111 \rangle$  direction

#### 4.1.2 Experimental procedure

Fig. 4.6 a), b) and c) show the EBSD measurements of the samples whose surface normal directions (ND's) are oriented, respectively, to the  $\langle 100 \rangle$ ,  $\langle 110 \rangle$  and  $\langle 111 \rangle$  directions and their surface parallel to the  $\{100\}$ ,  $\{110\}$  and  $\{111\}$  directions. These samples are respectively named  $\langle 100 \rangle$ ,  $\langle 110 \rangle$  and  $\langle 111 \rangle$ .

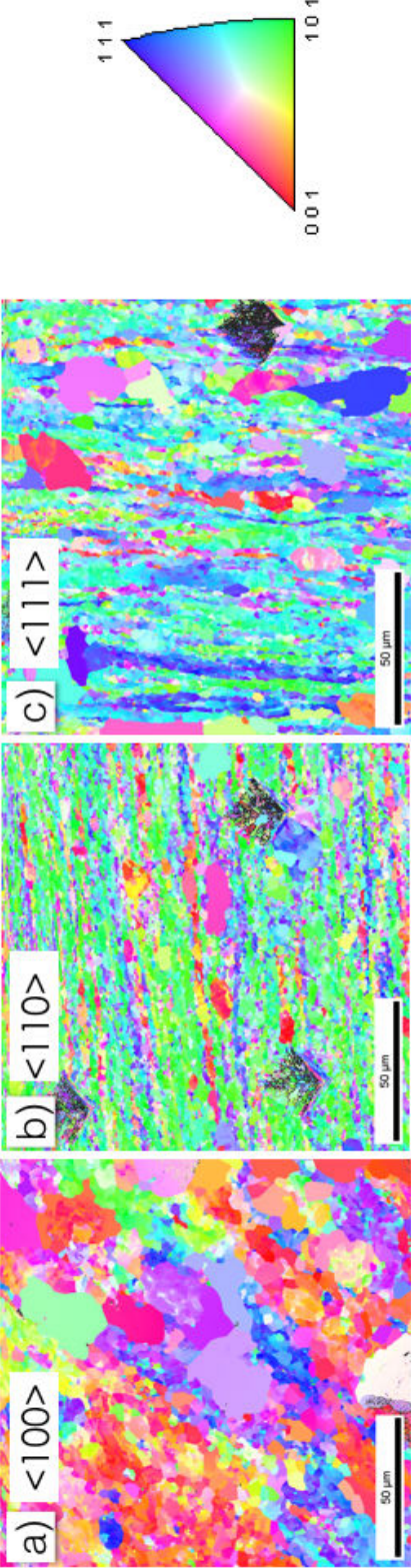


Fig. 4.6 EBSD measurements for the a)  $\langle 100 \rangle$  b)  $\langle 110 \rangle$  and c)  $\langle 111 \rangle$  tungsten samples

In the  $\langle 100 \rangle$  sample the grains may be qualitatively divided into two groups: small grains of approximately  $3 \mu\text{m}$  in size and larger grains of approximately  $35 \mu\text{m}$ . It is appreciated, in Fig. 4.6 a), that there are some  $\langle 110 \rangle$  grains (green colored grains, in the upper portion of the image). In addition, there is a large portion of  $\langle 111 \rangle$  grains (blue and purple grains). Both of the  $\langle 110 \rangle$  and  $\langle 111 \rangle$  groups are present as either small or large grains. Nevertheless, the  $\langle 100 \rangle$  sample shows almost equiaxed grains and overall  $\langle 100 \rangle$  texture.

The  $\langle 110 \rangle$  sample has smaller grains with sizes of approximately  $2 \mu\text{m}$ , as observed in Fig. 4.6 b). It may be observed that the sample effectively shows an overall  $\langle 110 \rangle$  texture and is mainly observed along horizontal lines. There are also some much more equiaxed  $\langle 100 \rangle$  and  $\langle 111 \rangle$  grains, with sizes of approximately  $10 \mu\text{m}$ . Finally, the  $\langle 111 \rangle$  sample also has small grains with sizes of approximately  $2 \mu\text{m}$ , as seen in Fig. 4.6 c). This sample shows more complex structures and shows highly anisotropic grains. There are some  $\langle 100 \rangle$  and  $\langle 111 \rangle$  grains that have a size of approximately  $2 \mu\text{m}$  that are observed along vertical lines. It also presents some  $\langle 100 \rangle$  and  $\langle 111 \rangle$  grains of  $25 \mu\text{m}$  in length. The texture deviation observed in the  $\langle 111 \rangle$  sample is probably due to the complexity of the cutting process, which requires 2 different rotations to be performed.

Performing analysis on these samples is useful to the understanding of the influence the grain boundaries, grain size and crystallographic orientation may have on surface morphology in tungsten samples. To perform the experiments the samples were annealed during 1 h at 1373 K. This temperature is below the recommended temperature for recrystallization (Manhard, 2011). However, the maximum achievable temperature in our vacuum furnace is 1373 K. Therefore, tungsten samples were annealed at 1373 K for 1 hour and a partial recrystallization was observed. Prior to annealing, grains were not visible whereas after annealing grains were discernible as seen in the EBSD measurements in Fig. 4.6. After the heat treatment, the samples were exposed to the following experimental conditions: incident ion flux of  $1.6 \times 10^{20}$  ions/ $\text{m}^2\text{s}$ , sample temperature of 600 K, fluence of  $3.3 \times 10^{24}$  ions/ $\text{m}^2$  and incident ion energy of 220 eV.

### 4.1.3 Experimental results

Different phenomena can be distinguished on the surface of the tungsten sample after plasma exposure: swelling and blisters with different sizes and heights, as seen in Fig. 4.7. Swelling corresponds to the upward deformation large areas that comprises several grains (*i.e.* multigrain phenomenon). Swelling has an average size of approximately 10 to  $15 \mu\text{m}$  and height between  $2.5$  and  $6.7 \mu\text{m}$ . Unlike blisters, material swelling does not have a defined boundary. Therefore, this phenomenon was assumed to be different from blisters.

Fig. 4.7 also shows several blisters with different sizes and heights. Smaller blisters with sizes of less than  $1\ \mu\text{m}$  and height of  $0.03\ \mu\text{m}$  are observed in the surface. In addition, there are larger blisters with sizes between  $5$  and  $10\ \mu\text{m}$  that have either a low or a high dome. Low dome blisters have an average height of  $0.05\ \mu\text{m}$  whereas high dome blisters have an average height of  $0.8\ \mu\text{m}$ . Shu *et al.* (Shu *et al.*, 2007) determined that these high dome blisters occur due to an enhanced ductility in the material due to the accumulation of  $H_2 - v$  clusters. These  $H_2 - v$  clusters diffuse into the bulk and agglomerate, resulting in the diffusion of tungsten atoms to the surface, which in turn generates blisters. They named this phenomena *deuterium-induced superplasticity* (Shu, 2008). In fact, several authors (Condon and Schober, 1993; Ren *et al.*, 2008) agree that voids may form in materials due to clustering of hydrogen or  $H_2 - v$  complexes.

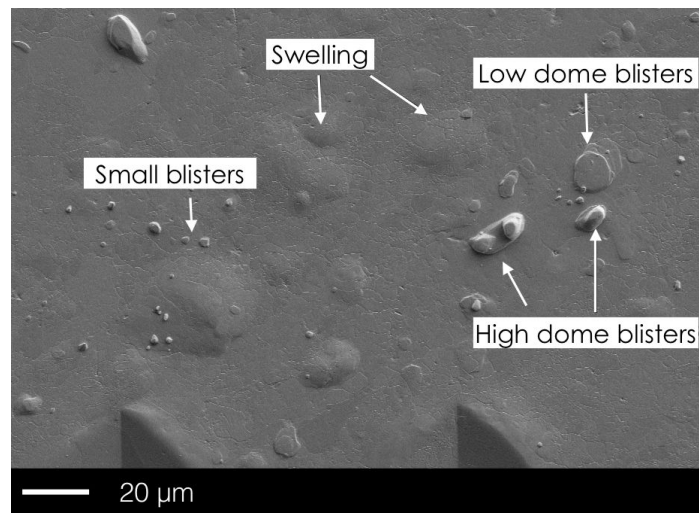


Fig. 4.7 SEM micrographs showing the phenomena occurring at the surface of a tungsten sample after exposure to hydrogen plasma with a flux of  $1.6 \times 10^{20}$  ions/ $\text{m}^2\text{s}$ , fluence of  $3.3 \times 10^{24}$  ions/ $\text{m}^2$  and incident ion energy of  $220\ \text{eV}$

In order to perform a thorough analysis of the samples, the SEM micrographs of each sample are analyzed separately. Fig. 4.8 a) shows the EBSD measurements of the  $\langle 100 \rangle$  sample and Fig. 4.8 b) shows the SEM micrograph of the corresponding surface area after hydrogen plasma exposure. It may be observed that the high and low dome blisters occur mainly in the  $\langle 111 \rangle$  grains, as depicted by the black dashed rectangle. On the other hand, multigrain swelling in the sample is indicated by black dashed circles. By comparing the SEM micrograph with the EBSD image, it may be observed that swelling appears on several grains regardless of their orientation. Finally, small blisters were observed in the  $\langle 111 \rangle$  grains (blue and purple grains) and grains with an orientation between the  $\langle 111 \rangle$  and the  $\langle 100 \rangle$  direction (pink grains).

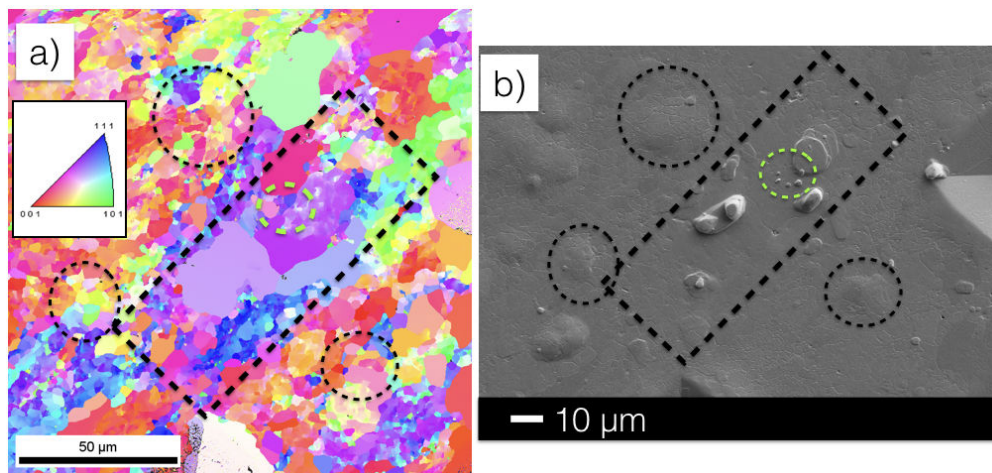


Fig. 4.8 a) EBSD of the  $\langle 100 \rangle$  surface prior to plasma exposure and b) SEM micrograph of the  $\langle 100 \rangle$  surface after exposure to hydrogen plasma with a flux of  $1.6 \times 10^{20}$  ions/ $m^2s$ , fluence of  $3.3 \times 10^{24}$  ions/ $m^2$  and incident ion energy of 220 eV. The areas enclosed by geometrical forms correspond to the same surface in the EBSD image and the SEM micrograph

Fig. 4.9 a) shows the EBSD measurements of the  $\langle 110 \rangle$  sample and Fig. 4.9 b) shows the SEM micrograph of the corresponding surface area after hydrogen plasma exposure. It may be observed that this sample has a very low blister density. Two small blisters are observed in the surface: one on a  $\langle 100 \rangle$  grain (black dashed square) and the other one on a  $\langle 110 \rangle$  grain (black dashed circle). The two alterations seen in the upper portion in Fig. 4.9 b) correspond to contamination, hence they were not analyzed with the EBSD image.

Fig. 4.10 a) shows the EBSD measurements of the  $\langle 111 \rangle$  sample and Fig. 4.10 b) shows the SEM micrograph of the corresponding surface area after hydrogen plasma exposure. It may be observed that the grain density is low. The largest blister, of approximately  $7 \mu m$  occurs on a large grain, with an orientation between the  $\langle 100 \rangle$  and  $\langle 110 \rangle$  direction (black dashed circle). Two smaller blisters are observed in a  $\langle 100 \rangle$  and  $\langle 110 \rangle$  grains, as indicated by the black dashed rectangle. Finally, the black dashed triangle indicates the presence of a low dome blister with a size of approximately  $2 \mu m$  on a  $\langle 100 \rangle$  grain.

One important aspect to notice is that blisters occur within the grains *i.e.* *intragrain blisters*. An example of one of these intragrain blister is shown in Fig. 4.11. High and low dome intragrain blisters have sizes in the range of  $5\text{-}10 \mu m$ . This size is actually larger than the size of most of the grains in the sample, which can be as small as  $2 \mu m$ . Small blisters on the other hand, have a size of less than  $1 \mu m$  and appear on grains with an size range of  $2\text{-}4 \mu m$ . It may be concluded, that under the analyzed conditions surface modifications occur within the grains and hence their size is determined by the grain size.

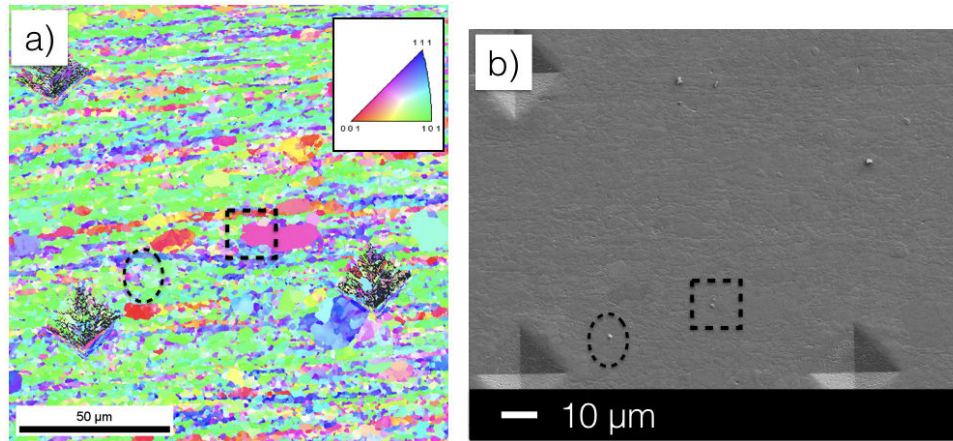


Fig. 4.9 a) EBSD of the  $\langle 110 \rangle$  surface prior to plasma exposure and b) SEM micrograph of the  $\langle 110 \rangle$  surface after exposure to hydrogen plasma with a flux of  $1.6 \times 10^{20}$  ions/m<sup>2</sup>s, fluence of  $3.3 \times 10^{24}$  ions/m<sup>2</sup> and incident ion energy of 220 eV. The areas enclosed by geometrical forms correspond to the same surface area in the EBSD image and the SEM micrograph

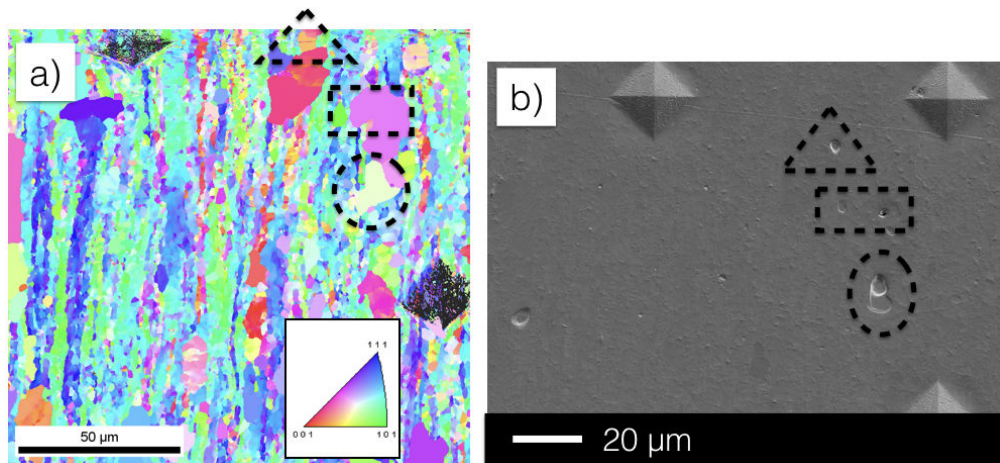


Fig. 4.10 a) EBSD of the  $\langle 111 \rangle$  surface prior to plasma exposure and b) SEM micrograph of the  $\langle 111 \rangle$  surface after exposure to hydrogen plasma with a flux of  $1.6 \times 10^{20}$  ions/m<sup>2</sup>s, fluence of  $3.3 \times 10^{24}$  ions/m<sup>2</sup> and incident ion energy of 220 eV. The areas enclosed by geometrical forms correspond to the same surface area in the EBSD image and the SEM micrograph

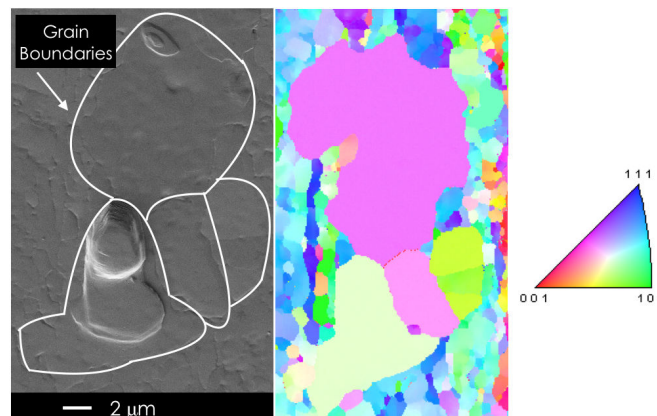


Fig. 4.11 SEM micrograph and EBSD measurement of an intragrain blister on a tungsten sample after exposure to hydrogen plasma with a flux of  $1.6 \times 10^{20}$  ions/m<sup>2</sup>s, fluence of  $3.3 \times 10^{24}$  ions/m<sup>2</sup> and incident ion energy of 220 eV

The analysis of the tungsten samples after hydrogen plasma exposure showed several surface modifications that occur on tungsten samples after hydrogen plasma exposure: small blisters, high and low dome blisters and multigrain swelling. However, paradoxical results were found regarding a preferred crystallographic orientation for blister growth. It was observed that the  $\langle 100 \rangle$  sample has the highest blister density but most of the blisters were observed on the  $\langle 111 \rangle$  grains. On the other hand, the  $\langle 110 \rangle$  sample has the lowest blister density and most of the blisters were observed on the  $\langle 100 \rangle$  and  $\langle 111 \rangle$  grains. Similarly, the blisters on the  $\langle 111 \rangle$  sample were observed on the  $\langle 100 \rangle$  and  $\langle 110 \rangle$  grains. This may imply that other factors, different from crystallographic orientation, play a role in blistering. One factor that influences blistering is the number of defects in the sample. It is possible that the grains in the sample that do not correspond to the sample texture are subject to stresses and have an increased defect density than the textured grains. As a result, these grains may have higher nucleation centers that allow a higher blister density to form. A more thorough analysis on the influence crystallographic structure has on blister growth dynamics may be performed by analyzing single crystals. Therefore, the next section is devoted to the analysis of tungsten single crystals after hydrogen plasma exposure.

## 4.2 Tungsten single crystals

In order to analyze the effect crystallographic orientations on blister morphology, experiments were performed on three tungsten single crystal samples (WSC) respectively named  $\langle 100 \rangle$ ,  $\langle 110 \rangle$  and  $\langle 111 \rangle$  WSC. These samples were purchased at Goodfellow and their dimension are: 0.5-2 cm in diameter and a thickness of 2 mm. As shown in Fig. 4.12, their ND's

are perpendicular to the  $\{100\}$ ,  $\{110\}$  and  $\{111\}$  planes and parallel to the  $\langle 100 \rangle$ ,  $\langle 110 \rangle$  and  $\langle 111 \rangle$  directions. An analysis of grain orientation and pole figures of the samples was performed by EBSD. A direct macroscopic reference ( $x_1$ ,  $x_2$ ,  $x_3$ ) is attached on the analyzed face, where  $x_3$  is the normal direction, and  $x_1$  and  $x_2$  are the complementary directions lying on the surface.

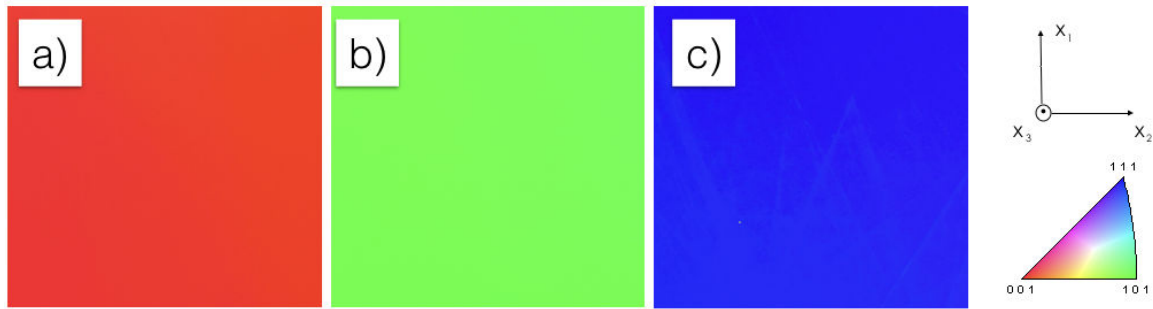


Fig. 4.12 EBSD measurements of the a)  $\langle 100 \rangle$ , b)  $\langle 110 \rangle$  and c)  $\langle 111 \rangle$  WSC samples

It is worthy to mention that in order to perform an analysis on blister morphology, the slip system of the material has to be taken into account. During plastic deformation, the slip system determines the motion of dislocations. In tungsten there are two slip systems: the  $\{110\}$  slip plane associated with the  $\langle 111 \rangle$  slip direction and the  $\{211\}$  slip plane associated with the  $\langle 111 \rangle$  slip direction (Calister and Rethwisch, 2010). Studies have shown that the activation of these slip systems is a temperature dependent process (Buzi, 2015). At temperatures below 670 K, dislocations move in the  $\{110\}$  slip plane along the  $\langle 111 \rangle$  slip direction whereas at higher temperature they move in the  $\{211\}$  slip plane along the  $\langle 111 \rangle$  slip direction.

In this study, the objective is to analyze the influence the  $\{110\}\langle 111 \rangle$  slip system has on blister morphology. To do this, the samples were kept at 300 K during plasma exposure. Therefore, after polishing to a mirror-like finish the samples were exposed to  $H_2$  plasma with an incident ion flux of  $1.6 \times 10^{20}$  ions/m<sup>2</sup>s, sample temperature of 300 K, fluence of  $1.7 \times 10^{25}$  ions/m<sup>2</sup> and incident ion energy to the biased sample of 220 eV.

After plasma exposure, the samples are analyzed by SEM instead of the confocal optical microscope. The latter was used for the analysis of aluminum single crystals because it has a higher height resolution than SEM and is an useful tool to measure the angles formed by the terraces formed in blisters during plastic deformation. However, for our conditions, blister size in WSC is of a few hundred nanometers. It is not possible to obtain high resolution images for such small sizes by confocal optical microscopy. Therefore, the analyses were performed using SEM, which allows obtaining clear images for blisters in this size range.

### Surface morphology of tungsten single crystals after hydrogen plasma exposure

Fig. 4.13 shows the SEM micrographs of the tungsten single crystal samples after hydrogen plasma exposure. After exposure, the surface shows the growth of blisters and their density depends on the crystallographic orientation of the sample. The  $\langle 111 \rangle$  WSC has the highest blister density with a value of approximately 15 000 blisters/mm<sup>2</sup>. On the other hand, the  $\langle 110 \rangle$  and  $\langle 100 \rangle$  WSC have the lowest density with approximately 48 blisters/mm<sup>2</sup> and 55 blisters/mm<sup>2</sup>, respectively. Blister size, however, is larger on the  $\langle 110 \rangle$  WSC, with sizes ranging between 200 nm and 1.7  $\mu\text{m}$ . The smallest blisters are observed in the  $\langle 111 \rangle$  and  $\langle 100 \rangle$  WSC with a blister size that ranges between 200 nm and 700 nm. Surface coverage in the samples is very low with a value of 0.01%, 0.02% and 0.3% for the  $\langle 100 \rangle$ ,  $\langle 110 \rangle$  and  $\langle 111 \rangle$  WSC, respectively. This shows that even though blister density for the  $\langle 111 \rangle$  WSC exceed the blister density for the  $\langle 100 \rangle$  and  $\langle 110 \rangle$  WSC by almost three orders of magnitude, the difference between the surface coverage is less than one order of magnitude. This means that the  $\langle 111 \rangle$  WSC has a higher density of smaller blisters and the  $\langle 100 \rangle$  and  $\langle 110 \rangle$  WSC have a lower density of larger blisters.

It may be concluded the  $\langle 111 \rangle$  tungsten surface is more prone to blistering due to the higher density. Several studies have already reported that blister nucleation in tungsten is enhanced in the  $\langle 111 \rangle$  direction. Miyamoto *et al.* attribute this phenomenon to the fact that the  $\langle 111 \rangle$  direction is the most open direction in the bcc lattice and hence ions are able to penetrate deeper in regions with this orientation (Miyamoto *et al.*, 2009). However, in this study a low incident ion energy of approximately 55 eV was used. At these low incident ion energies, ions have only a small implantation range of 1 nm (Ziegler *et al.*, 2010). Based on the ion penetration depth value, this assumption is therefore questionable.

On the other hand, Jia *et al.* attributed this phenomenon to the gas pressure inside the cavities that are able to deform more efficiently the surface perpendicular to the  $\langle 111 \rangle$  direction (Jia *et al.*, 2015, 2016). This assumption correlates with the observations made in Chapter 3, in which it was determined that under stress, plastic deformation occurs in the slip directions along the slip planes. As a result, bubble growth was observed to be enhanced when the surface ND is perpendicular to the slip plane. This means that bubbles may still nucleate in surfaces whose ND is not perpendicular to the slip plane. However since plastic deformation occurs with a certain angle with respect to the surface ND, bubble height is usually smaller.

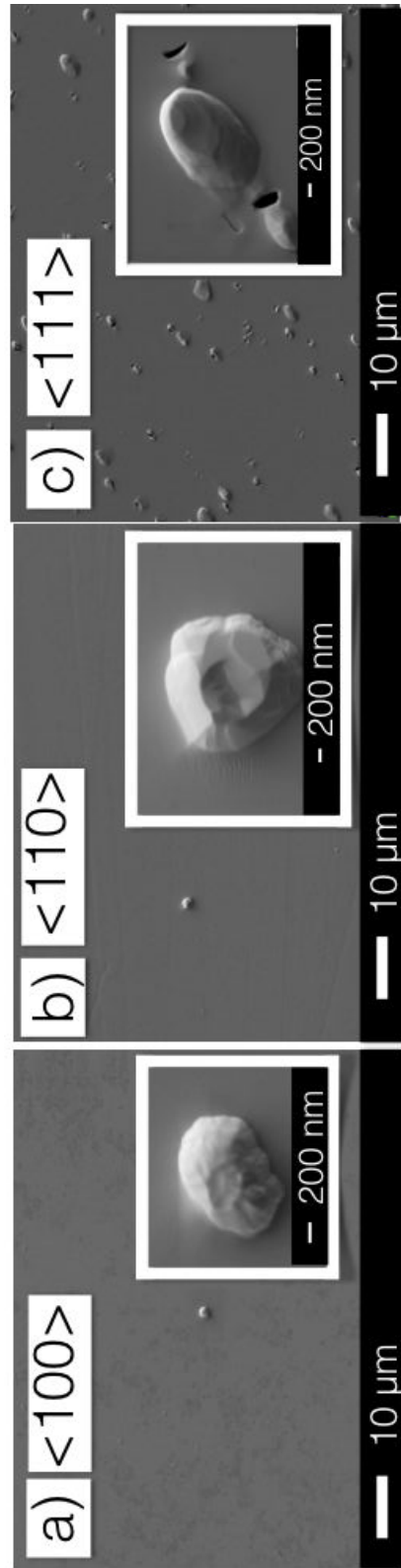


Fig. 4.13 SEM micrographs of the a)  $\langle 100 \rangle$ , b)  $\langle 110 \rangle$  and c)  $\langle 111 \rangle$  WSC samples exposed continuously to  $H_2$  plasma with an incident ion flux of  $1.6 \times 10^{20}$  ions/m<sup>2</sup>-s, sample temperature of 300 K, incident ion energy of 220 eV and fluence of  $2 \times 10^{23}$  ions/m<sup>2</sup>.

Another aspect to notice in Fig. 4.13 is the irregular blister morphology in each sample. According to previous studies and the results obtained in Chapter 3, this morphology should be consistent with the crystallographic direction of the sample (Jia et al., 2016; Lindig et al., 2009). In order to perform the analysis on blister morphology, each case is studied separately.

### <100> Tungsten single crystal

The first step when analyzing the effect the crystallographic orientation has on blister morphology consists in analyzing the stereographic projection associated to the sample. To do this, the stereographic projection has to be tilted around the  $x_3$  axis so that it coincides with the  $x_1$  and  $x_2$  directions of the analyzed WSC sample. Fig. 4.14 shows the associated stereographic projection for cubic crystals where the blue circles correspond to the <110> directions.

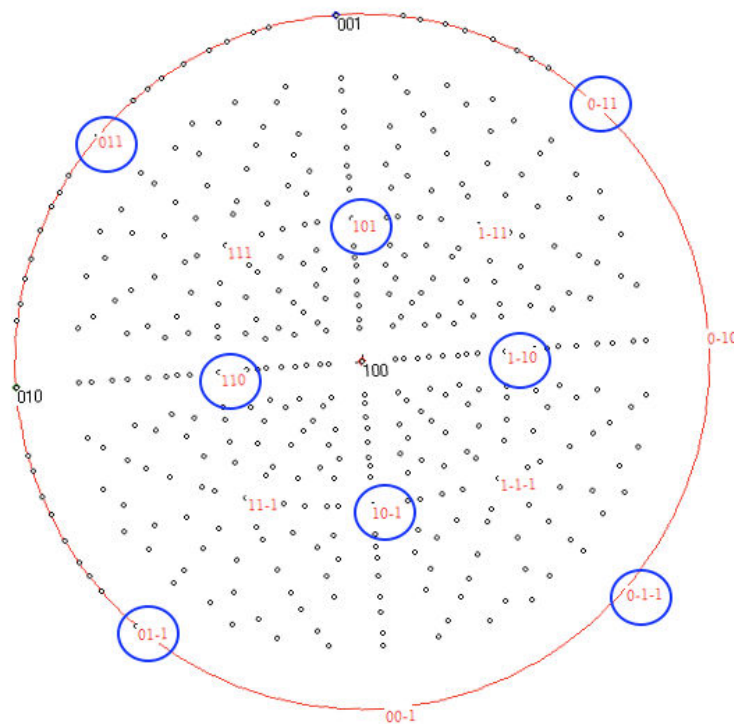


Fig. 4.14  $\{100\}$  stereographic projection for cubic crystals tilted to coincide with the analyzed direction of the WSC sample

Fig. 4.15 a) shows two blisters on the  $\langle 100 \rangle$  ASC sample. It may be observed that these blisters have an approximate octagonal shape. Following the same procedure as in Chapter 3, these blisters should have steps with a ND parallel to the  $\langle 110 \rangle$  direction. The steps ND should form a  $90^\circ$  angle and a  $45^\circ$  angle with the surface ND, as determined by the stereographic projection. The directions forming a  $90^\circ$  angle are located in the circumference of the stereographic projection. Since it is not possible to measure these angles, the blister octagonal shape is compared with its associated stereographic projection in Fig. 4.14. It may be observed that the sides of the octagon correspond to the  $\langle 110 \rangle$  directions, as shown in Fig. 4.15.

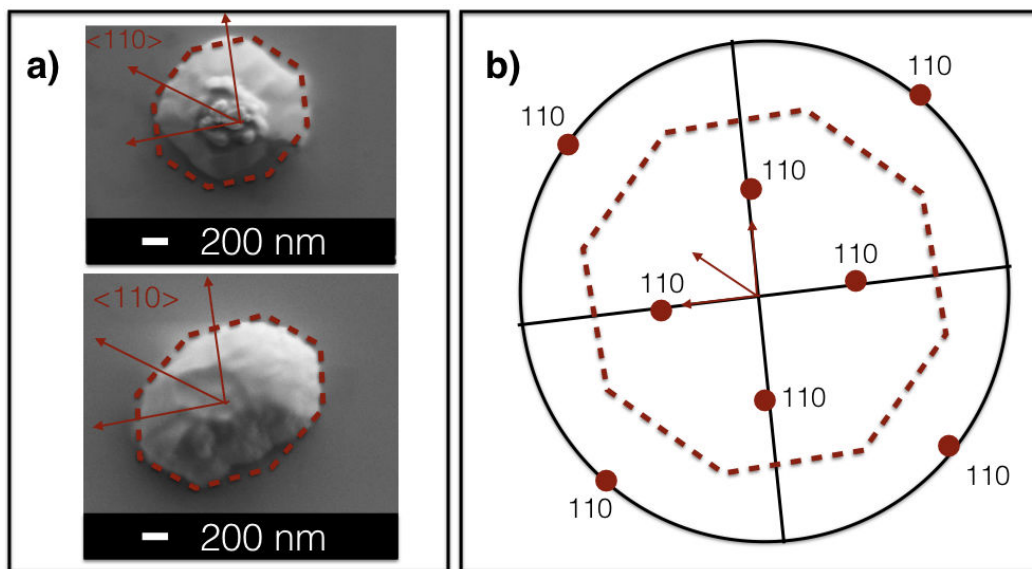


Fig. 4.15 a) Blister morphology on the  $\langle 100 \rangle$  WSC surface and b) the associated stereographic projection containing only the  $\langle 110 \rangle$  directions

### $\langle 110 \rangle$ Tungsten single crystal

As in the previous case, to analyze blister morphology in  $\langle 110 \rangle$  WSC, the stereographic projection has to be tilted around the  $x_3$  axis so that it coincides with the  $x_1$  and  $x_2$  directions of the analyzed WSC sample. Fig. 4.16 shows the associated stereographic projection for cubic crystals where the blue circles correspond to the  $\langle 110 \rangle$  directions.

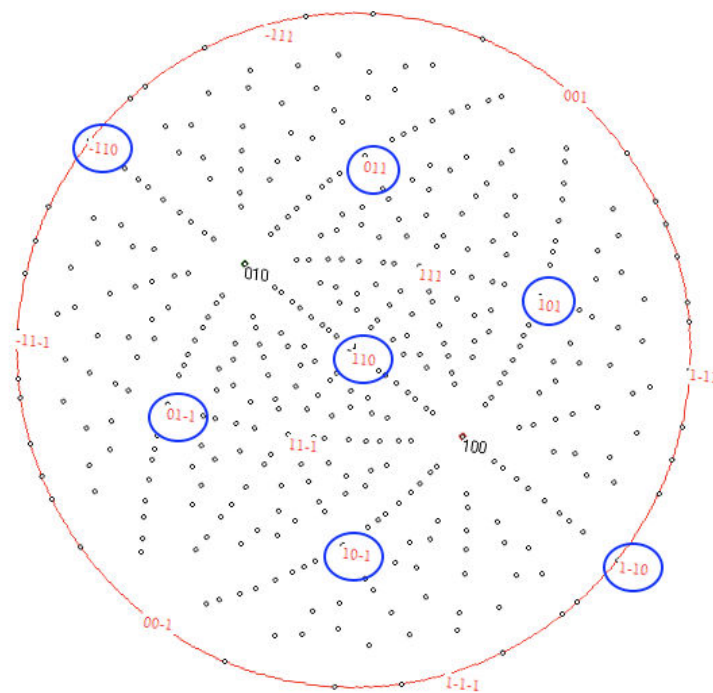


Fig. 4.16  $\{110\}$  stereographic projection for cubic crystals tilted to coincide with the analyzed direction of the WSC sample

Fig. 4.17 a) shows two different blisters found in the  $\langle 110 \rangle$  WSC. It may be observed that they have an approximate hexagonal shape. By comparing these blisters with the associated stereographic projection, it is observed that they are consistent with the  $\langle 110 \rangle$  directions. As a matter of fact, Fig. 4.17 b) shows the associated stereographic projection containing only the  $\langle 110 \rangle$  directions along with an example of the hexagonal shape found in blisters.

In this case, the blister steps ND should form either a  $90^\circ$  angle (directions located in the circumference of the stereographic projection) or a  $60^\circ$  angle with the surface ND. This means that the planes do not form the same angle with the surface and the displacement during blister growth is not the same. As a result, blisters do not show a perfect hexagonal shape.

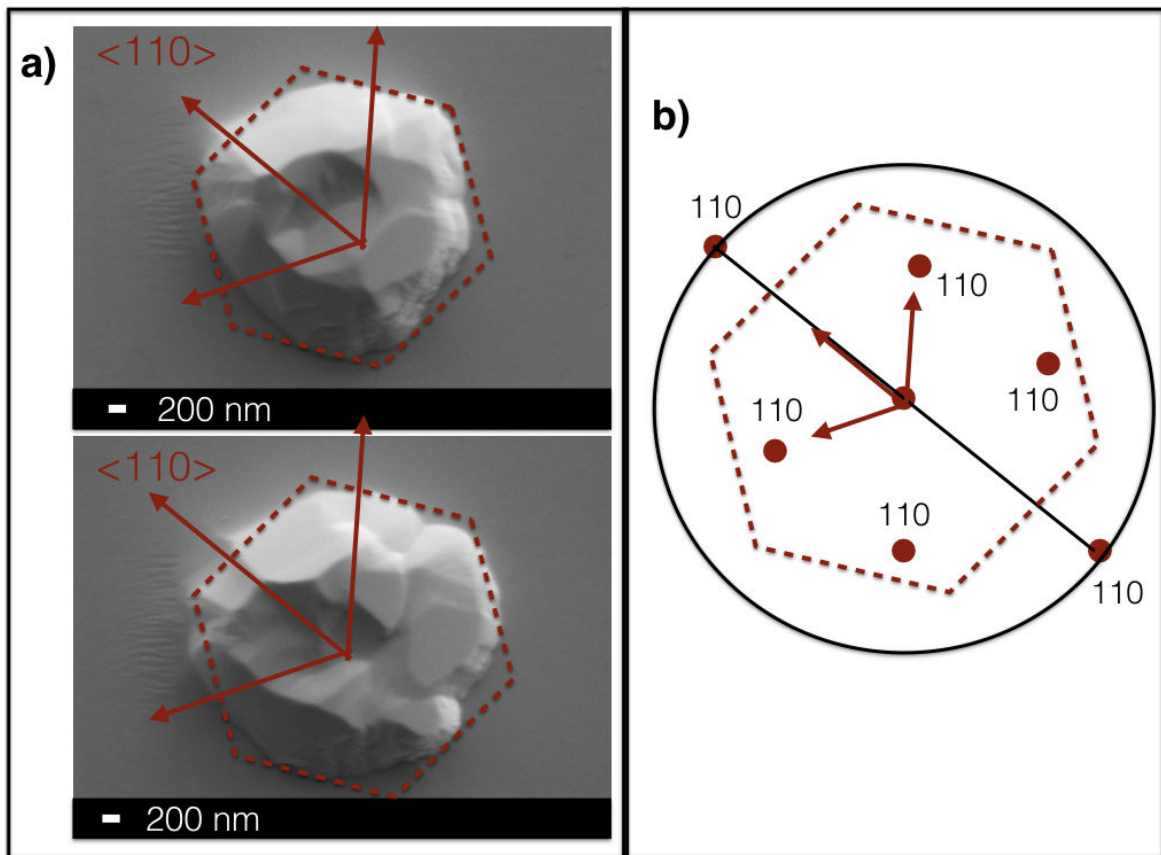


Fig. 4.17 a) Blister morphology on the  $\langle 110 \rangle$  WSC surface and b) the associated stereographic projection containing only the  $\langle 110 \rangle$  directions

### $\langle 111 \rangle$ Tungsten single crystal

In this case, to analyze blister morphology in  $\langle 111 \rangle$  WSC the stereographic projection has to be tilted around the  $x_3$  axis so that it coincides with the  $x_1$  and  $x_2$  directions of the analyzed WSC sample. Fig. 4.18 shows the associated stereographic projection for cubic crystals where the blue circles correspond to the  $\langle 110 \rangle$  directions.

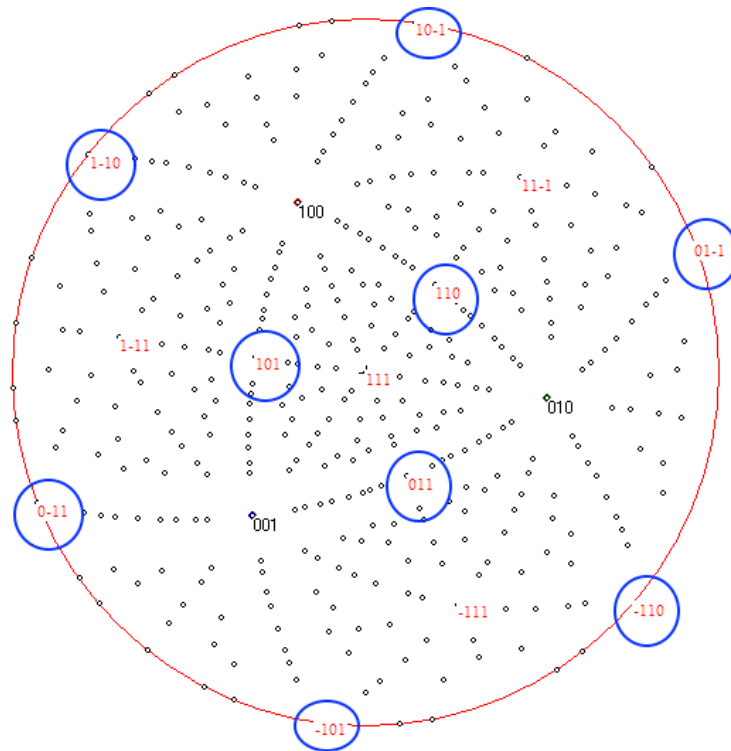


Fig. 4.18  $\{111\}$  stereographic projection for cubic crystals tilted to coincide with the analyzed direction of the WSC sample

Blister morphology in the  $\langle 111 \rangle$  WSC is more complex than in the previous cases. Fig. 4.19 a) shows three different blisters found in the  $\langle 111 \rangle$  WSC. At first glance, the morphology of these blisters corresponds to an approximate hexagonal shape. This hexagonal shape may be compared to the associated stereographic projection containing only the  $\langle 110 \rangle$  directions, as shown in Fig. 4.19 b). It may be observed that the hexagonal shape is coherent with the  $\langle 110 \rangle$  directions perpendicular to the surface ND. There are, however, three additional  $\langle 110 \rangle$  directions that form a  $35^\circ$  angle with the surface ND, represented with green circles in Fig. 4.19 b). Actually, these  $\langle 110 \rangle$  directions should also determine the blister morphology in the  $\langle 111 \rangle$  WSC, since they form part of the sample slip system.

However, as observed in the case of Al in Chapter 3, blister growth is enhanced in the slip directions perpendicular to the surface. In this case, there are six  $\langle 110 \rangle$  directions perpendicular to the surface and only three that form a  $35^\circ$  angle with the surface ND. As a result, during blister growth there will be an overlap of planes, that results in an approximate hexagonal blister morphology observed in Fig. 4.19 a).

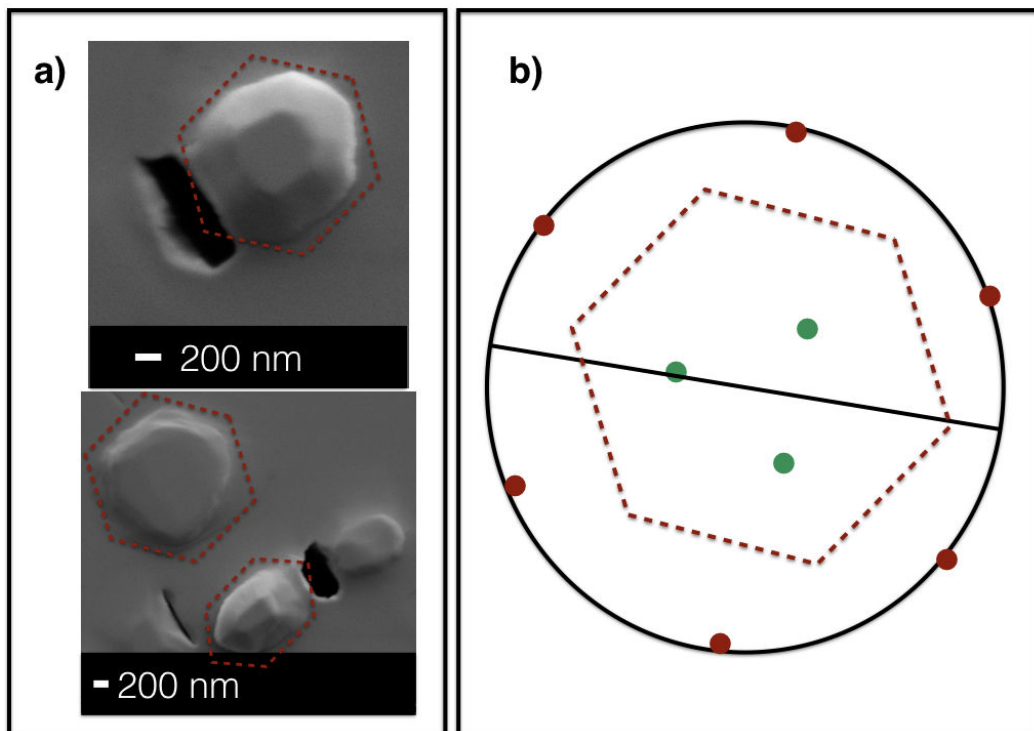


Fig. 4.19 a) Blister morphology on the  $\langle 111 \rangle$  WSC surface and b) the associated stereographic projection containing only the  $\langle 110 \rangle$  directions, with red circles depicting the  $\langle 110 \rangle$  directions perpendicular to the surface ND and green circles for the ones that form a  $35^\circ$  angle with the surface ND

### Blister burst in the $\langle 111 \rangle$ tungsten single crystal sample

After hydrogen plasma exposure, the  $\langle 111 \rangle$  WSC showed the highest blister density on its surface. In addition, most of the blisters have an opening or burst at their edge. Fig. 4.20 shows an example of several burst blisters in the  $\langle 111 \rangle$  WSC. Blister burst occurs when the high pressures inside the blisters exceed the tensile strength of the material (*i.e.* the maximum stress a material can withstand before breaking). These stresses are capable of inducing fractures in the material. Since the three single crystals were exposed to the same plasma fluxes and fluences, why are there only burst blisters in the  $\langle 111 \rangle$  WSC?

One explanation was proposed by Shu *et al.* where it is assumed that there is a tunnel of bubbles that connects the blisters with the surface. As the pressures inside the blister increase a fracture may be induced in a weak point in the region surrounding the blisters. This weak point may be located at the top of the blister or on the side and determines the region that bursts due to the high pressures (Shu *et al.*, 2007). However, this assumption fails to explain the fact that burst blisters are only observed in the  $\langle 111 \rangle$  WSC and the openings or bursts are always observed in the same two regions (see Fig. 4.20).

There is another possible explanation related to the slip system of the sample. The  $\langle 111 \rangle$  WSC has 9 different slip planes, six of which are perpendicular to the surface. Since blister growth is enhanced for the slip directions perpendicular to the surface, in this sample blisters are able to plastically deform more easily in the direction parallel to the surface ND. In addition, by comparing the burst blisters in Fig. 4.20 with the associated stereographic projection in Fig. 4.19 b), it may be noticed that the burst region coincides with the  $\langle 110 \rangle$  directions that form a  $35^\circ$  angle with the surface ND. It was previously explained that during plastic deformation there is an overlapping of slip planes. In this case, the overlapping occurs in planes with a high angle difference. That is, some planes grow in the direction perpendicular to the surface whereas others grow with a  $35^\circ$  angle with the surface ND. This may contribute to an increase in local stresses. It is possible that the combination of enhanced plastic deformation in the direction parallel to the surface ND and the overlapping of planes during blister growth, contribute in achieving the fracture limit more promptly in the  $\langle 111 \rangle$  WSC than in the other two single crystals.

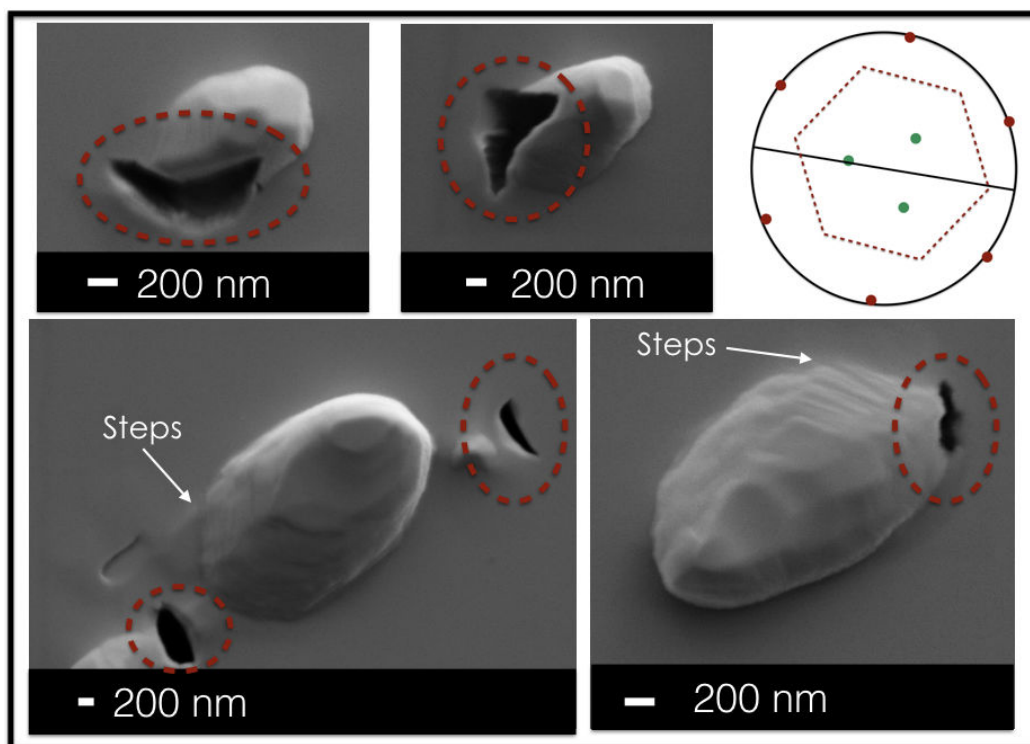


Fig. 4.20 Burst blisters in the  $\langle 111 \rangle$  WSC

It is worthy to notice that some blisters in Fig. 4.20 have steps. As discussed in Chapter 3, these steps are typical of blister growth by loop punching and correspond to the macroscopic traces of the atomic scale crystallographic planes of the sample.

### 4.3 Summary and discussion

During plasma exposure, ions are implanted in the surface of the material at a certain depth. In the case of tungsten exposed to our experimental conditions this depth is calculated to be 3.3 nm (Ziegler et al., 2010). After implantation, these ions diffuse they may be trapped in trapping sites such as vacancies, cracks or grain boundaries. At high fluences, as is the case in our experimental conditions, along with the low hydrogen solubility in tungsten (Serra et al., 1998), hydrogen concentration is able to reach high levels in the near surface regions. When a certain hydrogen concentration is reached, blisters are able to nucleate in the surface of the material (Behrish, 1983; Post and Behrish, 1986).

The initial nucleation mechanism for bubbles is the agglomeration of vacancies. Once they nucleate, their growth is determined by several parameters. Some parameters are external, such as plasma flux, fluence and incident ion energy, whereas other parameters are intrinsic to the material itself, such as microstructure and crystallographic orientation. Experiments performed with polycrystalline samples show that, in our conditions, blisters grow within the grains, specially in grains of a few  $\mu\text{m}$  in size. Different phenomena were distinguished in the sample surface after hydrogen plasma exposure. Multigrain swelling with sizes of approximately 10  $\mu\text{m}$  heights between 2.5 and 6.7  $\mu\text{m}$ . Several types of blisters were also observed: small blisters, low dome blisters and high dome blisters. Small blisters have sizes of less than 1  $\mu\text{m}$  and height of approximately 0.03  $\mu\text{m}$ . Low dome blisters have an average height of 0.05  $\mu\text{m}$  whereas high dome blisters have an average height of 0.8  $\mu\text{m}$ . Both high dome and low dome blisters have a few  $\mu\text{m}$  in size. Paradoxical results were found regarding a preferred crystallographic orientation for blister growth. It was observed that blisters tend to nucleate in grains that do not correspond to the overall sample texture. It is believed that these grains are subject to stresses and have an increased defect density than the textured grains. As a result, they have more nucleation centers for blistering.

In order to analyze blister growth dynamics without the effects of grain boundaries, experiments were performed with single crystals. These experiments showed that blister density and size depends on the crystallographic structure of the material. The  $\langle 111 \rangle$  WSC has the highest blister density whereas the  $\langle 110 \rangle$  and  $\langle 100 \rangle$  WSC have the lowest density. However, the blister surface coverage is 0.01%, 0.02% and 0.3% for the  $\langle 100 \rangle$ ,  $\langle 110 \rangle$  and  $\langle 111 \rangle$  WSC, respectively. This means that the  $\langle 111 \rangle$  WSC has a higher density of smaller blisters and the  $\langle 100 \rangle$  and  $\langle 110 \rangle$  WSC have a lower density of larger blisters. Experiments with WSC also showed that blister growth is affected by the crystallographic structure of the material:  $\langle 100 \rangle$  WSC samples shows octagonal shaped blisters,  $\langle 110 \rangle$  WSC samples show hexagonal shaped blisters and finally  $\langle 111 \rangle$  WSC samples also show hexagonal blisters. It was determined that the hexagonal blisters in the  $\langle 111 \rangle$  WSC are actually influenced by nine

different slip directions; however, due to the slip plane overlapping during blister growth, the blisters show a hexagonal shape. In addition, blisters in the  $\langle 111 \rangle$  WSC show opening or bursts in their edges. This is due to the high pressures inside the blisters that are able to rupture the material. These openings or burst also seem to be related with crystallographic orientation.

Plastic deformation in crystalline materials occurs by the motion of dislocations in the slip system of the material. Therefore, the plastic deformation during blistering leads to the emergence of slip planes at the sample surface. The surface ND of these planes should be coherent with the slip direction of the sample. The experiments performed with tungsten single crystals confirm that blister morphology is consistent with the information obtained in the stereographic projection. This confirms the hypothesis that blister growth is due to loop punching and that in fact, blisters correspond to the macroscopic traces of the atomic scale crystallographic planes of the sample.

Experiments performed with aluminum and tungsten single crystals show the influence crystallographic structure has on blister morphology. The experiments performed with both materials focused in analyzing blister morphology in cubic crystal systems. The information obtained in these studies set the basis for analyzing more complex, hexagonal systems.

## Chapter 5

# Macroscopic Rate Equations model of hydrogen retention in metals

A crucial aspect of PWI in fusion reactors is hydrogen isotope (HI) implantation and retention. Implantation of ions leads to fuel retention and fuel recycling, which affects the plasma density and the delivered fusion power. In addition, tritium, one of the hydrogen isotopes used as fuel, is radioactive, hence its inventory is considerably limited in fusion reactors and its retention should be kept as low as possible (Conn et al., 1997; Konings, 2012). It is therefore important to understand the mechanisms involved in fuel retention and to estimate the retained quantities expected in fusion reactors.

A convenient tool to analyze and understand HI retention in solids is the use of numerical models such as those based on the use of macroscopic rate equations (MRE). These models are based on mass balances of HI that take into account the states in which the HI's are found in the material bulk. They consider the HI transfer between the gas phase and the material bulk, along with the migration of HI in the material bulk and the conversion between these states. The model equations allow predicting the amount of retained HI in materials and estimating the relative importance of the different physical processes, such as HI implantation, migration, and trapping, involved in this interaction. This chapter presents a model, based on macroscopic rate equations for hydrogen transport in materials, that allows obtaining valuable information for a better understanding of the HI dynamics in ITER-relevant materials.

- Section 5.1 introduces the different models developed using the macroscopic rate equations approach to simulate HI dynamics in metals.
- Section 5.2 describes the phenomena taken into account in MRE models used in this thesis.
- Section 5.3 briefly describes the resolution methods used in the Hydrogen Isotope Inventory Processes Code (HIIPC).

- Section 5.4 shows the different results obtained with the HIIPC model with aluminum, beryllium and tungsten. A comparison is made between the simulations and the different experimental measurements.

## 5.1 Overview of MRE models

MRE models present a practical way of simulating the interaction of HI with solids. In these models the material is represented as a collection of traps with different energies and densities, whose values may be obtained by experimental methods or by density functional theory results. The flux deposited by implantation is simulated in terms of a volume source term, the value of which depends on the position in the material. The implanted HI may diffuse in the material or be trapped in trap sites. Also, atoms at the surface may recombine with another atom and desorb as a molecule. As a result, fuel retention is described by a set of partial differential equations that govern the mass balance of HI in the material. Their main advantage is that they allow the study of large scale information with a low computation time. However, they rely on various adjustable parameters, which need to be fitted using experimental results. The various models that have been developed using this approach are described in this section.

The Tritium Migration Analysis Program (TMAP) model is one of the most well-known in this domain (Longhurst et al., 1992; Longhurst, 2008). It is a versatile model that describes the processes of implantation, retention and re-emission of HI from different materials and multi-layered material structures (Baldwin et al., 2014). This model is used to simulate HI retention in various materials. It takes into account multiple traps or distributions of trap sites, which allows the simulation of neutron irradiation and surface erosion (Anderl et al., 1999; Berardinucci, 1998; Brad Merrill and Humrickhouse, 2013; Roszell et al., 2012). It successfully simulates a phenomenon observed in high-ion-flux experiments where there is a saturation of implanted particles in the material. This is performed by allowing the recombination coefficient to grow exponentially when the surface concentration reaches saturation (Anderl et al., 1999; Berardinucci, 1998). The TMAP model assumes a constant trap density and distinguishes a low temperature trap density value for the temperature range 360 – 480 K and a different trap density value for high temperatures ranging between 700 and 950 K. This assumption is due to the fact that data cannot be fitted over the whole 360-950 K range using the same trap density; the high temperature case is fitted using a lower trap concentration. Therefore, it is assumed that traps are annealed during plasma exposure (Wright et al., 2011).

The Coupled Reaction Diffusion System (CRDS) was developed to overcome some deficiencies of the TMAP7 model (Oberkofler et al., 2011; Piechoczek et al., 2013). This model takes into account an arbitrary collection of mobile and static components such as HI, traps and HI-trap complexes, which can react with each other (Oberkofler et al., 2011). Additionally, it takes into account anisotropic diffusion effects. This model takes into account the annihilation of Frenkel pairs and a self trapping term. The CRDS model is capable of simulating HI trapping-detrapping mechanisms in single crystals as well as in polycrystalline samples. The latter is described by taking into account an enhanced effective transport in grain boundaries (Piechoczek et al., 2013).

Ogorodnikova *et al.* (Ogorodnikova et al., 2003) developed a model to simulate the behavior of deuterium in tungsten after plasma exposure. The main innovation of this model is the addition of an ion induced extrinsic trap located near the implantation zone. The rate of ion-induced trap production depends on the energy of incident ions, ion flux, target temperature and exposure time. This model properly simulates low fluence experiments, however at higher fluences hydrogen retention was overestimated. Therefore, it was updated to introduce a variation of the diffusion coefficient, with fluence, in the implantation zone (Ogorodnikova et al., 2008). The model was also updated to take into account multiple HI trapping within a defect and to include different types of defects such as grain boundaries, dislocations, vacancies and vacancy clusters. Finally, an analytical model was developed to include the effect of enhanced trapping of HI in tungsten at high fluxes by assuming that the mechanisms of hydrogen isotope trapping in a vacancy cluster is similar to a chemisorption on a surface (Ogorodnikova, 2015).

The Hydrogen Isotope Inventory Processes Code (HIIPC) was initially developed at LSPM by Bonnin and Sang *et al.* (Sang et al., 2012) and included 3 modules: a heating module to simulate the temperature distribution in the wall, a metal module to simulate hydrogen transport in tungsten and beryllium, and a module for porous media. The latter describes the transport in a porous layer that may result from the material transformation under the plasma ion bombardment. This model was used to study the behavior of HI in tungsten with different diffusivities and recombination rate coefficients as well as the effect the diffusivity, the trap concentration and the recombination rate have on the effective diffusion (Sang et al., 2014). The model was later updated to include bubble growth in materials after nucleation at an already existing defect in the material. Bubble growth is governed by loop punching, which is driven by a deviation of the pressure from an equilibrium value. It assumes 3 forms of HI inside the material: solute, trapped and HI molecular gas precipitates (Sang et al., 2013).

Finally, a two dimensional hybrid code combining rate theory and Monte Carlo methods (HIIPC-MC) was developed to simulate bubble growth in tungsten. It takes into account the wall temperature and ion flux and considers that the bubble growth is due to migration of  $H_2 - v$  complexes and bubble coalescence (Sang et al., 2015). Recent developments are being made to implement a 3D code that takes into account mechanical and stress fields in the material.

The TESSIM code (Schmid et al., 2012) simulates hydrogen isotope retention in tungsten during normal plasma operation and edge localized modes (ELM's) (Schmid, 2016). It makes use of density functional theory results so as to take into account the dependence between trap and de-trapping energies that depend on the number of HI trapped in the vacancies (Schmid et al., 2014). It was used to compare the HI behavior on W and W/Ta alloys, which shows that the alloys have a higher intrinsic trap density and hence retain more D than pure W. Finally, this code was used to simulate the D uptake in W exposed to the plasma at different temperatures. The dependence of the reflection coefficient with temperature was considered in order to fully take into account the effect of temperature (Manhard et al., 2014).

The Migration of Hydrogen Isotopes in MaterialS code (MHIMS) (Hodille et al., 2015) developed at CEA simulates the behavior of hydrogen in single and polycrystalline tungsten. It assumes the material has 3 different traps: two intrinsic ones and one extrinsic one created by ion irradiation. This model was updated under the name MHIMS-R to take into account recent density functional theory results, which state that tungsten mono-vacancies can contain up to 6 hydrogen isotopes at 300 K with detrapping energies that vary according to the number of HI's present the vacancy (Hodille et al., 2016). Recent developments in this code include taking into account HI's sticking on the surface, HI molecule desorption from the surface, HI recombination with the surface atom, and transport from the bulk to the surface. The latter in addition to using three different extrinsic traps allowed the simulation of self-damaged tungsten, which makes it possible to simulate and analysis of neutron-irradiated samples (Hodille et al., 2017).

Hu *et al.* (Hu and Hassanein, 2014) developed a ID code that simulates deuterium retention in tungsten. This model takes into account a diffusion relaxation process known as the Gorsky effect. This effect is considered to occur through three different processes. The first one is the classical Gorsky effect, in which an external stress is applied to the sample. This causes interstitial atoms to migrate from the compressive side to the stretching side. The second one is the intercrystalline Gorsky effect in which the relaxation mechanism for

hydrogen diffusion is due to a stress field gradient generated either by internal grain stresses or stresses at the grain boundaries. In the trap-induced Gorsky effect the relaxation mechanism for hydrogen diffusion occurs due to the internal lattice distortions due to the traps present in the material. In addition, this model assumes the effect of a radiation-enhanced diffusion coefficient and takes into account the creation of traps due to ion bombardment.

The Diffusion Trapping Model for Isotopic eXchange (DITMIX) (Kogut, 2014) model was developed to understand the mechanisms of the isotopic exchange at the microscopic level. Unlike the previous models, this model distinguishes deuterium and tritium as far as transport and trapping effects in the material are concerned.

The main characteristics of these codes are summarized in Table 5.1.

Model	Material	Dimensions	Temperature Module	Trap Creation	Bubble Growth	Multiple trap occupation
TMAP	Be and W	1D				
CDRS	Be	2D				✓
Ogordonikova <i>et. al</i>	W	1D		✓		✓
HIIPC	Be, Al and W	2D	✓	✓	✓	
TESSIM	W	1D				✓
MHIMS	W	1D		✓		✓
Hu <i>et. al</i>	W	1D		✓		
DITMIX	Be	1D				✓

Table 5.1 Summary of the main characteristics of the different MRE codes

## 5.2 HIIPC model

HIIPC is an innovative code able to simulate hydrogen dynamics in materials. This code is available in two versions: 1D and 2D. Both versions take into account the temperature change during ion implantation as well as the formation of defects such as damage created by ion impact and bubble growth. It is a versatile code capable of working with 3 different materials: tungsten, aluminum and beryllium. Additionally, it is capable of simulating ion implantation cycles to fully simulate current experimental campaigns in fusion reactors.

In this work, the main objective of the simulations is to understand the different phenomena that govern HI loading dynamics, to compare hydrogen loading in different materials and to analyze the possibility to induce bubble formation under different discharge conditions.

Therefore, the simulations are performed based on the experimental conditions used in the previous chapters, *i.e.* 2.5 mm thick samples are implanted during several plasma on/ plasma off cycles for long periods of time . Therefore, model with a low computation time designed to simulate depths of up to a few mm was needed. The code that fulfills these requirements is the 1D HIIPC code, and hence it was chosen in order to perform the simulations throughout this work.

### 5.2.1 Rate equation for diffusion and trapping

The HIIPC code takes into account four important processes concerning the HI's: diffusion, trapping, detrapping and backscattering. Diffusion occurs when the HI diffuse from regions of high concentration to regions of low concentration during HI flux implantation. Due to diffusion, the atoms reach depths larger than the implantation zone. While the HI diffuse, they may be trapped by trap sites. Therefore, this model considers two types of HI inside the material: solute or trapped (Bonnin et al., 2015; Sang et al., 2014). It is important to stress that in order to penetrate into the bulk, a molecule needs to dissociate into atoms; meaning that there are only HI atoms inside the material.

The energy of the diffusion and trapping in materials can be seen in Fig. 5.1. This figure depicts the potential energy diagram of HI inside a metal with two types of trapping sites present in the bulk.  $E_m$  corresponds to the energy barrier of diffusion of HI in the metal matrix through solute sites.  $E_{b1}$  and  $E_{b2}$  are the discrete trapping energies of the trapping sites. Finally,  $E_{d1} = E_m + E_{b1}$  and  $E_{d2} = E_m + E_{b2}$  correspond to the detrapping energy that corresponds to the energy required for the atoms to leave the traps (Hodille et al., 2015; Izumi and Itoh, 2011). Usually, atoms at the surface may recombine with another atom and desorb as a molecule. The release of an HI trapped in the bulk is a 3-step process. First, the atom has to detrapp and diffuse in the bulk until it reaches the surface. Once at the surface this atom has to recombine with a gas phase atom in order to be released. Experimental results on deuterium release from tungsten suggest that recombination is not a rate-limiting step for the release of HI (Bisson et al., 2015); therefore recombination is not included in the simulation. Finally, it is worthy to mention that there is no absorption of ions occurring in the surface given that during impact ions are implanted in the material.

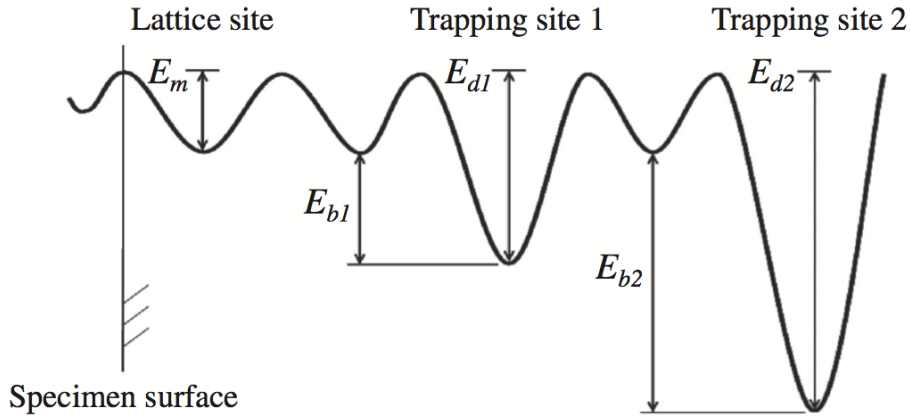


Fig. 5.1 Schematic potential energy diagram for HI in metals (Izumi and Itoh, 2011).

The Hydrogen Isotope Inventory Processes Code (HIIPC) is based on the transport equations proposed by McNabb et al. (McNabb and Foster, 1963), where contrary to the Oriani approach (Oriani, 1970), trapping and detrapping processes are not at equilibrium. The temporal evolution of the retained HI's in the material is described by (Hodille et al., 2015):

$$\frac{\partial C_{t,i}(x,t)}{\partial t} = S_{mobile \rightarrow trap,i} - S_{trap,i \rightarrow mobile} \quad (5.1)$$

$$\frac{\partial C_s(x,t)}{\partial t} = \frac{\partial}{\partial x} \left[ D(T) \cdot \frac{\partial C_s(x,t)}{\partial x} \right] - \sum_i \frac{\partial C_{t,i}(x,t)}{\partial t} + \Gamma(x,t) \quad (5.2)$$

where:

$C_{t,i}(x,t)$  is the trapped HI concentration in the  $i$ th trap (either vacancies or dislocations) (atoms/m<sup>3</sup>)

$C_s(x,t)$  is the solute HI concentration (atoms/m<sup>3</sup>)

$S_{trap,i \rightarrow mobile}$  is the variation of trapped particles being detrapped

$S_{mobile \rightarrow trap,i}$  corresponds to the solute or mobile particles in the lattice being trapped

$\Gamma(x,t)$  is the volumic implantation term due to plasma bombardment (atoms/m<sup>2</sup>s)

$D(T)$  is the diffusion coefficient (m<sup>2</sup>/s)

The diffusion coefficient of HI is given in equation 1.14. This coefficient is mass dependent and hence  $D_{HI} = \frac{D_H}{\sqrt{m_{HI}}}$  is used for the calculations, where  $m_{HI}$  is the atomic mass of the HI.

The implantation term of ions that impact the surface is defined by:

$$\Gamma(x,t) = (1-r)f_{distr} \cdot \varphi \quad (5.3)$$

where  $r$  is the backscattering coefficient, that is, ratio of reflected ions with respect to the incident ions,  $f_{distr}$  is the implantation profile and  $\varphi$  is the incident flux in atoms. Usually, the implantation profile has a Gaussian shape and is defined as

$$f_{distr} = I e^{-\frac{(x-d_{max})^2}{2\sigma^2}} \quad (5.4)$$

where  $d_{max}$  is the average ion range and  $\sigma$  is the standard deviation and  $I$  is defined in such a way that the space integral of  $f_{distr}$  is equal to 1.

Taking into consideration the equations stated above, the terms in equation 5.1 can be rewritten in the following way:

$$S_{trap,i \rightarrow mobile} = v_{d,i} C_{t,i}(x,t) \quad (5.5)$$

$$S_{mobile \rightarrow trap,i} = v_{t,i} \left[ 1 - \frac{C_{t,i}}{n_{t,i}} \right] C_s(x,t) \quad (5.6)$$

where  $S_{trap,i \rightarrow mobile}$  is a first order process in terms of trap concentration and  $S_{mobile \rightarrow trap,i}$  is a first order process in solute and has no order as far as trap concentration is concerned. The trapping frequency  $v_{t,i}$  in equation 5.6 is defined by:

$$v_{t,i} = \frac{n_{t,i} D(T)}{n_s L^2} \quad (5.7)$$

where  $n_{t,i}$  is the trap density,  $n_s$  is the number of hydrogen atoms that can be contained in a lattice site, which in our case it is assumed to be 1, and  $L$  is the jumping length, which depends on the lattice structure of the material. Table 5.2 shows the jumping length for different lattices structures and sites in the material.

Lattice Structure	octahedral	tetrahedral
bcc	$\frac{a}{2}$	$\frac{a}{2\sqrt{2}}$
hcp	$\frac{a}{\sqrt{2}}$	$\frac{a}{2}$
fcc	$\frac{a}{\sqrt{2}}$	$\frac{a}{2}$

Table 5.2 Jumping lengths for different lattice structures and sites (Fukai, 2005; Ogorodnikova, 2002)

The detrapping frequency  $\nu_{d,i}$  is defined by:

$$\nu_{d,i} = \nu_0 e^{-\frac{E_m + E_{b,i}}{kT}} \quad (5.8)$$

where  $E_m$  is the diffusion energy,  $E_{b,i}$  is the trapping energy and  $\nu_0$  is the pre-exponential factor (or attempt frequency) in  $s^{-1}$ . The latter is obtained from the density functional theory and the typical values are in the order of  $10^{13} - 10^{14} s^{-1}$ .

Therefore equation 5.1 and equation 5.2 are expressed as:

$$\frac{\partial C_{t,i}(x,t)}{\partial t} = \frac{n_{t,i} D(T)}{n_s \lambda^2} \left[ 1 - \frac{C_{t,i}}{n_{t,i}} \right] C_s(x,t) - \nu_0 e^{-\frac{E_m - E_{b,i}}{kT}} C_{t,i}(x,t) \quad (5.9)$$

$$\frac{\partial C_s(x,t)}{\partial t} = \frac{\partial}{\partial x} \left[ D(T) \cdot \frac{\partial C_s(x,t)}{\partial x} \right] - \sum_i \frac{\partial C_{t,i}(x,t)}{\partial t} + (1-r) f_{dist} \cdot \varphi \quad (5.10)$$

The parameters used in the simulations made for Al, Be and W were obtained from literature and are summarized in Table 5.3. Two intrinsic traps were taken into account for simulations: vacancies and dislocations. **The trap density corresponds to the number of traps to number of atoms ratio, that is the atomic fraction (*i.e.* at.fr.)**

It can be noticed that both traps have a higher energy in Be than in Al and W. Moreover, for Be and W, vacancies have a lower energy but higher density than dislocations. In the case of Al, the value of the density of dislocations was not found in the literature. Therefore, it was assumed to be lower than that of Be but higher than that of W.

Parameters	Aluminum	Beryllium	Tungsten
Atomic number Z	13	4	74
Lattice structure [1]	fcc	hcp	bcc
Lattice constants (Å) [1]	$a = b = c = 4.06$	$a = b = 2.28 \ c = 3.60$	$a = b = c = 4.06$
Diffusivity (m <sup>2</sup> /s)	$D_0 = 2.0 \times 10^{-6}$ [2] $E_m = 0.52 \text{ eV}$	$D_0 = 6.7 \times 10^{-9}$ [3] $E_m = 0.29 \text{ eV}$	$D_0 = 4.1 \times 10^{-7}$ [4] $E_m = 0.39 \text{ eV}$
Melting point (K) [1]	933	1590	3695
Density (kg/m <sup>3</sup> ) [1]	62.71	1.86	19.3
Energy of vacancies $E_{d,1}$ (eV)	0.73 [5]	1.0 [6]	0.88 [7]
Density of vacancies (at.fr.) $n_{t,1}$	$1 \times 10^{-3}$ [8]	$3.0 \times 10^{-2}$ [6]	$1 \times 10^{-3}$ [9]
Energy of dislocations $E_{d,2}$ (eV)	1.01 [5]	1.80 [6]	1.05 [9]
Density of dislocations (at.fr.) $n_{t,2}$	$2.5 \times 10^{-3}$	$7.5 \times 10^{-3}$ [6]	$4 \times 10^{-4}$ [9]
Jump frequency $\nu_0$ (Hz)	$2.45 \times 10^{13}$ [10]	$1.4 \times 10^{14}$ [11]	$1.0 \times 10^{13}$ [12]

[1] Calister and Rethwisch (2010)

[2] Young and Scully (1998)

[3] Abramov et al. (1990)

[4] Serra et al. (1998)

[5] Izumi and Itoh (2011)

[6] Anderl et al. (1992); Causey and Wilson (1994)

[7] Bonnin et al. (2015)

[8] Detemple et al. (1995)

[9] Bonnin et al. (2015)

[10] Wolverton et al. (2004)

[11] Zhang et al. (2012)

[12] Hodille (2016)

Table 5.3 Parameters of Al and Be and W used in our model

The values for the diffusivity of hydrogen isotopes in Al, Be and W were chosen based on several parameters, such as temperature and purity of the sample. Sample temperature plays an important role when measuring this value because at higher temperatures the hydrogen atoms diffuse freely in the material without being trapped. Conversely, at lower temperatures the hydrogen atoms might be trapped and the measured value will not be accurate. Therefore, a value measured at high temperatures was chosen.

Additionally, in the case of Be and Al, the choice of the diffusivity value was made based on the purity of the measured samples. Both materials are easily oxidized and hence it is important to choose a diffusivity measured for non-oxidized samples. The values chosen and their corresponding energy are shown in Table 5.3. Fig. 5.2 shows the diffusivity values with respect to temperature for Al, Be and W. It is seen that W has the highest diffusivity among the three materials. Al has the lowest diffusivity value below 450 K and Be has the lowest diffusivity value above 450 K. Nevertheless, all three elements are considered to have high hydrogen diffusivity values (Serra et al., 1998).

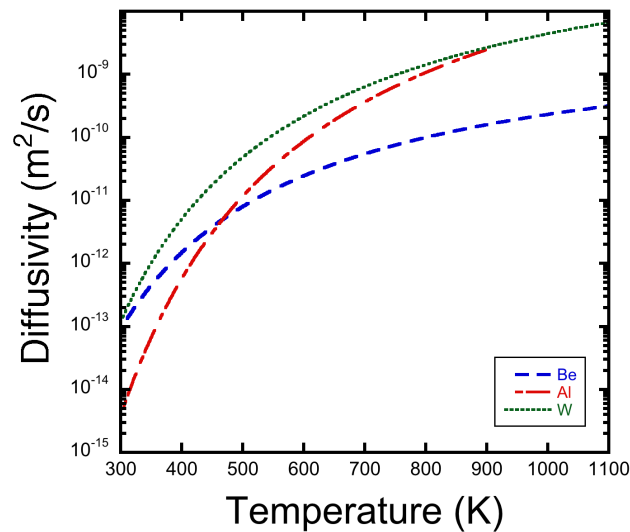


Fig. 5.2 Diffusivity values for Al, Be and W with respect to temperature

The SRIM code was used to calculate the implantation profile as well as the backscattering coefficients (Ziegler et al., 2010). Table 5.4 shows the values used to perform simulations in aluminum.

Parameters	Values for 120 eV ions	Values for 220 eV ions	Values for 320 eV ions
Ion range $d_{max}$ (m)	$4.4 \times 10^{-9}$	$6.6 \times 10^{-9}$	$8.1 \times 10^{-9}$
Standard deviation $\sigma$ (m)	$3.6 \times 10^{-9}$	$3.7 \times 10^{-9}$	$3.8 \times 10^{-9}$
Backscattering coefficient	0.226	0.189	0.147

Table 5.4 Parameters used to calculate the implantation profile in Al and the backscattering coefficient at different energies (Ziegler et al., 2010)

Table 5.5 shows the implantation profile as well as the backscattering coefficient values for tungsten and beryllium, calculated using SRIM.

Parameters	Energy	Values for Be	Energy	Values for W
Ion range $d_{max}$ (m)	320 eV	$8.6 \times 10^{-9}$	220 eV	$3.3 \times 10^{-9}$
Standard deviation $\sigma$		$7.0 \times 10^{-9}$		$3.6 \times 10^{-9}$
Backscattering coefficient		0.074		0.426

Table 5.5 Parameters used to calculate the implantation profile in Be and W and the backscattering coefficient for both Be and W (Ziegler et al., 2010)

The implantation profiles corresponding to the values shown in Tables 5.4 and 5.5 are depicted in Fig. 5.3. For the Al case, it is observed how the implantation profiles are slightly shifted towards the surface (depth = 0). This is due to the fact that at higher energies, the ions are implanted deeper in the material.

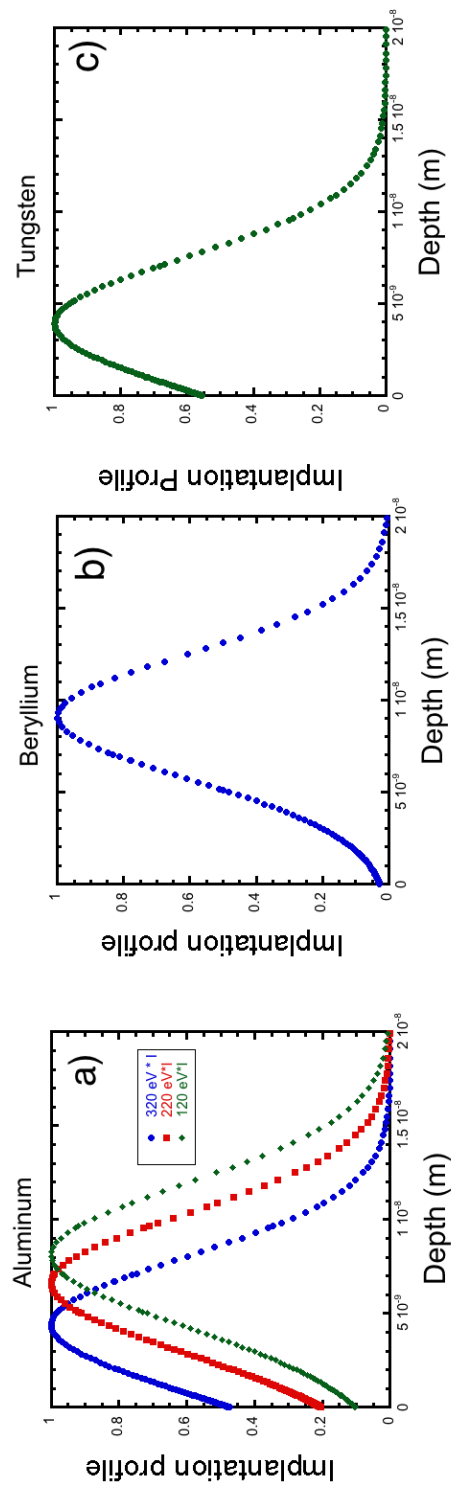


Fig. 5.3 Implantation profiles for a) Al, b) Be and c) W

### 5.2.2 Traps creation due to ion bombardment

As energetic particles are implanted on a solid surface, they may be backscattered or implanted in the material. Ions with a sufficiently high energy are able to transfer enough energy to the material leading to atom sputtering. These ions can even induce defects in the material such as vacancies (Post and Behrisch, 1986; Zinkle, 2012). The ion-induced defects or traps may be described by calculating their concentration as follows (Duesing et al., 1969; Ogorodnikova et al., 2008):

$$\frac{dn_{ion}}{dt} = (1 - r)\varphi f_{dist} \left[ 1 - \eta \frac{n_{ion}}{n_{ion,max}} \right] \quad (5.11)$$

where  $\varphi$  is the depth distribution of ion-induced defects,  $\eta$  is the defect production efficiency (*i.e.* the probability a defect will be created by an incident ion) and  $n_{ion,max}$  is the maximum defect concentration.

The values of energy and maximum density of created traps are shown in Table 5.6. As a first approximation, it is assumed that the created defects correspond solely to vacancies. Therefore, the energy of these defects is assumed to be the same as the energy of vacancies shown in Table 5.3. The maximum density of created vacancies was determined by Ogorodnikova *et. al* (Ogorodnikova et al., 2008) for tungsten. This value was also used for aluminum and beryllium.

Material	Aluminum	Beryllium	Tungsten
Energy of created vacancies $E_{d,3}$ (eV)	0.73	1.0	0.88
Maximum density of created vacancies $n_{ion,max}$ (at.fr.)	$1 \times 10^{-1}$	$1 \times 10^{-1}$	$1 \times 10^{-1}$

Table 5.6 Parameters of Al and Be and W used in the MRE code

The minimum energy required for  $H^+$  ions to create defects in Al at normal incidence is 194 eV (Broeders and Konobeyev, 2004; Hotston, 1975). The simulations were performed with different energy values consistent with those used in the experiments. Defect production efficiency  $\eta$  values for several impact energy values were obtained using SRIM software (Ziegler et al., 2010). Based on these values, a linear curve was constructed to estimate  $\eta$  over the 100-1500 eV range. The different values of  $\eta$  corresponding to the

different energies are shown in Fig. 5.4. The values of  $\eta$ , obtained from the linear fitting, for 220 eV and 320 eV are 0.05 and 0.15 respectively.

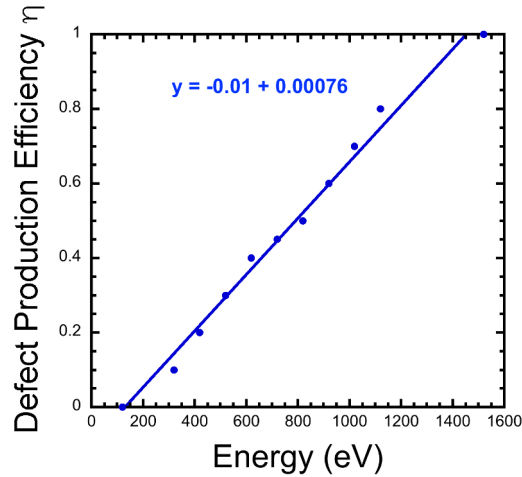


Fig. 5.4 Defect production efficiency  $\eta$  for Al with ions impinging at different energies (Ziegler et al., 2010)

Beryllium has a threshold energy for defect creation of 261 eV for  $H^+$  ions impinging at normal incidence (Broeders and Konobeyev, 2004; Hotston, 1975). The simulations performed with this material include 320 eV hydrogen ions being implanted in the material. This energy is higher than the threshold for defect production. Therefore in this case, the trap creation model is used with a value of  $\eta$  equal to 0.09, as calculated by SRIM (Ziegler et al., 2010).

On the other hand, tungsten has higher threshold energies for defect creation by  $H^+$  ions impinging at normal incidence, with a value of 4150 eV (Broeders and Konobeyev, 2004; Hotston, 1975). This energy is higher than the one used in the experiments. Therefore, the values for  $\eta$  were not calculated for this material.

### 5.2.3 Bubble kinetics growth model

Section 1.3.4 discussed how ion implantation in solids leads to HI retention. In addition, for the cases where the incident ion energy is high enough, damage may be created in the material. However, as materials are exposed for longer periods of time to energetic ions, these ions can accumulate in the lattice reaching a point where the traps are fully occupied. The resulting internal pressure generates stresses that are able to punch interstitials loops out of their lattice position. This process may generate bubbles in the material (Behrish, 1983).

Since experiments in Chapter 3 and Chapter 4 focused on bubble and blister formation, it was important for us to study this phenomenon in order to link the simulation with the experimental results. For this reason a bubble growth module was implemented in the HIIPC

code. In this module, hydrogen production in the bubble takes place through a recombination of solute hydrogen and its precipitation in the gas phase ( $k_r C_s^2(t)$ ). Hydrogen in the gas phase may be lost through a dissolution process in the materials surrounding the cavity ( $k_r k_s^2 f$ ). The number of H atoms in a bubble  $N_b$  is given by (Condon and Schober, 1993):

$$\frac{\partial N_b}{\partial t} = 4\pi r_b^2(t) [k_r C_s^2(t) - k_r k_s^2 f] \quad (5.12)$$

where  $k_r C_s^2(t)$  represents the  $H_2$  formation reaction, *i.e.*, hydrogen that enters the bubble while  $k_r k_s^2 f$  denotes the  $H_2$  dissociation process on the bubble surface, *i.e.*, hydrogen that leaves the bubble,  $r_b$  is the radius of the bubble,  $k_s$  is the solubility at atmospheric pressure (previously calculated in equation 1.13),  $E_s$  is the heat or enthalpy of solution,  $k_r$  is the recombination rate coefficient and  $f$  is the fugacity inside the bubble.

The number of atoms in the bubble allows us calculating the molar volume of hydrogen inside the bubble as follows:

$$v_m = \frac{4\pi r_b^3}{3(N_b/2)N_a} \quad (5.13)$$

where  $N_b/2$  is the number of  $H_2$  molecules inside the bubble and  $N_a$  is the Avogadro constant.

The increase in the number of hydrogen atoms in the bubble results in an increase of the molar volume. This results in the increase of the pressure inside the bubble, which is calculated by the procedure given by Tkacz *et. al* (Tkacz and Litwiniuk, 2002).

When the pressure inside the bubble is high enough, it is able to create an interstitial loop that allows the bubble to expand. This process is known as dislocation loop punching. The minimum pressure  $P_{lim}$  required for such a process to occur is given by (Greenwood *et al.*, 1959):

$$P_{lim} = \frac{2\gamma}{r_b} + \frac{\mu_0 b}{r_b} \left[ 1 - \frac{\alpha T}{T_m} \right] \quad (5.14)$$

where  $\gamma$  is the surface tension of the bubble interface,  $\mu_0$  is the shear modulus at zero temperature,  $T_m$  is the melting temperature of the material and  $\alpha$  is a material constant.

The parameters used to simulate bubble formation in the bulk of the materials are summarized in Table 5.7.

Parameters	Aluminum	Beryllium	Tungsten
Recombination rate coefficient $k_r$ ( $m^4/s$ )	$[7.0021 \times 10^{-21} / T] e^{1.09eV/KT}$ [1]	$3.4 \times 10^{-29} e^{-0.28eV/KT}$ [2]	$3.2 \times 10^{-15} e^{-1.16eV/KT}$ [3]
Sievert's constant $S_o$ ( $atoms/m^3 \sqrt{Pa}$ ) [4]	$3.011 \times 10^{23}$	$3.55 \times 10^{24}$	$8.85 \times 10^{23}$
Heat or enthalpy of solution $E_s$ (eV) [4]	0.65	1	1.03
Burgers vector $b$ (m) [5]	$3 \times 10^{-10}$	$3 \times 10^{-10}$	$3 \times 10^{-10}$
Surface Tension $\gamma$ (N/m) [6]	1.1	1.1	2.5
Shear Modulus when temperature is zero $G_0$ (GPa)	25 [7]	134 [8]	160 [7]
Melting temperature $T_m$ (K) [7]	933	1560	3695
Material constant $\alpha$ [9]	0.18	0.23	0.18

[1] Baskes (1980)  
[2] Anderl et al. (1992); Causey and Wilson (1994)  
[3] Causey (2002)  
[4] Serra et al. (1998)  
[5] Greenwood et al. (1959)  
[6] Keene (1993)  
[7] Calister and Rethwisch (2010)  
[8] Mishra (2009)  
[9] Preston and Wallace (1992)

Table 5.7 Parameters of Al, Be and W used in the bubble formation code

One of the most important parameters as far as bubble formation is concerned is the hydrogen solubility in the material. The values of solubility for Al, Be and W as a function of temperature are shown in Fig. 5.5. It is seen that hydrogen solubility increases with increasing temperature; the typical behavior of materials with low solubility for hydrogen (Post and Behrisch, 1986). Among the three studied materials, Al is the one that has the highest hydrogen solubility whereas W has the lowest value.

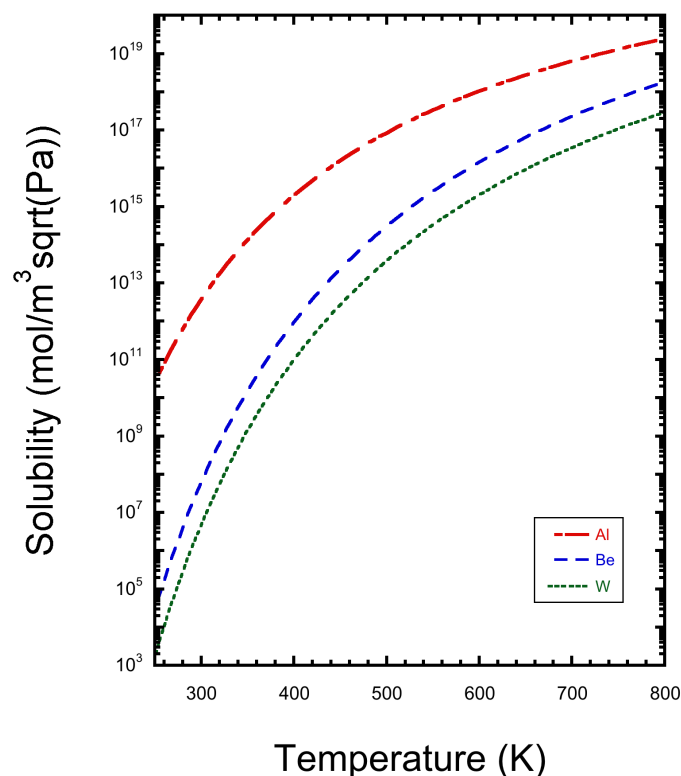


Fig. 5.5 Solubility values for Al, Be and W with respect to temperature

The values of the recombination rate coefficient (RRC) for Al, Be and W as a function of temperature are shown in Fig. 5.6. It is seen that the RRC decreases with temperature. Among the three studied materials, Al and W have the highest RRC whereas Be has the lowest value. The difference between the value for Be and the values for W and Al is of 20 orders of magnitude. The RRC for tungsten was determined experimentally by using 3 keV ions on foils with a purity of 99.95%. The RRC for aluminum was obtained from Baskes model (Baskes, 1980), in which the value depends on the diffusivity and solubility of the materials. This model is the most commonly used for high flux conditions. The RRC for beryllium was determined by Anderl *et.al* (Anderl et al., 1992) and Hsu *et.al.* (Hsu et al., 1990) based on Baskes model. Both of these values are unusually low and since no other RRC values were found for beryllium, the one obtained by Anderl *et.al* (Anderl et al., 1992)

is taken into account for the simulations. The inconsistency of this parameter is taken into account for the analysis, keeping in mind that the objective in the near future is to find a more accurate value.

The recombination rate coefficient plays an important role in bubble growth. The higher this value, the easier for hydrogen atoms to enter the bubble. As more atoms enter the bubble, the pressure has a higher probability of increasing and reaching the threshold pressure required to grow by loop punching. Therefore, as this value increases the bubble has a higher probability to grow.

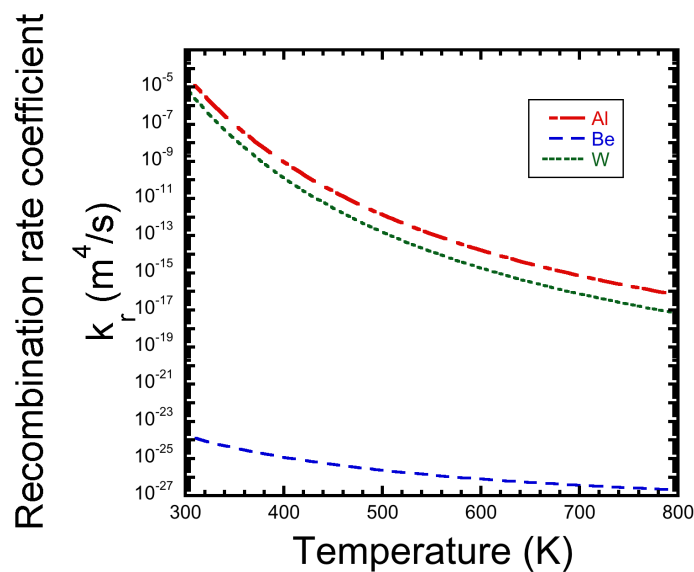


Fig. 5.6 Recombination rate coefficient values for Al, Be and W with respect to temperature

### 5.3 Model Solution

The set of equation 5.9 and equation 5.10 was solved using a finite difference method. These partial difference equations were first discretized in space using a 1D regular mesh and centered difference scheme. This results in a large set of ordinary differential equations, the unknowns of which are the values of concentrations at each grid mesh. This ODE was solved using a backward differentiation formula (BDF) numerical scheme with the help of LSODE solver (Radhakrisnan and Hindmarsh, 1993) over a 2.5 mm sample thickness with 6911 grid points.

As far as the boundary conditions are concerned, it is assumed that there are no solute or trapped HI atoms on the surface and hence  $C_s(x = 0/L, t) = 0$  and  $C_{t,i}(x = 0/L, t) = 0$ . In

other words, any mobile particle arriving on the surface recombines immediately with incident ions. Bisson *et al.* determined that in the case of ion exposure at low flux ( $2 \times 10^{16}$  ions/m<sup>2</sup>s) and fluence ( $10^{17} - 10^{21}$  ions/m<sup>2</sup>), the desorption of HI's from a tungsten surface is not a rate limiting step. Similar boundary conditions were used by Hodille *et al.* (Hodille et al., 2015). It is worthy to mention here that with such an extremely low RRC value for beryllium, hydrogen desorption from the surface would be a rate limiting step. Nevertheless, similar boundary conditions are used for the three materials. Of course, if the very low RRC value is confirmed, the zero surface density boundary condition should be reviewed.

It is also considered that at the beginning of the simulation the material has no HI inside, that is,  $C_s(x, t = 0) = C_{t,i}(x, t = 0) = 0$ . Finally, it is assumed as a first approximation that there are no impurities in the material and hence the possible formation of an oxide layer on the surface of the material is neglected.

It is worthy to mention that the hydrogen flux deposited by implantation is simulated in terms of a volume source term, which depends on the position in the material. This source terms allow us to set the above mentioned boundary conditions.

In order to be consistent with experiments and unless otherwise indicated, the simulations consist of three phases:

- An implantation phase, or exposure time, where the sample has a temperature  $T = T_{imp}$  and  $\varphi$  is equal to the incident flux.  $T_{imp}$  does not necessarily remain constant during implantation.
- A post-exposure phase that corresponds to the time between the end of the implantation and the beginning of the HI retention measurements. In this phase the samples are kept at a constant temperature of  $T = T_{rest}$  and are not exposed to HI flux, that is  $\varphi = 0$ . During this period some HI, corresponding to solute HI or HI trapped in low energy traps, may desorb (Hodille et al., 2015).
- A thermal desorption phase (TDS) in which the sample is heated up to a very high temperature in order to desorb the HI inside the material.

## 5.4 General Model Results

This section gives a first brief description of the results that can be obtained with the MRE model for different conditions. It is divided as follows:

- The isothermal hydrogen dynamics in an aluminum sample are discussed.
- A non-isothermal case of hydrogen dynamics in aluminum is presented.
- A non-isothermal case of an aluminum sample subject to cyclical hydrogen implantation is analyzed.

- The MRE simulation of thermal desorption for the case of tungsten is discussed.

### 5.4.1 Isothermal hydrogen dynamics

Fig. 5.7 shows an illustration of the three phases included in the simulations for an Al sample exposed to hydrogen plasma with a flux of  $1.6 \times 10^{20}$  ions/m<sup>2</sup>s and a temperature of 300 K. Specifically, Fig. 5.7 a) shows the imposed temperature dynamics during these phases and Fig. 5.7 b) shows the time variation of the number of trapped hydrogen per unit sample surface (*i.e.* retained hydrogen). It can be observed that during the implantation phase, hydrogen concentration increases in the material. When the hydrogen flux is off, during post-exposure phase, hydrogen is desorbed from the material. This desorption kinetics is due to the diffusion of hydrogen to the surface and the desorbed hydrogen corresponds to solute hydrogen or trapped in low energy traps (Hodille et al., 2015). Finally, when the temperature ramp is applied during the TDS phase, there is an exponential decrease in hydrogen concentration.

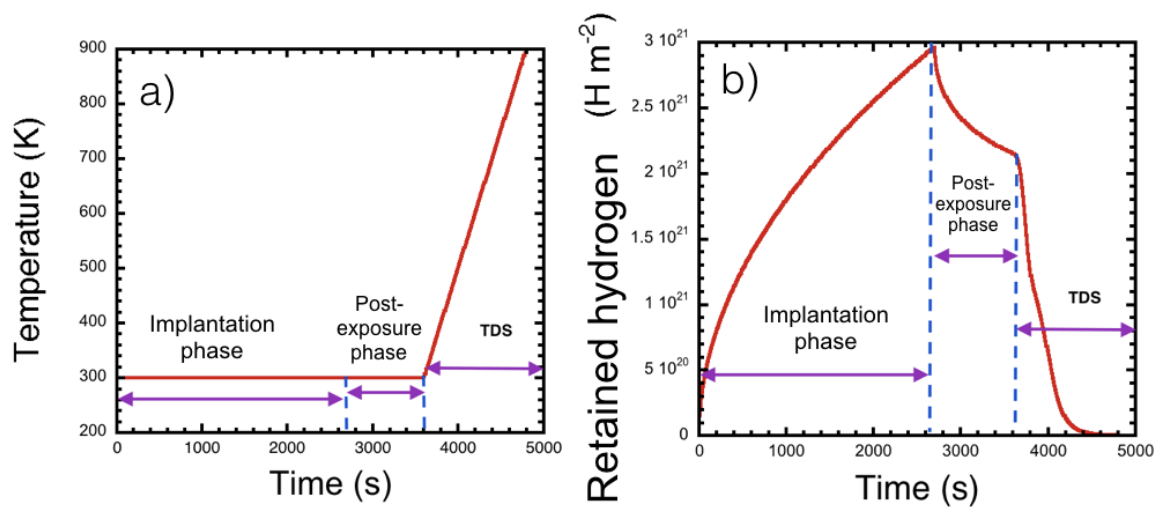


Fig. 5.7 Time variation of the a) temperature and b) retained hydrogen for Al sample implanted with a hydrogen flux of  $1.6 \times 10^{20}$  ions/m<sup>2</sup>s and a sample temperature of 300 K

### 5.4.2 Non-isothermal hydrogen dynamics

This model enables the temperature change in the samples during the implantation phase. The increase and decrease in temperature are exponential, respectively,  $T = T_{exposure} + (T_{rest} - T_{exposure})e^{-(t-t_1)/a}$  and  $T_{rest} + (T_{exposure} - T_{rest})e^{-(t-t_1)/a}$ . In this equation  $a$  can be adjusted to fit experimental results. In this case the value was arbitrarily fixed at  $a = 50$  s.

The imposed time variation of the sample temperature is shown in Fig. 5.8 a) and the time variation of the retained hydrogen is shown in Fig. 5.8 b). It may be observed that the retained hydrogen reaches a local maximum and then decreases when the temperature reaches a stationary value. Then there is a slight desorption followed by an increase in retained hydrogen until it reaches a maximum at the end of the discharge. The first increase corresponds to a non established thermal regime, which means that both the temperature and trapped hydrogen vary, while the second increase correspond to hydrogen loading under an established thermal regime. The non-monotonous phase is due to the interplay between absorption and desorption, and temperature dynamics whereas the monotonous phase occurs once the temperature is established. Once the hydrogen flux is off, we observe a slight decrease of the hydrogen concentration in the material. This decrease is due to the fact that the temperatures keep a high value during the beginning of the post-exposure phase and hence hydrogen is desorbed from the sample. Once the temperature is established during the post-exposure phase, the retained hydrogen in the material remains constant.

The characteristic time for the increase of hydrogen concentration during the beginning of the implantation phase and for the decrease of hydrogen concentration during the beginning of the post-exposure phase may be inferred from Fig. 5.8 b) and is around 50 s. This is comparable to the characteristic time of the increase and decrease of the temperature, which means that the change in hydrogen concentration is limited by the thermal heating kinetics. This would indicate that the absorption and desorption processes are fast.

Fig. 5.8 a) and Fig. 5.8 b) also report the case where the temperature waveform is square (blue dashed lines), which corresponds to an instantaneous heating and instantaneous temperature decrease. In this case, it may be observed that the increase in retained hydrogen is monotonous during the discharge phase. The kink in the retained hydrogen, that characterizes the non-isothermal case at the beginning of the implantation phase, disappears, The slight desorption that takes place just at the beginning of the cooling phase also disappears and the retained hydrogen remains constant up to the beginning of the TDS phase.

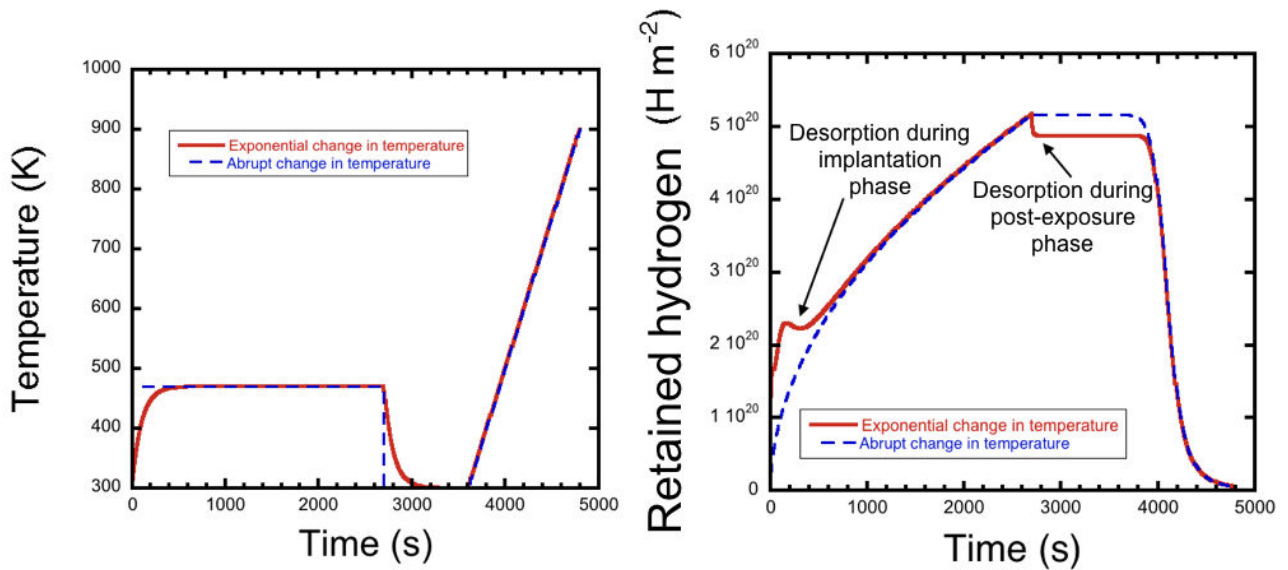


Fig. 5.8 Time variation of the a) temperature and b) retained hydrogen for Al sample implanted with a hydrogen flux of  $1.6 \times 10^{20}$  ions/ $\text{m}^2\text{s}$  and a temperature of 470 K

### 5.4.3 Non-isothermal cyclic hydrogen dynamics

The results corresponding to a simulation of 8 cycles is shown in Fig. 5.9. Fig. 5.9 b) shows the temperature dynamics during the two phases. It is observed that the temperature increases or decreases exponentially during each cycle or phase. At the end of the post-exposure phase, the temperature rapidly increases during the TDS phase.

Fig. 5.9 b) shows the time variation of the retained hydrogen during the two phases. Retained hydrogen showed two time scale variations. The first one is a short time scale that corresponds to the absorption/desorption kinetics. This phenomenon is closely related to the temperature kinetics in the sample and corresponds to the 8 peaks seen during the implantation phase. The second time scale variation is much longer and corresponds to a progressive loading of the samples that increases with and increase of the residual hydrogen retained in the sample (residual retained hydrogen).

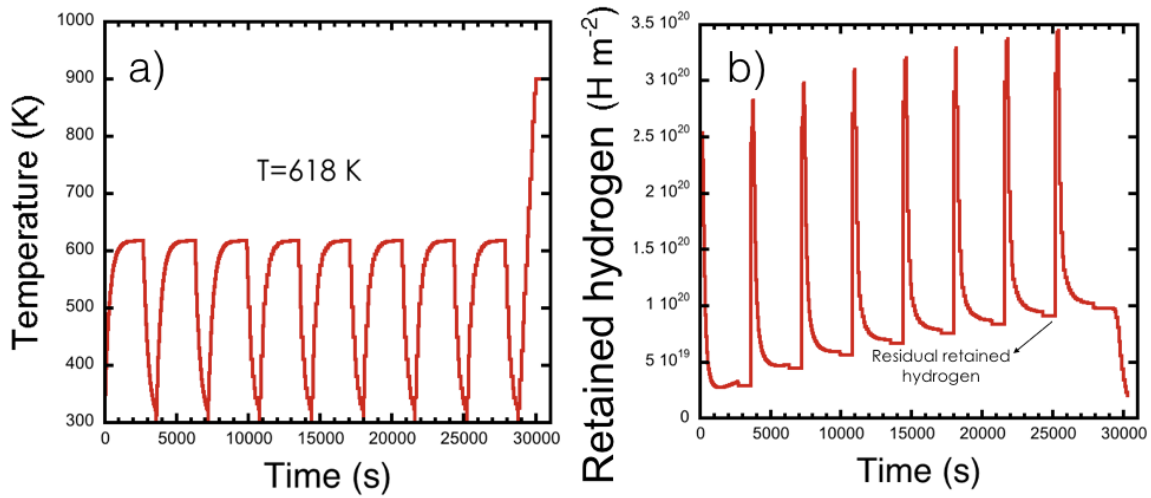


Fig. 5.9 Time variation of the a) temperature and b) retained hydrogen for Al sample implanted during 8 cycles with a hydrogen flux of  $1.6 \times 10^{20}$  ions/m<sup>2</sup>s and a sample temperature of 610 K

#### 5.4.4 MRE simulation of thermal desorption

Thermal desorption spectroscopy (TDS), also known as Temperature-Programmed Desorption (TPD), consists in heating a sample with a controlled evolution of temperature ( $\beta(t) = dT/dt$ ) and measuring quantitatively (*i.e.* by mass spectrometry) the partial pressures of molecules being desorbed from the sample (Schroeder and Gottfried, 2002). Thermal desorption along with the MRE simulations of these TDS may be performed in order to characterize the number of traps and their energy characteristics.

This section consists in performing a simulation of the experimental TDS obtained by Ogorodnikova *et al.* (Ogorodnikova *et al.*, 2003). Fig. 5.10 shows the simulated TDS spectrum performed with HIIPC and its corresponding comparison with the experimental TDS spectrum and the simulation obtained from Ogorodnikova *et al.*.

The experimental procedure used by Ogorodnikova *et al.* consisted in implanting tungsten samples with a deuterium plasma with 250 eV/D and a flux of  $2.5 \times 10^{19}$  D/m<sup>2</sup>s. The TDS was performed with a maximum temperature of 1373 K and a heating rate of 8 K/s.

The HIIPC simulation was performed by taking into account one extrinsic trap creating during ion bombardment. Good agreement is observed between the experiment and the simulation for an ion-induced trap with  $E_{d,3} = 1.5$  eV,  $n_{t,3} = 10^{-1}$  at.fr. and  $\eta = 10^{-3}$ . The maximum defect concentration  $n_{t,3}$  value was chosen given that the vacancy concentration

reaches a saturation about  $10^{-3}$  at.fr at fluences above  $10^{21}$  ions/m<sup>2</sup>. In addition, the trap creation efficiency  $\eta = 10^{-3}$  was obtained by an evaluation performed by Ogorodnikova *et al.* (Ogorodnikova *et al.*, 2003) of the defects as a function of fluence for implantation of 200 eV deuterium ions in polycrystalline tungsten.

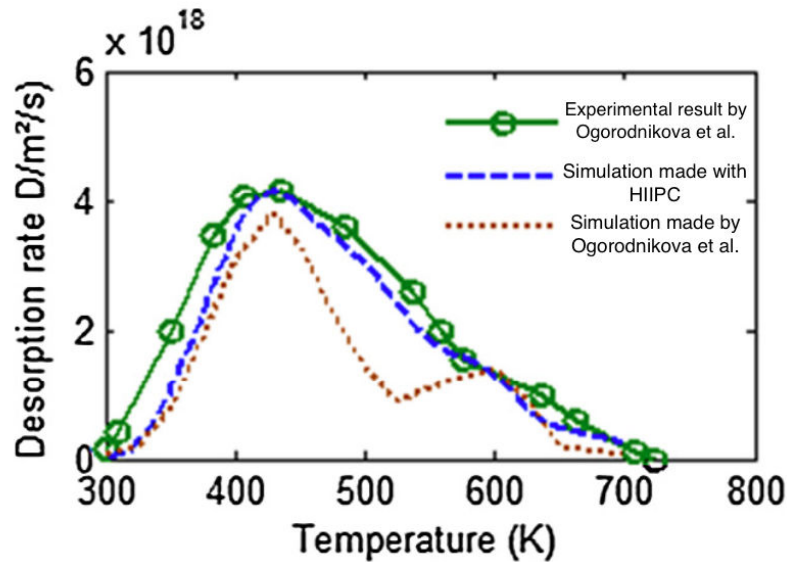


Fig. 5.10 Simulated TDS spectrum with HIIPC (blue dashed line) compared with an experimental TDS spectrum and its simulation obtained from Ogorodnikova *et al.* (Bonnin *et al.*, 2015)

## 5.5 Simulations for specific aluminum loading experiments

The main objective of this section is to apply HIIPC to simulate specific aluminum experiments. First, the results for single crystals are presented followed by a parametric study of the impact incident ion energy has on hydrogen retention dynamics. Finally, the bubble growth kinetics in an aluminum sample is investigated. It is worthy to mention that the simulations in this section are performed assuming aluminum samples with a thickness of 2.5 mm.

### 5.5.1 Aluminum single crystals exposed to hydrogen plasma

This section focuses on analyzing the hydrogen concentration in aluminum after hydrogen implantation. The simulations are performed assuming single crystal aluminum samples. These materials consists of a continuous crystal lattice throughout the whole sample and hence they have an absence of defects associated with the grain boundaries. In other words, single crystals have a lower density of intrinsic defects such as dislocations (Calister and Rethwisch, 2010; Ogorodnikova *et al.*, 2003). As an approximation, for the simulations

it is assumed that single crystals have no dislocations. Therefore, in the simulations only vacancies are taken into account as intrinsic traps in the material.

The simulation consists of an implantation phase, in which the sample is subject to an incident flux of  $\phi = 1.6 \times 10^{20}$  ions/m<sup>2</sup>s with an exposure temperature of  $T = 618$  K and incident ion energy of 320 eV for 30 minutes. The energy used in this simulation is above the threshold energy for defect creation by hydrogen ions in aluminum (195 eV for  $H^+$  ions) so the ion-induced traps, given in equation 5.2.2, are considered for the simulations. The parameters used for the simulations are summarized in Table 5.3 and Table 5.6.

Fig. 5.11 shows the hydrogen depth profile at the end of the implantation phase in ion induced traps, vacancies and solute states. It can be observed that the maximum depth reached by solute hydrogen and hydrogen retained in vacancies is  $10^{-3}$  m. The depth reached by the implanted ions is almost equal to the thickness of the sample. It is worthy to mention that hydrogen diffusion in aluminum is very fast. For our conditions, the characteristic time scale for hydrogen atoms to diffuse over a distance of 1 mm in aluminum is 2 h. This time scale is of the same order of magnitude as the 30 min of implantation time used in this section. Fig. 5.11 also shows that the maximum depth reached by hydrogen trapped by ion-induced defects is  $2.3 \times 10^{-8}$  m.

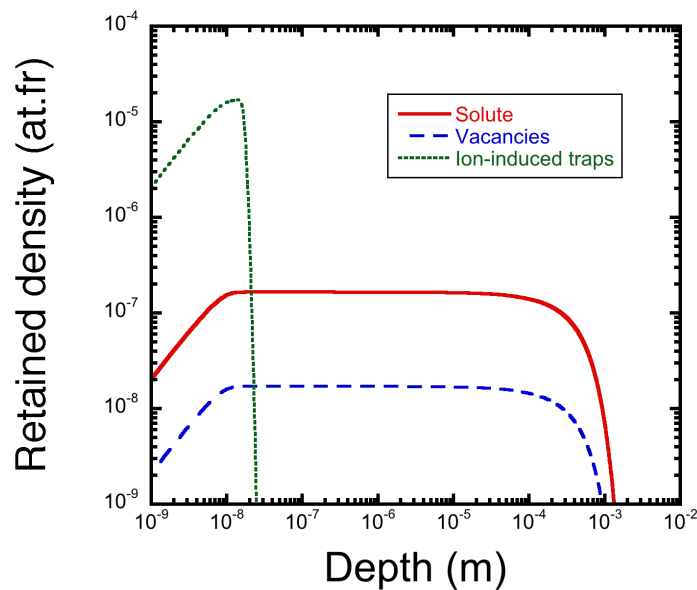


Fig. 5.11 Hydrogen depth profile at the end of the implantation phase in ion induced traps, vacancies and solute states in an aluminum single crystal

The initial slope observed in the depth profiles is due to the desorption process during the implantation phase and to the imposed boundary condition implying that hydrogen recombination is not a rate limiting step. In addition, the diffusion process in aluminum is very fast. The combined effect of fast diffusion to the surface, fast hydrogen recombination at the surface and high temperatures during the implantation phase leads to the observed desorption process.

It can be observed, in Fig. 5.11, that the hydrogen concentration in the traps does not reach the initial imposed density. In other words, the traps are not fully occupied. This process can be quantitatively demonstrated by taking the trapping site occupancy  $\theta_{T,i}$  for each trap, which is defined by:

$$\theta_{T,i} = \frac{C_{t,i}}{n_{t,i}} \quad (5.15)$$

where  $C_{t,i}(x,t)$  is the trapped HI concentration in the  $i$ th trap and  $n_{t,i}$  is the corresponding trap density. This ratio approaches the value of 1 when the trapping process is faster than the de-trapping process, meaning that the traps are completely filled.

The calculated value of  $\theta_{vac}$  is  $4 \times 10^{-5} \ll 1$  and  $\theta_{ind}$  is  $2 \times 10^{-4} \ll 1$ . The latter was performed by taking  $n_{t,i} = 10^{-1}$  at.fr., since the induced trap density reaches the imposed maximum value during the implantation phase. The trap occupancy is low during the implantation phase due to their binding energy and the sample exposure temperature; at higher temperatures atoms have enough energy to leave lower energy traps. Specifically, in this case, the exposure temperature is so high that atoms have enough energy to desorb from the traps in the material.

It is worthy to mention that the density of trapped hydrogen is above the equilibrium value for the two traps, vacancies and ion-induced. As a matter of fact, the equilibrium value obtained for ion induced traps is  $2.7 \times 10^{-7}$  at.fr. and for vacancies is  $2.7 \times 10^{-8}$  at.fr. Therefore, even though these traps are not completely filled, their site occupancy is higher than the one determined for equilibrium conditions. The occupied trap density at equilibrium conditions represents the solubility limit, above which bubbles may precipitate in the material. Since the trap site occupancy is above this limit for ion induced traps and vacancies, hydrogen trapped in both defects may precipitate into bubbles. These results are put in parallel with those obtained experimentally in Section 3.6. This section showed that under the simulation conditions, blisters form all over the surface. That is, the hydrogen trapped in the material precipitates into bubbles that deform the material surface. It is important to notice that

the cross-section of the samples were not analyzed so the depth of the bubbles was not determined.

### 5.5.2 Aluminum exposed to hydrogen plasma at different incident ion energies

This section focuses on investigating the differences that arise when analyzing samples exposed to hydrogen plasma with different incident ion energies. Three different cases were considered: 120 eV, 220 eV and 320 eV. The energy values were chosen based on the value for ion induced defect production, which is 195 eV for  $H^+$  ions (Broeders and Konobeyev, 2004; Hotston, 1975) The lowest energy, 120 eV, is lower than the value needed for vacancy production. The energy of 220 eV, is close to the ion defect generation value and the energy of 320 eV lies above the threshold for ion induced defect production. The objective of this section is to understand hydrogen trapping and diffusion in these samples by using the MRE code.

The analysis on the effect incident ion energy has on hydrogen dynamics in aluminum is carried out by performing three simulations with the three different incident ion energies. The hydrogen dynamics was followed over 3 phases:

- The implantation phase at a temperature of  $T = 618$  K and an incident flux of  $\phi = 1.6 \times 10^{20}$  ions/m<sup>2</sup>s. This phase consists of 8 cycles of 45 minutes of effective implantation followed by 15 minutes of relaxation without any plasma flux. The effective implantation consists of 6 hours plus 2 hours of relaxation time, for a total of 8 hours. The cycles are included in the simulation in order to properly describe plasma exposure in CASIMIR, which is performed in similar cycles.
- A post-exposure phase of 1 hour where the sample is kept at 300 K.
- A TDS phase between 300 K and 900 K with a heating ramp of 1.0 K/s.

Two intrinsic traps are used for the simulations: vacancies and dislocations. For the 220 eV and 320 eV case, the trap creation model is included in the simulations. The specific energies and densities for each trap are presented in Table 5.3 and Table 5.6.

The simulations performed under these conditions show that the total hydrogen concentration in the material increases with incident ion energy. The total hydrogen concentration at the end of the implantation phase is  $7.7 \times 10^{19}$  H/m<sup>2</sup>,  $1.0 \times 10^{20}$  H/m<sup>2</sup> and  $2.0 \times 10^{20}$  H/m<sup>2</sup>

in the samples implanted with an incident ion energy of 120 eV, 220 eV and 320 eV, respectively. The increase in hydrogen concentration may be attributed to different factors: at higher energies there is less ion backscattering and hence more ions are implanted in the material. Also, as energy increases ions are implanted deeper in the material and for sufficiently high energies, ion-induced defects are created in the material. These defects act as traps for hydrogen and as a result the concentration of hydrogen is higher in the material with a higher trap density.

Fig. 5.12 shows the hydrogen depth profile at the end of the implantation phase of solute hydrogen and different retained hydrogen densities in vacancies, dislocations and ion-induced traps in aluminum for each incident ion energy. In the case of the highest incident ion energies, that is 220 eV and 320 eV, hydrogen has enough energy to generate defects in the material. Therefore, the depth profile of the retained hydrogen density in ion-induced traps is shown in Fig. 5.12 b) and c). The ion-induced traps reach a maximum retained density of  $5 \times 10^{-7}$  at.fr. for the case of 220 eV ions and  $1.5 \times 10^{-6}$  at.fr for the case of 320 eV ions. This value is higher for the case of 320 eV given that at this energy more defects are generated in the material and more hydrogen atoms are trapped during the implantation phase.

Fig. 5.12 also shows the maximum depth reached by hydrogen atoms in the material. This depth is in the order of  $10^{-3}$  m for all the analyzed cases. This depth is close to the total thickness of the sample. For the case of ion induced traps, the maximum depth is almost the same for both cases, with a value of  $2 \times 10^{-8}$  m for the 220 eV case and  $3 \times 10^{-8}$  m for the 320 eV case.

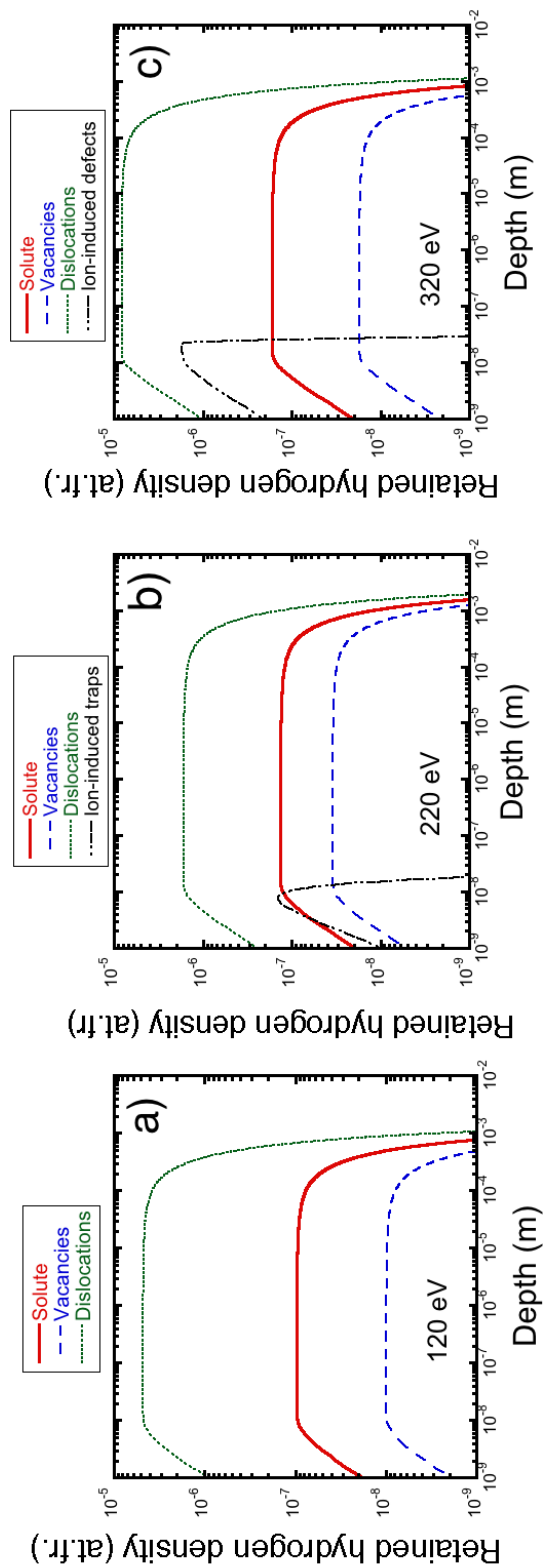


Fig. 5.12 Hydrogen depth profile at the end of the implantation phase of solute hydrogen and different retained hydrogen densities in vacancies, dislocations and ion-induced traps in aluminum for a) 120 eV, b) 220 eV and c) 320 eV incident hydrogen ions

The values of  $\theta_{T,i}$ , defined in equation 5.5.1, for the different traps and incident ion energies are summarized in Table. 5.8. For the ion-induced traps, the maximum created defect density was taken into account as  $n_{t,i}$ . This value corresponds to  $5 \times 10^{-2}$  at.fr. for 220 eV ions and  $1 \times 10^{-1}$  at.fr. for 320 eV ions. It may be observed that the occupation rate increases with energy. This is due to the fact that at higher energies, there is a lower ion backscattering and so less ions are reflected back to the plasma. In addition, ions are implanted deeper in the material. The combination of these two effects lead to a higher probability for ions to remain in the material, which increases the trap occupation rate.

Energy	$\theta_{ind}$	$\theta_{vac}$	$\theta_{dis}$
120 eV	-	$1 \times 10^{-5}$	$1.6 \times 10^{-3}$
220 eV	$5 \times 10^{-5}$	$1.2 \times 10^{-5}$	$2.4 \times 10^{-3}$
320 eV	$8 \times 10^{-6}$	$2 \times 10^{-5}$	$3.6 \times 10^{-3}$

Table 5.8 The value of  $\theta_{T,i}$  for the different traps and incident ion energies

The equilibrium value of  $\theta_{T,i}^{eq}$  is shown in Table. 5.9. These values are lower than those obtained for our conditions (Table. 5.8). This means that even though at our conditions, the traps are not completely filled, the trap site occupancy is higher than at equilibrium conditions.

Energy	$\theta_{ind}^{eq}$	$\theta_{vac}^{eq}$	$\theta_{dis}^{eq}$
120 eV	-	$1.3 \times 10^{-8}$	$1.3 \times 10^{-8}$
220 eV	$8.7 \times 10^{-7}$	$2.0 \times 10^{-8}$	$9.6 \times 10^{-6}$
320 eV	$1.7 \times 10^{-6}$	$2.6 \times 10^{-8}$	$6.4 \times 10^{-6}$

Table 5.9 The value of  $\theta_{T,i}^{eq}$  for the different traps and incident ion energies at equilibrium conditions

Fig. 5.13 shows the depth profile of the total retained hydrogen densities in aluminum for different incident ion energies. It may be observed that maximum retained density increases with energy. These results may be put in parallel with those obtained experimentally since it was determined in Section 3.2 that bubble density and size increase with increasing energy. Therefore, the increase in hydrogen concentration in the material causes a higher bubble nucleation in the material. In addition, as observed in Fig. 5.12 there is an important hydrogen concentration trapped in dislocations. This may be interpreted as an indication that hydrogen trapped in dislocations is able to precipitate into bubbles.

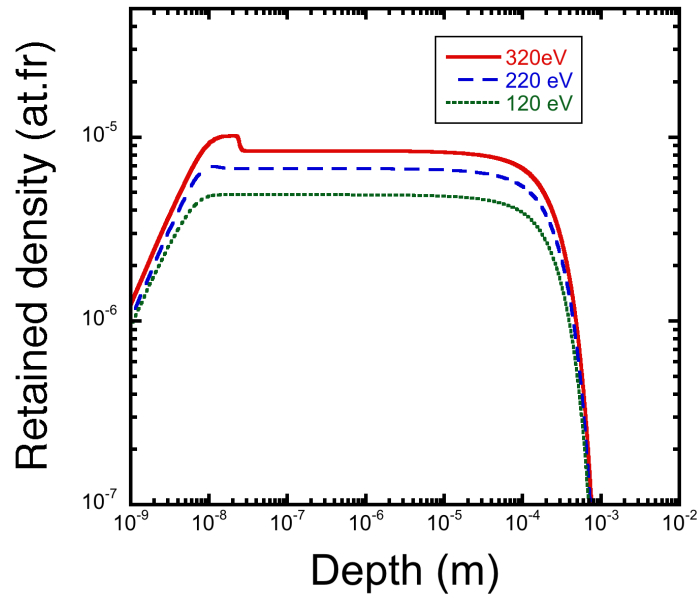


Fig. 5.13 Hydrogen depth profile of the total retained hydrogen densities in aluminum for different incident ion energies

It is important to keep in mind that ion-induced defects play an important role in bubble nucleation. As more defects are generated in the material, bubbles have a higher probability of nucleating. The trap creation model used in the simulations takes only into account the probability a defect will be created by an incident ion, without taking into consideration the dependence this phenomenon has on the hydrogen concentration in the material. As a result, the ion-induced trap density might have been underestimated. As a matter of fact, hydrogen trapped as interstitials leads to an increase in the energy of the system. To compensate for this energy increase, the formation energy of vacancies decreases, which in turn leads to the creation of more vacancies. If further vacancies are created, there is an additional energy increase in the system. To counteract this energy increase vacancies tend to organize into clusters (Condon and Schober, 1993; Ren et al., 2008).

### 5.5.3 Bubble growth in an aluminum sample

Vacancies are able to diffuse in the material at temperatures higher than  $T_m/4$  (with  $T_m$  being the melting temperature) given that vacancies have enough energy to be mobile and agglomerate into clusters (Post and Behrisch, 1986). At lower temperatures vacancies can agglomerate into clusters in the presence of high concentrations of hydrogen in the material. If enough hydrogen filled vacancies diffuse to an intrinsic defect in the material, a bubble may nucleate. This bubble usually lies deeper than the implantation range at a depth of a

few  $\mu\text{m}$ .

The experimental results obtained in Section 3.2 showed that the average depth of bubbles in aluminum samples exposed to hydrogen plasma, with a flux of  $1.6 \times 10^{20}$  ions/m<sup>2</sup>s, a fluence of  $3.3 \times 10^{24}$  ions/m<sup>2</sup> and 320 eV incident ions, is  $92 \mu\text{m}$  reaching an average radius of  $6.7 \mu\text{m}$ .

It is possible to simulate bubble growth by loop punching using HIIPC. In this section, the simulations are performed by using the conditions and parameters already reported in Section 5.5.2. The objective in this section is to show that it is possible for bubbles in aluminum to grow by loop punching, therefore the simulations are performed by using one cycle of 6 h during the implantation phase.

Bubble growth is simulated by taking into account the number of hydrogen atoms in the bubble. An increase in the number of atoms, leads to an increase in the bubble pressure. When the pressure value exceeds the Greenwood pressure, an interstitial loop is created, which allows the bubble to expand. Fig. 5.14 shows the evolution of the bubble pressure during the implantation phase along with the evolution of the Greenwood pressure. It may be observed that the pressure in the bubble increases and at approximately 3 h 30 min it exceeds the Greenwood pressure. This denotes the moment when the bubble starts to grow. On the other hand, the Greenwood pressure remains constant and at 3 h 30 min it starts to decrease. This occurs because the minimum pressure required for a bubble to grow by loop punching decreases with bubble size.

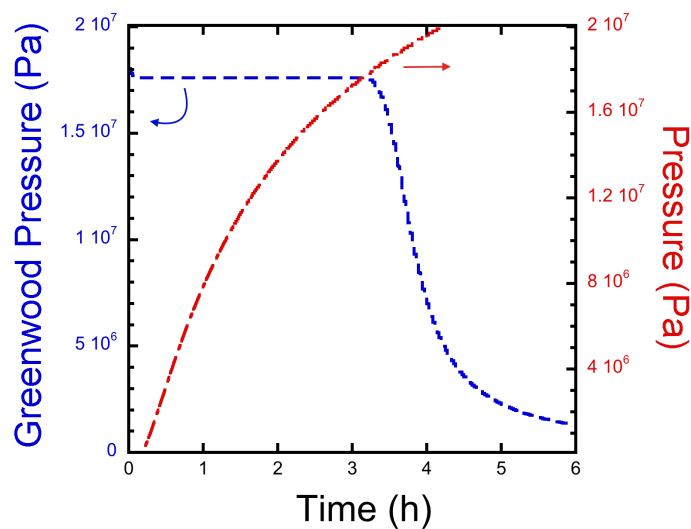


Fig. 5.14 Evolution of the bubble pressure and Greenwood pressure with time

The increase of the bubble radius in aluminum with respect to time is shown in Fig. 5.15. The bubble grows from a pre-existing defect in the material of  $0.5 \mu\text{m}$  that lies at a depth of  $92 \mu\text{m}$ . As was previously determined by analyzing the bubble pressure, the bubble starts to grow after 3 h 30 min. At the end of the implantation phase the radius has increased up to  $6.7 \mu\text{m}$ , the internal pressure has a value of 23 MPa and the total number of hydrogen atoms is  $7.8 \times 10^{21}$ .

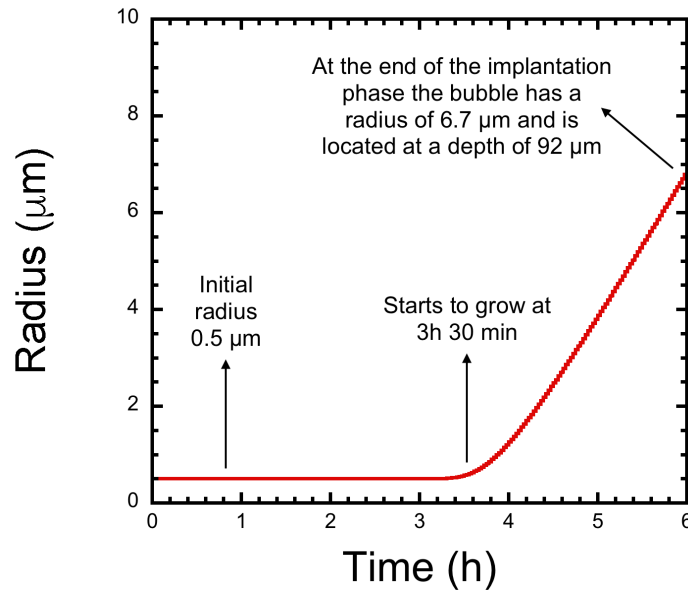


Fig. 5.15 Simulation of bubble growth in aluminum during hydrogen plasma exposure

It is important to remark that the bubble growth shown in Fig. 5.15 is a qualitative result and not a quantitative one. This growth model was used to show that bubble growth by loop punching is possible for our conditions. As a matter of fact, in order to properly reproduce the average bubble radius, a growth law was considered:

$$\frac{dr_b}{dt} = \alpha \left[ 1 - \frac{P_{lim}}{P} \right] \quad (5.16)$$

where  $\alpha$  is imposed to  $9.0 \times 10^{-10}$  m/s.

#### 5.5.4 Thermal desorption Spectroscopy

The simulated TDS spectra simulated after hydrogen implantation with different energy values is depicted in Fig. 5.16. In order to analyze the trapping kinetics in more detail, Fig. 5.16 a) shows the TDS for each different trap, in a log scale, simulated for a sample implanted with 320 eV hydrogen atoms and Fig. 5.16 b) shows the total simulated TDS

spectra for the three different cases.

Fig. 5.16 a) shows that the desorbed hydrogen in the TDS phase comes mainly from dislocations even though there is a small contribution of solute hydrogen and hydrogen trapped in dislocations. It is worthy to mention that due to the high temperatures during the discharge, an important fraction of the solute hydrogen and hydrogen trapped in vacancies and ion-induced defects is desorbed from the sample during the implantation phase. For this reason, it may be observed that the highest desorption during the TDS comes from hydrogen trapped in dislocations. In addition during the post-exposure phase, hydrogen may be desorbed from solutes sites or low energy traps. In this case, the hydrogen trapped in the ion-induced traps was desorbed during the post-exposure phase. As a result, it does not appear in the TDS phase.

It may be observed in Fig. 5.16 b) that for each case there is only one peak at 800 K that increases with incident ion energy. As mentioned above, this peak corresponds mainly to hydrogen trapped in dislocations.

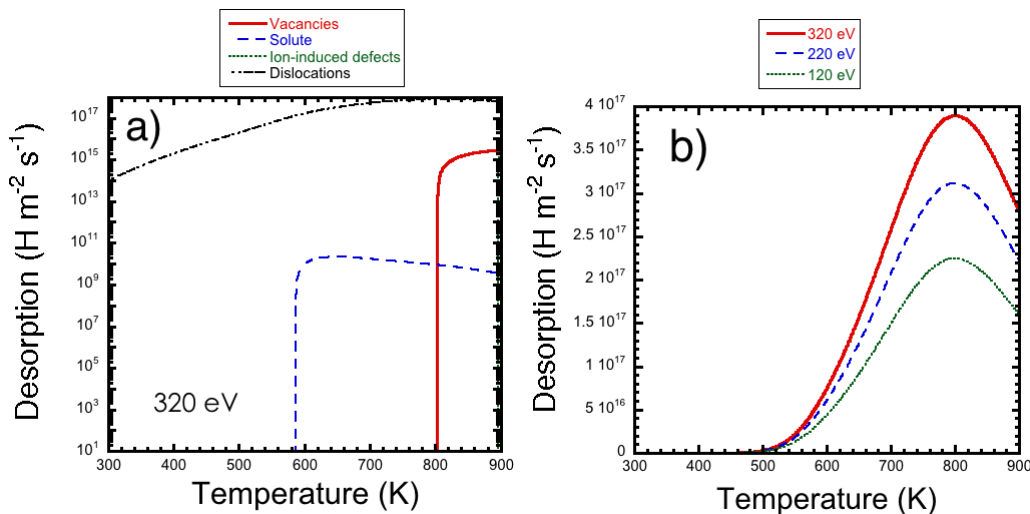


Fig. 5.16 Simulated TDS spectra for aluminum samples implanted with a) 320 eV hydrogen ions and b) different incident ion energies

Fig. 5.16 also shows that hydrogen is not completely desorbed from the material after the TDS. It may be observed that hydrogen desorption flux is not equal to 0 at 900 K. Full desorption requires a much slower time ramp ( $\beta$ ).

## 5.6 Differences in HI retention mechanisms between aluminum and beryllium

This section describes the main differences between the trapping mechanisms of aluminum and beryllium. The simulation is performed for both aluminum and beryllium and consists of three different phases:

- The implantation phase at a temperature of  $T = 618$  K and an incident flux of  $\varphi = 1.6 \times 10^{20}$  ions/m<sup>2</sup>s and incident ion energy of 320 eV. This phase is performed in one cycle with a total duration of 6 h.
- A post-exposure time of 1 hour where the sample is kept at 300 K.
- A TDS phase that starts at 300 K. In this phase the temperature increases with a heating ramp of 1.0 K/s up to 900 K for aluminum and 1100 K for beryllium.

Hydrogen ions with an energy of 320 eV are able to generate defects in both aluminum and beryllium. Therefore, ion-induced trapping was taken into account for the simulations.

Fig. 5.17 a) and b) show the hydrogen depth profile at the end of the implantation phase of solute hydrogen and different retained densities for vacancies and dislocations for Al and Be respectively. One difference may be observed in the ion-induced traps: for aluminum the occupancy density reaches a maximum value of  $2 \times 10^{-5}$  at.fr. whereas for beryllium it reaches a maximum density of  $5 \times 10^{-4}$  at.fr. Even though hydrogen ions are more effective at inducing defects in aluminum, the retained density is lower in ion-induced traps in this material. This is due to the fact that ion-induced traps have a higher energy in beryllium. As a result, a smaller fraction of hydrogen gets desorbed from ion-induced traps in beryllium.

Additionally, it can be appreciated, in Fig. 5.17 b), that dislocations in Be are fully occupied: concentrations reach the imposed density of  $7.5 \times 10^{-3}$  at.fr. This is not the case for Al where the maximum concentration reached in dislocations is  $2.3 \times 10^{-6}$  at.fr. By calculating the value of  $\theta_T$  from equation 5.5.1 it is observed that for dislocations in Be  $\theta_{dis}^{Be}$  has a value of  $0.98 \approx 1$  whereas for dislocations in Al  $\theta_{dis}^{Al}$  has a value of  $1 \times 10^{-5} \ll 1$ . This means that for our conditions, during the implantation phase hydrogen desorbs from dislocations in aluminum whereas this is not the case for beryllium. Desorption during the implantation phase occurs given that for our conditions ( $T = 618$  K) hydrogen atoms may be desorbed from low energy traps. As a matter of fact, the energy of dislocations is lower in Al than in Be (see Table 5.3) and hence hydrogen atoms need a lower energy to desorb from dislocations in aluminum. The desorption kinetics occurring in dislocations in

aluminum explains the reason why the retained hydrogen density in dislocations drops off more smoothly in Al than in Be.

In the case of vacancies, the traps are not fully occupied for either Al or Be. This is due to the low binding energy of this trap. In beryllium and aluminum the trapping site occupancy  $\theta_{vac}$  has values of  $5.7 \times 10^{-4}$  and  $4 \times 10^{-7}$ , respectively. Note that  $\theta_{vac}^{Be}$  is higher than  $\theta_{vac}^{Al}$  because the trapping energy of vacancies in beryllium is higher than aluminum. Therefore a higher temperature is needed to desorb hydrogen trapped in vacancies in beryllium. It is important to notice that the trap occupancy at equilibrium  $\theta_{vac}^{eq}$  for vacancies in beryllium and aluminum is  $6.7 \times 10^{-5}$  and  $2.6 \times 10^{-8}$ , respectively. In both cases, the trap site occupancy is higher than at equilibrium conditions and due to the higher detrapping kinetics in aluminum, this value is higher for beryllium.

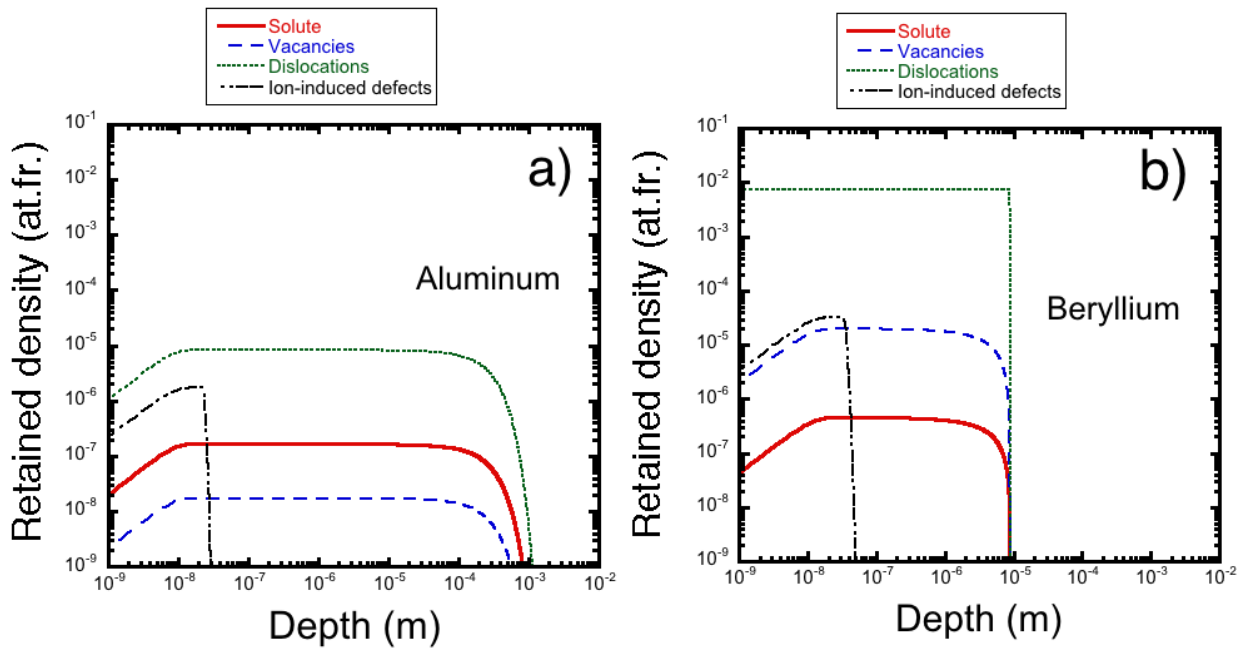


Fig. 5.17 Hydrogen depth profile of different retained densities in solute, vacancies, dislocations and ion-induced traps in a) aluminum and b) beryllium.

The total hydrogen retained density at the end of the discharge was calculated and corresponds to  $9 \times 10^{19}$  at.fr. for Al and  $7.9 \times 10^{21}$  at.fr. for Be, so there is a higher hydrogen concentration in Be than in Al. Fig. 5.17 also shows the maximum depth reached by hydrogen atoms in Al and Be, with values of the order of  $10^{-3}$  m and  $10^{-5}$  m respectively. This difference is due to their different diffusivity values, which are higher for Al. The characteristic time scale for hydrogen to diffuse a distance of 1 mm in aluminum is in the order of 2 h whereas for beryllium is in the order of 10 h. Hence, hydrogen diffuses more

quickly in aluminum than beryllium. In addition, it may be observed that even if hydrogen atoms penetrate deeper in Al than in Be, there is more hydrogen retained in the latter. This is due to the fact that Be has a higher density of traps and the binding energy of these traps is higher. As a result, there is less hydrogen detrapping despite the high temperature of the sample during the discharge.

The simulated TDS spectra for both aluminum and beryllium is depicted in Fig. 5.18. For each case there is only one peak that corresponds mainly to hydrogen trapped in dislocations. In the case of aluminum this peak is located at 800 K and for beryllium it is located at 950 K. Due to the high temperatures, hydrogen is desorbed during the implantation phase and during the TDS phase hydrogen concentration comes mainly from higher energy traps (*i.e.* dislocations).

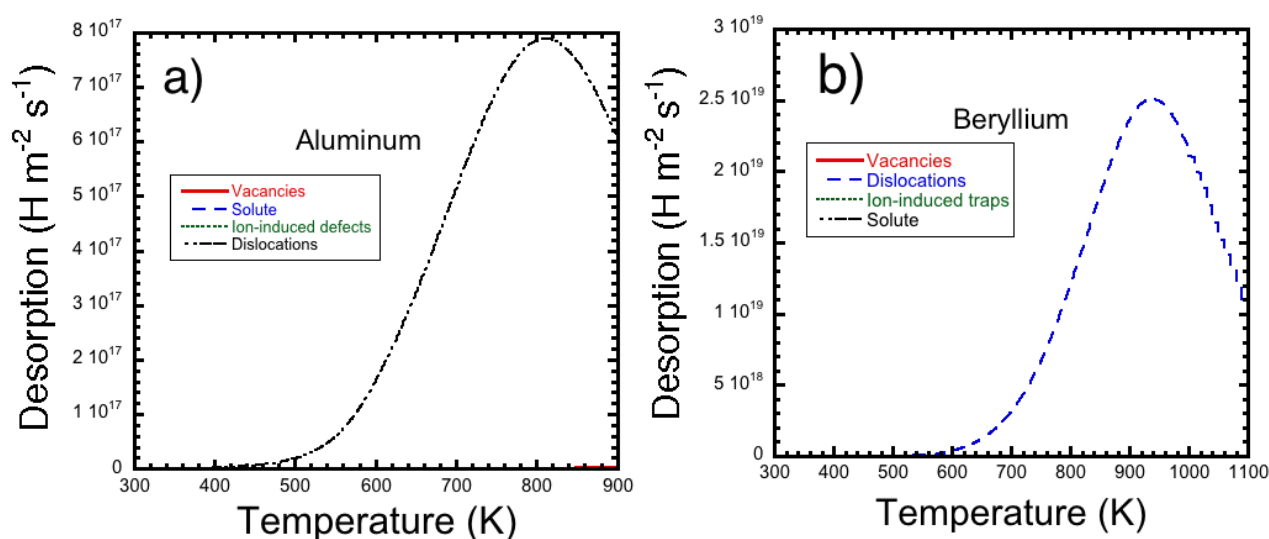


Fig. 5.18 Depth profile of different retained densities in solute, vacancies, dislocations and ion-induced traps in a) aluminum and b) beryllium.

Another main difference between aluminum and beryllium is related to their bubble growth kinetics. As shown in Fig. 5.15, for the simulated conditions a bubble grows up to a  $6.7 \mu\text{m}$  radius and lies at a depth of  $92 \mu\text{m}$ . For Be no bubble growth was observed during the simulations. The recombination rate coefficient shows a very low probability of hydrogen recombination at the bubble edge, as shown in Fig 5.6. This means that it is easier for hydrogen atoms to enter a bubble in Al than in Be. Therefore bubbles are very hardly formed in beryllium at our conditions.

Fig. 5.19 shows the threshold or minimum pressure  $P_{lim}$  required for a bubble to grow by loop punching in Al and Be. This threshold pressure decreases with the bubble radius for both materials. Therefore, as the bubble grows, it requires lower pressures in order to continue increasing in size. Also, since bubbles grow for an existing defect in the material, the larger this intrinsic defect the lower the threshold pressure it requires to grow.

It may also be observed that the threshold pressure is much greater for beryllium than for aluminum. Therefore, a bubble with a given size needs higher pressures to grow in beryllium than in aluminum. It was already determined that due to its low surface recombination value, is more difficult for hydrogen atoms to enter the bubble in Be. As a result, the threshold pressure required to grow by loop punching it is more difficult to achieve in this material. This may explain the fact that it was not possible to simulate bubble growth in beryllium for our conditions.

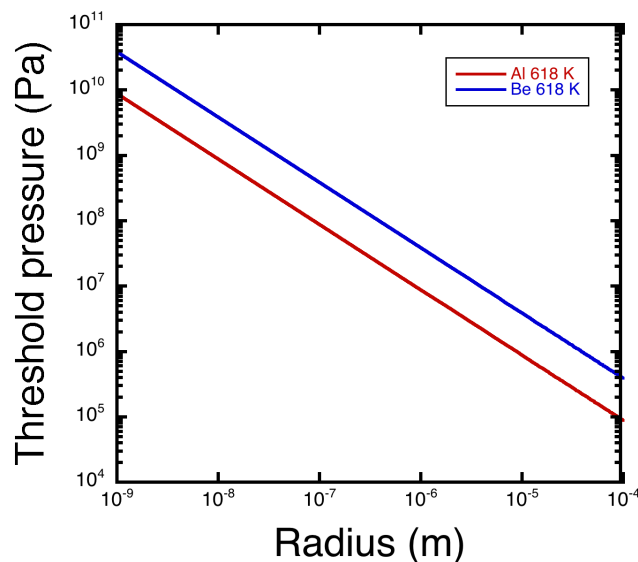


Fig. 5.19 Greenwood pressure  $P_{lim}$  required for a bubble to grow by loop punching in Al and Be

The results obtained in this section show that for our conditions hydrogen dynamics in aluminum and beryllium is completely different. Based on the results aluminum may not be considered an appropriate proxy for beryllium.

## 5.7 Simulation for specific tungsten experiments

Tungsten is a widely studied material both experimentally and numerically using MRE models. During the last few years, great progress has been made by the MHIMS code and in

the scope of the WISCHI project. The MHIMS code is a versatile code, developed in the frame of this project, that is able to simulate hydrogen retention dynamics in tungsten that allows the simulation of ion and neutron induced defects and trapping of multiple HI's in a single vacancy (Hodille, 2016). However, one aspect that has not been widely studied is the bubble formation mechanisms using MRE models deals with the temperature dependence on bubble formation.

This section discusses the effect of the sample temperature on bubble formation kinetics in tungsten. The objective is simulate bubble growth in a temperature range and verify if growth by loop punching is possible in that range. Bubble growth simulations are performed by taking into account experimentally obtained results at a given temperature. Fig. 5.20 shows a SEM micrograph of a tungsten sample exposed to hydrogen plasma with a flux of  $2.0 \times 10^{20}$  ions/m<sup>2</sup>s, fluence of  $2.3 \times 10^{24}$  ions/m<sup>2</sup>, sample exposure temperature of 550 K and incident ion energy of 220 eV. Several blisters with sizes raging between 500 nm and 0.5  $\mu$ m can be observed in the surface. There are also some swollen areas with a size of approximately 5.5  $\mu$ m. For the simulations, the family of blisters with sizes ranging between 0.1 and 0.5  $\mu$ m are taken into account.

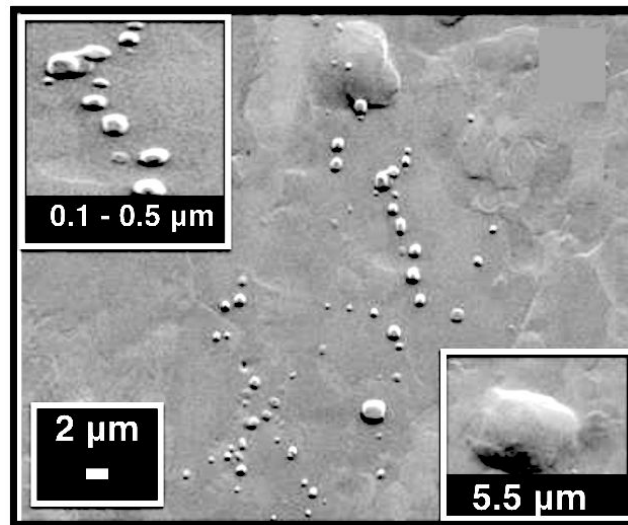


Fig. 5.20 SEM micrograph of a tungsten sample exposed to hydrogen plasma with a flux of  $2.0 \times 10^{20}$  ions/m<sup>2</sup>s, fluence of  $2.3 \times 10^{24}$  ions/m<sup>2</sup> and incident ion energy of 220 eV

To perform the simulations six different cases for sample temperatures ranging between 400 K and 650 K were taken into account. The implantation phase is simulated with a flux of  $2.0 \times 10^{20}$  ions/m<sup>2</sup>s, incident ion energy of 220 eV for 3 h30 min. During this implantation phase, bubble growth takes place.

Bubble growth simulation takes place within an intrinsic defect of 50 nm at a depth of 0.5  $\mu\text{m}$ . Fig. 5.21 shows the simulation of bubble growth in tungsten during hydrogen plasma exposure at different temperatures. It can be observed that the bubble starts to grow at temperatures above 400 K. Below this temperature there is no bubble growth in the material. The bubble radius increases with the temperature reaching a maximum radius at a temperature of 600 K. Above this temperature blister growth does not occur. It can be observed that at 550 K the bubble reaches a radius of 0.3  $\mu\text{m}$ , as obtained from the experimental results shown in Fig. 5.20. In other to reach this value,  $\alpha$  is imposed to  $1.0 \times 10^{-9}$  m/s.

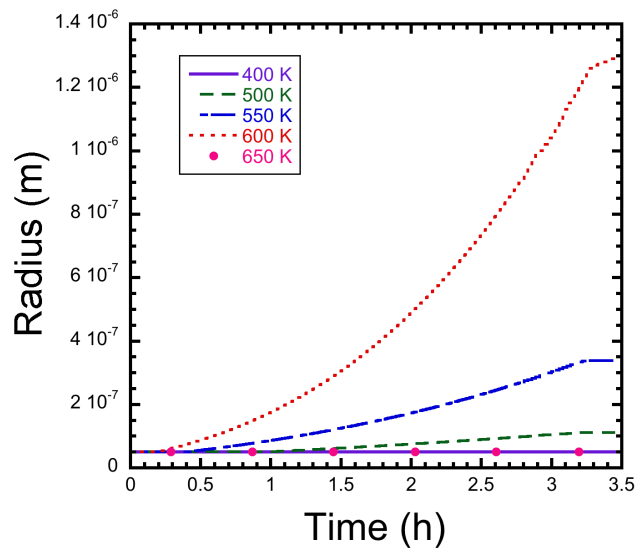


Fig. 5.21 Simulation of bubble growth in tungsten during hydrogen plasma exposure at different temperatures

It is worthy to mention that hydrogen diffusion in the material increases with temperature. The simulated depth ranges between  $2 \times 10^{-5}$  m to  $1 \times 10^{-3}$  m for the simulated temperatures ranging between 400 K and 650 K. The characteristic time scale for hydrogen atoms to diffuse 1 mm in tungsten is in the order of 1 h. This means that hydrogen diffuses quickly in tungsten. At higher diffusion rates, there is a lower local hydrogen concentration for bubble growth. In addition, as shown in Fig. 5.5, hydrogen solubility increases with temperature. This means that as the temperature increases, more hydrogen is able to leave the bubble. It may be concluded that bubble growth does not occur at temperatures higher than 650 K due to a combined effect between an increased hydrogen diffusion and solubility.

The differences in bubble growth at different temperature agrees with experimental studies performed at similar plasma conditions (*i.e.* flux of  $10^{21}$  ions/m<sup>2</sup>s, fluence of  $10^{24}$  ions/m<sup>2</sup> and incident ion energy of 200 eV). These studies determined that blister density and size

increase with temperature, reaching a maximum at 500 K before decreasing for increasing temperatures. No blisters were observed at exposure temperatures above 700 K (Alimov et al., 2008). Similarly, tungsten samples exposed to high flux ( $10^{22}$  ions/m<sup>2</sup>s) deuterium plasma, with an incident ion energy of 38 eV and fluences between  $10^{26}$  and  $10^{27}$  ions/m<sup>2</sup>, show blister formation in the temperature range of 330 K to 650 K. The highest blister density is observed in samples exposed to temperatures ranging between 450 K and 550 K (Lindig et al., 2009).

Both of the experimental cases show that blister formation is a temperature dependent phenomenon. Blister formation was observed in the temperature range of 300 K to 650 K, with a maximum blister density for sample temperatures between 450 K and 550 K. In addition, as determined in the simulation results, bubble growth is observed for temperatures ranging between 400 K and 600 K, with a maximum blister radius obtained at 600 K. This means that it is easier for bubbles to grow by loop punching at temperatures of approximately 600 K. As a result, a higher blister density would be expected for tungsten samples exposed at similar temperatures. There is a slight deviation in the bubble growth temperature range for the simulations and the experimental results. This may be due to the fact that the simulations only take into account growth by loop punching whereas this phenomenon also depends on  $H_2 - v$  clustering and growth by coalescence.

According to these studies, blistering is highly dependent on the sample temperature. Blister density increases for increasing temperatures, reaching a maximum value and then starts to decrease until there is no blister formation in the sample. This phenomenon is due to the fact that at low temperatures (below 500 K) there is a high HI concentration in the material that precipitates into bubbles. However, at higher temperatures (above 500 K) detrapping of HI occurs during the plasma discharge. Therefore, hydrogen concentration decreases in the material and hence the remaining hydrogen is not able to precipitate in blisters.

## 5.8 Summary and discussion

MRE models provide a very useful tool to understand hydrogen trapping and diffusion in materials during and after plasma exposure. They are able to simulate hydrogen trapping in materials, as well as defect creation and bubble growth. In this work, the HIIPC model was used to simulate hydrogen dynamics in aluminum and beryllium, and the possibility to induce bubble formation under different discharge conditions in aluminum, beryllium and

tungsten.

Simulations were performed for hydrogen implantation in aluminum show that the sample temperature plays an important role in hydrogen dynamics. The hydrogen concentration during the implantation phase, the post-exposure phase and the TDS phase were simulated for isothermal and non-isothermal case. The former shows that during the entire post exposure phase, hydrogen is desorbed from the material. This hydrogen corresponds to solute hydrogen or trapped in low energy traps. On the other hand, the non-isothermal case, shows hydrogen desorption during the implantation phase and the post exposure phase. The desorption corresponds to a non established thermal regime, which means that both the temperature and trapped hydrogen vary. Once the temperature is established during the post-exposure phase, the retained hydrogen in the material increases during the implantation phase and remains constant during the post-exposure phase.

Simulations were also performed for hydrogen implantation in aluminum at different energies. The results indicate that hydrogen diffusion in aluminum is very fast. For the analyzed conditions, hydrogen was able to diffuse up to a depth of 1 mm. In addition, the results show that hydrogen concentration increase with energy. This is due to the fact that at higher energies a smaller fraction of ions are backscattered and more defects are induced in the material. It is important to mention that for the analyzed cases, **the hydrogen concentration in traps do not reach the initial imposed density. This means that during the implantation phase, the detrapping kinetics is high and the traps are not completely filled. Nonetheless, the trap site occupancy is higher than in equilibrium conditions.**

Hydrogen trapping dynamics were compared for aluminum and beryllium. An important difference between these two materials is their trapping energy. Beryllium has higher energy traps, which means that hydrogen needs higher energies to be able to leave the traps. Since **at our conditions, detrapping kinetics is high, the energy of traps plays an important role in hydrogen dynamics.** For aluminum, hydrogen is able to be desorbed in ion-induced defects, vacancies and dislocations whereas in beryllium hydrogen is only desorbed from vacancies and ion-induced defects. It is worthy to mention that this desorption kinetics is also due to the imposed boundary conditions, in which it was assumed that hydrogen recombination is not a rate limiting step. This leads to a fast hydrogen recombination, which contributes to the desorption kinetics in the material. This boundary condition is coherent with the RRC values for aluminum and tungsten. However, for beryllium this assumption is questionable. Nonetheless, due to the high energy of traps in beryllium, hydrogen dynamics

in this material is not greatly influenced by the detrapping kinetics and the conclusions drawn from the hydrogen dynamics simulations are accurate.

Bubble growth was also simulated for aluminum and beryllium. The bubbles were assumed to grow from an already intrinsic defect. The high pressures inside this defect allow the bubble to expand by loop punching. In this case, the RRC value play an important role because it determines the number of atoms that are able to enter to the bubble. Therefore, for materials with a low RRC value, bubbles have a lower probability to grow. As a matter of fact, **it was not possible to simulate bubble growth for beryllium**. For aluminum, bubble growth was possible and a bubble obtained from experimental results was simulated.

Bubble growth simulations were performed for tungsten samples in the 400 K-650 K temperature range. **It was determined that bubble growth by loop punching is possible in tungsten for temperatures between 400 K and 600 K**. Bubble growth does not occur at temperatures higher than 600 K because of the high detrapping occurring during the implantation phase. This leads to a lower hydrogen concentration in the material, which inhibits bubble growth.

# Chapter 6

## Conclusions and Perspectives

### 6.1 Conclusions

This work was focused on the study of plasma wall interactions for fusion reactors. In these reactors, plasma facing components may undergo different surface and volume modifications (*i.e.* blister and bubble formation) due to the hard conditions present in the vacuum chamber. The main objective of this work was to analyze these surface and volume modification mechanisms involved in PSI relevant for edge fusion plasmas. Emphasis was made on modifications of either ITER relevant materials, or a suggested proxy of these materials, after hydrogen plasma exposure. An important part of this work was dedicated to the study of blister and bubble growth dynamics in endothermic materials with a cubic crystal system. This was performed with the objective of setting up the methodology for studying similar effects in more complex hexagonal systems such as beryllium, which has a real interest for the fusion community. The materials with a cubic crystal system chosen to perform the experiments were tungsten and aluminum.

In the frame of analyzing blister and bubble dynamics in tungsten and aluminum, experiments were carried out with polycrystalline samples and single crystals. The aim was to separate the effects of grain boundaries on blister and bubble growth and to study the effect the crystallographic structure has on blister growth and morphology. In addition, aluminum samples were exposed to different plasma conditions with the aim of analyzing the effect different plasma parameters (*i.e.* incident ion energy, fluence and discharge regime) have on blister and bubble growth.

Aluminum polycrystalline samples were exposed to a hydrogen plasma with an ion flux of  $1.6 \times 10^{20}$  ions/m<sup>2</sup>s, sample temperature of 618 K, fluence of  $3.3 \times 10^{24}$  ions/m<sup>2</sup> and

incident ion energy between 20 eV and 320 eV. Results showed that blister density and size increase with increasing ion energy. Also, cross-section analysis showed that there are three different cavities in the bulk: blisters, bubbles and cracks. Blisters are bubbles or cavities that can deform the surface material and hence are located closer to the surface. Bubbles are circular cavities that do not deform the material surface. Cracks are very far from the surface and usually located in grain boundaries. These experiments show that the density, size and depth of these cavities increase with energy. The increase in density and size may be attributed to the fact that at higher energies, larger quantity of defects are created in the material, which enhances blister nucleation and growth.

Aluminum polycrystalline samples were also exposed to different plasma fluences in the  $1.4 \times 10^{23} - 4.7 \times 10^{24}$  ions/m<sup>2</sup> range. This was performed by using the same conditions as in the energy analysis and using an incident ion energy of 320 eV. Results showed that blister density and size increase with fluence. In addition, it was observed that intergrain blister kinetics is faster than intragrain blister kinetics. During the experiments it was determined that blister density and size is governed by three processes: appearance (nucleation), blister growth by loop punching and blister growth by coalescence. Finally, experiments performed at higher fluences ( $1.7 \times 10^{25}$  ions/m<sup>2</sup>) show the appearance of cone-like structures that form all over the material surface.

One parameter that greatly affects blister growth dynamics is the plasma discharge regime. Aluminum polycrystalline samples exposed continuously to plasma were exposed to continuous stresses that induce continuous deformation. In this case, blistering was determined to be governed by three processes: blister appearance, blister growth by loop punching and blister coalescence. On the other hand, aluminum polycrystalline samples exposed cyclically to plasma experience cycles of stress and relaxation that leads to a cyclic deformation. Such cyclic deformation leads to a local hardening and decrease in ductility. As a result, existing blisters have a tendency to burst and blisters preferentially nucleate in non-deformed areas, which are easier to deform. For cyclic exposure, blistering was determined to be governed by two processes: blister appearance and blister growth by loop punching.

The issues related to the continuous nature of the discharge should be taken into account for fusion reactors, such as ITER. Since these devices work in a cyclic manner, their plasma facing components should be affected by material hardening and ductility decrease. These phenomena lead to an increased density of burst blisters in the material. On one hand, when blisters burst, hydrogen is desorbed from the material. This helps in minimizing hydrogen

trapping in the material. However, during blister burst dust particles are ejected and may contaminate the core plasma.

Another experimental campaign focused in exposing textured polycrystalline tungsten samples to hydrogen plasma with an incident ion flux of  $1.6 \times 10^{20}$  ions/m<sup>2</sup>s, sample temperature of 600 K, fluence of  $3.3 \times 10^{24}$  ions/m<sup>2</sup> and incident ion energy of 220 eV. Experiments showed different phenomena on the sample surface: multigrain swelling, small blisters, low dome blisters and high dome blisters. Paradoxical results were found regarding a preferred crystallographic orientation for blister growth. It was observed that blisters tend to nucleate in grains that do not correspond to the overall sample texture. It is believed that these grains are subject to stresses and have an increased defect density than the textured grains. As a result, they have more nucleation centers for blistering. On the other hand, experimental results on single crystals show the <111> sample has the higher blister density. However, the difference between the blister surface coverage in the <100>, <110> and <111> samples is more than one order of magnitude. This means that the <111> WSC has a higher density of smaller blisters and the <100> and <110> WSC have a lower density of larger blisters.

Asides from the experimental procedures, simulations were performed with the aim of analyzing hydrogen retention dynamics and bubble growth in aluminum, tungsten and beryllium. This was performed using the macroscopic rate equations approach implemented in The Hydrogen Isotope Inventory Processes Code (HIIPC). For hydrogen implantation in aluminum it was determined that during the hydrogen implantation phase the detrapping kinetics are very high. This is due to the low energy of traps in aluminum and the high temperatures of the sample. Due to this detrapping kinetics, the hydrogen concentration in the traps does not reach the initial imposed density, meaning that the traps are not completely filled. Nonetheless, the trap site occupancy was determined to be higher than the expected for equilibrium conditions. On the other hand, detrapping kinetics in beryllium are not as fast as in aluminum. This is due to the fact that beryllium has higher energy traps and hence hydrogen atoms need higher energies in order to detrapp.

Another important result that may be obtained with HIIPC simulations is to determine the possibility to induce bubble growth by loop punching under different discharge conditions. For aluminum it was possible to simulate bubble growth based on experimental results. However, this was not possible for beryllium. This is due to the fact that the considered recombination rate coefficient (RRC) for this material is very low. The RRC determines the number of atoms that are able to enter the bubble; hence in beryllium not enough hydrogen

was able to enter the bubble and the pressures needed for bubble growth were not reached. On the other hand, bubble growth simulations were performed for tungsten samples in the 400 K-650 K temperature range. It was determined that bubble growth by loop punching is possible in tungsten for temperatures between 400 K and 600 K. Bubble growth does not occur at temperatures higher than 600 K because of the high detrapping occurring during the implantation phase. This leads to a lower hydrogen concentration in the material, which inhibits bubble growth.

These analyses performed in this work showed that blister growth dynamics is a complex phenomenon affected by a large number of parameters. Due to this complexity, and the differences between aluminum and beryllium regarding their physical properties and hydrogen retention dynamics, it may be concluded that aluminum is not a suitable proxy for beryllium. However, it is important to remark that the studies performed during this work were carried out with materials with a low hydrogen solubility (*i.e.* endothermic materials) with a cubic crystal system. It was determined that the crystallographic structure of the material has an important influence in bubble morphology. Experiments performed with tungsten and aluminum single crystals showed that blisters have a step or terraced structure, which is a consequence of the punching of dislocation loops during the growth process. These blister steps are coherent with the slip system of the sample. As a matter of fact, these steps correspond to the macroscopic traces of the atomic scale slip planes of the material and their ND forms a well-defined angle with the surface ND. In the case of aluminum, these angles were measured and found to be consistent with the values given by the stereographic projection. The investigation performed on these two materials enabled us to understand this phenomenon for cubic crystal systems and set the basis for understanding blister morphology in more complex, hexagonal systems such as beryllium.

## 6.2 Perspectives

Taking into account the results obtained during the present work, there is still plenty of work that needs to be performed in order to fully understand the different mechanisms involved in blister growth dynamics. Therefore, many perspectives may be considered.

Experiments related with blister growth dynamics should be performed with beryllium or an appropriate proxy. As an example, in order to understand the influence the crystallographic structure has on blister growth on beryllium, experiments should be performed with a sample that has a hexagonal crystal system. In addition, this material should have the

same slip system as beryllium: a  $\langle 1120 \rangle$  slip direction and a  $\{0001\}$  slip plane (Calister and Rethwisch, 2010). Magnesium has previously been proposed as a proxy for beryllium (Marot et al., 2013); however this material has two additional slip systems than those of beryllium, and hence different systems are activated when subject to the same stresses. In addition, magnesium is an exothermic material whereas beryllium is an endothermic one. In other words, magnesium has a higher affinity to hydrogen and is likely to form hydrides whereas beryllium is not likely to form such compounds. Therefore, an endothermic material with an hexagonal crystal system should be used to perform crystallographic structure analysis. A material that fulfills these conditions is zinc and it may be used to analyze the effect the crystallographic structure has on blister growth. Some physical properties of beryllium and zinc are shown in Table 6.1. It may be observed that this material is not an exact proxy for beryllium; nevertheless, it is a suitable stand-in to analyze blister morphology and growth.

Properties	Beryllium	Zinc
Melting temperature (K)	1560	693
Young's Modulus (GPa)	287	108
Tensile Strength (MPa)	370	200
Moh's Hardness	5.5	2.5
Crystal system	hcp	hcp
Slip System	Slip plane $\{0001\}$	Slip plane $\{0001\}$
	Slip Direction $\langle 1120 \rangle$	Slip Direction $\langle 1120 \rangle$
Solubility	Endothermic	Endothermic

Table 6.1 Some physical properties of beryllium and zinc (Calister and Rethwisch, 2010)

It is worthy to mention that one parameter that plays an important role in blister and bubble formation is temperature. Results in tungsten and beryllium show that blister size and density differ after exposure with different temperatures (Alimov et al., 2008; Jia et al., 2015; Touhouche and B.Terreault, 1994). This parameter was not analyzed in this work; however it is foreseen to implement a mechanism that allows controlling the sample temperature in CASIMIR and thus facilitating the temperature analysis under different conditions and samples.

An important aspect of the analysis of blister growth dynamics is the detection of  $H_2 - v$  clusters in materials after hydrogen plasma exposure. This is possible by performing the analysis under cryogenic conditions and using transmission electron microscopy to charac-

terize the  $H_2 - \nu$  clusters. The detection of  $H_2 - \nu$  clusters was not performed in this work, even though their existence was inferred in the incident ion energy experiments performed on aluminum samples.

A crucial aspect in the study of plasma wall interactions is the dust growth dynamics in plasma environments. During this work, some dust particles were detected however the detected dust density was very low and the dust growth dynamics were not studied. It is important to find the conditions under which an important density of aluminum dust particles may be found in order to perform dust growth measurements. In addition, studies shown in the literature determine that aluminum can be used as a proxy in experiments focused in the formation of hydrides, oxides and alloys with tungsten (Marot et al., 2013). Therefore, dust formation studies using aluminum as a proxy for beryllium may be performed to study mixed material formation. It is important to remark that currently, research is being done at LPSM in relation with the generation of tungsten dust particles. This is being performed in the scope of the STANDS project, in collaboration with the IRSN (Institut de Radioprotection et de Sûreté Nucléaire) and the CEA. This project is focused in analyzing the specific properties of tungsten dust, taking into account its interaction with tritium.

The HIIPC is a versatile model that provides a very useful tool to understand hydrogen trapping and diffusion in materials. Since this is a very complex phenomenon, there are many upgrades that may be included in this model. An update to HIIPC may be performed by including the effect of vacancy diffusion in the simulations. As explained throughout this work, vacancy migration plays a key role in vacancy nucleation and growth. Therefore it is of great importance to include this phenomenon in the simulations. Also, the RRC for beryllium must be revised. If the RRC for this material is as low as the value found in the literature, then it is not possible to assume that this phenomenon is not a rate limiting step. Therefore, either an appropriate boundary condition that considers the RRC must be taken into account or the RRC value for beryllium must be revised.

Another important update in HIIPC concerns including the coupled diffusion, mechanical fields and trapping due to plastic deformation in the material. This upgrade is being performed by proposing a solution method using finite elements of the 3D diffusion and kinetics of trapping with the mechanical fields. The objective is to establish a general equation and to implement it in the Abaqus code. The main complexity of this update relies on the fact that the hydrogen dynamics of trapping and detrapping in HIIPC are calculated for non-equilibrium conditions whereas the coupled diffusion and mechanical fields are calculated

---

for equilibrium conditions. At the present moment, this task is the main focus of Sofiane Benannoune's thesis work.



# References

- E. Abramov, M.P. Riehm, D.A. Thompson, and W.W. Smeltzer. Deuterium permeation and diffusion in high-purity beryllium. *Journal of Nuclear Materials*, 175(1–2):90 – 95, 1990. ISSN 0022-3115. doi: [http://dx.doi.org/10.1016/0022-3115\(90\)90274-Q](http://dx.doi.org/10.1016/0022-3115(90)90274-Q).
- I Adamovich, S D Baalrud, A Bogaerts, P J Bruggeman, M Cappelli, V Colombo, U Czarnetzki, U Ebert, J G Eden, P Favia, D B Graves, S Hamaguchi, G Hieftje, M Hori, I D Kaganovich, U Kortshagen, M J Kushner, N J Mason, S Mazouffre, S Mededovic Thagard, H-R Metelmann, A Mizuno, E Moreau, A B Murphy, B A Niemira, G S Oehrlein, Z Lj Petrovic, L C Pitchford, Y-K Pu, S Rauf, O Sakai, S Samukawa, S Starikovskaia, J Tenyson, K Terashima, M M Turner, M C M van de Sanden, and A Vardelle. The 2017 plasma roadmap: Low temperature plasma science and technology. *Journal of Physics D: Applied Physics*, 50(32):323001, 2017. URL <http://stacks.iop.org/0022-3727/50/i=32/a=323001>.
- V Kh Alimov, W M Shu, J Roth, K Sugiyama, S Lindig, M Balden, K Isobe, and T Yamanishi. Surface morphology and deuterium retention in tungsten exposed to low-energy, high flux pure and helium-seeded deuterium plasmas. *Physica Scripta*, 2009(T138):014048, 2009. URL <http://stacks.iop.org/1402-4896/2009/i=T138/a=014048>.
- V.Kh. Alimov, J. Roth, R.A Causey, D.A. Komarov, CH. Linsmeier, A. Wiltner, F. Kost, and S. Lindig. Deuterium retention in tungsten exposed to low-energy, high flux clean and carbon-seeded deuterium plasmas. *Journal of Nuclear Materials*, 375:192–201, 2008.
- R.A. Anderl, M.R. Hankins, G.R. Longhurst, R.J. Pawelko, and R.G. Macaulay-Newcombe. Hydrogen transport behavior of beryllium. *Journal of Nuclear Materials*, 196:986 – 991, 1992. ISSN 0022-3115. doi: [http://dx.doi.org/10.1016/S0022-3115\(06\)80181-9](http://dx.doi.org/10.1016/S0022-3115(06)80181-9).
- R.A. Anderl, R.A. Causey, J.W. Davis, R.P. Doerner, G. Federici, A.A. Haasz, G.R. Longhurst, W.R. Wampler, and K.L. Wilson. Hydrogen isotope retention in beryllium for tokamak plasma-facing applications. *Journal of Nuclear Materials*, 273(1):1 – 26, 1999. ISSN 0022-3115. doi: [http://dx.doi.org/10.1016/S0022-3115\(99\)00022-7](http://dx.doi.org/10.1016/S0022-3115(99)00022-7).
- M. Balden, N. Endstrasser, P.W. Humrickhouse, V. Rohde, M. Rasinski, U. von Toussaint, S. Elgeti, R. Neu, and the ASDEX Upgrade Team. Collection strategy, inner morphology, and size distribution of dust particles in asdex upgrade. *Nuclear Fusion*, 54(7):073010, 2014. URL <http://stacks.iop.org/0029-5515/54/i=7/a=073010>.
- Martin Balden, Stefan Lindig, Armin Manhard, and Jeong-Ha You. D<sub>2</sub> gas-filled blisters on deuterium-bombarded tungsten. *Journal of Nuclear Materials*, 414(1):69 – 72, 2011. ISSN 0022-3115. doi: <http://dx.doi.org/10.1016/j.jnucmat.2011.04.031>.

- M.J. Baldwin, R.P. Doerner, D. Nishijima, D. Buchenauer, W.M. Clift, R.A. Causer, and K. Schmid. Be-W alloy formation in static and divertor-plasma simulator experiments. *Journal of Nuclear Materials*, 363-365:1179–1183, 2007.
- M.J. Baldwin, T. Schwarz-Selinger, and R.P. Doerner. Experimental study and modelling of deuterium thermal release from Be-D co-deposited layers. *Nuclear Fusion*, 54(7):073005, 2014. URL <http://stacks.iop.org/0029-5515/54/i=7/a=073005>.
- M.I. Baskes. A calculation of the surface recombination rate constant for hydrogen isotopes on metals. *Journal of Nuclear Materials*, 92(2-3):318 – 324, 1980. ISSN 0022-3115. doi: [http://dx.doi.org/10.1016/0022-3115\(80\)90117-8](http://dx.doi.org/10.1016/0022-3115(80)90117-8).
- Rainer Behrish. *Sputtering by Particle Bombardment II: Sputtering of alloys and compounds, electron and neutron sputtering, surface topography*, volume 52. Springer, Germany, 1983.
- Rainer Behrish and Wolfgang Eckstein. *Sputtering by Particle Bombardment: Experiments and computer calculations from threshold to MeV energies*, volume 110. Springer, Germany, 2007.
- L. Berardinucci. Modelling of tritium permeation through beryllium as plasma facing material. *Journal of Nuclear Materials*, 258–263, Part 1:777 – 781, 1998. ISSN 0022-3115. doi: [http://dx.doi.org/10.1016/S0022-3115\(98\)00116-0](http://dx.doi.org/10.1016/S0022-3115(98)00116-0).
- R. Bisson, S. Markelj, O. Mourey, F. Ghiorghiu, K. Achkasov, J.-M. Layet, P. Roubin, G. Cartry, C. Grisolia, and T. Angot. Dynamic fuel retention in tokamak wall materials: An in situ laboratory study of deuterium release from polycrystalline tungsten at room temperature. *Journal of Nuclear Materials*, 467, Part 1:432 – 438, 2015. ISSN 0022-3115. doi: <http://dx.doi.org/10.1016/j.jnucmat.2015.07.028>.
- X. Bonnin, E. Hodille, N. Ning, C. Sang, and Ch. Grisolia. Rate equations modeling for hydrogen inventory studies during a real tokamak material thermal cycle. *Journal of Nuclear Materials*, 463:970 – 973, 2015. ISSN 0022-3115. doi: <http://dx.doi.org/10.1016/j.jnucmat.2014.10.053>. 21Proceedings of the 21st International Conference on Plasma-Surface Interactions in Controlled Fusion Devices Kanazawa, Japan May 26-30, 2014.
- Masashi Shimada Brad Merrill and Paul W. Humrickhouse. Simulating tritium retention in tungsten with a multiple trap model in the TMAP code. *Journal of Plasma and Fusion Research*, 45(40):71 – 75, 2013. URL [http://www.jspf.or.jp/JPFERS/index\\_vol10.html](http://www.jspf.or.jp/JPFERS/index_vol10.html).
- W.H. Bragg and W.L. Bragg. The reflection of X-rays by crystals. *Proceedings of the Royal Society of London: Series A, Containing papers of a mathematical and physical character*, 605(88):428–438, 1913. doi: 10.1098/rspa.1913.0040. URL <http://rspa.royalsocietypublishing.org/content/88/605/428>.
- Bruce L. Bramfitt and Arlan O. Benschoter. *Metallographer's Guide: Practices and Procedures for irons and steels*. ASM International, United States, 2002.
- G.J. Brendel, E.M. Marlett, and L.M. Niebylski. Crystalline beryllium hydride. *Inorganic Chemistry*, 17(12):3589–3592, 1978. URL <http://pubs.acs.org/doi/abs/10.1021/ic50190a051>.

- C.H.M. Broeders and A.Yu Konobeyev. Defect production efficiency in metals under neutron irradiation. *Journal of Nuclear Materials*, 328:197–214, 2004.
- V.L. Bukhovets, A.E. Gorodetsky, R.Kh. Zalavutdinov, A.P. Zakharov, E.E. Mukhin, and A.G. Razdobarin. Sputtering of w and al in D<sub>2</sub>/O<sub>2</sub> plasma cleaning discharge. *Journal of Nuclear Materials*, 463:255 – 257, 2015. ISSN 0022-3115. doi: <http://dx.doi.org/10.1016/j.jnucmat.2014.12.059>. 21Proceedings of the 21st International Conference on Plasma-Surface Interactions in Controlled Fusion Devices Kanazawa, Japan May 26-30, 2014.
- Luxertha Buzi. *Influence of the Particle Flux on Surface Modifications of Tungsten*. PhD thesis, Ghent University and Lorraine University, 2015.
- William D. Calister and David G. Rethwisch. *Materials Science and Engineering An Introduction*. Jonh Wiley and Sons, United States, eight edition, 2010.
- Rion A Causey. Hydrogen isotope retention and recycling in fusion reactor plasma-facing components. *Journal of Nuclear Materials*, 300(2–3):91 – 117, 2002. ISSN 0022-3115. doi: [http://dx.doi.org/10.1016/S0022-3115\(01\)00732-2](http://dx.doi.org/10.1016/S0022-3115(01)00732-2).
- Rion A Causey. Hydrogen in beryllium: Solubility, transport and trapping. *Physial Review B*, 79:134101, 2009.
- Rion A. Causey and Kenneth L. Wilson. Fusion reactor materials tritium inventory and permeation in the ITER beryllium. *Journal of Nuclear Materials*, 212:1436 – 1442, 1994. ISSN 0022-3115. doi: [http://dx.doi.org/10.1016/0022-3115\(94\)91065-0](http://dx.doi.org/10.1016/0022-3115(94)91065-0).
- Francis Chen. *An Indispensable Truth. How Fusion Power Can Save the Planet*. Springer, United States, 2011.
- J.B. Condon and T. Schober. Hydrogen bubbles in metals. *Journal of Nuclear Materials*, 207: 1 – 24, 1993. ISSN 0022-3115. doi: [http://dx.doi.org/10.1016/0022-3115\(93\)90244-S](http://dx.doi.org/10.1016/0022-3115(93)90244-S).
- Robert W Conn, Russell P Doerner, and Jongik Won. Beryllium as the plasma-facing material in fusion energy systems—experiments, evaluation, and comparison with alternative materials. *Fusion Engineering and Design*, 37(4):481 – 513, 1997. ISSN 0920-3796. doi: [http://dx.doi.org/10.1016/S0920-3796\(97\)00092-6](http://dx.doi.org/10.1016/S0920-3796(97)00092-6).
- B.D Cullity and S.R. Stock. *Elements of X-Ray Diffraction*. Pearson Education Limited, United States, third edition, 2014.
- Ligia Colina Delacqua. *Modélisation/diagnostic de production de poussières dans un plasma hydrogène au contat d'une cible C/W. Contribution à l'étude des interactions plasma/surface dans les machines de fusion thermonucléaire*. PhD thesis, Université Paris XIII, 2012.
- K. Detemple, O. Kanert, J. Th. M. De Hosson, and K.L Murty. In situ nuclear magnetic resonance investigation of deformation-generated vacancies in aluminum. *Physical Review B*, 52(1):125 – 133, 1995.

- R.P. Doerner, C. Björkas, D. Nishijima, and T. Schwarz-Selinger. Erosion of beryllium under high-flux plasma impact. *Journal of Nuclear Materials*, 438, Supplement:S272 – S275, 2013. ISSN 0022-3115. doi: <http://dx.doi.org/10.1016/j.jnucmat.2013.01.045>. Proceedings of the 20th International Conference on Plasma-Surface Interactions in Controlled Fusion Devices.
- R.P. Doerner, M.J. Baldwin, and D. Nishijima. Plasma-induced morphology of beryllium targets exposed in piscis-b. *Journal of Nuclear Materials*, 455(1–3):1 – 4, 2014. ISSN 0022-3115. doi: <http://dx.doi.org/10.1016/j.jnucmat.2014.02.010>. Proceedings of the 16th International Conference on Fusion Reactor Materials (ICFRM-16).
- G. Duesing, W. Sassin, W. Schilling, and H. Hemmerich. Defect production during low temperature electron irradiation. *Crystal Lattice Defects*, 1:55–68, 1969.
- Stéphane Dufrenoy. *Influence des transformations surfaciques induites par traitements thermomécaniques sur la tenue en fatigue du Ti-10V-2Fe-3Al*. PhD thesis, Université Paris XIII, 2016.
- Wolfgang Eckstein. Calculated sputtering, reflection and range values. Technical report, Max-Planck Institut, 2002.
- G. Effenberg and S. Ilyenko, editors. *Al-Ni-W (Aluminium - Nickel - Tungsten)*, pages 1–11. Springer Berlin Heidelberg, Berlin, Heidelberg, 2005. ISBN 978-3-540-31694-7. doi: 10.1007/10915998\_34. URL [http://dx.doi.org/10.1007/10915998\\_34](http://dx.doi.org/10.1007/10915998_34).
- Olaf Engler and Valerie Randle. *Texture Analysis: Macrotecture, Microtexture and Orientation Mapping*. CRC Press Taylor and Francis Group, United States, second edition, 2010.
- Baran Eren, Laurent Marot, Marco Wisse, Daniel Mathys, Maryline Joanny, Jean-Marcel Travère, Roland Steiner, and Ernst Meyer. In situ evaluation of the reflectivity of molybdenum and rhodium coatings in an iter-like mixed environment. *Journal of Nuclear Materials*, 438, Supplement:S852 – S855, 2013. ISSN 0022-3115. doi: <http://dx.doi.org/10.1016/j.jnucmat.2013.01.184>. Proceedings of the 20th International Conference on Plasma-Surface Interactions in Controlled Fusion Devices.
- J.H. Evans. An interbubble fracture mechanism of blister formation on helium-irradiated metals. *Journal of Nuclear Materials*, 68(2):129 – 140, 1977. ISSN 0022-3115. doi: [http://dx.doi.org/10.1016/0022-3115\(77\)90232-X](http://dx.doi.org/10.1016/0022-3115(77)90232-X).
- G. Federici, C.H. Skinner, J.N. Brooks, J.P. Coad, C. Grisolia, A.A. Haasz, A. Hassanein, V. Philipps, C.S. Pitcher, J. Roth, W.R. Wampler, and D.G. Whyte. Plasma-material interactions in current tokamaks and their implications for next step fusion reactors. *Nuclear Fusion*, 41(12):1967, 2001. URL <http://stacks.iop.org/0029-5515/41/i=12/a=218>.
- G. Federici, R. Doerner, P. Lorenzetto, and V. Barbash. *Beryllium as a Plasma-Facing Material for Near Term Fusion Devices*, chapter Beryllium as a Plasma-Facing Material for Near Term Fusion Devices. Elsevier, 2012.
- Peter E.J. Flewitt and R.K. Wild. *Physical Methods for Materials Characterisation*. IOP publishing, United Kingdom, second edition, 2003.

- Alexander Fridman. *Plasma Chemistry*. Cambridge University Press, United States, 2008.
- Francisco Eiichi Fujita. The role of hydrogen in the fracture of iron and steel. *Transactions of the Japan Institute of Metals*, 17(4):232–238, 1976. doi: 10.2320/matertrans1960.17.232.
- Y. Fukai. *The Metal-Hydrogen System. The basic bulk properties*, volume 2nd. Springer, Germany, 2005.
- Y. Fukai and H. Sugimoto. Diffusion of hydrogen in metals. *Advances in Physics*, 34(2):263–326, 1985. doi: 10.1080/00018738500101751. URL <http://dx.doi.org/10.1080/00018738500101751>.
- Vikram Gavini, Kaushik Bhattacharya, and Michael Ortiz. Vacancy clustering and prismatic dislocation loop formation in aluminum. *Phys. Rev. B*, 76:180101, Nov 2007. doi: 10.1103/PhysRevB.76.180101. URL <https://link.aps.org/doi/10.1103/PhysRevB.76.180101>.
- Joseph I. Goldstein, Dale Newbury, David Joy, Charles Lyman, Patrick Echlin, Eric Lifshin, Linda Sawyer, and Joseph Michael. *Scanning Electron Microscopy and X-Ray Microanalysis*. Springer Science, United States, 2012.
- G.W. Greenwood, A.J.E. Foreman, and D.E. Rimmer. The role of vacancies and dislocations in the nucleation and growth of gas bubbles in irradiated fissile material. *Journal of Nuclear Materials*, 4:305–324, 1959.
- K. Heinola and T. Ahlgren. Diffusion of hydrogen in bcc tungsten studied with first principle calculations. *Journal of Applied physics*, 107(11), 2010.
- E A Hodille, Y Ferro, N Fernandez, C S Becquart, T Angot, J M Layet, R Bisson, and C Grisolia. Study of hydrogen isotopes behavior in tungsten by a multi trapping macroscopic rate equation model. *Physica Scripta*, 2016(T167):014011, 2016. URL <http://stacks.iop.org/1402-4896/2016/i=T167/a=014011>.
- E.A. Hodille, X. Bonnin, R. Bisson, T. Angot, C.S. Becquart, J.M. Layet, and C. Grisolia. Macroscopic rate equation modeling of trapping/detrapping of hydrogen isotopes in tungsten materials. *Journal of Nuclear Materials*, 467, Part 1:424 – 431, 2015. ISSN 0022-3115. doi: <http://dx.doi.org/10.1016/j.jnucmat.2015.06.041>.
- E.A. Hodille, A. Založnik, S. Markelj, T. Schwarz-Selinger, C.S. Becquart, R. Bisson, and C. Grisolia. Simulations of atomic deuterium exposure in self-damaged tungsten. *Nuclear Fusion*, 57(5):056002, 2017. URL <http://stacks.iop.org/0029-5515/57/i=5/a=056002>.
- Etienne Hodille. *Etude de l'implantation du deutérium dans les composés face au plasma constituants du tokamak ITER*. PhD thesis, Université d'Aix Marseille, November 2016.
- E. Hotston. Threshold energies for sputtering. *Nuclear Fusion*, 15(3):544, 1975. URL <http://stacks.iop.org/0029-5515/15/i=3/a=018>.
- W.L. Hsu, R.A. Causey, B.E. Mills, J. Ehrenberg, and V. Philipps. Transient release of deuterium from beryllium after plasma ion implantation. *Journal of Nuclear Materials*, 176–177:218 – 225, 1990. ISSN 0022-3115. doi: [http://dx.doi.org/10.1016/0022-3115\(90\)90049-S](http://dx.doi.org/10.1016/0022-3115(90)90049-S). URL <http://www.sciencedirect.com/science/article/pii/002231159090049S>.

- Alice Hu and Ahmed Hassanein. Modeling hydrogen isotope behavior in fusion plasma-facing components. *Journal of Nuclear Materials*, 446(1–3):56 – 62, 2014. ISSN 0022-3115. doi: <http://dx.doi.org/10.1016/j.jnucmat.2013.11.033>.
- Minoru Ichimura, Yasushi Sasajima, and Mamoru Imabayashi. Grain boundary effect on diffusion of hydrogen in pure aluminum. *Materials Transactions, JIM*, 32(12):1109–1114, 1991. doi: 10.2320/matertrans1989.32.1109.
- ITER. Chapter 2: Plasma confinement and transport. *Nuclear Fusion*, 39(12):2175, 1999. URL <http://stacks.iop.org/0029-5515/39/i=12/a=302>.
- ITER. Iter, 2017. URL <http://www.iter.org>.
- Takahiro Izumi and Goroh Itoh. Thermal desorption spectroscopy study on the hydrogen trapping states in a pure aluminum. *Material Transactions*, 52(2):130 – 134, 2011.
- R.G. Saint Jacques. La formation des cloques. *Nuclear Instruments and Methods*, 209-210: 333–343, 1983.
- G. A. Jeffrey, G.S. Parry, and R.L. Mozzi. Study of the wurtzite type binary compounds. structures of aluminum nitride and beryllium oxide. *The Journal of Chemical Physics*, 25: 1024, 1956.
- Y.Z. Jia, G. De Temmerman, G.-N. Luo, H.Y. Xu, C. Li, B.Q. Fu, and W. Liu. Surface morphology and deuterium retention in tungsten exposed to high flux d plasma at high temperatures. *Journal of Nuclear Materials*, 457:213 – 219, 2015. ISSN 0022-3115. doi: <http://dx.doi.org/10.1016/j.jnucmat.2014.11.079>.
- Y.Z. Jia, W. Liu, B. Xu, G.-N. Luo, S.L. Qu, T.W. Morgan, and G. De Temmerman. Mechanism for orientation dependence of blisters on w surface exposed to d plasma at low temperature. *Journal of Nuclear Materials*, 477:165 – 171, 2016. ISSN 0022-3115. doi: <http://dx.doi.org/10.1016/j.jnucmat.2016.05.011>.
- John B. Sullivan Jr. and Gary R. Krieger. *Clinical Environmental Health and Toxic Exposures*. Lippincott Williams and Wilkins, United States, second edition, 2001.
- Kohji Kamada. Hydrogen implantation effects in the subsurface layer of aluminum -bubble pressure and surface modifications. *Journal of Nuclear Materials*, 169:141 – 150, 1989. ISSN 0022-3115. doi: [http://dx.doi.org/10.1016/0022-3115\(89\)90529-1](http://dx.doi.org/10.1016/0022-3115(89)90529-1).
- Hiroaki Kawamura, Vijay Kumar, Qiang Sun, and Yoshiyuki Kawazoe. Bonding character of hydrogen in aluminum clusters. *Materials Transactions*, 42(11):2175–2179, 2001. doi: 10.2320/matertrans.42.2175.
- B.J Keene. Review of data for the surface tension of pure metals. *International Materials Reviews*, 38(4):157–192, 1993. URL <http://www.tandfonline.com/doi/abs/10.1179/imr.1993.38.4.157?journalCode=yimr20>.
- Charles Kittel. *Introduction to solid state physics*, volume 8th. John Wiley and Sons Inc, United States, 2005.

- Dmitry Kogut. *Study of wall conditioning in tokamaks with application to ITER*. PhD thesis, Aix Marseille Université, November 2014.
- R.D. Kolasinski, D.F. Cowgill, and R.A. Causey. A continuum-scale model of hydrogen precipitate growth in tungsten plasma-facing materials. *Journal of Nuclear Materials*, 415(1, Supplement):S676 – S679, 2011. ISSN 0022-3115. doi: <http://doi.org/10.1016/j.jnucmat.2010.10.077>. Proceedings of the 19th International Conference on Plasma-Surface Interactions in Controlled Fusion.
- Rudy Konings. *Comprehensive Nuclear Materials*. Elsevier, United States, first edition, 2012.
- K.Pawlik and P.Ozga. Labosoft: The texture analysis for windows, 1999. URL <http://www.labosoft.com.pl>.
- A Kreter, T Dittmar, D Nishijima, R P Doerner, M J Baldwin, and K Schmid. Erosion, formation of deposited layers and fuel retention for beryllium under the influence of plasma impurities. *Physica Scripta*, 2014(T159):014039, 2014. URL <http://stacks.iop.org/1402-4896/2014/i=T159/a=014039>.
- A Lacoste, T Lagarde, S Béchu, Y Arnal, and J Pelletier. Multi-dipolar plasmas for uniform processing: physics, design and performance. *Plasma Sources Science and Technology*, 11(4):407, 2002. URL <http://stacks.iop.org/0963-0252/11/i=4/a=307>.
- Legifrance. Legifrance, 2001. URL <https://www.legifrance.gouv.fr/affichTexte.do?cidTexte=JORFTEXT000000220917&categorieLien=id>.
- Michael A. Lieberman and Allan J. Lichtenberg. *Principles of plasma discharges and materials processing*. John Wiley and sons, United States, 2005.
- S. Lindig, M. Balden, V. Alimov, T. Yamanishi, W. M. Shu, and J. Roth. Subsurface morphology changes due to deuterium bombardment of tungsten. *Physica Scripta*, 2009(T138):014040, 2009. URL <http://stacks.iop.org/1402-4896/2009/i=T138/a=014040>.
- G. R. Longhurst, D.F. Holland, J.L. Jones, and B.J. Merrill. *TMAP4 User Manual*, June 1992. URL <http://www.osti.gov/scitech/servlets/purl/7205576/>.
- Glen R. Longhurst. *TMAP7 User Manual*, Dec 2008. URL <http://www.osti.gov/scitech/servlets/purl/952013>.
- Evgenii G Maksimov and O A Pankratov. Hydrogen in metals. *Soviet Physics Uspekhi*, 18(7):481, 1975. URL <http://stacks.iop.org/0038-5670/18/i=7/a=R01>.
- A. Manhard, G. Matern, and M. Balden. A step-by-step analysis of the polishing process for tungsten specimens. *Practical Metallography*, 50(1):5–16, 2013. URL <http://www.hanser-elibrary.com/doi/abs/10.3139/147.110215>.
- A. Manhard, T. Schwarz-Selinger, K. Schmid, and U. von Toussaint. Comparison of a quantitative diffusion-trapping model with experiments on D uptake in damaged W. In *Joint ICTP-IAEA Conference on Models and Data for Plasma-Material Interaction in Fusion Devices*, Miramare, Trieste, November 2014.

- Armin Manhard. *Deuterium Inventory in Tungsten after Plasma Exposure: A Microstructural Survey*. PhD thesis, Augsburg University, 2011.
- Nicola Manini. *Introduction to the Physics of Matter. Basic Atomic, Molecular, and Solid-State Physics*. Springer, Switzerland, 2014.
- Andrey V. Markin, Vladimir N. Chernikov, Sergey Yu. Rybakov, and Andrey P. Zakharov. Thermal desorption of deuterium implanted into beryllium. *Journal of Nuclear Materials*, 233:865 – 869, 1996. ISSN 0022-3115. doi: [http://dx.doi.org/10.1016/S0022-3115\(96\)00044-X](http://dx.doi.org/10.1016/S0022-3115(96)00044-X).
- Laurent Marot, Christian Linsmeier, Baran Eren, Lucas Moser, Roland Steiner, and Ernst Meyer. Can aluminium or magnesium be a surrogate for beryllium: A critical investigation of their chemistry. *Fusion Engineering and Design*, 88(9–10):1718 – 1721, 2013. ISSN 0920-3796. doi: <http://dx.doi.org/10.1016/j.fusengdes.2013.04.040>. Proceedings of the 27th Symposium On Fusion Technology (SOFT-27); Liège, Belgium, September 24–28, 2012.
- A. McNabb and P.K Foster. A new analysis of the diffusion of hydrogen in iron and ferritic steels. *Transactions of the metallurgical society of Aime*, 227:618 – 627, 1963.
- Edgar E. Vidal Alfred Goldberg Edward. N.C. Dalder David L. Olson Nrajendra Mishra, editor. *Beryllium Chemistry and Processing*. ASM International, 2009.
- M. Miyamoto, D. Nishijima, Y. Ueda, R.P. Doerner, H. Kurishita, M.J. Baldwin, S. Morito, K. Ono, and J. Hanna. Observations of suppressed retention and blistering for tungsten exposed to deuterium–helium mixture plasmas. *Nuclear Fusion*, 49(6):065035, 2009. URL <http://stacks.iop.org/0029-5515/49/i=6/a=065035>.
- A. Mutzke, G. Bandelow, and R. Schneider. Sputtering of mixed materials of beryllium and tungsten by hydrogen and helium. *Journal of Nuclear Materials*, 467 Part 1:413 – 417, 2015. ISSN 0022-3115. doi: <https://doi.org/10.1016/j.jnucmat.2015.05.052>.
- NIH. Image processing and analysis in java, 2017. URL <https://imagej.nih.gov/ij/>.
- D. Nishijima, H. Iwakiri, K. Amano, M.Y. Ye, N. Ohno, K. Tokunaga, N. Yoshida, and S. Takamura. Suppression of blister formation and deuterium retention on tungsten surface due to mechanical polishing and helium pre-exposure. *Nuclear Fusion*, 45(7):669, 2005. URL <http://stacks.iop.org/0029-5515/45/i=7/a=016>.
- NIST. Nist, 2016. URL <http://www.nist.gov/pml/data/handbook/>.
- M. Oberkofler and Ch. Linsmeier. Properties of nitrogen-implanted beryllium and its interaction with energetic deuterium. *Nuclear Fusion*, 50(12):125001, 2010. URL <http://stacks.iop.org/0029-5515/50/i=12/a=125001>.
- M. Oberkofler, M. Reinelt, and Ch. Linsmeier. Retention and release mechanisms of deuterium implanted into beryllium. *Nuclear Instruments and Methods in Physics Research Section B: Beam Interactions with Materials and Atoms*, 269(11):1266 – 1270, 2011. ISSN 0168-583X. doi: <http://dx.doi.org/10.1016/j.nimb.2010.11.058>. Proceedings of the 18th International Workshop on Inelastic Ion-Surface Collisions (IISC-18).

- O.V Ogorodnikova. *Hydrogen and Helium Recycling at Plasma Facing Materials: Trapping effect in Hydrogen Retention in Metals*, chapter Trapping effect in hydrogen retention in metals. Springer, 1st ed edition, 2002.
- O.V Ogorodnikova. Fundamental aspects of deuterium retention in tungsten at high flux plasma exposure. *Journal of Applied Physics*, 118:074902, 2015. doi: 10.1063/1.4928407. URL <http://dx.doi.org/10.1063/1.4928407>.
- O.V Ogorodnikova, J Roth, and M Mayer. Deuterium retention in tungsten in dependence of the surface conditions. *Journal of Nuclear Materials*, 313–316:469 – 477, 2003. ISSN 0022-3115. doi: [http://dx.doi.org/10.1016/S0022-3115\(02\)01375-2](http://dx.doi.org/10.1016/S0022-3115(02)01375-2). Plasma-Surface Interactions in Controlled Fusion Devices 15.
- O.V Ogorodnikova, J Roth, and M Mayer. Ion-driven deuterium retention in tungsten. *Journal of Applied Physics*, 103:034902, 2008. doi: 10.1063/1.2828139. URL <http://dx.doi.org/10.1063/1.2828139>.
- J.G.O. Ojwang, Rutger A. van Santen, Gert Jan Kramer, Adri C. T van Duin, and William A. Goddard. Parametrization of a reactive force field for aluminum hydride. *The journal of chemical physics*, 131:044501, 2009.
- R.A. Oriani. The diffusion and trapping in steel. *Acta Metallurgica*, 18:147–157, 1970.
- K. Ouaras, M. Redolfi, C. Quiros, X. Bonnin, G. Lombardi, D. Vrel, and K. Hassouni. Blister investigation on tungsten surface under hydrogen environment: grain orientation dependence and blister bursts. Private communication at LSPM, 2016.
- Karim Ouaras. *Mécanismes de formation et dynamique du transport des poussières de carbone et de tungstène dans un plasma Micro-onde magnétisé et non-magnétisé*. PhD thesis, Université Paris XIII, 2016.
- Edward D. Palik. *Handbook of Optical Constants of Solids*. Elsevier, United States, 1998a.
- Edward. D. Palik. *Handbook of Optical Constants of Solids*. Elsevier, United States, 1998b.
- V. Philipps. Tungsten as material for plasma-facing components in fusion devices. *Journal of Nuclear Materials*, 415(1, Supplement):S2 – S9, 2011. ISSN 0022-3115. doi: <http://dx.doi.org/10.1016/j.jnucmat.2011.01.110>. Proceedings of the 19th International Conference on Plasma-Surface Interactions in Controlled Fusion.
- V Philipps, J Roth, and A Loarte. Key issues in plasma–wall interactions for iter: a european approach. *Plasma Physics and Controlled Fusion*, 45(12A):A17, 2003. URL <http://stacks.iop.org/0741-3335/45/i=12A/a=002>.
- R. Piechoczek, M. Reinelt, M. Oberkofler, A. Allouche, and Ch. Linsmeier. Deuterium trapping and release in Be(0 0 0 1), Be(11–20) and polycrystalline beryllium. *Journal of Nuclear Materials*, 438, Supplement:S1072 – S1075, 2013. ISSN 0022-3115. doi: <http://dx.doi.org/10.1016/j.jnucmat.2013.01.235>. Proceedings of the 20th International Conference on Plasma-Surface Interactions in Controlled Fusion Devices.
- D.E. Post and R. Behrisch. *Physics of Plasma-Wall Interactions in Controlled Fusion*. Plenum Press, United States, first edition, 1986.

- Jean-Louis Pouchou. *L'analyse EBSD: Principes et applications*. Réunion thématique de décembre Université Paris VI, France, 2002.
- Dean L. Preston and Duane C. Wallace. A model of the shear modulus. *Solid State Communications*, 81(3):277 – 281, 1992. ISSN 0038-1098. doi: [http://dx.doi.org/10.1016/0038-1098\(92\)90514-A](http://dx.doi.org/10.1016/0038-1098(92)90514-A).
- Robert L. Price and W. Gray Jerome. *Basic Confocal Microscopy*. Springer, United States, first edition, 2011.
- Krishnan Radhakrisnan and Alan C. Hindmarsh. *Description and use of LSODE, the Livermore Solver for Ordinary Differential Equations*. National Aeronautics and Space Administration, United States of America, 1993.
- George T. Rado and Harry Suhl. *Spin Arrangements and crystal structure, domains and micromagnetics: A treatise on Modern Theory and Materials*. Elsevier, United States, 1963.
- X. Ren, G. Shan, W. Chu, Y. Su, K. Gao, L. Qiao, B. Jiang, G. Chen, and Y. Cui. Initiating, growing and cracking of hydrogen blisters. *Chinese Science Bulletin*, 50(17):1962–1965, 2005. ISSN 1861-9541. doi: <http://dx.doi.org/10.1360/982004-581>.
- X.C. Ren, Q.J. Zhou, G.B. Shan, W.Y. Chu, J.X. Li, Y.J. Su, and L.J. Qiao. A nucleation mechanism of hydrogen blister in metals and alloys. *Metallurgical and Materials Transactions A*, 39(1):87–97, 2008. ISSN 1543-1940. doi: <http://dx.doi.org/10.1007/s11661-007-9391-3>.
- J.P. Roszell, J.W. Davis, and A.A. Haasz. Temperature dependence of deuterium retention mechanisms in tungsten. *Journal of Nuclear Materials*, 429(1–3):48 – 54, 2012. ISSN 0022-3115. doi: <http://dx.doi.org/10.1016/j.jnucmat.2012.05.018>.
- J. Roth, R. Preuss, W. Bohmeyer, S. Brezinsek, A. Cambe, E. Casarotto, R. Doerner, E. Gauthier, G. Federici, S. Higashijima, J. Hogan, A. Kallenbach, A. Kirschner, H. Kubo, J.M. Layet, T. Nakano, V. Philipps, A. Pospieszczyk, R. Pugno, R. Ruggiéri, B. Schweer, G. Sergienko, and M. Stamp. Flux dependence of carbon chemical erosion by deuterium ions. *Nuclear Fusion*, 44(11):L21, 2004. URL <http://stacks.iop.org/0029-5515/44/i=11/a=L01>.
- Joachim Roth and Klaus Schmid. Hydrogen in tungsten as plasma-facing material. *Physica Scripta*, 2011(T145):014031, 2011. URL <http://stacks.iop.org/1402-4896/2011/i=T145/a=014031>.
- Jacky Ruste. Microscopie électronique à balayage -principe et équipement, September 2016. URL <http://www.techniques-ingenieur.fr>.
- A. San-Martin and F.D. Manchester. The Al-H (Aluminum-Hydrogen) system. *Journal of Phase Equilibria*, 13(1), 1992.
- Chaofeng Sang, Xavier Bonnin, Manoj Warriar, Abha Rai, Ralf Schneider, Jizhong Sun, and Dezhen Wang. Modelling of hydrogen isotope inventory in mixed materials including porous deposited layers in fusion devices. *Nuclear Fusion*, 52(4):043003, 2012. URL <http://stacks.iop.org/0029-5515/52/i=4/a=043003>.

- Chaofeng Sang, Jizhong Sun, Xavier Bonnin, Shengguang Liu, and Dezhen Wang. Numerical simulation of the bubble growth due to hydrogen isotopes inventory processes in plasma-irradiated tungsten. *Journal of Nuclear Materials*, 443(1–3):403 – 408, 2013. ISSN 0022-3115. doi: <http://dx.doi.org/10.1016/j.jnucmat.2013.07.052>.
- Chaofeng Sang, Jizhong Sun, Xavier Bonnin, Shuyu Dai, Wanpeng Hu, and Dezhen Wang. Numerical study of the effects of physical parameters on the dynamic fuel retention in tungsten materials. *Journal of Nuclear Materials*, 455(1–3):111 – 115, 2014. ISSN 0022-3115. doi: <http://dx.doi.org/10.1016/j.jnucmat.2014.05.025>. Proceedings of the 16th International Conference on Fusion Reactor Materials (ICFRM-16).
- Chaofeng Sang, Jizhong Sun, Xavier Bonnin, L. Wang, and Dezhen Wang. Simulation of hydrogen bubble growth in tungsten by a hybrid model. *Journal of Nuclear Materials*, 463: 367 – 371, 2015. ISSN 0022-3115. doi: <http://dx.doi.org/10.1016/j.jnucmat.2014.11.063>. 21 Proceedings of the 21st International Conference on Plasma-Surface Interactions in Controlled Fusion Devices Kanazawa, Japan May 26-30, 2014.
- K Schmid. Diffusion-trapping modelling of hydrogen recycling in tungsten under ELM-like heat loads. *Physica Scripta*, 2016(T167):014025, 2016. URL <http://stacks.iop.org/1402-4896/2016/i=T167/a=014025>.
- K. Schmid, V. Rieger, and A. Manhard. Comparison of hydrogen retention in W and W/Ta alloys. *Journal of Nuclear Materials*, 426(1–3):247 – 253, 2012. ISSN 0022-3115. doi: <http://dx.doi.org/10.1016/j.jnucmat.2012.04.003>.
- K Schmid, U. von Toussaint, and T. Scharzw-Sellinger. Transport of hydrogen in metals with occupancy dependent trap energies. *Journal of applied physics*, 116(134901):12, 2014. URL <http://dx.doi.org/10.1063/1.4896580>.
- Sven L.M. Schroeder and Michael Gottfried. Temperature-Programmed Desorption (TPD) Thermal Desorption Spectroscopy(TDS). Technical report, Advanced Physical Chemistry Laboratory, FU Berlin, 2002.
- E Serra, G Benamati, and O.V Ogorodnikova. Hydrogen isotopes transport parameters in fusion reactor materials. *Journal of Nuclear Materials*, 255(2–3):105 – 115, 1998. ISSN 0022-3115. doi: [http://dx.doi.org/10.1016/S0022-3115\(98\)00038-5](http://dx.doi.org/10.1016/S0022-3115(98)00038-5).
- W.M. Shu. High-dome blisters formed by deuterium-induced local superplasticity. *Applied Physics Letters*, 92(21), 2008. doi: <http://dx.doi.org/10.1063/1.2937139>.
- W.M. Shu, E. Wakai, and T. Yamanishi. Blister bursting and deuterium bursting release from tungsten exposed to high fluences of high flux and low energy deuterium plasma. *Nuclear Fusion*, 47(3):201, 2007. URL <http://stacks.iop.org/0029-5515/47/i=3/a=006>.
- D.A. Skinn, J.P. Gallagher, A.P. Berens, P.D. Huber, and J. Smith. *Damage Tolerant Design Handbook*. University of Dayton, United States, 1994.
- Peter C. Stangeby. *The plasma boundary of magnetic fusion devices*. IOP Publishing, England, 2000.

- Struers. Metallographic preparation of aluminum and aluminum alloys, 2016. URL <http://www.struers.com/-/media/Library/Brochures/English/Application-Note-Aluminium.pdf?dmc=1&ts=20170405T1227150496>.
- G. De Temmerman, J. Daniels, K. Bystrov, M.A. van den Berg, and J.J. Zielinski. Melt-layer motion and droplet ejection under divertor-relevant plasma conditions. *Nuclear Fusion*, 53(2):023008, 2013. URL <http://stacks.iop.org/0029-5515/53/i=2/a=023008>.
- M Tkacz and A Litwiniuk. Useful equations of state of hydrogen and deuterium. *Journal of Alloys and Compounds*, 330(Supplement C):89 – 92, 2002. ISSN 0925-8388. doi: [https://doi.org/10.1016/S0925-8388\(01\)01488-8](https://doi.org/10.1016/S0925-8388(01)01488-8). URL <http://www.sciencedirect.com/science/article/pii/S0925838801014888>. Proceedings of the International Symposium on Metal-Hydrogen Systems, Fundamentals and Applications (MH2000).
- K. Touhouche and B.Terreault. Surface microstructure of high temperature beryllium implanted with deuterium. *Materials Research Society Symposium Proceedings*, 316:987–992, 1994.
- R. Z. Valiev, I. V. Alexandrov, Y. T. Zhu, and T. C. Lowe. Paradox of strength and ductility in metals processed by severe plastic deformation. *Journal of Materials Research*, 17(1): 5–8, 2002. doi: 10.1557/JMR.2002.0002.
- Brian D. Wirth, K.D. Hammond, S.I. Krasheninnikov, and D. Maroudas. Challenges and opportunities of modeling plasma–surface interactions in tungsten using high-performance computing. *Journal of Nuclear Materials*, 463:30 – 38, 2015. ISSN 0022-3115. doi: <http://dx.doi.org/10.1016/j.jnucmat.2014.11.072>. Plasma-Surface Interactions 21 Proceedings of the 21st International Conference on Plasma-Surface Interactions in Controlled Fusion Devices Kanazawa, Japan May 26-30, 2014.
- M. Wisse, B. Eren L. Marot, R. Steiner, D. Mathys, and E. Meyer. Laser damage thresholds of ITER mirror materials and first results on in situ laser cleaning of stainless steel mirrors. *Fusion Engineering and Design*, 88(2):388–399, 2013.
- C. Wolverton, V. Ozolins, and M. Asta. Hydrogen in aluminum: First-principle calculations of structure and thermodynamics. *Physical Review B*, 69:144109, 2004.
- G.M. Wright, M. Mayer, K. Ertl, G. de Saint-Aubin, and J. Rapp. TMAP7 simulations of deuterium trapping in pre-irradiated tungsten exposed to high-flux plasma. *Journal of Nuclear Materials*, 415(1, Supplement):S636 – S640, 2011. ISSN 0022-3115. doi: <http://dx.doi.org/10.1016/j.jnucmat.2011.01.011>. Proceedings of the 19th International Conference on Plasma-Surface Interactions in Controlled Fusion.
- H.Y. Xu, G.N. Luo, H. Schut, Y. Yuan, B.Q. Fu, A. Godfrey, W. Liu, and G.De. Temmerman. Enhanced modification of tungsten surface by nanostructure formation during high flux deuterium plasma exposure. *Journal of Nuclear Materials*, 447(1–3):22 – 27, 2014. ISSN 0022-3115. doi: <http://dx.doi.org/10.1016/j.jnucmat.2013.12.010>.
- H.Y. Xu, W. Liu, G.N. Luo, Y. Yuan, Y.Z. Jia, B.Q. Fu, and G. De Temmerman. Blistering on tungsten surface exposed to high flux deuterium plasma. *Journal of Nuclear Materials*, 471: 51 – 58, 2016. ISSN 0022-3115. doi: <http://dx.doi.org/10.1016/j.jnucmat.2015.12.025>.

- G.A. Young and J.R. Scully. The diffusion and trapping of hydrogen in high purity aluminum. *Acta Materialia*, 46(18):6337 – 6349, 1998. ISSN 1359-6454. doi: [http://dx.doi.org/10.1016/S1359-6454\(98\)00333-4](http://dx.doi.org/10.1016/S1359-6454(98)00333-4).
- S. Zalkind, M. Polak, and N. Shamir. The adsorption of H<sub>2</sub>O vs O<sub>2</sub> on beryllium. *Surface Science*, 385:318–327, 1997.
- Pengbo Zhang, Jijun Zhao, and Bin Wen. Retention and diffusion of H, He, O, C impurities in Be. *Journal of Nuclear Materials*, 423(1–3):164 – 169, 2012. ISSN 0022-3115. doi: <http://dx.doi.org/10.1016/j.jnucmat.2012.01.027>.
- James F. Ziegler, M.D. Ziegler, and J.P. Biersack. SRIM – the stopping and range of ions in matter (2010). *Nuclear Instruments and Methods in Physics Research Section B: Beam Interactions with Materials and Atoms*, 268(11–12):1818 – 1823, 2010. ISSN 0168-583X. doi: <http://dx.doi.org/10.1016/j.nimb.2010.02.091>. 19th International Conference on Ion Beam Analysis.
- S.J. Zinkle. *Comprehensive Nuclear Materials*, chapter Radiation-Induced Effects on Microstructure, pages 65–98. Elsevier, 2012.

